

**Search for the weak vector boson scattering
in semileptonic final states in pp collisions
at $\sqrt{s} = 13$ TeV with the ATLAS detector**

重心系エネルギー 13TeV の陽子-陽子衝突
におけるアトラス検出器を用いた
セミレプトニック終状態を持つ弱ボソン散乱の探索

February 2020

Tatsumi NITTA
新田 龍海

**Search for the weak vector boson scattering
in semileptonic final states in pp collisions
at $\sqrt{s} = 13$ TeV with the ATLAS detector**

重心系エネルギー 13TeV の陽子 - 陽子衝突
におけるアトラス検出器を用いた
セミレプトニック終状態を持つ弱ボソン散乱の探索

February 2020

Waseda University

Graduate School of Advanced Science and Engineering

Department of Pure and Applied Physics

Research on Experimental Particle Physics

Tatsumi NITTA

新田 龍海

Abstract

The discovery of a Higgs boson in 2012 at the Large Hadron Collider and subsequent measurements of its properties represent a major milestone in the understanding of electroweak symmetry breaking. A study of the vector boson scattering provides essential tests that the Higgs mechanism is the sole source of the electroweak symmetry breaking. Additionally, new physics beyond the standard model that alters the quartic gauge couplings or the presence of additional resonances predicts enhancements for amplitudes of the vector boson scattering at high transverse momentum of the vector bosons and high invariant mass of the diboson system.

This thesis reports the first study for the weak vector boson scattering processes with semileptonic final states ($WW/WZ/ZZ + jj \rightarrow lvqq/llqq/\nu\nu qq + jj$) with data collected by the ATLAS detector in 2015 and 2016 at the Large Hadron Collider corresponding to an integrated luminosity of 35.5 fb^{-1} . The vector boson scattering processes with semileptonic final states are measured with an observed (expected) significance of 2.7 (2.5) standard deviations, and the fiducial cross-section is measured to be $\sigma_{EWVVjj}^{\text{fid,obs}} = 45.1 \pm 8.6(\text{stat.})_{-14.6}^{+15.9}(\text{syst.}) \text{ fb}$, where stat and syst represent the statistical and the sum of systematic uncertainties, respectively.

Since the measurement is compatible with the standard model prediction, the results are interpreted in terms of anomalous quartic gauge couplings in the context of the dimension-8 effective field theory. The limits obtained by this thesis are the most stringent to date.

In addition, this thesis achieved several remarkable improvements on the hadronically decaying weak boson identification techniques; the first measurement on the large- R jet energy resolution with the observed data; the first development for the machine learning based weak boson identification algorithms; and the first development for the polarization-sensitive large- R jet observable. Those results open new windows to detailed inspections of the vector boson scattering processes at the high invariant mass of the diboson system. Moreover, those results can be applied to other physics analyses using the highly boosted W or Z boson, for example, searches for new physics beyond the standard model with signatures of WW , WZ , and ZZ , and measurements of high-momentum W or Z boson differential cross-sections.

Acknowledgments

I appreciate all those who have been involved in the completion of this thesis, in particular for the persons described below.

To begin with, I would like to express my gratitude to my supervisor, Prof. Kohei Yorita for his plenty of supports. Since my early years as a graduate student, he has given me a lot of advice. His wide view of particle physics is always attracted my attention.

I would like to appreciate one of the analysis contacts of the semileptonic VBS analysis, Dr. Lailin Xu for many fruitful discussions. I have frequently discussed the details of the analysis with him at any time. His reasonable solutions based on deep insights always inspired me. I am truly grateful that we could work together. I also appreciate the other analysis contact, Dmitri Tsybyshev for his general supports for publishing the semileptonic VBS paper.

I much appreciate Dr. Koji Terashi who has taken care of my studies. His deep understandings of theoretical and experimental particle physics have fascinated me.

Dr. Takuya Nobe has kindly helped my studies from technical details to a big picture of the analysis. His foresight steadily has improved our analysis and avoids any hindrances. I have learned a lot from his attitude toward experimental particle physics.

My office life with Dr. Tatsuya Masubuchi was awesome. He is always positive, funny, and having a huge passion for particle physics. The moments hearing from him about progress on $VH \rightarrow b\bar{b}$ analysis was always very impressive.

I would like to thank Dr. Samuel Meehan for supporting jet related studies from the beginning of my work at CERN. A seminar which I have given in at the University of Washington, moreover, the whole stay with him is one of the impressive memory during my Ph.D. student life.

I would like to offer my special thanks to Prof. Hiroyuki Abe, Prof. Jun Kataoka, and Prof. Sachio Komamiya for their proof-readings of this thesis. In particular, Prof. Sachio Komamiya has given me a lot of highly sophisticated comments on this thesis from general understandings about theoretical particle physics to verification of calculations, which largely improve the quality of this thesis. In addition, his manifold encouragement, huge supports to arrange my career, practices of the defense, and interesting story of his experiences in his career, was quite helpful to become an experimental particle physicist.

Table of Contents

1	Introduction	10
2	Theoretical Foundation	12
2.1	The Standard Model of Elementary Particle Physics	12
2.1.1	Gauge Principle and SM Lagrangian	12
2.1.2	Higgs Potential and Electroweak Symmetry Breaking	13
2.1.3	Elementary Particles	13
2.2	Weak Vector Boson Scattering	15
2.2.1	Role of Higgs Boson in VBS	15
2.2.2	Production Cross-Sections and Branching Fractions	18
2.3	Anomalous Quartic Gauge Coupling and Effective Field Theory	21
2.3.1	Effective Field Theory for Vector Boson Scattering	21
2.3.2	Latest Limits on Coefficients for Dimension-8 Operators	23
2.4	Jet Phenomenology	25
2.4.1	Factorization	25
2.4.2	Parton Shower	26
2.4.3	Hadronization	26
2.4.4	Jet Mass	27
2.4.5	Jet Substructure	28
3	The ATLAS Experiment at the LHC	33
3.1	CERN Accelerator Complex	33
3.2	ATLAS Coordinate System	35
3.3	ATLAS Detector	35
3.3.1	Magnet	35
3.3.2	Luminosity Detectors	37

TABLE OF CONTENTS

3.3.3	Inner Tracker	37
3.3.4	Calorimeters	39
3.3.5	Muon Spectrometer	41
3.3.6	Trigger and Data Acquisition System	43
4	Physics Object Reconstruction and Identification	45
4.1	Tracks and Vertices	46
4.2	Topological-Clusters	46
4.3	Electrons	47
4.3.1	Reconstruction	47
4.3.2	Identification	48
4.3.3	Calibration	49
4.3.4	Trigger	51
4.4	Muons	53
4.4.1	Reconstruction	53
4.4.2	Identification	53
4.4.3	Calibration	54
4.4.4	Trigger	55
4.5	Jets	56
4.5.1	Reconstruction	56
4.5.2	Calibration	57
4.5.3	Identification	58
4.6	Overlap Removal	61
4.7	Missing Transverse Momentum	62
4.7.1	Reconstruction	62
4.7.2	Calibration	62
4.7.3	Trigger	62

5	Large-R Jet Calibration and Weak Vector Boson Identification	65
5.1	Large-R Jet Calibration	65
5.1.1	Grooming	65
5.1.2	MC Calibration	66
5.1.3	<i>in-situ</i> Calibration	67
5.2	Weak Vector Boson Identification	76
5.2.1	Track Assisted Mass	76
5.2.2	Two-Variable-Tagger	78
5.2.3	Jet-Substructure-Based Machine Learning Tagger	81
6	Search for Semileptonic Vector Boson Scattering	89
6.1	Experimental Signature of Semileptonic VBS and Backgrounds	89
6.2	Experimental Datasets and Monte-Carlo Simulations	91
6.2.1	Experimental Datasets	91
6.2.2	Trigger selection	92
6.2.3	Monte-Carlo Simulations	94
6.3	Event Selection	97
6.3.1	Preselection	98
6.3.2	0-lepton	98
6.3.3	1-lepton	98
6.3.4	2-lepton	99
6.3.5	Signal Regions and Control Regions	99
6.4	Multivariate Analysis	101
6.4.1	Training Setup	101
6.4.2	Input Variables	101
6.4.3	Output Variables	104
6.5	Background Modeling and Estimation	109
6.5.1	V+jets background	109
6.5.2	QCD multijet background	113
6.5.3	Interference between QCDVWjj and EWVWjj	116

TABLE OF CONTENTS

6.6	Fiducial Volume Definition and Measurement Procedure	118
6.6.1	Fiducial Volume Definition	118
6.6.2	Cross-Section Measurement Procedure	118
6.7	Systematic Uncertainties	120
6.7.1	Systematic Uncertainties in Signal Prediction	120
6.7.2	Systematic Uncertainties in Background Prediction	121
6.7.3	Experimental Systematic Uncertainties	122
6.8	Statistical Analysis and Interpretation	123
6.8.1	Methodology	123
6.8.2	Setup	124
6.9	Results	125
6.9.1	Event Yields	125
6.9.2	m_{jj}^{tag} Distributions at CR after Fitting	128
6.9.3	BDT Output Distributions at SR after Fitting	128
6.9.4	BDT Input Distributions at SR after Fitting	128
6.9.5	Nuisance Parameter Pulls, Constraints, and Correlations	138
6.9.6	Impacts of Nuisance Parameters	140
6.9.7	The Observed Signal-Strength and Fiducial Cross-Sections	142
7	Interpretation with Effective Field Theory	144
7.1	Setup for EFT interpretation	144
7.2	Statistical Test	148
7.3	Limits on Coefficient of Operators	148
8	Conclusions	151
9	Prospect for Future Measurement	152
9.1	Expected Sensitivity	152
9.2	Polarization-Sensitive Large-R jets Observable	153
9.2.1	Polarization-Sensitive Variables	154
9.2.2	Template of $\cos \theta^*$ Distribution for Purely Polarized W boson	154

TABLE OF CONTENTS

9.2.3	Event Selection	156
9.2.4	Results	158
Appendices		160
A	Matrix Elements of W^+W^- scattering	160
B	BDT Input Modeling for Semileptonic VBS Analysis	161
B.1	0-lepton channel	161
B.2	1-lepton channel	161
B.3	2-lepton channel	161
C	Understanding of BDT Input Correlation for Semileptonic VBS Analysis	185
D	Summary of Nuisance Parameters for Semileptonic VBS Analysis	195

CHAPTER 1

Introduction

The ultimate goal of particle physics is the discovery of the equation of motion of elementary particles governing our universe. Physicists have been uncovering the nature of “elementary” over time, and they reached the standard model of elementary particle physics (SM) which is the state-of-the-art understanding of particle physics to date. It is experimentally confirmed that the SM precisely predicts phenomena up to around the electroweak scale. In spite of its great success, there are plenty of uncovered mysteries such as dark matter [1, 2], dark energy [3, 4], Higgs boson mass [5, 6], and strong CP problem [7–9] among other things. Therefore, new physics beyond the SM (BSM) must exist at the TeV-scale or higher.

The Large Hadron Collider (LHC) [10] is the largest collider in the world, which accelerates protons up to a center-of-mass energy $\sqrt{s} = 13$ TeV. The LHC reproduces situations of the universe after 10^{-10} seconds since the birth of the universe which gives us an opportunity to test elementary particle physics theory around the TeV-scale. The ATLAS detector is made for the full reconstruction of those collision events incorporating the latest experimental technologies. In 2012, both the ATLAS [11] and CMS [12] experiments discover the last piece of the SM, the Higgs boson [13, 14].

Although four years of the successful operation of the LHC at $\sqrt{s} = 13$ TeV, no clear evidence of BSM has been found. Of course, physicists may have missed BSM phenomena while those have already been produced, however, the LHC might not reach to produce the lowest energy scale of BSM. The search for non-resonant objects which searches for deviations from the expectations of the differential cross-sections for the SM has attracted attention in recent years because it is sensible to BSM signals at the energy scale higher than the experimental reaches of direct resonant searches. Interestingly, this approach follows a history of the discovery of W boson. Beta-decay is explained by Fermi’s interaction while the theory is valid up to 100 GeV^1 , this leads to the theoretical necessity of W boson found by Glashow-Weinberg-Salam [15–17].

Weak vector boson scattering (VBS) is the most essential process to probe the electroweak sector of the SM since the leading order of Feynman diagrams only involve electroweak or Higgs bosons. The corresponding differential cross-sections are highly sensitive to theories for the alternative solution of electroweak symmetry breaking (EWSB) [18, 19]. Notably, such deviations are generally expected to be more significant in higher energy scatterings.

Both the ATLAS and CMS experiments have observed the existence of the VBS processes by using same-sign $W^\pm W^\pm jj$ channel [20, 21], $WZjj$ channel [22], and $ZZjj$ channel [23] with the 5 standard deviations in the fully leptonic final states (full-leptonic). An evidence with 3 standard deviations of the

¹⁾This thesis is based on the Planck units.

VBS process is also obtained in $Z\gamma jj$ [24] channel using pp collisions at $\sqrt{s} = 13$ TeV. Measurements of fiducial cross-sections for the VBS processes are reported for the $WZjj$ [25, 26], $Z\gamma jj$ [24, 27], and $W\gamma jj$ [28] channels. Constraints on anomalous quartic gauge couplings are reported in References [24, 26–34].

All of the above discoveries and an evidence for the VBS processes have been reported with full-leptonic final states. In general, backgrounds for most of collider physics searches are induced by quantum chromodynamics (QCD), hence requiring full-leptonic final states can reduce backgrounds drastically and extract very pure signal events from huge collision datasets. Thanks to this, full-leptonic final states have an advantage in discoveries and precise measurements for relatively low-energy phenomena, thus analyses with full-leptonic final states have been reported discoveries of the VBS processes sooner than analyses with the other final states. On the other hand, the leptonic decay of the weak vector boson loses its statistics due to its tiny branching fraction; for instance, the branching fraction of full-leptonic decay of $W^\pm W^\pm jj$ is less than 10% out of total. Consequently, the experimental energy reach for vector boson scatterings by full-leptonic channels is $\mathcal{O}(100)$ GeV at the highest. This leads to huge loss for opportunities to prove EWSB because *the SM without the Higgs boson* predicts divergence of scattering amplitude around 1 TeV and various BSMs predict deviations from the scattering amplitude of the SM at higher energy ranges than 1 TeV. More details on the theory and models are described in Chapter 2. The semileptonic decay of vector bosons ($WV \rightarrow \ell\nu qq$, $ZV \rightarrow \nu\nu qq$, $ZV \rightarrow \ell\ell qq$, where V represents W and Z) for the VBS processes have typically five times larger branching fractions than full-leptonic ones. Therefore, the semileptonic VBS analysis is a great probe for the highest energy VBS, i.e. it has one of the best sensitivity to BSMs related to EWSB. References [32, 34] report analyses similar to study in this thesis, while the former focused on the EW production of $VVjj$ in the $WV \rightarrow \ell\nu qq$ channel only and performed at $\sqrt{s} = 8$ TeV, the latter focused on only BSM search in $WV \rightarrow \ell\nu qq$, $ZV \rightarrow \nu\nu qq$ final states at $\sqrt{s} = 13$ TeV. This thesis presents the first search for both the SM VBS processes and anomalous quartic gauge couplings with the vector boson pair decaying semileptonically at $\sqrt{s} = 13$ TeV.

This thesis consists of nine chapters: Chapter 2 introduces theoretical foundations for this study with a brief introduction to particle physics. The CERN accelerator complex and the ATLAS detector are described in Chapter 3. Definitions of the physics objects and those identifications are summarized in Chapter 4. The large-R jet is the key object to the semileptonic VBS analysis, and the algorithms attendant on it are fairly complex, thus Chapter 5 describes large-R jet reconstruction and identification techniques in detail. The main component of this thesis, the search for semileptonic VBS is described in Chapter 6. Chapter 7 describes interpretations of the results with the effective field theory. The conclusions of this thesis are described in Chapter 8. Further discussions for future measurements are summarized in Chapter 9.

CHAPTER 2

Theoretical Foundation

This chapter describes theoretical foundations for the semileptonic VBS analysis. Section 2.1 describes specific introductions to the SM related to EWSB. Section 2.2 demonstrates the unitarity violation in the SM without the Higgs boson and its recovery by the processes related to Higgs-exchanges. Introductions to the anomalous quartic gauge couplings (aQGC) and the effective field theory (EFT) are described in Section 2.3. Due to its importance in the semileptonic analysis, the jet phenomenology is separately summarized in Section 2.4.

2.1 The Standard Model of Elementary Particle Physics

The standard model of particle physics (SM) consists of three parts: the gauge interaction, the fermion fields, and the Higgs mechanism. The gauge interaction explains the interaction between fermions and gauge self-interaction known as the strong force, weak force, and electromagnetism based on the gauge principle explained in Section 2.1.1. Fermion fields form the matters themselves due to the nature of Fermi-Dirac statistics, the list of the fermion fields is described in Section 2.1.3. The Higgs mechanism gives masses to elementary particles by EWSB explained in Section 2.1.2.

2.1.1 Gauge Principle and SM Lagrangian

The gauge transformation is a phase transformation of a field. A simple case for a one-parameter gauge transformation ($U(1)$) is shown in

$$\phi \rightarrow \phi' = e^{-i\alpha} \phi, \quad \phi^\dagger \rightarrow \phi'^\dagger = \phi^\dagger e^{i\alpha}, \quad (2.1)$$

where ϕ is a complex scalar field. α is a gauge parameter limited in an arbitrary real number. A special case in which α depends on space-time is called local gauge transformation. The gauge principle requires that a Lagrangian is invariant under the local gauge transformation. In the SM, the strong, weak and electromagnetic forces are the results of internal symmetries of the SM Lagrangian, $SU(3)$, $SU(2)$, and $U(1)$ gauge symmetries, respectively.

The SM Lagrangian density is symbolically given by

$$\mathcal{L} = -\frac{1}{4}(F_{\mu\nu}^a)^2 + \bar{\psi}(i\gamma^\mu D_\mu\psi) + y_{ij}\bar{\psi}_i\psi_j\phi + \text{h.c.} + |D_\mu\phi|^2 + \mu^2\phi^\dagger\phi - \lambda(\phi^\dagger\phi)^2, \quad (2.2)$$

where $F_{\mu\nu}^a = \partial_\mu A_\nu^a - \partial_\nu A_\mu^a + gf^{abc}A_\mu^b A_\nu^c$ and $D_\mu = \partial_\mu - igA_\mu^a t_r^a$ for fermion field ψ , scalar field ϕ , gauge field A , Yukawa coupling y_{ij} , Higgs self-coupling λ , representation matrices t_r^a , gauge coupling g , structure constant f^{abc} , matrix representation of the Clifford algebra γ^μ , and h.c. stands for Hermitian conjugate. Structure constants f^{abc} are non-zero for non-Abelian groups such as strong and weak forces, therefore, the forces interact with themselves, namely, they have Quartic Gauge Coupling (QGC) described in Section 2.2.

Notably, although fermions in nature have masses, there is no explicit mass term in Equation 2.2, and charged SU(2) fields can only have the Dirac mass expressed by $m\psi_L\psi_R + \text{h.c.}$ which explicitly breaks the gauge symmetry. Hence, the gauge symmetry, which is one of the most fundamental symmetry ever in physics is actually broken in our universe. A beautiful mechanism that explains masses of elementary particles despite preserving gauge symmetry at the early universe is EWSB by the Higgs potential.

2.1.2 Higgs Potential and Electroweak Symmetry Breaking

Let a SU(2) doublet: $\phi = \begin{bmatrix} \phi_1 \\ \phi_2 \end{bmatrix}$ with a potential $\mathcal{V}(\phi^\dagger\phi) = \mu^2\phi^\dagger\phi + \lambda(\phi^\dagger\phi)^2$ adds to a Lagrangian with SU(2) \times U(1) symmetry. Let μ have a dependency on temperature, the ground state of the potential has a non-zero value for $\mu^2 < 0$ which is called vacuum expectation value v . This is the EWSB, and as a result, three of four degrees of freedom mix with force carriers of SU(2) \times U(1) (W^\pm/Z bosons in the SM), and fermions obtain masses by Yukawa interaction [35]. The remaining degree of freedom of the Higgs potential becomes a scalar boson, the Higgs boson.

2.1.3 Elementary Particles

The elementary particles which follow Equation 2.2 and discovered to date are summarized in Table 2.1, and those constants are summarized in Table 2.2. All of the particles have already been observed in experiments. The weak bosons are the spin-1 particles obeying the Bose-Einstein statistics which have masses around 100 GeV. The weak bosons decay pairs of fermions whose branching fractions are discussed in Section 2.2.2. The fermions are the spin-1/2 particles obeying the Fermi-Dirac statistics which have masses proportion to the Yukawa couplings. The color triplet (singlet) fermions are called quarks (leptons). The Higgs boson is the only spin-0 particle obeying the Bose-Einstein statistics, and its mass is measured as ~ 125 GeV.

Table 2.1: A list of the elementary particles of the SM after EWSB and those representative quantum numbers is shown. J, Q, and SU(3) stand for spin, electric charge, and color charge. Bold characters represent the color multiplet, singlet, triplet, and octet.

Field	J	Q	SU(3)
u, c, t	1/2	2/3	3
d, s, b	1/2	-1/3	3
ν_e, ν_μ, ν_τ	1/2	0	1
e, μ, τ	1/2	-1	1
h	0	0	1
γ	1	0	1
Z	1	0	1
W^\pm	1	± 1	1
g	1	0	8

Table 2.2: A list of parameters related to particle fields shown in Table 2.1 is shown. $s_W = \sin(\theta_W)$ is a sine of the Weinberg angle. Values are taken from Reference [36].

Parameter Name	Expected or Measured Value
Yukawa Couplings	$y_u = 10^{-5}, y_c = 7 \times 10^{-5}, y_t = 1,$ $y_d = 3 \times 10^{-5}, y_s = 5 \times 10^{-4}, y_b = 0.03,$ $y_e = 3 \times 10^{-6}, y_\mu = 6 \times 10^{-4}, y_\tau = 0.01$
Fine Structure Constant	$\alpha = 1/127$
Strong Coupling Constant	$\alpha_s = 0.12$
Weinberg Angle	$s_W^2 = 0.23$
Higgs Self Coupling Constant	$\lambda = 0.1$
PMNS matrix (parametric representation)	$\theta_{12} = 34, \theta_{13} = 8.5, \theta_{23} = 247, \delta_{CP} = 200$
CKM matrix (parametric representation)	$\theta_{12} = 13.0, \theta_{13} = 0.2, \theta_{23} = 2.4, \delta_{13} = 1.2$

2.2 Weak Vector Boson Scattering

Due to the non-Abelian structure of $SU(2)$, electroweak bosons have triple and quartic vertices. In the hadron collider physics, the VBS processes are one of the best probes to examine the structure of EWSB at the highest energies since those are only related to the Higgs bosons or electroweak bosons at the leading order of Feynman diagrams. The leading order of Feynman diagrams for the VBS processes are shown in Figure 2.1.

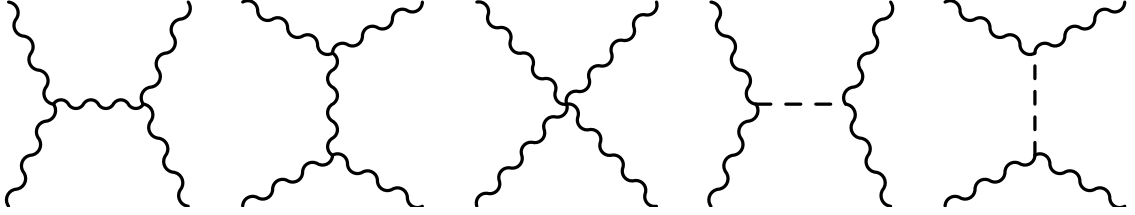


Fig. 2.1: The leading order Feynman diagrams of VBS are shown. From the left, those correspond to \mathcal{M}_1 , \mathcal{M}_2 , \mathcal{M}_3 , \mathcal{M}_4 , and \mathcal{M}_5 of Equation 2.8. The wavy and dashed lines represent the vector boson fields and Higgs fields, respectively.

2.2.1 Role of Higgs Boson in VBS

The virtue of the VBS processes derives from the cancellation of the unitarity violation by the quartic gauge couplings and the Higgs boson exchange explained as follows ¹⁾. Let a W^+W^- scattering be considered,

$$W^+(k_1, \lambda_1) + W^-(k_2, \lambda_2) \rightarrow W^+(k_3, \lambda_3) + W^-(k_4, \lambda_4), \quad (2.3)$$

where k_i and λ_i are the momenta and helicities of the W bosons, respectively.

The z -axis is defined by direction of an incoming W^- boson, and the x -axis is defined by a perpendicular component to z -axis of an outgoing W^- boson direction. The k_i and polarization vectors $\epsilon_i(\lambda_i)$ are expressed explicitly in the center-of-mass frame as follows,

$$\begin{aligned} k_1^\mu &= (E_W, 0, 0, -p_W), \\ k_2^\mu &= (E_W, 0, 0, p_W), \\ k_3^\mu &= (E_W, -p_W \sin \theta, 0, -p_W \cos \theta), \\ k_4^\mu &= (E_W, p_W \sin \theta, 0, p_W \cos \theta), \\ \epsilon_1^\mu(0) &= (-p_W, 0, 0, E_W)/M_W, \\ \epsilon_2^\mu(0) &= (-p_W, 0, 0, -E_W)/M_W, \end{aligned}$$

¹⁾This discussion is based on Reference [37].

2.2. WEAK VECTOR BOSON SCATTERING

$$\begin{aligned}
\epsilon_3^\mu(0) &= (p_W, -E_W \sin \theta, 0, -E_W \cos \theta)/M_W, \\
\epsilon_4^\mu(0) &= (p_W, E_W \sin \theta, 0, E_W \cos \theta)/M_W, \\
\epsilon_1^\mu(\pm) &= (0, -1, \pm i, 0)/\sqrt{2}, \\
\epsilon_2^\mu(\pm) &= (0, 1, \pm i, 0)/\sqrt{2}, \\
\epsilon_3^\mu(\pm) &= (0, -\cos \theta, \mp i, \sin \theta)/\sqrt{2}, \\
\epsilon_4^\mu(\pm) &= (0, \cos \theta, \mp i, -\sin \theta)/\sqrt{2},
\end{aligned} \tag{2.4}$$

where θ is a scattering angle between \vec{k}_3 and z-axis, m_W , E_W , and p_W are mass, energy, and absolute value of momentum of W boson, respectively. The Mandelstam variables are defined as

$$\begin{aligned}
s &= (k_1 + k_2)^2 = 4E_W^2, \\
t &= (k_1 - k_3)^2 = 4p_W^2 \sin^2 \theta/2, \\
u &= (k_1 - k_4)^2 = -4p_W^2 \cos^2 \theta/2.
\end{aligned} \tag{2.5}$$

Polarized and unpolarized (unpol.) differential cross-sections are represented as

$$\left(\frac{d\sigma}{d\Omega} \right)_{\lambda_1, \lambda_2, \lambda_3, \lambda_4} = \frac{1}{64\pi^2 s} |\mathcal{M}_{\lambda_1, \lambda_2, \lambda_3, \lambda_4}|^2, \tag{2.6}$$

$$\left(\frac{d\sigma}{d\Omega} \right)_{\text{unpol.}} = \frac{1}{9} \sum_{\lambda_1, \lambda_2 = -1}^1 \sum_{\lambda_3, \lambda_4 = -1}^1 \left(\frac{d\sigma}{d\Omega} \right)_{\lambda_1, \lambda_2, \lambda_3, \lambda_4}^2, \tag{2.7}$$

$$\begin{aligned}
\text{where } \mathcal{M}_{\lambda_1, \lambda_2, \lambda_3, \lambda_4} &= -e^2 \left(\frac{1}{s} + \frac{c_W^2}{s_W^2} \frac{1}{s - m_Z^2} \right) \mathcal{M}_1 \\
&\quad - e^2 \left(\frac{1}{t} + \frac{c_W^2}{s_W^2} \frac{1}{t - m_Z^2} \right) \mathcal{M}_2 \\
&\quad - \frac{e^2}{s_W^2} \mathcal{M}_3 \\
&\quad - \frac{e^2 M_W^2}{s_W^2} \frac{1}{s - m_H^2} \mathcal{M}_4 \\
&\quad - \frac{e^2 M_W^2}{s_W^2} \frac{1}{t - m_H^2} \mathcal{M}_5,
\end{aligned} \tag{2.8}$$

where σ , Ω , e , m_H , and m_Z stand for cross-section, solid angle, electric charge, masses of the Higgs and Z bosons, respectively. c_W and s_W represent cosine and sine of Weinberg angles, respectively. \mathcal{M}_1 - \mathcal{M}_5 represent matrix elements corresponding to the Feynman diagrams in Figure 2.1, which are explicitly shown in Appendix A. At high energies ($s \gg m_H, t$), \mathcal{M}_2 and \mathcal{M}_5 are the dominant components, and $\mathcal{M}_2 \propto s$ while $\mathcal{M}_5 \propto -s$. If there is no Higgs boson, i.e. $m_H \rightarrow \infty$, the \mathcal{M}_5 term disappears and $\mathcal{M}_2 \propto s$ violates unitarity. The existence of the Higgs boson implies that the \mathcal{M}_5 term cancels the \mathcal{M}_2 term, as a result, the unitarity for the VBS processes preserves.

2.2. WEAK VECTOR BOSON SCATTERING

Total cross-sections are given by integration over the range for the phase-spaces:

$$\sigma = \int_{0^\circ}^{360^\circ} d\phi \int_{\theta_{\text{cut}}}^{180^\circ - \theta_{\text{cut}}} d\theta \sin \theta \frac{d\sigma}{d\Omega}, \quad (2.9)$$

where θ_{cut} represents a polar angular cut. Cross-sections at high-energy for each polarization state are expressed as

$$\sigma_{\text{LLLL}} = \pi \frac{\alpha^2}{s_W^4} \frac{1}{s} \left(\frac{(M_H^2 + M_Z^2)(2M_Z^2 L_c + M_H^2 c)}{4M_W^4} + c \frac{75 - 26c^2 - c^4}{48c_W^4(1 - c^2)} \right), \quad (2.10)$$

$$\begin{aligned} \sigma_{\text{LLLT}} &= -\pi \frac{\alpha^2}{s_W^4} \frac{1}{s^2} \left(\frac{(M_H^2 + 4M_W^2 + M_Z^2)^2 L_c}{4M_W^4} \right. \\ &\quad \left. + c \frac{3(M_H^2 + 2(3M_W^2 + M_Z^2))^2 - (6 - c^2)(2M_W^2 + M_Z^2)^2}{12M_W^2} \right), \\ &= \sigma_{\text{LLTL}} = 2\sigma_{\text{LTLL}} = 2\sigma_{\text{TLLL}}, \end{aligned} \quad (2.11)$$

$$\sigma_{\text{LLTT}} = \pi \frac{\alpha^2}{s_W^4} \frac{1}{s} \frac{c(3 + c^2)}{6} = 4\sigma_{\text{TLLL}}, \quad (2.12)$$

$$\sigma_{\text{LTLT}} = \pi \frac{\alpha^2}{s_W^4} \frac{1}{s} \left(\frac{c(5 - c^2)}{1 - c^2} + 2L_c \right) = \sigma_{\text{TLLL}}, \quad (2.13)$$

$$\begin{aligned} \sigma_{\text{LTLL}} &= \pi \frac{\alpha^2}{s_W^4} \frac{1}{s^3} \left((M_H^4 + M_Z^4 + 2M_H^2(8M_W^2 + M_Z^2))L_c + c \frac{(5 - c^2)(M_H^4 + M_Z^4)}{2(1 - c^2)} \right. \\ &\quad \left. + \frac{c(8M_W^2 + M_Z^2)(18M_H^2 + (3 + c^2)(8M_W^2 + M_Z^2))}{6} \right) = \sigma_{\text{TLLL}}, \end{aligned} \quad (2.14)$$

$$\sigma_{\text{LTTT}} = -\pi \frac{\alpha^2}{s_W^4} \frac{1}{s^2} M_W^2 (29c + 3c^3 + 20L_c) = \sigma_{\text{LTTT}} = 2\sigma_{\text{TTLT}} = 2\sigma_{\text{TTLL}}, \quad (2.15)$$

$$\sigma_{\text{TTTT}} = \pi \frac{\alpha^2}{s_W^4} \frac{1}{s} \left(c \frac{75 - 26c^2 - c^4}{3(1 - c^2)} + 8L_c \right), \quad (2.16)$$

where $c = \cos \theta_{\text{cut}}$, $L_c = \ln \frac{1-c}{1+c}$, L and T denote longitudinal and transverse polarizations, respectively. \sqrt{s} dependency for each polarization state combination is shown in Figure 2.2.

The cross-sections for each polarization combination and the cross-section without the QGC nor Higgs diagram are illustrated in Figure 2.2. The $W^T W^T \rightarrow W^T W^T$ scattering is dominant in the whole amplitude of the SM, and $W^L W^T \rightarrow W^L W^T$ and $W^L W^L \rightarrow W^L W^L$ processes are following. The processes containing polarization flips are suppressed by two or more orders of magnitude. If either QGC or Higgs diagrams are missing in the SM, the electroweak coupling becomes strong around $\sqrt{s} \sim 1$ TeV, and the unitarity of the $W^L W^L \rightarrow W^L W^L$ process is ultimately violated. In other words, the SM without the Higgs boson is no longer valid above TeV-scale. This extending of the validity of the SM is the other essential role of the Higgs boson besides a well-known mass generation mechanism. Therefore, a measurement of the cross-section around $\sqrt{s} \sim 1$ TeV is one of the crucial tests of EWSB. The discussions on cases of existing another source of EWSB adding to the Higgs mechanism are introduced in Section 2.3.

2.2. WEAK VECTOR BOSON SCATTERING

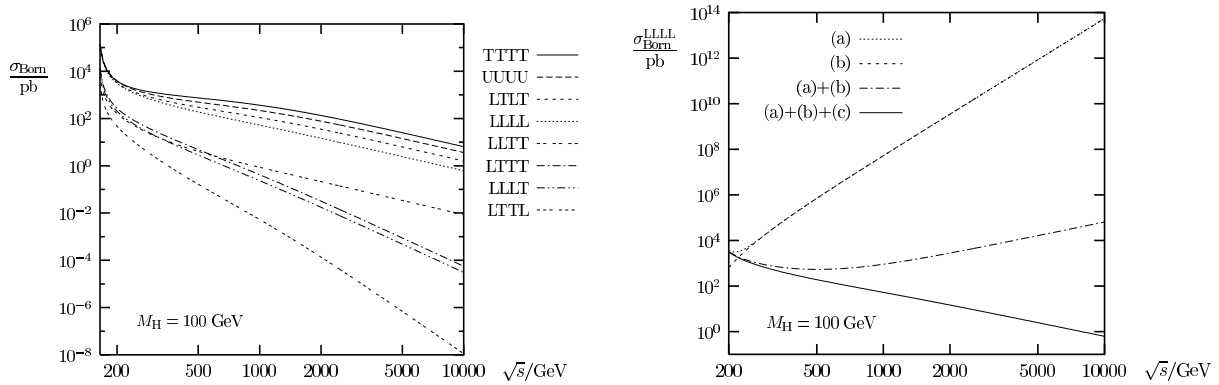


Fig. 2.2: Individual cross-section for each polarization combination (left) and cross-sections for various cases in which (a) Triple Gauge Coupling, (b) Quadratic Gauge Coupling, and (c) Higgs exchanges [37] are shown. The solid, dashed, dash-dotted lines represent the SM, SM without QGC nor Higgs changes, and SM without Higgs exchanges, respectively.

2.2.2 Production Cross-Sections and Branching Fractions

The total production cross-sections for each vector boson combination, $W^\pm W^\pm$, $W^\pm W^\mp$, $W^\pm Z$, and ZZ at a center-of-mass energy of 13 TeV are calculated with the MADGRAPH5_aMC@NLO 2.6.7 [38] event generator as shown in Table 2.3. The leading contribution to the total cross-section comes from

Table 2.3: A list of the total production cross-sections for each process calculated with the MADGRAPH5_aMC@NLO 2.6.7 event generator at 13 TeV proton-proton collisions. The Electroweak $t\bar{t}$ contributions are removed from the calculations by the Feynman diagram level.

Process	cross-section [pb]
$pp \rightarrow W^\pm W^\pm jj$	0.36
$pp \rightarrow W^\pm W^\mp jj$	1.13
$pp \rightarrow W^\pm Zjj$	0.65
$pp \rightarrow ZZjj$	0.14

the opposite-sign WW scattering process which is three times larger than that of the same-sign WW scattering process. The $W^\pm Z$ and ZZ scattering processes have subdominant contributions. For the purpose of observations of the highest energy VBS events which primarily need statistics, utilizing the opposite-sign WW scattering process is important.

The branching fractions for W and Z bosons are shown in Figure 2.3. For both of them, hadronic final states have dominant fractions, approximately 70%. Leptonic decays are subdominant, 10% and 3% for each W and Z boson. Moreover, the decays to τ are significantly hard to analyze because those are various decay modes, and the dominant hadronic decay is similar to jets. Thus making use of hadronic decay earns rich statistics to analyze.

Final states of the VBS processes are categorized as full-leptonic, semileptonic, and full-hadronic where

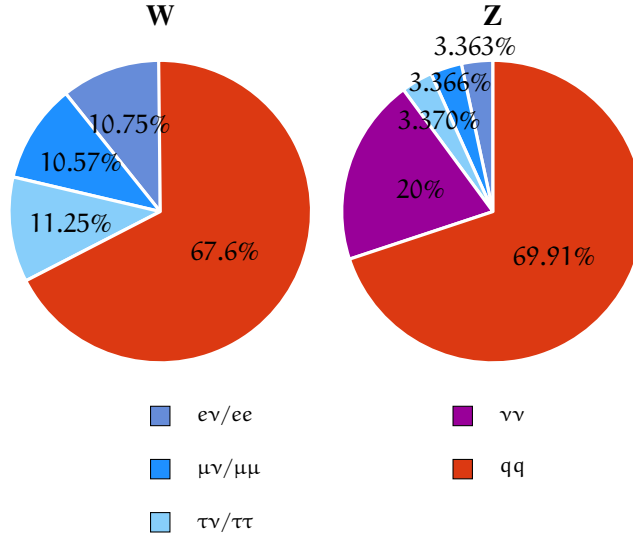


Fig. 2.3: Pie charts representing branching fractions for W (left) and Z (right) boson are shown. Antiparticles are not explicitly shown. q represents $u, d, s, c,$ and b quarks. Values are taken from Reference [36].

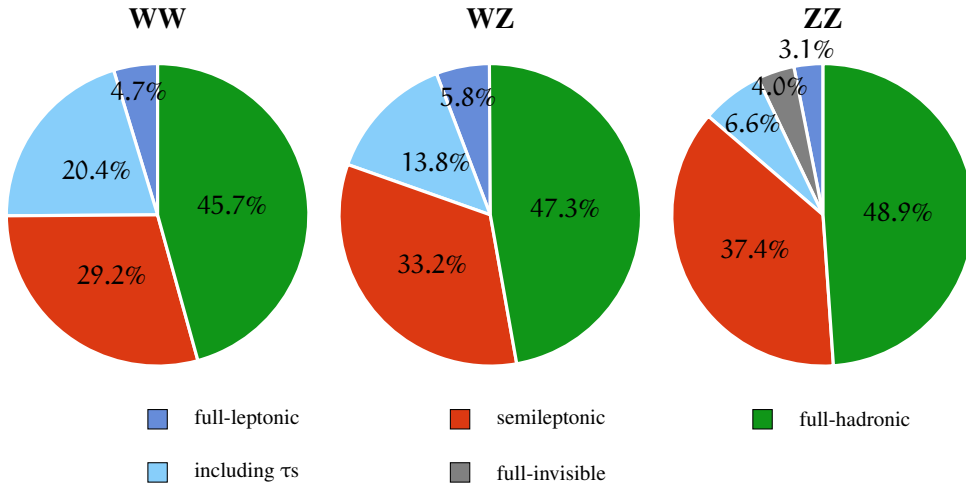


Fig. 2.4: Pie charts representing ratios of each final state are shown. The full-leptonic includes $WW \rightarrow l\nu l\nu$, $WZ \rightarrow l\nu ll$, and $ZZ \rightarrow ll ll/ll\nu\nu$, where l and ν represent charged leptons (e/μ) and neutrinos ($\nu_e/\nu_\mu/\nu_\tau$), and spectator quarks coming from protons are not explicitly shown. The including τ s represents final states including one or more τ s. The full-invisible represents $ZZ \rightarrow \nu\nu\nu\nu$. The semileptonic includes $WW \rightarrow l\nu qq$, $WZ \rightarrow l\nu qq/llqq$, and $ZZ \rightarrow llqq/\nu\nu qq$. The full-hadronic includes $WW/WZ/ZZ \rightarrow qq qq$.

2.2. WEAK VECTOR BOSON SCATTERING

both vector bosons decaying leptonically, only one of them decaying leptonically, and both of them decaying hadronically, respectively. Decays including taus and full-invisible decay where $ZZ \rightarrow \nu\nu\nu\nu$ are categorized separately. The branching fractions for each category are summarized in Figure 2.4. The semileptonic analysis has typically 6-10 times larger branching fractions than that of full-leptonic analysis.

The production cross-sections times branching ratios, which are proportional to the number of events produced in the LHC, are summarized in Figure 2.5. The same-sign dilepton analysis which has already

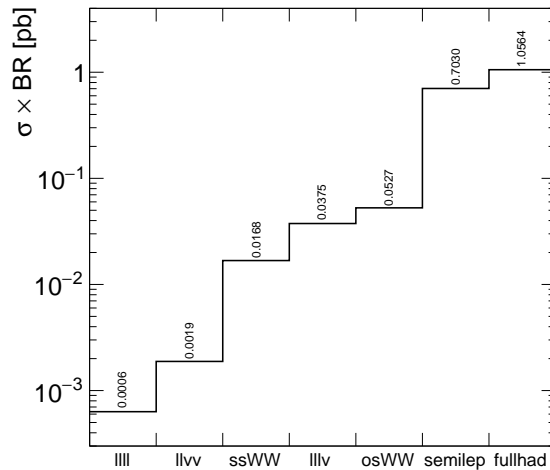


Fig. 2.5: A summary of production cross-section times branching ratio (BR), where llll, llvv, and llv indicate $ZZ \rightarrow llll/llvv$, and $WZ \rightarrow llv$, respectively. ssWW and osWW denote $W^\pm W^\pm \rightarrow l^\pm \nu l^\pm \nu$ and $W^\pm W^\mp \rightarrow l^\pm \nu l^\mp \nu$, respectively.

been reported observations is roughly 40 times less than that of the semileptonic analysis. Thus, for observations of the highest energy scatterings, the semileptonic or full-hadronic final states have huge advantages. The full-hadronic final states have enormous backgrounds from QCD induced multijet processes, hence, it is hard to reduce the background enough to observe the VBS processes. Therefore, the semileptonic final states are the most appropriate for the physics motivations mentioned in the previous section.

2.3 Anomalous Quartic Gauge Coupling and Effective Field Theory

The unitarity of the amplitude recovered by quartic gauge boson couplings and the Higgs boson exchanges can be broken again by additional modification of quartic gauge coupling by BSM. It is referred to as *anomalous quartic gauge couplings* (aQGC). For example, if an additional source of EWSB exists, the mediator must be coupled to the vector bosons and it affects the amplitudes of the VBS processes where the momentum transfer squared close to the mediator mass squared. Experimentally, aQGC can be observed as a deviation of the scattering amplitude from the SM prediction. There are three classifications of aQGC. A first classification of BSM is a composite Higgs model which explains the observed Higgs boson as a composite state of new particles. This classification consists of the technicolor theory and Pseudo-Nambu-Goldstone bosons. The former regards that the Higgs boson is generated by a technicolor mechanism [39, 40], the latter regards the Higgs boson as a pseudo-Nambu-Goldstone boson arising from the spontaneous breaking of an approximate global symmetry, such as $SO(5) \rightarrow SO(4)$ [41]. A second classification of BSM explains dark matter without any new particles. An example of this classification is that The Electroweak-Skyrmion [19, 42] which explains dark matter with an effective theory of the electroweak sector as an analogy with Skyrme solution of the nucleon [43]. The last classification of BSM is that there are additional heavy Higgs bosons [44], such as the Two Higgs Doublet Model [45]. The effects for aQGC are suppressed at low-energy phenomena such as Higgs boson total cross-section measurements, therefore, the direct VBS measurements bring invaluable information.

2.3.1 Effective Field Theory for Vector Boson Scattering

Since aQGC can claim many different models, model-independent interpretation is desired. Effective Field Theory (EFT) [46] is used for new physics interpretations throughout this thesis, which is a widely used theoretical framework to search for general new physics effects from much higher energy scales than the current experimental reach.

The Lagrangian of the EFT is given by

$$\mathcal{L}_{\text{EFT}} = \mathcal{L}_{\text{SM}} + \sum_{n>4} \sum_{\mathcal{O} \in \text{operators}} \frac{f_X^{\text{dim}-n}}{\Lambda^{n-4}} \mathcal{O}_X^{\text{dim}-n}, \quad (2.17)$$

where \mathcal{L}_{SM} is Equation 2.2, $f_X^{\text{dim}-n}$ is coupling constant, Λ is a cutoff scale, \mathcal{O} is operator, and n is mass dimension fulfilling $n > 4$. Since $\mathcal{L}_{\text{EFT}} = \mathcal{L}_{\text{SM}}$ for $\Lambda \rightarrow \infty$, the SM is a low-energy effective field theory in the context of the EFT framework. The EFT is particularly useful because heavy particles too heavy to produce are ignored in the EFT, and it gives a vast simplification for calculations. One awful feature of eliminating heavy particles is a nonrenormalizability, in which nontrivial effects of the heavy particles appear in higher dimensional interactions. Thus the validity of the EFT is bounded up to masses for the heavy particles (Λ) where is ensured to be renormalizable.

Examples of 6- and 8-dimensional EFT diagrams for gauge interaction are shown in Figure 2.6. Note that stringent limits on dim-6 interaction have already been set by using simple diboson processes in

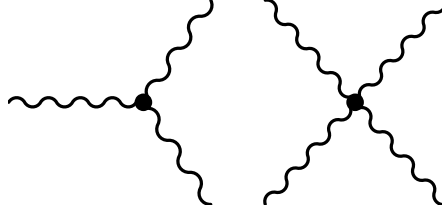


Fig. 2.6: Examples of 6- (left) and 8-dimensional (right) vertices. The wavy line denotes the vector boson field. The dot represents an anomalous gauge coupling.

$WV \rightarrow lvqq$ final states at CMS [47], $ZZ \rightarrow ll\nu\nu$ at ATLAS [48] at $\sqrt{s} = 13$ TeV with 36 fb^{-1} data. Therefore, searches for aQGC in this thesis focus on only 8-dimensional operators.

The Eboli model [49] classifies all aQGC in the linear/non-linear realizations of the gauge symmetry including up to two derivatives action on the gauge boson fields, which is used as a benchmark model of dimension-8 EFT for gauge interaction in Chapter 7. The operators are explicitly shown as follows.

The operators which contain only Higgs doublet ϕ are

$$L_{S0} = \left[(D_\mu \phi)^\dagger D_\nu \phi \right] \times \left[(D^\mu \phi)^\dagger D^\nu \phi \right], \quad (2.18)$$

$$L_{S1} = \left[(D_\mu \phi)^\dagger D^\mu \phi \right] \times \left[(D_\nu \phi)^\dagger D^\nu \phi \right], \quad (2.19)$$

$$L_{S2} = \left[(D_\mu \phi)^\dagger D_\nu \phi \right] \times \left[(D^\nu \phi)^\dagger D^\mu \phi \right]. \quad (2.20)$$

The operators which contain both Higgs doublet ϕ , $SU(2)_L$ field strength $\hat{W}_{\mu\nu} = \sum_j W_{\mu\nu}^j \sigma^j / 2$, and $U(1)_Y$ field strength $B_{\mu\nu}$ are ²⁾

$$L_{M0} = \text{Tr} \left[\hat{W}_{\mu\nu} \hat{W}^{\mu\nu} \right] \times \left[(D_\beta \phi)^\dagger D^\beta \phi \right], \quad (2.21)$$

$$L_{M1} = \text{Tr} \left[\hat{W}_{\mu\nu} \hat{W}^{\mu\beta} \right] \times \left[(D_\beta \phi)^\dagger D^\mu \phi \right], \quad (2.22)$$

$$L_{M2} = [B_{\mu\nu} B^{\mu\nu}] \times \left[(D_\beta \phi)^\dagger D^\beta \phi \right], \quad (2.23)$$

$$L_{M3} = [B_{\mu\nu} B^{\mu\beta}] \times \left[(D_\beta \phi)^\dagger D^\mu \phi \right], \quad (2.24)$$

$$L_{M4} = \left[(D_\mu \phi)^\dagger \hat{W}_{\beta\nu} D^\mu \phi \right] \times B^{\beta\nu}, \quad (2.25)$$

$$L_{M5} = \left[(D_\mu \phi)^\dagger \hat{W}_{\beta\nu} D^\nu \phi \right] \times B^{\beta\mu}, \quad (2.26)$$

$$L_{M7} = \left[(D_\mu \phi)^\dagger \hat{W}_{\beta\nu} \hat{W}^{\beta\nu} D^\nu \phi \right]. \quad (2.27)$$

²⁾ L_{M6} , L_{T3} , and L_{T4} are turned out to be verbose afterward.

The operators which contain only gauge fields are

$$L_{T0} = \text{Tr} [\hat{W}_{\mu\nu} \hat{W}^{\mu\nu}] \times \text{Tr} [\hat{W}_{\alpha\beta} \hat{W}^{\alpha\beta}], \quad (2.28)$$

$$L_{T1} = \text{Tr} [\hat{W}_{\alpha\nu} \hat{W}^{\mu\beta}] \times \text{Tr} [\hat{W}_{\mu\beta} \hat{W}^{\alpha\nu}], \quad (2.29)$$

$$L_{T2} = \text{Tr} [\hat{W}_{\alpha\mu} \hat{W}^{\mu\beta}] \times \text{Tr} [\hat{W}_{\beta\mu} \hat{W}^{\nu\alpha}], \quad (2.30)$$

$$L_{T5} = \text{Tr} [\hat{W}_{\mu\nu} \hat{W}^{\mu\nu}] \times B_{\alpha\beta} B^{\alpha\beta}, \quad (2.31)$$

$$L_{T6} = \text{Tr} [\hat{W}_{\alpha\nu} \hat{W}^{\mu\beta}] \times B_{\mu\beta} B^{\alpha\nu}, \quad (2.32)$$

$$L_{T7} = \text{Tr} [\hat{W}_{\alpha\mu} \hat{W}^{\mu\beta}] \times B_{\beta\mu} B^{\nu\alpha}, \quad (2.33)$$

$$L_{T8} = B_{\mu\nu} B^{\mu\nu} B_{\alpha\beta} B^{\alpha\beta}, \quad (2.34)$$

$$L_{T9} = B_{\alpha\mu} B^{\mu\beta} B_{\alpha\nu} B^{\nu\beta}. \quad (2.35)$$

Hence L_{S0} is the Hermitian conjugate of L_{S2} , those coefficients move proportionally ($f_{S0}/\Lambda^4 = f_{S2}/\Lambda^4$). Those two operators and coefficients are hereafter collectively called L_{S02} and f_{S02} , respectively. As shown in the above, operators having similar structures are grouped (as L_{SX} , L_{MX} , and L_{TX}), accordingly, events interacted by the operators in each group have similar kinematics. One obvious difference between those groups is polarization states of vector bosons. Weak bosons interacted by L_{SX} operators are longitudinally polarized, whereas ones interacted by L_{TX} operators are transversely polarized, and ones interacted by L_{MX} are those mixtures.

To organize correspondence between operators and vertices, quartic gauge vertices affected by those operators are summarized in Table 2.4. Since the semileptonic VBS analysis is contributed by WW , WZ , and ZZ outgoing weak boson pair, it is possible to search all of the dimension-8 EFT operators.

Table 2.4: Correspondences between operators and vertices are shown. A small circle (●) stands for the existence of the vertex with the interaction by the operator.

operators	WWWW	WWZZ	ZZZZ	WWγZ	WWγγ	ZZZγ	ZZγγ	Zγγγ	γγγγ
L_{S02}, L_{S1}	●	●	●						
L_{M0}, L_{M1}, L_{M7}	●	●	●	●	●	●	●		
$L_{M2}, L_{M3}, L_{M4}, L_{M5}$		●	●	●	●	●	●		
L_{T0}, L_{T1}, L_{T2}	●	●	●	●	●	●	●	●	●
L_{T5}, L_{T6}, L_{T7}		●	●	●	●	●	●	●	●
L_{T8}, L_{T9}			●			●	●	●	●

2.3.2 Latest Limits on Coefficients for Dimension-8 Operators

The latest limits on the coefficients of dimension-8 EFT operators for vector boson interactions in terms of the Eboli model with full-leptonic final states are summarized in Table 2.5. Most of the limits are provided by $W^\pm W^\pm \rightarrow l\nu l\nu$ and $Z^\pm \gamma \rightarrow ll\gamma$ processes. aQGC searches with semileptonic final states by CMS have better sensitivity than full-leptonic searches as shown in Reference [34].

Table 2.5: The best limits by leptonic search on coefficients for dimension-8 EFT operators shown in Equations 2.18-2.35 are shown. Currently, all the limits are provided by the CMS collaboration, and results from the ATLAS collaboration are in preparation.

Operator	Full-leptonic analyses Observed Limit [TeV ⁻⁴]	Process	Center of mass energy, Integrated Luminosity, Experiment	Reference
L _{S02}	[-7.7, 7.7]	$W^\pm W^\pm \rightarrow \nu \nu$	13 TeV, 35.9 fb ⁻¹ , CMS	[21]
L _{S1}	[-21.6, 21.8]	$W^\pm W^\pm \rightarrow \nu \nu$	13 TeV, 35.9 fb ⁻¹ , CMS	[21]
L _{M0}	[-4.2, 4.2]	$\gamma\gamma \rightarrow W^\pm W^\pm \rightarrow e\nu\mu\nu$	8 TeV, 19.7 fb ⁻¹ , CMS	[50]
L _{M1}	[-8.7, 9.1]	$W^\pm W^\pm \rightarrow \nu \nu$	13 TeV, 35.9 fb ⁻¹ , CMS	[21]
L _{M2}	[-8.2, 8.0]	$Z^\pm \gamma \rightarrow \ell\gamma$	13 TeV, 35.9 fb ⁻¹ , CMS	[24]
L _{M3}	[-21.0, 21.0]	$Z^\pm \gamma \rightarrow \ell\gamma$	13 TeV, 35.9 fb ⁻¹ , CMS	[24]
L _{M4}	[-15.0, 16.0]	$Z^\pm \gamma \rightarrow \ell\gamma$	13 TeV, 35.9 fb ⁻¹ , CMS	[24]
L _{M5}	[-25.0, 24.0]	$Z^\pm \gamma \rightarrow \ell\gamma$	13 TeV, 35.9 fb ⁻¹ , CMS	[24]
L _{M7}	[-12.0, 12.0]	$W^\pm W^\pm \rightarrow \nu \nu$	13 TeV, 35.9 fb ⁻¹ , CMS	[21]
L _{T0}	[-0.46, 0.44]	$ZZ \rightarrow \ell\ell\ell$	13 TeV, 35.9 fb ⁻¹ , CMS	[51]
L _{T1}	[-0.28, 0.31]	$W^\pm W^\pm \rightarrow \nu \nu$	13 TeV, 35.9 fb ⁻¹ , CMS	[21]
L _{T2}	[-0.89, 1.0]	$W^\pm W^\pm \rightarrow \nu \nu$	13 TeV, 35.9 fb ⁻¹ , CMS	[21]
L _{T5}	[-0.70, 0.74]	$Z^\pm \gamma \rightarrow \ell\gamma$	13 TeV, 35.9 fb ⁻¹ , CMS	[24]
L _{T6}	[-1.6, 1.7]	$Z^\pm \gamma \rightarrow \ell\gamma$	13 TeV, 35.9 fb ⁻¹ , CMS	[24]
L _{T7}	[-2.6, 2.8]	$Z^\pm \gamma \rightarrow \ell\gamma$	13 TeV, 35.9 fb ⁻¹ , CMS	[24]
L _{T8}	[-0.47, 0.47]	$Z^\pm \gamma \rightarrow \ell\gamma$	13 TeV, 35.9 fb ⁻¹ , CMS	[24]
L _{T9}	[-1.3, 1.3]	$Z^\pm \gamma \rightarrow \ell\gamma$	13 TeV, 35.9 fb ⁻¹ , CMS	[24]

2.4 Jet Phenomenology

Due to the nature of the asymptotic freedom [52] in $SU(3)$, an out-going high-energy colored particle transforms a shower of partons (*Parton shower*), the shower stops when each parton cooled down to an energy of approximately 1 GeV, then the partons become hadrons by picking up partons from a vacuum to be color singlets (*Hadronization*). Therefore, a colored particle itself cannot be directly observed. Experimentally, the resultant parton shower and hadronization, a bunch of hadrons is reconstructed as a *Jet*. This section describes theoretical and phenomenological understandings of jets in Sections 2.4.1-2.4.3³⁾.

This thesis handles two sorts of jets which have different origins, one is hadronically decaying W/Z jets (boson jets), and the other is the quark and gluon jets (q/g jets). An identification of boson jets from q/g jets takes an essential role in the semileptonic VBS analysis. The invariant mass of a jet and D_2 are used in Chapter 5. Sections 2.4.4 and 2.4.5 describe phenomenological understandings of the invariant mass of a jet and D_2 , respectively.

2.4.1 Factorization

The number of events generated by proton collisions with instantaneous luminosity \mathcal{L} is given by

$$N_{\text{events}} = \sigma \int \mathcal{L} dt, \quad (2.36)$$

where σ stands for the cross-section for a certain physics process. The cross-section σ for a hadron collider is not calculatable directly because it includes nonperturbative low-energy QCD. The factorization theorem allows us to calculate it approximately from the product of low- and high-energy QCD term. The high-energy QCD term is perturbative, thus it can be calculated at the desired order of QCD couplings. The low-energy QCD term is approximated by phenomenological models constructed to fits experimental data. The cross-section for the observable \mathcal{O} can be written as

$$\frac{d\sigma}{d\mathcal{O}} = \sum_{a,b} \int_0^1 dx_a dx_b \sum_F \int d\Phi_F f_a^{h_1}(x_a, \mu_F) f_b^{h_2}(x_b, \mu_F) \frac{d\hat{\sigma}_{ab \rightarrow F}}{d\mathcal{O}} D_F(\hat{\mathcal{O}} \rightarrow \mathcal{O}, \mu_F), \quad (2.37)$$

$$\frac{d\hat{\sigma}_{ab \rightarrow F}}{d\mathcal{O}} = \int d\Phi_F |\mathcal{M}_F|^2 \delta(\hat{\mathcal{O}} - \hat{\mathcal{O}}(\Phi_F)), \quad (2.38)$$

a and b in the first summation run over all partonic constituents of the colliding hadrons $h_{1,2}$, respectively. $f_a^{h_1}(x_a, \mu_F)$ and $f_b^{h_2}(x_b, \mu_F)$ denote nonperturbative parton density function (PDF). The second summation includes all possible final states for F in the processes $ab \rightarrow F$ with phase-space Φ_F . $\hat{\sigma}$ represents the perturbative partonic cross-section for high-energy QCD, $D_F(\hat{\mathcal{O}} \rightarrow \mathcal{O}, \mu_F)$ is a nonperturbative fragmentation function⁴⁾, \mathcal{M}_F stands for the matrix element for the final state F with phase-space Φ_F .

³⁾Experimental definitions of the jets in this study are introduced in Section 4.5.

⁴⁾The fragmentation and hadronization sometimes are used in the same meaning, while in this thesis, fragmentation represents both the parton shower and hadronization.

Since the PDF is nonperturbative, it is estimated by fits to collision data. In this thesis, NNPDF30LO PDF set [53] and CTEQ6L1 [54] are mainly used.

The dividing line of the perturbative and the nonperturbative terms cannot be determined a priori. The arbitrary scale, *factorization scale* (μ_F) is defined for each calculation. Typically, it is an order of $\mathcal{O}(10 - 100)$ GeV.

The idea of the factorization is not to try to explain fragmentation part from the first principle, in other words, the calculation for the fragmentation is needed to rely on the phenomenological model. The fragmentation process divided into parton shower and hadronization is described in the following sections.

2.4.2 Parton Shower

The parton shower takes the role of evolving outgoing colored partons from a scale of $t_{\text{hard}} \sim \mathcal{O}(10-100)$ GeV down to a cutoff t_{cutoff} at which QCD is no longer perturbative. There is no first principle for the parton shower, implementations of most of the Monte-Carlo (MC) simulations are based on a Markov Chain of $1 \rightarrow 2$ splittings from scale t_i to t_{i+1} , which referred to as *leading logarithm* (LL) approximation. The two representative generators: PYTHIA [55] and HERWIG [56] use different choices of t_{cutoff} . PYTHIA uses a p_T ordered shower [57], whereas HERWIG uses angular ordering [58].

2.4.3 Hadronization

After the parton shower, outgoing partons become hadrons with a neutral color (hadronization). As is the case with the parton shower, there is no first principle for the hadronization, PYTHIA and HERWIG use different phenomenological models: *String Model* and *Cluster Model*. Both of them have various parameters to fit experimental data. Details for the models are described in Reference [59]. For simplicity, explanations below taking into account only the hadronization of a pair of quark and anti-quark ($q\bar{q}$).

String Model: The string model based on the dynamics of a relativistic string which represents the color flow stretched between initial $q\bar{q}$. The string generates a linear confinement potential and an area for matrix elements:

$$|\mathcal{M}(q\bar{q} \rightarrow h_1, \dots, h_n)|^2 \propto e^{-bA}, \quad (2.39)$$

where A is the space-time area swept out as shown in Figure 2.7, b is a coefficient. Kinks for the string are generated by gluon radiations. This model has extra parameters for the distribution of transverse momentum and heavy particle suppression. It has several difficulties in the baryon production as described in Reference [60].

Cluster Model: Before making hadrons, the model splits a gluon into two quarks ($g \rightarrow q\bar{q}$) nonperturbatively after the parton shower. This operation makes the final states having only color-singlet $q\bar{q}$ combinations. Those color-singlet combinations are referred to as clusters, which mostly decay into pairs of hadrons isotropically. This model has fewer parameters, however, it has difficulties in the decay of

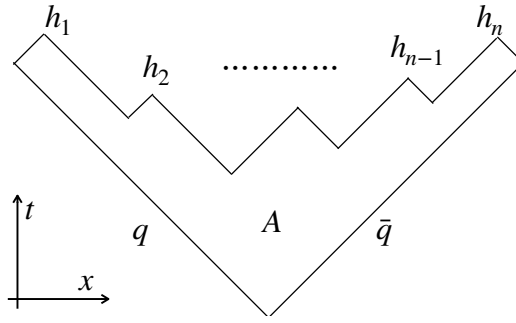


Fig. 2.7: A schematic graph of $q\bar{q}$ string in space-time is shown. The h_n represents resultant hadrons by the hadronization. The swept out area is referred to as A .

very massive clusters and appropriate suppressing of baryons and heavy quark productions. More details for the cluster model are described in Reference [61].

Both of the string and cluster models (i.e. PYTHIA and HERWIG) reproduce jets reasonably, but not perfectly. Therefore, PYTHIA and HERWIG are compared with each other for measurements of jet substructure variables, and the difference is taken as systematic uncertainty for each measurement. Details are described in Section 5.1.

2.4.4 Jet Mass

The invariant mass of jet is defined as

$$m_J = \sqrt{\left(\sum_i E_i\right)^2 - \left(\sum_i \vec{p}_i\right)^2}, \quad (2.40)$$

where E_i and \vec{p}_i is energy and momentum of i -th particle in the given jet, respectively.

Ideally, the boson jet mass is identical to the mass of the boson, however, it acquires additional mass from intrinsic sources such as large-angle gluon radiations during the parton shower and experimental sources such as pileup collisions and detector noises. The trimming algorithm introduced in Chapter 5 removes the extra contributions, experimentally.

As for the q/g jet mass, the jet forms non-negligible mass by large-angle gluon radiation, though those have tiny masses in elementary particle level. Assuming the leading order of Feynman diagrams, the invariant mass distribution can be expressed by

$$f_{LO}(m_J) = -\frac{4\alpha_s C}{\pi m_J} \log \frac{m_J}{ER}, \quad (2.41)$$

where C is the color factor $4/3$ for the color triplet and 3 for the color octet, E is the energy for the quark or gluon, and R is a radius of the jet.

Simulated invariant mass for q/g jets and boson jets distributions and p_T dependence for q/g jets are

shown in Figure 2.8. As shown in the distribution, q/g jets obtain extra masses extended to a few hundred GeV, although the mass peak for W jets are clearly distinguishable, therefore, the mass has discriminant powers again jets from other origins.

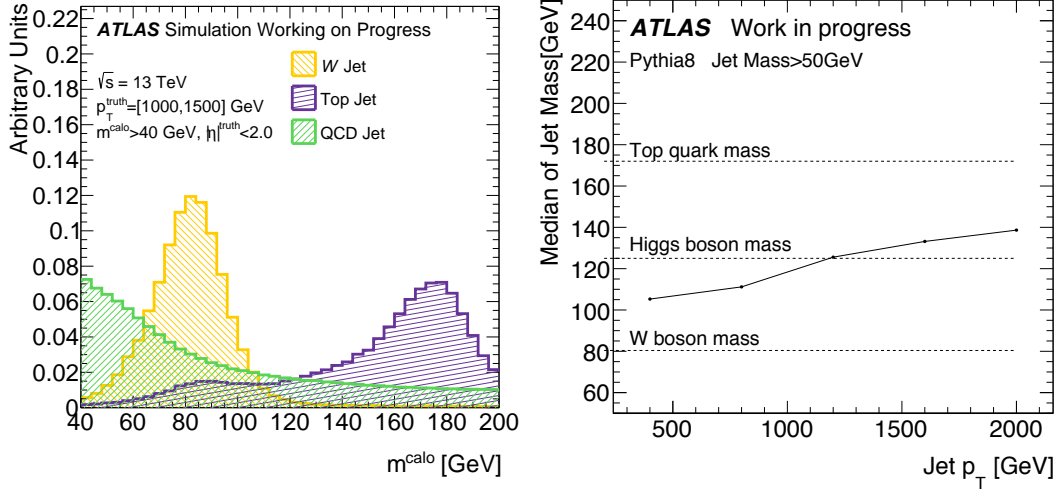


Fig. 2.8: Simulated W/top/q/g jets mass distributions (left) and median of the invariant mass for q/g jets with respect to the jet p_T (right) are shown. The jet masses originated from W bosons and top-quarks are peaked on those pole masses (80 and 170 GeV). The masses of q/g jets peak at low mass but extend to a few hundred GeV, therefore, those fake a massive elementary particle.

2.4.5 Jet Substructure

The 2-prong nature of boson jets is a key probe to distinguish it from q/g jets. Experimentally, the *jet substructure variables* differentiate those two by emerging the internal structure given by the four-momentum of constituents (typically hadrons) in a given jet. A representative variable is the D_2 which widely used in LHC analyses.

The definition of the D_2 is given by

$$D_2 = \frac{e_3^\beta}{(e_2^\beta)^3}, \quad (2.42)$$

$$\text{where } e_n^\beta = \frac{1}{p_{T,J}^n} \sum_{i_1 < i_2 < \dots < i_n \in J} \left(\prod_{a=1}^n p_{T,i_a} \right) \left(\prod_{b=1}^{n-1} \prod_{c=b+1}^n \Delta R_{i_b i_c} \right)^\beta, \quad (2.43)$$

where $p_{T,i}$ and $p_{T,J}$ represent transverse momentum of an i -th constituent and a given jet, respectively. R_{ij} denotes the spatial angle between i and j , and β is a constant. The e_n^β has two components, one is the p_T related term (the first product), and the other is angle related term (the second product), and those two relative effects are controlled by β , typically, $\beta = 1$ ($e_n^{\beta=1}, D_2^{\beta=1}$) is used in analyses including this thesis. The e_n^β is defined to be dimensionless by the division of n -th power of p_T of a given jet. The D_2

2.4. JET PHENOMENOLOGY

for a 2-prong jet (W jet) tends to have a lower value, whereas a background jet (q/g jets) tends to have a higher value.

To look into how the D_2 works as a 1- or 2-prong discriminant jet substructure variable, an analytical discussion is performed as follows⁵⁾.

Let jet constituents categorize as soft emissions (symbol s), collinear emissions (symbol c), and soft-collinear emissions (symbol sc) belonging to a given jet (symbol J) or leading and subleading subjets⁶⁾ (symbol 1 or 2). Schematic graphs for 1- and 2-prong jets are shown in Figure 2.9, where $z_X = p_{T,X}/p_{T,J}$, ΔR_{XY} is the angle between X and Y . The collinear emissions denote the core of jets formed by a tree-level quark or gluon before parton shower. The soft emissions represent gluon radiations. The soft-collinear emissions stand for a soft dipole-shower from a pair of color singlet quarks (boson jet) having a color connection between them.

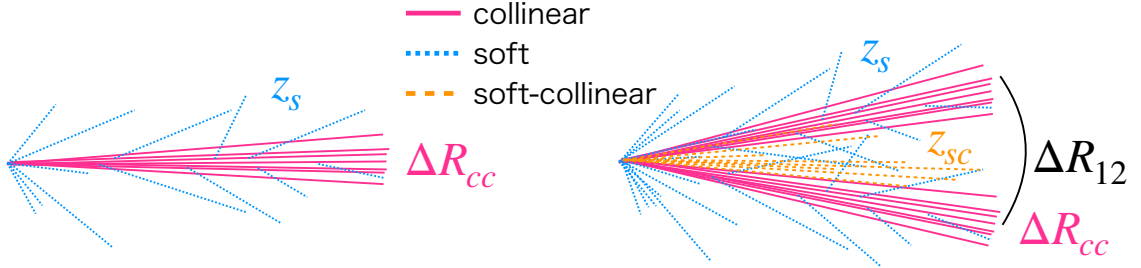


Fig. 2.9: Schematic graphs of 1-prong jet (left) and 2-prong jet (right) are shown. The 1-prong jet consists of collinear emissions (magenta) and soft radiations (cyan). The 2-prong jet consists of two subjets that having collinear emissions (magenta) and soft radiation (cyan), and soft-collinear emission from the dipole formed by two subjets (orange).

The given sort of jets is characterized by angle and p_T as shown in Table 2.6.

Table 2.6: Representative expressions for soft emissions, collinear emissions, soft-collinear emissions, and subjets are summarized. The small j (j) represents any other emissions in the jet.

soft	collinear	soft-collinear	subjet
$z_s = \frac{p_{T,s}}{p_{T,J}} \ll 1$	$z_c \sim O(1)$	$z_{sc} \ll 1$	$p_{T,1} \sim p_{T,2}$
$\Delta R_{s,J} \sim O(1)$	$\Delta R_{c,j} \sim O(1)$		$\Delta R_{cc} \ll \Delta R_{12} < 1$
	$\Delta R_{cc} \ll 1$		$p_{T,1} \cdot p_{T,2}/p_{T,J} \sim O(1)$

⁵⁾This discussion follows the thesis [62].

⁶⁾A few jets subdivided from a mother jet, which represent the expected number of hard cores.

For 1-prong (quark/gluon) jets, the e_2^β can be expanded with z_s and soft and collinear emissions,

$$e_2^\beta = \frac{1}{p_{T,J}^2} \sum_{i<j}^{N_{cl}} p_{T,i} p_{T,j} \Delta R_{ij}^\beta \quad (2.44)$$

$$\sim \frac{1}{p_{T,J}^2} \sum_s p_{T,s} p_{T,s} \Delta R_{ss}^\beta + \frac{1}{p_{T,J}^2} \sum_{s,c} p_{T,s} p_{T,c} \Delta R_{sc}^\beta + \frac{1}{p_{T,J}^2} \sum_c p_{T,c} p_{T,c} \Delta R_{cc}^\beta, \quad (2.45)$$

where \sum_s , $\sum_{s,c}$, and \sum_c represent summation over all soft emissions, all pairs of soft and collinear emissions, and all collinear emissions, respectively. The first term can be neglected because of $p_{T,s} \ll p_{T,J}$. The second term can be simplified as $\sum_s z_s$ by using $\Delta R_{sc} \sim 1$ and $p_{T,c} \sim p_{T,J}$. Then one can obtain,

$$e_2^\beta \sim \sum_s z_s + \sum_c \Delta R_{cc}^\beta. \quad (2.46)$$

Same as e_2^β , e_3^β which is the denominator of the D_2 can be simplified as

$$e_3^\beta \sim \sum_c \Delta R_{cc}^{3\beta} + \sum_s z_s^2 + \sum_{s,c} \Delta R_{cc}^\beta z_s. \quad (2.47)$$

A relation between e_3^β and e_2^β is obtained from Equation 2.46 and 2.47 as follows. In the case of $z_s \gg \Delta R_{cc}^\beta$, e_2^β and e_3^β are expressed as

$$\left. \begin{array}{l} e_2^\beta \rightarrow \sum_s z_s \\ e_3^\beta \rightarrow \sum_s z_s^2 \end{array} \right\} e_3^\beta \sim e_2^{2\beta}. \quad (2.48)$$

Whereas in the case of $z_s \ll \Delta R_{cc}^\beta$, e_2^β and e_3^β are expressed as

$$\left. \begin{array}{l} e_2^\beta \rightarrow \sum_c \Delta R_{cc}^\beta \\ e_3^\beta \rightarrow \sum_c \Delta R_{cc}^{3\beta} \end{array} \right\} e_3^\beta \sim e_2^{3\beta}. \quad (2.49)$$

As a result, one can obtain a condition between e_2^β and e_3^β for a 1-prong jet:

$$e_2^{3\beta} \leq e_3^\beta \leq e_2^{2\beta}. \quad (2.50)$$

As for the 2-prong jet (boson jet), the first term of Equation 2.46 is significantly smaller than the second term because two subjects have higher momenta than soft emissions. Hence, the e_2^β for 2-prong jet can be expressed as

$$e_2^\beta \sim \Delta R_{12}^\beta. \quad (2.51)$$

$$(2.52)$$

2.4. JET PHENOMENOLOGY

Same as e_2^β, e_3^β can be simplified as

$$e_3^\beta \sim \Delta R_{12}^{3\beta} \sum_{s,c} z_{sc}. \quad (2.53)$$

With a condition of $z_{sc} \ll 1$, one obtains a relation between e_2^β and e_3^β for a 2-prong jet as follows,

$$e_2^{3\beta} \sim \Delta R_{12}^{3\beta} \gg \Delta R_{12}^{3\beta} \sum_{s,c} z_{sc} \sim e_3^\beta \quad (2.54)$$

$$\rightarrow 0 < e_3^\beta < e_2^{3\beta}. \quad (2.55)$$

Summarizing the above, the 1- and 2-prong jets are populated in

$$\begin{aligned} \text{1-prong :} & \quad e_2^{3\beta} \leq e_3^\beta \leq e_2^{2\beta}, \\ \text{2-prong :} & \quad 0 < e_3^\beta < e_2^{3\beta}, \end{aligned} \quad (2.56)$$

as illustrated in Figure 2.10.

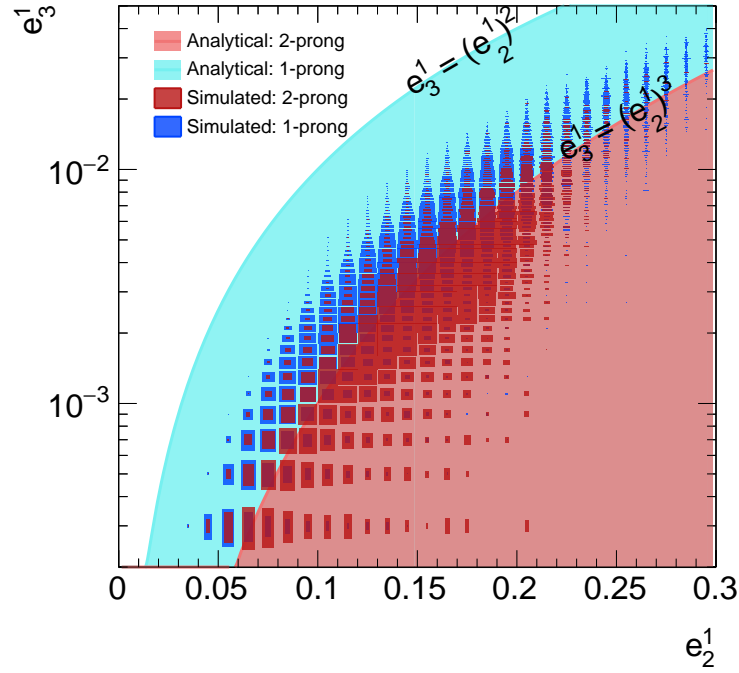


Fig. 2.10: Phase-spaces for 1-prong (light blue) and 2-prong jet (light red) on a $(e_2^{\beta=1}, e_3^{\beta=1})$ plane are shown. The phase-space is divided by a $e_3^\beta = e_2^{3\beta}$ line. Distributions for simulated W jets (deep red) and q/g jets (deep blue) are plotted on the same plane. Simulated samples are the same ones used in the boson identification study, details on the samples are described in Section 5.2.

1- and 2-prong jets are separated on a $e_2^\beta - e_3^\beta$ plane, i.e. that $D_2 = e_3^\beta / (e_2^\beta)^3$ variable can distinguish

2.4. JET PHENOMENOLOGY

1- and 2-prong jets. In practice, overlaid simulated samples are separated on the border of $e_3^\beta = e_2^{3\beta}$. Both of simulated boson jets and q/g jets distributions are shrunk around $e_3^\beta = e_2^{3\beta}$ due to finite detector resolutions, the pileup collisions contamination, and inadequate grooming (c.f. Section 5.1.1).

In summary, this calculation indicates that the virtue of the D_2 relies on the neglecting soft and/or collinear emissions which are difficult to handle from both the theoretical and experimental aspects.

CHAPTER 3

The ATLAS Experiment at the LHC

The ATLAS detector, the largest volume detector ever constructed for the collider experiment, is installed on the LHC accelerator which is in 100 m underground of CERN (European Organization for Nuclear Research) in Geneva, Switzerland. The collision events made by the LHC are recorded by the ATLAS detector, then used for particle physics analyses including the main body of this thesis, the semileptonic VBS analysis. Section 3.1 briefly introduces the accelerator complex at CERN. The coordinate system used in this thesis is described before the explanation of the ATLAS detector, in Section 3.2. The overview of the ATLAS detector and its important components are described in Section 3.3.

3.1 CERN Accelerator Complex

The CERN accelerator complex for the high energy proton-proton collisions is composed of the several proceeding colliders and the LHC. A schematic graph of the CERN accelerator complex is shown in Figure 3.1.

Protons are extracted from hydrogen atoms and accelerated up to 50 MeV by a linear accelerator (LINAC2). Then those protons are accelerated by sequential circulated synchrotron accelerators, BOOSTER (up to 1.4 GeV), PS (up to 25 GeV), and SPS (up to 450 GeV). Those accelerated protons are divided into two beams and injected into the LHC in the opposite direction. Protons are bent by 1,232 superconductive dipole magnets cooled by superfluid helium down to 1.9 K with the peak magnet field of 8.33 T. Protons are accelerated up to 7 TeV by eight radio frequency (RF) cavities with an oscillation frequency of 400.9 MHz. The acceleration takes 20 minutes. Due to the RF acceleration, the LHC beam consists of 2808 bunched protons with the 25 ns spacing, each of the bunches contains 10^{11} protons. The parameters shown in the above are design values taken from Reference [64]. Finally, those protons come into collision at several collision points. The ATLAS detector is installed in one of those collision points.

Comparisons of LHC parameters between design and actual runs are summarized in Table 3.1. The LHC runs with several beam conditions. The BCMS (Bunch Compressions, Merging and Splitting) beam merges two bunches into one, it enables transverse emittance to 50%. The 8b4e (8 bunches 4 empties) beam is a special beam type for dealing with abnormal background radiations and sudden beam losses due to the air leak issue in 2017 [65].

In 2018, the LHC-ATLAS experiment recorded a peak luminosity¹⁾ of $2.1 \times 10^{34} \text{ cm}^{-2}\text{s}^{-1}$ with the Betatron function of $\beta^* = 30 \text{ cm}$ which is the highest recorded instantaneous luminosity ever.

¹⁾The luminosity represents the intensity of collision defined as $L = 1/\sigma \cdot dN/dt$, where σ , N , and t denote cross-section,

3.1. CERN ACCELERATOR COMPLEX

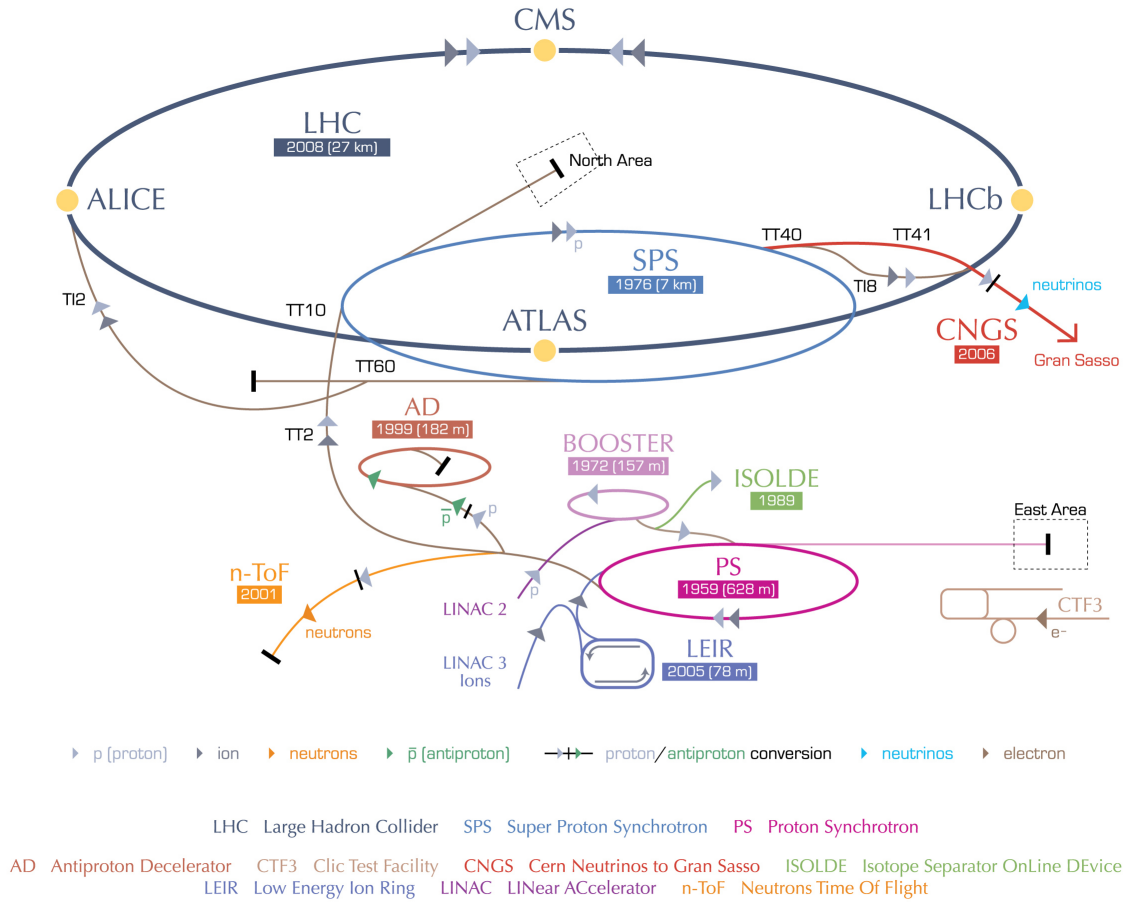


Fig. 3.1: A schematic graph of accelerators at CERN [63] is shown. The protons are accelerated by LINAC2, BOOSTER, PS, and SPS, and those are injected into LHC rings. The ATLAS detector is placed on one of the collision points of the LHC as well as the CMS, ALICE, and LHCb detectors.

Table 3.1: Comparisons of LHC parameters between designed ones and ones used in actual runs are summarized. Values are taken from Reference [64].

	Design	2015	2016	2017	2018
Beam type	Std	Std	Std/BCMS	8b4e/8b4e-BCS	BCMS
Energy [TeV]	7	6.5	6.5	6.5	6.5
Number of bunches per ring	2808	2244	2040/2076/2556	1916/1868	2556
Bunch spacing [ns]	25	25	25	25	25
Bunch population [10^{11}]	1.15	1.15	1.2	1.2/1.25	1.1
Transverse emittance [mm-mrad]	3.75	3.5	3.5/2.1	2.3/1.8	2
Betatron function @ IP1 [m]	0.55	0.8	0.4	0.4/0.3	0.3/0.25
Half crossing angle [μ rad]	142.5	145	185/140/150	150/120	160/130
Peak luminosity [$10^{34} \text{cm}^{-2} \text{s}^{-1}$]	1	0.55	0.83/1.4/1.74	1.5/1.9/2.06	2.1
Maximum pileup collision	~ 10	~ 15	$\sim 20/35/45$	$\sim 70/60/80$	~ 60
Stored beam energy [MJ]	360	270	345/320	240/245	320
Number of days	-	88	146	140	145
Integrated luminosity [fb^{-1}]	-	4.2	39.7	50.6	66

3.2 ATLAS Coordinate System

The ATLAS collaboration commonly uses a coordinate system as follows. The origin of the coordinate system is the interaction point. The z -axis runs along with the beam direction and the x - y plane is perpendicular to the beam direction. The positive x -axis points center of the LHC ring, the positive y -axis points the ground, and the positive z -axis points as coordinating a right-handed system. Frequently used definitions are as follows:

- Transverse particle momentum: $p_T = \sqrt{p_x^2 + p_y^2}$, where four-momentum of the particle is defined as $p_\mu = (E, p_x, p_y, p_z)$,
- Azimuthal angle: $\phi = \arctan p_y/p_x$,
- Polar angle: $\theta = \arctan p_z/p_x$,
- Rapidity: $y = \ln \left(\frac{E+p_z c}{E-p_z c} \right)$, where c is the speed of light,
- Pseudorapidity: $\eta = -\ln \tan (\theta/2)$,
- Opening angle in ϕ : $\Delta\phi_{ij} = \min(|\phi_i - \phi_j|, \pi - |\phi_i - \phi_j|)$,
- Opening angle in η : $\Delta\eta_{ij} = |\eta_i - \eta_j|$,
- Opening angle in the $\eta - \phi$ space: $\Delta R_{ij} = \sqrt{\Delta\phi_{ij}^2 + \Delta\eta_{ij}^2}$.

3.3 ATLAS Detector

The ATLAS Detector [11] was designed to measure all standard model particles ²⁾ produced by LHC collisions, a schematic overview of the whole ATLAS detector is shown in Figure 3.2. The detector position surrounding the beam pipe called *barrel*, and those aligned at the high η regions are referred to as *end-caps*.

The magnet system and the luminosity detector are introduced in Section 3.3.1 and 3.3.2, respectively. Four major subsystems, the inter tracker, the calorimeters, the muon spectrometer, and the trigger & data acquisition system are described in Section 3.3.3, 3.3.4, 3.3.5, and 3.3.6, respectively.

3.3.1 Magnet

The ATLAS magnet system consists of four large superconducting magnets with a dimension of 22 m in diameter and 26 m in length with a stored energy of 1.6 GJ. A solenoid aligned on the beam axis generates 2 T axial magnetic field for the inner detector, which placed inside the calorimeter system. A toroid on the barrel and two toroids on the end-caps are installed and those provide 0.5 and 1 T magnetic fields for muon detectors, respectively.

the number of collisions, and a certain time.

²⁾Neutrinos are detected as missing transverse momentum discussed in Section 4.7.

3.3. ATLAS DETECTOR

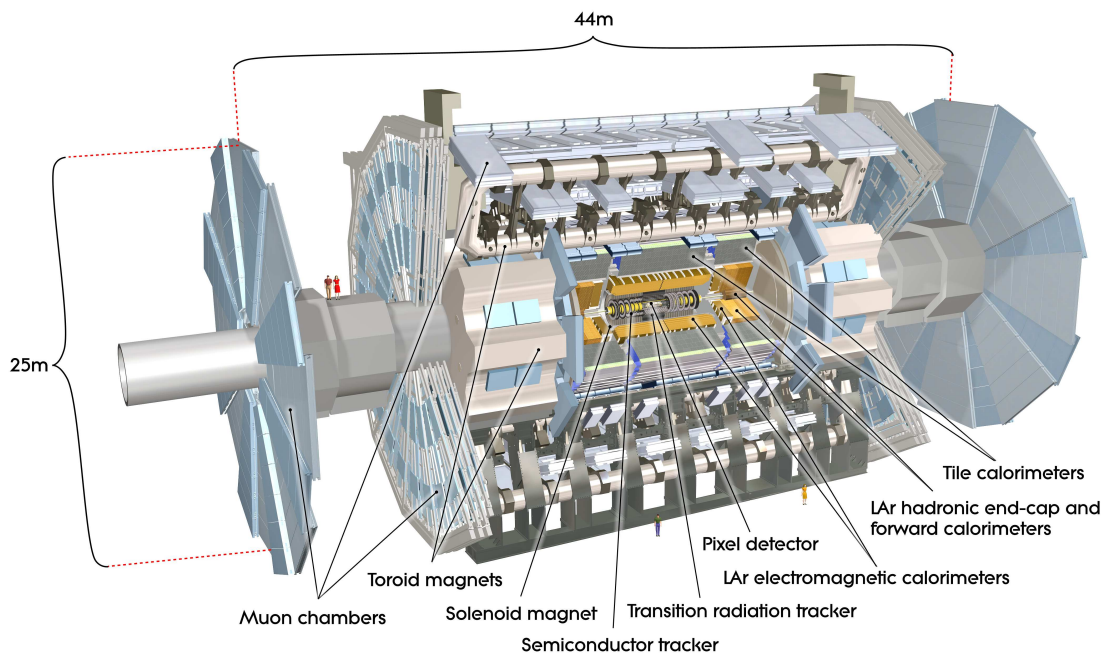


Fig. 3.2: A schematic overview of the ATLAS detector taken from Reference [11] is shown. The ATLAS has the dimensions of a 25 m diameter and a 44 m length, and its weight is 7000 tonnes. The several cylindrical detectors are explained in the main body.

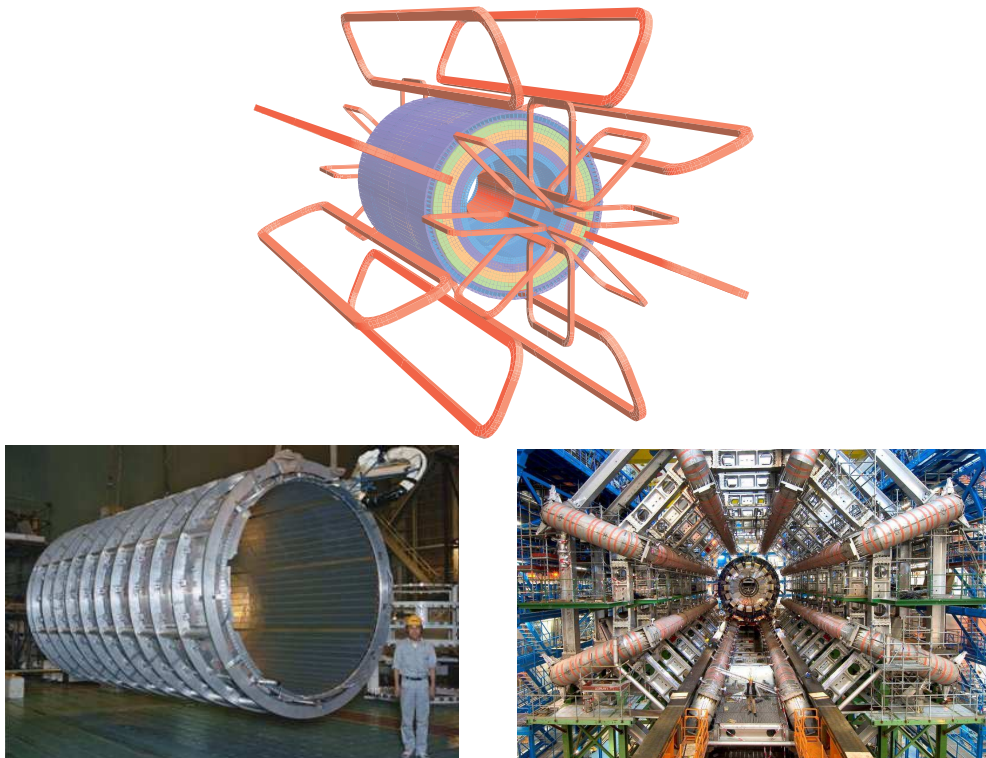


Fig. 3.3: A schematic diagram of the ATLAS magnet system (top), a photograph of the solenoid (left), and a photograph of the ATLAS magnet system (right) are shown. Those are taken from Reference [11].

3.3.2 Luminosity Detectors

A determination of luminosity is performed by LUCID³⁾ placed at ± 17 m from the center of the ATLAS detector aligned with the beam pipe. It is upgraded during a long shutdown in 2015 to enhance the radiation endurance [66]. The primary purpose of the LUCID is providing relative luminosity by detecting inelastic proton-proton scatterings in the forward region. The LUCID consists of Cerenkov tubes, and those enable us to count a number of charged particles proportion to the number of interactions per bunch crossing by using the pulse-height. A measurement in 2015 and 2016 achieved 2.1% accuracy on an absolute luminosity.

3.3.3 Inner Tracker

The tracking, the reconstruction of charged particle trajectory, is performed by the inner detectors. Those consist of three subsystems, *Pixels*, *SCT*, and *TRT*. The schematic graphs of the inner detectors are illustrated in Figure 3.4. Each subsystem is introduced as follows.

Pixel Detector: The most inner tracker system, the Pixel Detectors is made of four cylindrical layers of silicon pixel modules covering inner radii of 33.25-122.5 mm and $|\eta| < 2.5$. The most inner pixel layer called *IBL* (Insertable B-Layer) is newly added before the 2015 run for the better tracking quality and radiation endurance. The IBL is installed at 33.25 mm from the beamline, and it has $50 \times 250 \mu\text{m}$ pitch pixels and is qualified for a radiation hardness up to $5 \times 10^{15} \text{ 1-MeVn}_{\text{eq}}\text{cm}^{-2}$ ⁴⁾ corresponding to 550 fb^{-1} with a peak luminosity of $3 \times 10^{34} \text{ cm}^{-2}\text{s}^{-1}$ [67]. The next three outer cylindrical layers and two end-caps each with three discs cover $|\eta| < 2.5$ by 1744 pixel sensors with $250 \mu\text{m}$ thick and size of $50 \times 400 \mu\text{m}^2$. Each sensor has 47232 readout channels. The sensors are operated in the temperature between -5 and $-10 \text{ }^\circ\text{C}$ to reduce leakage current.

SCT: The subsystem placed at the next outer of the Pixel Detector is called *SCT* (Semiconductor Tracker) made by silicon microstrips located at 30-50 cm from the beamline. $80 \mu\text{m}$ pitch microstrips printed on the front and back with ± 20 mrad angled each other to reconstruct the two-dimensional location of the energy deposit. Modules are installed as four layers, there are 2112 modules on the barrel and 1976 modules in the end-cap regions.

TRT: The *TRT* made by transition radiation detectors located 50-100 cm from the beamline covering $|\eta| < 2.0$. Drift tubes with a dimension of 4 mm diameter and 144 cm length are filled by a mixture of Xenon (70%), CO_2 (27%), and Oxygen (3%). The TRT used not only tracking but also the separation between electrons and pions by using the difference of intensity of transition radiation characterized by those Lorentz factors.

Hits on the above detectors are collectively used for the tracking. Designed tracking resolution is $\sigma_{p_T}/p_T = 0.05\%p_T \oplus 1\%$ with coverage of $|\eta| \pm 2.5$.

³⁾LUCID stands for LUMinosity measurement using Cerenkov Integrating Detector.

⁴⁾ $1\text{-MeVn}_{\text{eq}}\text{cm}^{-2}$ is a unit for the number of neutrons with an energy of 1 MeV per squared centimeter.

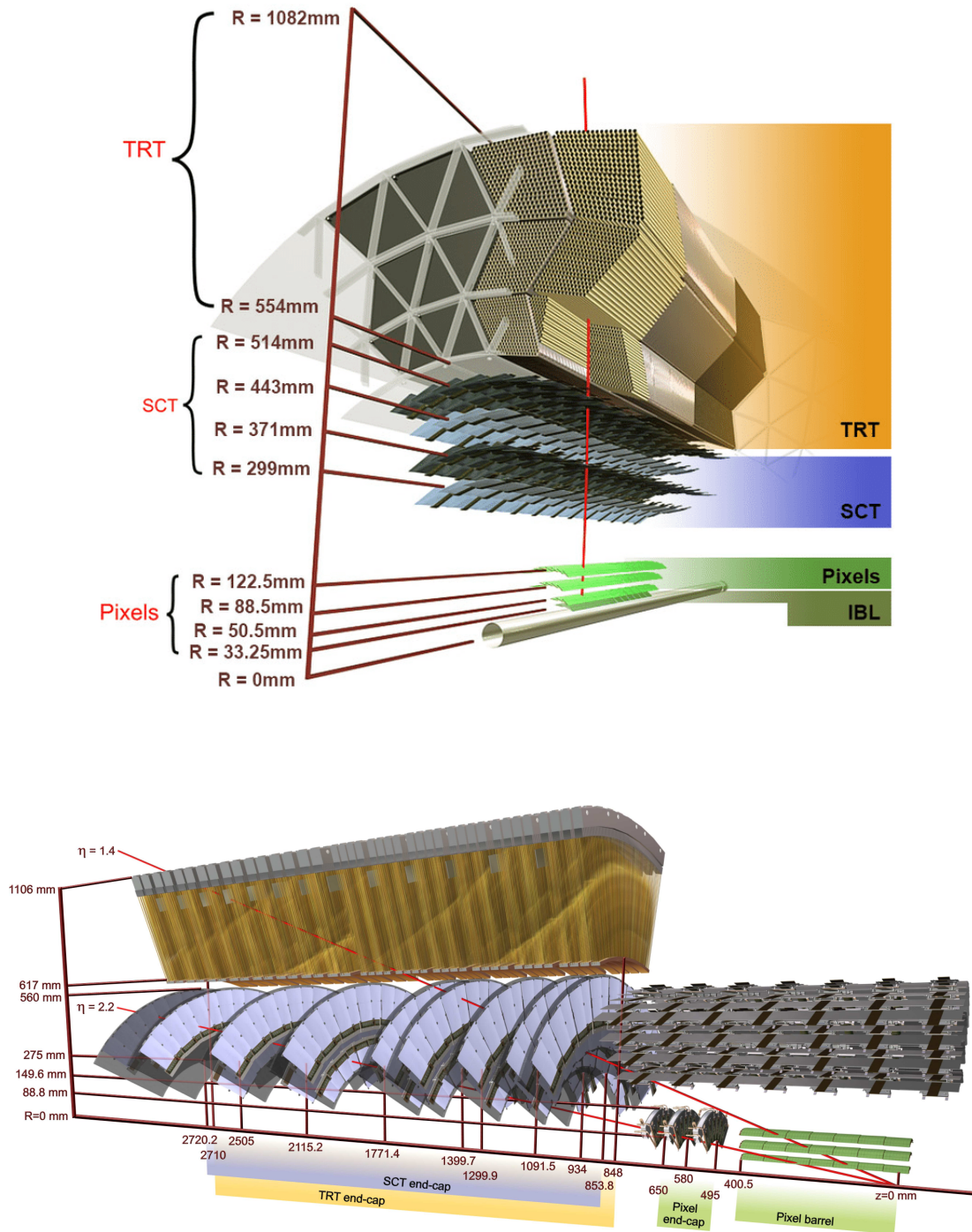


Fig. 3.4: Schematic graphs of the inner tracker system taken from Reference [11] are shown. The inner tracker has a dimension of a $\sim 1\text{ m}$ diameter which consists of the IBL at $R = 33.25\text{ mm}$, Pixel at $R = 50.5 - 122.5\text{ mm}$, SCT at $R = 299 - 514\text{ mm}$, and TRT at $R = 554 - 1082\text{ mm}$ as shown in the top graph. The barrel (end-cap) inner tracker covers pseudorapidity of 1.4 (2.5) as shown in the bottom graph.

3.3.4 Calorimeters

The calorimeters measure the energy of particles. Two major components, *Electromagnetic Calorimeter* and *Hadron Calorimeter* are built outside of the inner tracker as illustrated in Figure 3.5.

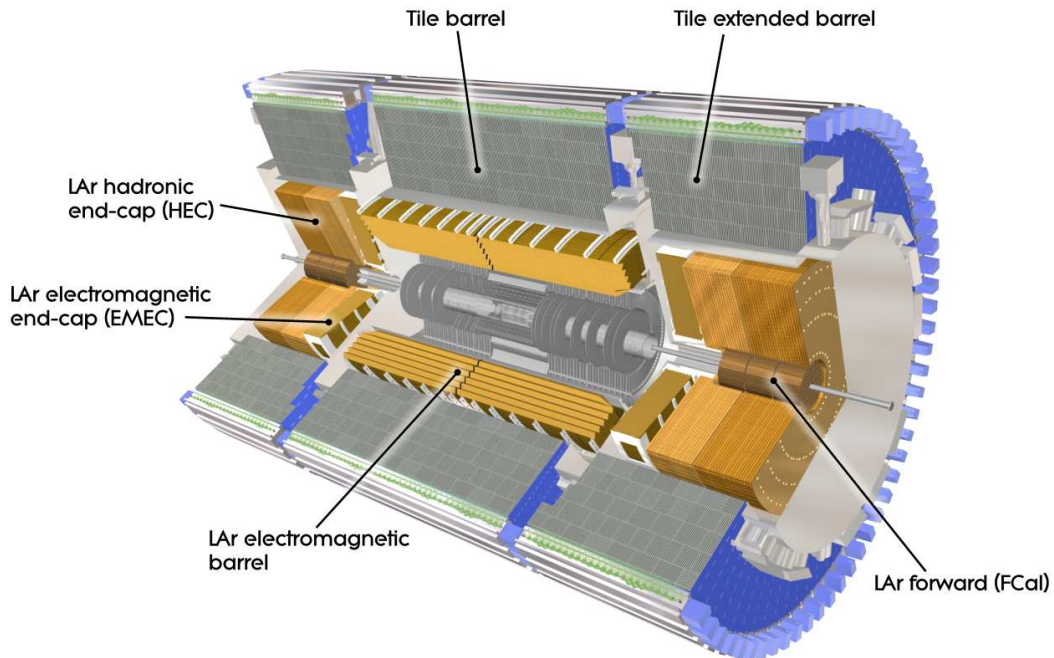


Fig. 3.5: A schematic graph of the calorimeter system taken from Reference [11] is shown. The calorimeter system consists of the LAr electromagnetic barrel, tile barrel, extended barrel, LAr electromagnetic end-cap, LAr hadronic end-cap, and LAr forward at the end-cap regions.

Electromagnetic Calorimeter: The electromagnetic calorimeter is made by lead and liquid Argon for detecting electromagnetic showers. It is subdivided into the barrel ($|\eta| < 1.4$) and end-caps ($1.4 < |\eta| < 3.2$) by pseudorapidity. The electromagnetic calorimeter is shaped like an accordion to cover complete ϕ ranges without any cracks and to extract signals rapidly at the tail or head of the electrodes. Both the barrel and end-cap electromagnetic calorimeters are divided into three longitudinal layers. The granularity and radiation length(X_0) for those at $\eta = 0$ are represented as $\Delta\eta \times \Delta\phi = 0.003 \times 0.1$ and $X_0 = 4.3$, $\Delta\eta \times \Delta\phi = 0.025 \times 0.025$ and $X_0 = 16$, and $\Delta\eta \times \Delta\phi = 0.05 \times 0.025$ and $X_0 = 2$. A schematic diagram for the barrel calorimeter cells is shown in Figure 3.6. The energy deposits in the liquid Argon gap induce electric current proportional to the deposited energy. The triangular input current pulse which has a length of the maximum drift time (typically 450 ns) is shaped by a bipolar filter in front-end boards [68] to avoid overlap with the next collision as shown in Figure 3.7. In order to cover the required dynamic range, three different gains, high, medium and low are implemented corresponding to 100, 10, and 1 linear gain scales, respectively. The amplified signals are sampled at 40 MHz and digitized by a 12-bit analog-to-digital (ADC) converter.

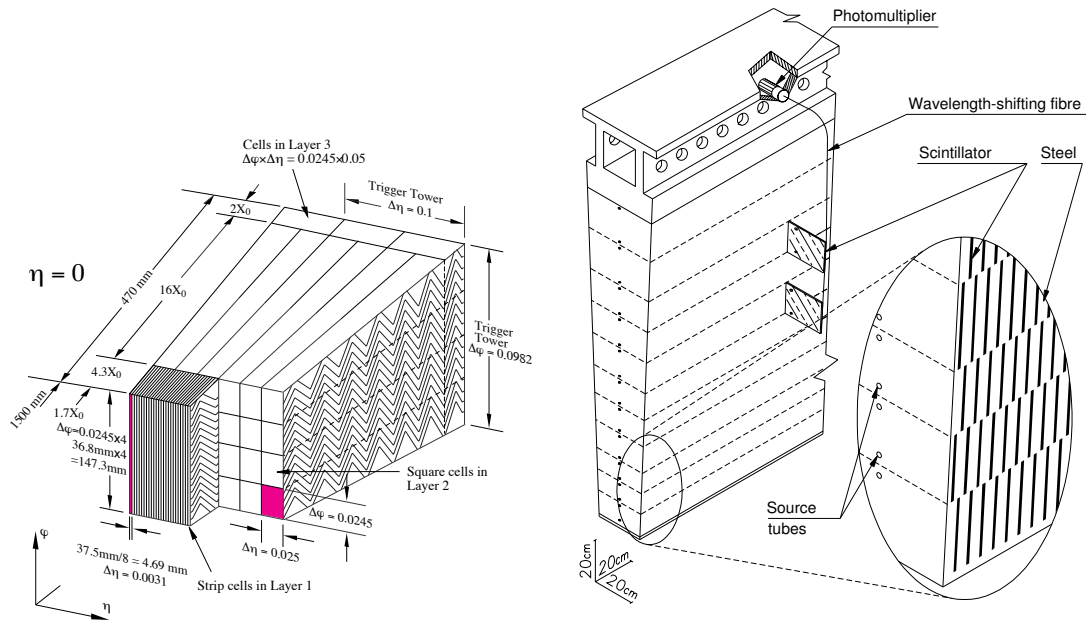


Fig. 3.6: A schematic graph of the electromagnetic calorimeter cells at pseudorapidity of 0 (left) and the barrel hadronic calorimeter cells (right) are shown. Those are taken from Reference [11]. The first layer of the electromagnetic calorimeter has a very thin width (4.69 mm) to separate γ and $\pi_0 \rightarrow \gamma\gamma$. The most of energy from electromagnetic shower deposits at the second layer having a 16 radiation length. The hadronic calorimeter cell consists of sandwiches of scintillator and steel, and the light produced by the scintillator is guided to the photomultiplier by wavelength-shifting fibers. Source tubes are made to calibrate photomultiplier gains.

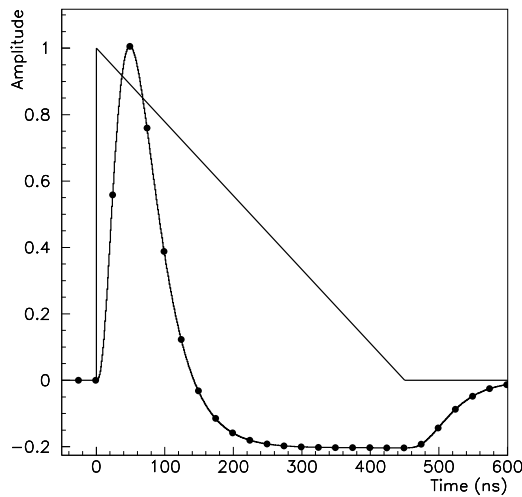


Fig. 3.7: A schematic graph of triangular pulse by the LAr calorimeter and a shaped amplitude are shown. The shaped amplitude is sampled every 25 ns. This plot is taken from [11].

Hadron Calorimeter: The hadronic calorimeter is placed outside of the electroweak calorimeter to detect the hadronic shower made by hadrons. It is separated into the barrel ($|\eta| < 1.7$), end-caps ($1.5 < |\eta| < 3.2$), and forward ($3.1 < |\eta| < 4.9$). The barrel is made by steel absorbers, scintillating tiles, and photomultipliers, which divided into three longitudinal layers having approximately 1.5, 4.1, and 1.8 interaction length thicks at $\eta = 0$. Each readout cell is segmented by $\Delta\eta \times \Delta\phi = 0.1 \times 0.1$ in the first and second layers and 0.1×0.2 in the third layer. A schematic diagram is shown in Figure 3.6. The end-cap calorimeters are a sampling calorimeter made by liquid Argon and copper plates. Cryostats are shared with the end-cap electromagnetic calorimeters and the forward hadron calorimeters. The size of a readout cell is $\Delta\eta \times \Delta\phi = 0.1 \times 0.1$ in the $1.5 < |\eta| < 2.5$ and 0.2×0.2 in the $2.5 < |\eta| < 3.2$. The forward hadron calorimeter the sampling calorimeter is made by liquid Argon and metal plates and is separated into three layers. The first layer uses copper plates as absorbers the same as the end-cap calorimeter. The second and third layer employs tungsten as absorbers. The absorption lengths are 2.66, 3.68 and 3.60 for each layer.

The hits in the calorimeters are collectively used in analyses to reconstruct the energy of particles. The designed energy resolution for the electromagnetic calorimeter is $\sigma_E/E = 10\%/\sqrt{E} \oplus 0.7\%$ with coverage of $|\eta| < 3.2$, and the barrel and end-cap hadron calorimeter are designed to be a resolution of $\sigma_E/E = 50\%/\sqrt{E} \oplus 3\%$ with coverage of $|\eta| < 3.2$. Design resolution of the forward hadron calorimeter is $\sigma_E/E = 100\%/\sqrt{E} \oplus 10\%$ covered $3.1 < |\eta| < 4.9$.

3.3.5 Muon Spectrometer

The muon spectrometers are placed on the most outside of the ATLAS detector to detect punch-through minimum ionization particles. It is used for both identification and triggering. Four types of modules are constructed as shown in Figure 3.8. The major parameters of them are shown in Table 3.2.

MDT and CSC: Precision measurements of muons are performed by Monitored Drift Tubes (MDT) and Cathode Strip Chambers (CSC). The MDT consists of three to eight layers of drift tubes with a diameter of 29.970 mm, filling with a mixture of Ar and CO₂ at 3 bar. Resultant electrons by the ionization are collected by a tungsten-rhenium wire with a diameter of 50 μm at a potential of 3080 V. Modules of multi-layer drift tubes with 1-6 m length and 1-2 m width are placed as three cylindrical layers with radii of 5, 7.5, and 10 m and four end-cap wheels at distances of $|z| \sim 7.4, 10.8, 14,$ and 21.5 m. 1088 MDT chambers cover $|\eta| < 2.7$ corresponding to 5500 m². The resolution of the MDT for the z -axis direction is 35 μm . Muon flux at the forward regions particularly higher than that of the barrel region, thus a position-sensitive detector, the CSC is aligned at $2 < |\eta| < 2.7$ for resolving multi-track ambiguities. The CSC system consists of two wheels with 16 chambers each. Each chamber consists of four CSC planes that have one layer of anode wire and orthogonally placed two layers of cathode strips. The orthogonal cathode strips allow measuring both η and ϕ positions. The total coverage of CSC is 65 m². The resolution of MDT for R and ϕ directions is 40 μm and 5 mm, respectively. The tracking resolution for the muon spectrometer is designed to be $\sigma_{p_T}/p_T = 10\%$ at $p_T = 1$ TeV.

RPC and TGC: The muon triggering is performed by Resistive Plate Chambers (RPC) and Thin Gap Chambers (TGC). For the barrel region ($|\eta| < 1.05$), three layers of the RPCs are placed. The RPC

3.3. ATLAS DETECTOR

is a simple chamber without wires filling with a mixture of $C_2H_2F_4$, Iso- C_4SF_6 , and SF_6 (94.7, 5, and 0.3% fractions for each) with a 2 mm gas gap operating a potential of 9.6 kV. In the end-cap regions ($1.05 < |\eta| < 2.4$), four layers of the TGCs are placed across an end-cap toroid magnet. The TGC operates as multi-wire proportional chambers with a 2.8 mm gas gap operating a potential of 2.9 kV. Both of the RPC and TGC have thinner gas gaps and higher voltages than the MDT and CSC, therefore, those achieved small average time jitters of 1.5 ns and 4 ns, respectively.

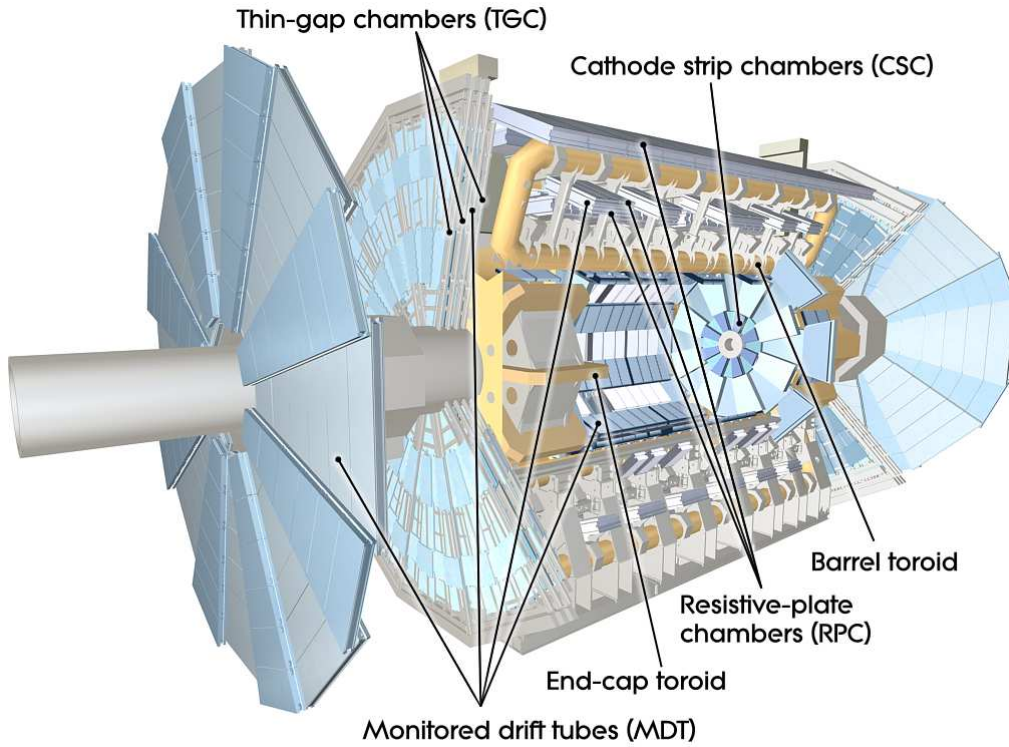


Fig. 3.8: A schematic graph of the muon spectrometer taken from Reference [11] is shown. The muon spectrometer consists of the MDT and RPC at the barrel region and the CSC and TGC at the end-cap regions. Muons are bent by the barrel toroid magnet to measure those charges and momenta.

Table 3.2: Major parameters of the muon spectrometer are summarized. The values are taken from Reference [11].

	Monitored drift tubes (MDT)	Cathode strip chambers (CSC)	Resistive plate chambers (RPC)	Thin gap chambers (TGC)
Coverage	$ \eta < 2.7$	$2.0 < \eta < 2.7$	$ \eta < 1.05$	$1.05 < \eta < 2.7$
#Chambers	1,088	32	544	3,588
#Channels	339,000	31,000	359,000	318,000
Function	Precision	Precision	Triggering	Triggering

3.3.6 Trigger and Data Acquisition System

It is impossible to store all information provided detectors for every 25 ns collision, the trigger system is installed to select physically motivated events as shown in Figure 3.9. Details of the trigger system are summarized in References [69, 70]. The ATLAS trigger system consists of a hardware-based Level-1 trigger (L1) and software-based High-Level Trigger (HLT).

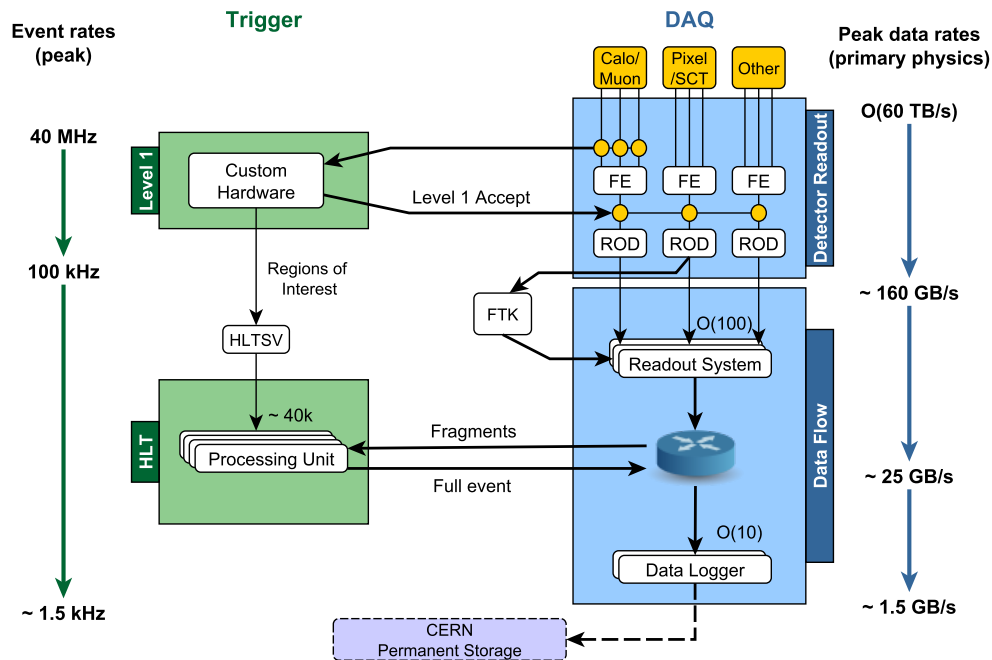


Fig. 3.9: A schematic graph of the trigger system taken from [69] is shown. The L1 trigger decisions are made for all collisions (40 MHz) with information about the calorimeters and the muon spectrometers. The L1 accept rate is approximately 100 kHz. The HLT trigger decisions are made for all events accepted by the L1 with information about full detectors and L1 objects. Approximately 1.5 kHz of events are accepted by the HLT, and all the hit information is stored in the permanent storage at CERN.

The L1 consists of L1Calo, L1Muon, L1Topo, and CTP (central trigger processor) for triggering electrons, muons, hadronic taus, photons, jets, and E_T^{miss} ⁵⁾. The L1Calo exploits 7168 calorimeter towers which made by the harsh granularity of $\Delta\phi \times \Delta\eta = 0.1 \times 0.1$ for fast readouts. For the L1 electron and L1 photon, 2×2 core towers and 12 surrounded towers of electromagnetic calorimeters are used for capturing the electron energy and calculating isolation requirement, respectively. For the L1 jet, wider 4×4 core towers of electromagnetic and hadron calorimeters are collectively used since the jet is typically wider than the showers for electrons and photons. The L1Muon makes use of RPC and TGC hits and fires if there is a coincidence between different chambers based on the predefined look-up-tables. Such

⁵⁾An experimental definition of E_T^{miss} is described in Section 4.7.

3.3. ATLAS DETECTOR

reconstructed L1 objects by the L1Calo and L1Muon are sent to the L1Topo. The L1Topo performs selections based on kinematical information about L1 objects. Then all information calculated by L1Calo, L1Muon, and L1Topo are sent to the CTP to make trigger decisions about up to 512 trigger items and defines the region of interests (ROI). The latency for the whole L1 trigger system is 2.5 μs .

The HLT reconstructs objects with offline like algorithms⁶⁾ with the full detector information around ROI in a large CPU farm (40,000 processor cores) and providing about 2500 independent trigger chains. Some triggers are worked as a *prescale* trigger. A prescale trigger is the one which fired at random $1/n$ events satisfying the trigger selection, where n referred to as prescale factor. The processing time of the HLT is typically within 300 ms.

L1 and HLT trigger rate decompositions for a typical fill are shown in Figure 3.10. In the L1, half of the total trigger rate is occupied by the lepton triggers. The E_T^{miss} trigger has a dependence on instantaneous luminosity, hence the HLT trigger rate was dominant at the beginning of collisions, but it was suppressed at the end of collisions.

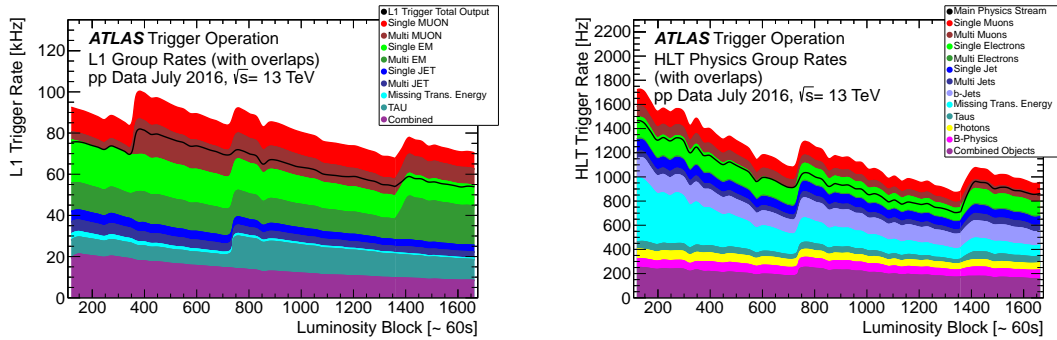


Fig. 3.10: A trigger rate decomposition for each the L1 (left) and HLT (right) in a data taking in July 2016 with a peak instantaneous luminosity of $1.2 \times 10^{34} \text{ cm}^{-2}\text{s}^{-1}$ are shown [70]. The x-axis corresponds to a running time since the collisions started. Due to the trigger multi-firing in an event, the total output rate (black) is less than the sum of the individual trigger rate. Generally, a trigger rate decreases with respect to a running time because of proton losses, but it increases several times in a run because of redefinitions of prescale factors.

In summary, an original event rate, 40 MHz is suppressed to 100 kHz by the L1 triggers, and the HLT suppresses the event rate down to ~ 1.5 kHz. All information about detector hits for triggered events is stored in the storage at CERN for analyses.

⁶⁾Offline reconstruction algorithm are shown in Chapter 4.

CHAPTER 4

Physics Object Reconstruction and Identification

Fundamental particles produced by collisions at the LHC are detected by ATLAS detectors introduced in the previous chapter. Hits of the detectors for triggered events are digitized and stored in the storage at CERN or data centers in the world. Physics objects such as electrons, muons, jets, are reconstructed from the digitized hits (*Reconstruction*). Those objects are calibrated by the simulated events and observed data (*Calibration*) and solved overlaps between objects (*Overlap Removal*). Missing transverse momentum E_T^{miss} is reconstructed from electrons, muons, and jets. Objects other than the q/g jet are identified themselves from enormous q/g jets by various criteria (*Identification*). The above workflow is summarized as a schematic graph shown in Figure 4.1.

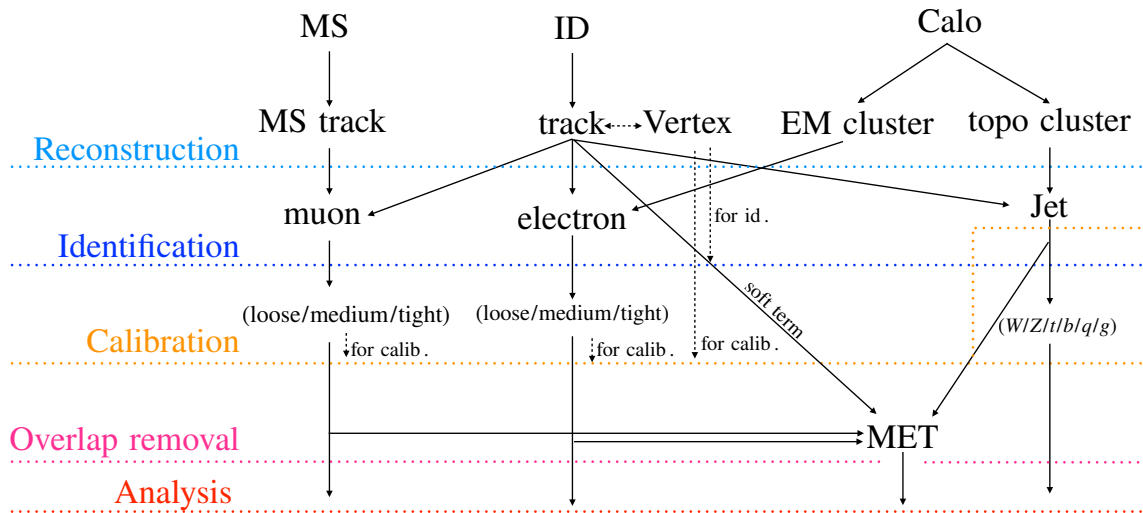


Fig. 4.1: A schematic graph of the workflow for the object reconstruction, identification, calibration, and overlap removal is shown. The ID, MS, and Calo stand for the inner detector, muon spectrometer, and calorimeters, respectively. The reconstruction and identification techniques are briefly introduced in the following sections. A dedicated schematic flow for large-R jets is described in Figure 5.1. The tau leptons and photons are not explicitly drawn in this schematic graph since those are not used in this study.

This chapter describes concise introductions to the object reconstruction and identification for each physics object (Physics object referred to as “Object” in short). As for jets, dedicated discussions are described in Chapter 5.

4.1 Tracks and Vertices

A standard track is reconstructed by the Inner Detectors (ID) with *space-points* which are the three-dimensional position of the hit converted from raw data of the ID. The multi-hits at pixels in the same sensor from a charged particle are merged as *clusters* by the Connected Component Analysis (CCA) [71] which groups hits neighbored on using a linear approximation and neural network-based algorithm [72]. The primary track referred to as a seed track is reconstructed from space-points at four layers of the pixel detector. The seed track is extended to TRT hits and tested by Kalman Filter [73] which characterized by the *track parameters* ($d_0, z_0, \phi_0, \theta, q/p$). The first fit is performed with a pion-track-hypothesis assuming the energy loss in the ID for a minimum ionization particle, the second fit assumes an electron-track-hypothesis which loses energy at each hit surface with the bremsstrahlung. The successful track candidates are performed χ^2 based quality checks. Detailed discussions can be found in Reference [74]. From the 2015 run, TIDE¹⁾ algorithm is used for the dense environment for the increasing pileup condition at $\sqrt{s} = 13$ TeV. Track reconstruction efficiencies are improved for light flavor jets (b-quark jets) from 82% (75%) to 94% (83%) at $0.006 < \Delta R(\text{jet}, \text{track}) < 0.01$.

A vertex is reconstructed from tracks with $p_T > 400$ GeV with the Interactive Vertex Finding algorithm [75] which identifies the peak in the z-axis position of extrapolated tracks to the beam spot. Further χ^2 based algorithm, the Adaptive Vertex Fitting algorithm [76] refines the accuracy of the vertex position. After the reconstruction of vertices, tracks are refitted until all of the tracks belong to any vertices. The vertex with the highest $\sum p_T^2$ is referred to as primary vertex.

4.2 Topological-Clusters

A topological-cluster (topo-cluster) is a four-momentum formed by hits of both the electromagnetic and hadron calorimeters. The reconstruction algorithm is as follows. The first step is a seed finding which searches calorimeter cells with $E_{\text{cell}}^{\text{EM}}/\sigma_{\text{noise,cell}}^{\text{EM}} > 4$, where $E_{\text{cell}}^{\text{EM}}$ stands for energy corrected by EM-scale²⁾. The found seed forms a *proto-cluster* which is a four-momentum pointing toward the cell from the primary vertex. In the second step, neighboring cells being geometrically adjacent in the given sampling layer or being overlapping in the (η, ϕ) in the adjacent layers with $E_{\text{cell}}^{\text{EM}}/\sigma_{\text{noise,cell}}^{\text{EM}} > 2$ are merged into the proto-cluster. If a cell with $E_{\text{cell}}^{\text{EM}}/\sigma_{\text{noise,cell}}^{\text{EM}} > 0$ is attached to two different proto-clusters, those are merged with each other. The second step is iteratively performed in the order of $E_{\text{cell}}^{\text{EM}}/\sigma_{\text{noise,cell}}^{\text{EM}}$ for proto-clusters. In the final step, cells with $E_{\text{cell}}^{\text{EM}}/\sigma_{\text{noise,cell}}^{\text{EM}} > 0$ neighboring to each proto-cluster are merged.

¹⁾TIDE stands for Tracking In Dense Environment.

²⁾EM-scale stands for scales of correction for e, γ without including the non-compensating character of the ATLAS calorimeters.

4.3 Electrons

4.3.1 Reconstruction

An electron is identified as energy deposits in the electromagnetic calorimeter matched to a track identified by the inner tracker. An electron loses its energy in the material by the bremsstrahlung, and resultant photons may decay to an electron-positron pair. Those electrons, positrons, and photons are typically emitted into almost the same direction from the original electron direction. Thus, those remnants are collectively detected by the electromagnetic calorimeter. A schematic diagram of an electron path and related detectors is shown in Figure 4.2.

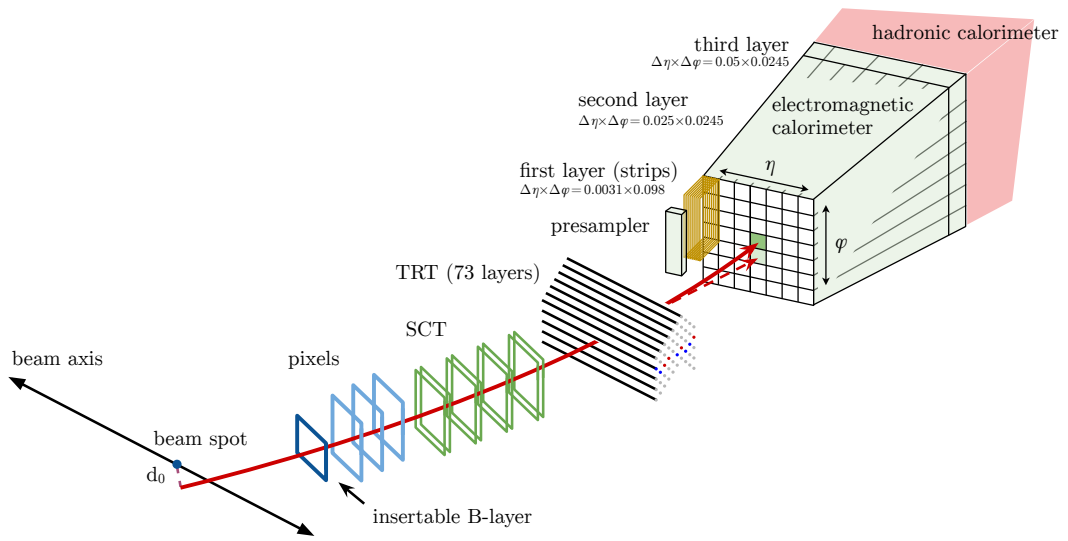


Fig. 4.2: A schematic graph of an electron path (red line) through detectors is shown [77]. An electron goes through four pixel layers, four SCT layers, and several TRT drift tubes. It makes then an electromagnetic shower in the electromagnetic calorimeter. The dashed red line denotes a radiated photon produced at TRT material.

Energy deposits of an electron in the electromagnetic calorimeter are reconstructed as follows. Calorimeter towers which are the sum of energy deposits in three layers of the electromagnetic calorimeter at the same $\Delta\eta \times \Delta\phi = 0.025 \times 0.025$ area. Scanning over combinations of 3×5 towers in $\eta \times \phi$, the local minimum of clusters are referred to as *seed-cluster*. If there are two seed-clusters inside the 5×9 towers, the candidate with higher transverse energy (E_T) is kept if its E_T is at least 10% higher than the other candidate. If the difference is less than 10%, the candidate with the highest E_T central tower is retained. Duplicate clusters are removed.

A track is reconstructed as described in Section 4.1, and matched to a seed-cluster with the angular distance of $-0.10 < \Delta^q\phi < 0.05$, where $\Delta^q\phi = -q(\phi_{\text{cluster}} - \phi_{\text{track}})$, q is an electric charge of a given electron. Duplicate tracks are removed by a dedicated algorithm taking into account the angular distance to cluster barycenter and the number of pixel layer hits. Then a matched cluster window is expanded from 3×5 to 3×7 in the barrel region ($|\eta| < 1.37$), to 5×5 in the end-cap regions ($1.52 < \eta < 2.47$), or

OR logic of the two expanded regions in the transition regions ($1.37 < \eta < 1.52$). The $\eta - \phi$ coordinate of a reconstructed electron is taken by the coordinate of the matched track, and its energy is assigned by the energy of the corresponding expanded cluster.

The reconstruction efficiency of electrons as a function of E_T is shown in Figure 4.3.

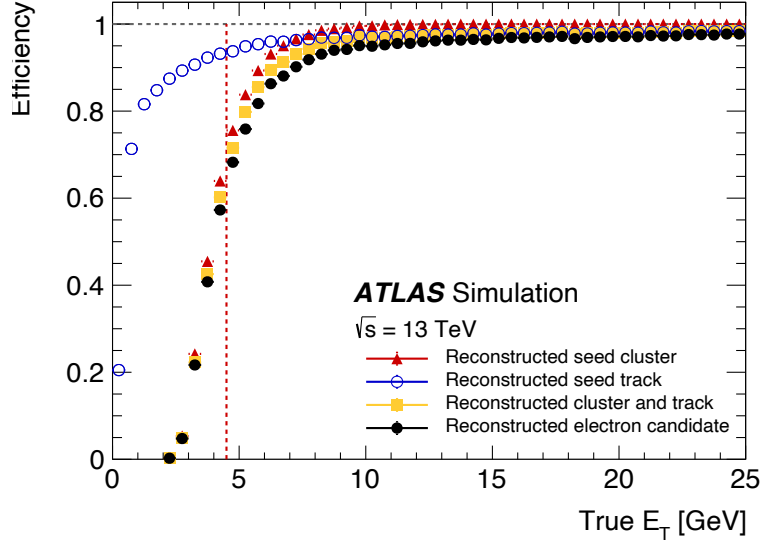


Fig. 4.3: The electron reconstruction efficiencies as a function of transverse energy (E_T) of a truth electron are shown [77]. The total reconstruction efficiency of electrons is less than 60% below 4.5 GeV (dashed line). Inefficiencies are coming from the seed-cluster reconstruction at low E_T regions and the track reconstruction at high E_T regions.

4.3.2 Identification

The reconstructed electron is required to have transverse energy of $E_T > 7$ GeV and pseudorapidity of $|\eta| < 2.47$, which is referred to as electron candidate. A likelihood-based (LH) identification [77] is required to reduce the backgrounds from leptons or hadrons in jets. The LH identification is based on shower shapes in the electromagnetic calorimeter, track quality requirements, and matching quality between a track and cluster. Electron candidates are categorized to “LooseLH”, “MediumLH”, and “TightLH” corresponding to 96%, 94%, and 88% of identification efficiencies to signal electrons at $E_T = 100$ GeV, respectively. Identification efficiencies with respect to E_T and η are shown in Figure 4.5.

A further isolation requirement is applied to reduce jet contamination which typically has much activity around the electron candidate. Two working points are used in this analysis, one is “LooseTrackOnly” that is required not to have sufficient scalar sum of track p_T ($p_{T,var}^{iso}$) within $\Delta R = \min(10\text{GeV}/p_T, 0.2)$ where p_T is for an electron candidate, the threshold on $p_{T,var}^{iso}$ is determined to have a signal efficiency of 99%. The other one is “FixedCutTight” that requires $p_{T,var}^{iso}/p_T < 0.06$. Also, a calorimeter based requirement: $E_{T,cone}^{isol}/p_T < 0.06$ where $E_{T,cone}^{isol}$ is the scalar sum of energy within a $\Delta R = 0.2$ cone is required. An isolation efficiency for each requirement is shown in Figure 4.6.

Table 4.1: Selections for electron and muon candidates used in the analysis are summarized. Two definitions are defined for each object.

	Electrons		Muons	
	“loose”	“tight”	“loose”	“tight”
p_T threshold	7 GeV	27 GeV	7 GeV	27 GeV
$ \eta $	$< 2.47 \notin [1.37, 1.52]$		< 2.7	< 2.5
Identification	LooseLH	TightLH	Loose	Medium
Isolation	LooseTrackOnly	FixedCutTight	LooseTrackOnly	FixedCutTightTrackOnly
$ d_0/\sigma(d_0) $	< 5		< 3	
$ z_0 \sin \theta $	< 0.5 mm			

Furthermore, a track of an electron candidate is required to be $|d_0/\sigma_{d_0}| < 5$ and $|z_0 \times \sin \theta| < 0.5$ mm, where d_0 is the transverse impact parameter relative to the beamline, σ_{d_0} is its uncertainty, and z_0 is the distance between the longitudinal position of the track along the beamline at the point where d_0 is measured and the longitudinal position of the primary vertex as shown in Figure 4.4. Combining them makes two categories as shown in Table 4.1³⁾.

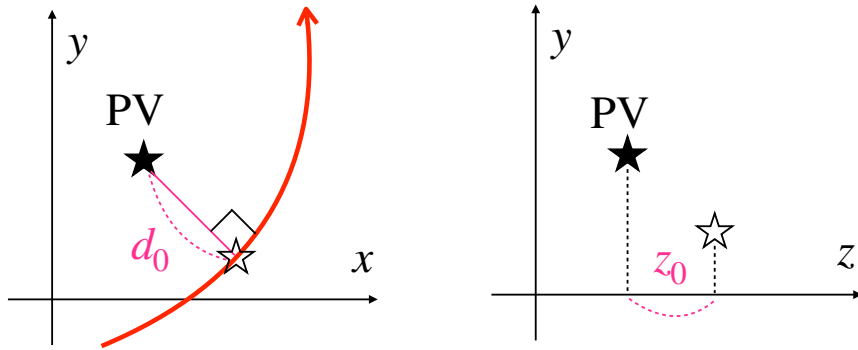


Fig. 4.4: Schematic graphs for d_0 (left) and z_0 (left) are shown. The “PV” and black filled stars denote the primary vertex; the red line is a track; d_0 is a minimum distance between the PV and the track. The white filled stars represent a two-dimensional position for an intersection of the track and a d_0 vector. The z_0 is defined as the difference between a black filled star and a white filled star on the z -axis.

4.3.3 Calibration

The energy of the identified electron is calibrated by the Boosted Decision Tree (BDT) [78] based regression to minimize the impact of material in front of the calorimeters. The BDT is trained by the Monte-Carlo (MC) simulations and applied to both the MC simulations and observed data. Then adjustments of relative energy scales for the different layers of the electromagnetic calorimeter are applied to calibrate residual local non-uniformities such as the boundaries between calorimeter modules and non-

³⁾There is a different definition of d_0 and z_0 exist, referred to as “3D d_0 and z_0 ” which define a green star by closest point in 3D coordinate.

4.3. ELECTRONS

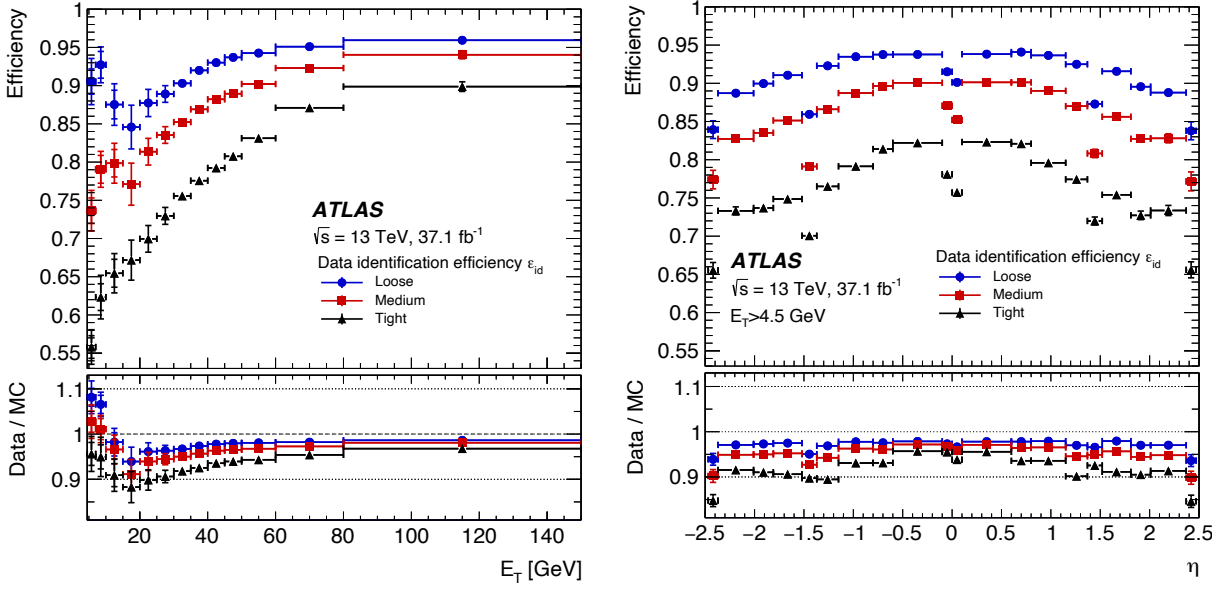


Fig. 4.5: Electron identification efficiencies for E_T (left) and η (right) measured in the observed data with $Z \rightarrow ee$ events are shown [77]. The Loose and Tight identification criteria are used in this analysis for the additional electron veto and leptonically decaying W/Z boson reconstruction, respectively. The discrepancy shown in the bottom pane for each plot is corrected in dedicated calibration described in Section 4.3.3.

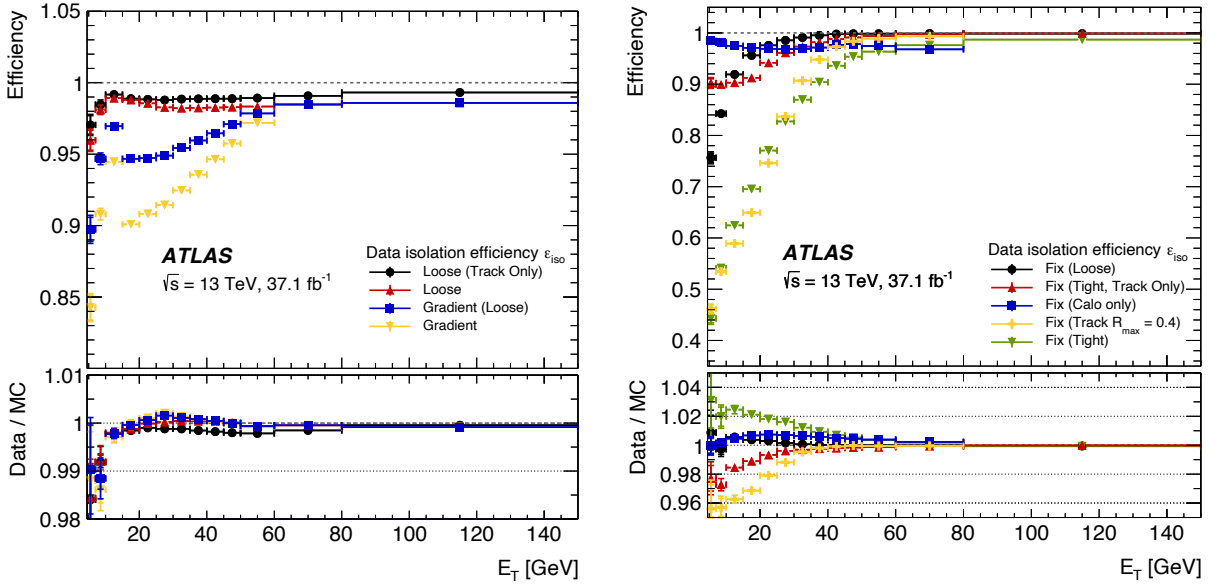


Fig. 4.6: Electron isolation efficiencies for E_T measured in the observed data with $Z \rightarrow ee$ events [77]. The left and right plots show different working points. The Loose (Track Only) and Fix (Tight) isolation criteria are used in this analysis for the additional electron veto and the reconstructions of leptonically decaying W/Z boson, respectively.

nominal high-voltage settings in particular regions. Finally, the MC simulations and observed data are compared, and deviations of the energy scale and resolution are corrected with $Z \rightarrow ee$ events. Systematic uncertainties are also evaluated at the same time. Figure 4.7 shows fractional uncertainties in the electron energy scale and resolution calibrations. The dominant uncertainties in the energy scale at $E_T > 20$ GeV are $\alpha_{1/2}\mu$ and MG/HG gain components. The former is an uncertainty in the relative response between the first and second layers of the electromagnetic calorimeter measured by energy deposits of muons. The latter is an uncertainty in a correction to the relative gain of the different readouts as described in Section 3.3.4. The dominant uncertainties in the energy resolution are sampling and material terms. The former represents a stochastic term due to the sampling nature of the calorimeter, the latter is an uncertainty associated with the effects of the material in front of the electromagnetic calorimeter. Details of the calibrations are summarized in Reference [79].

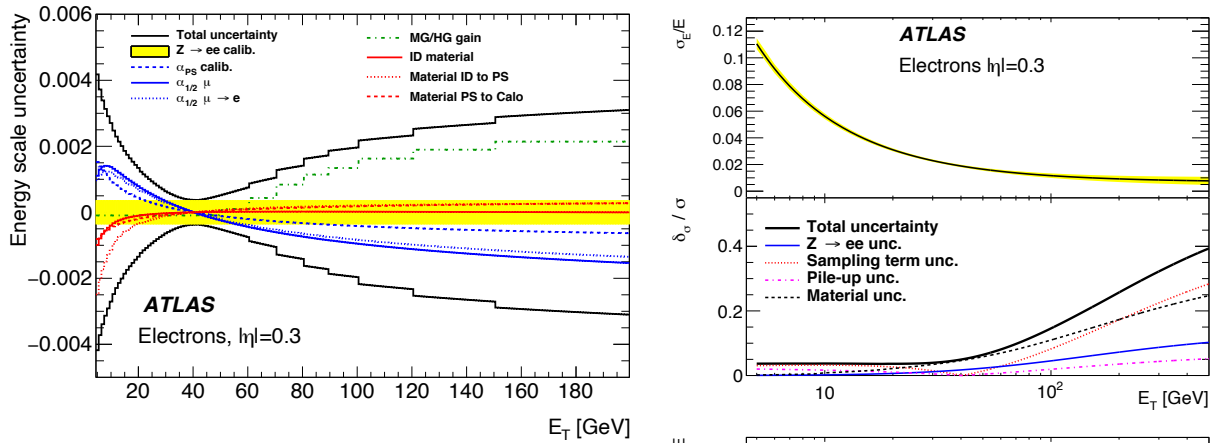


Fig. 4.7: Fractional uncertainties in the electron scale (left) and resolution (right) are shown [79]. For the left plot, the “ α_X ” corresponds to the calibrations of calorimeter responses, the “MG/HG gain” denotes a relative calibration between high- and medium-gain readout, and the “material X” represents an uncertainty associated with calibrations for effects on material X. For the right plot, a stochastic term due to the sampling nature of the calorimeter (Sampling term unc.) and non-desired radiation from material in front of the calorimeter (Material unc.) are dominant.

4.3.4 Trigger

As discussed in Section 3.3.6, the electron triggers consist of the ROI construction with the electromagnetic calorimeter information and the offline-like electron reconstruction at around the ROI. Triggers used in this thesis are summarized in Table 4.2. The offline identification algorithm shown in Section 4.3.2 is applied at HLT, however, there are several necessary differences: the bremsstrahlung-aware refit [80] is not performed, the LH only uses calorimeter variables, the number of primary vertices (N_{PV}) is used to assess pileup, whereas average number of interaction per crossing ($\langle \mu \rangle$)⁴⁾ is used in the offline

⁴⁾The mean number of interaction per crossing denotes the mean of the Poisson distribution of the number of interactions per crossing calculated for each bunch from the instantaneous luminosity (L_{bunch}) as $\mu = L_{\text{bunch}}\sigma_{\text{inel}}/f_r$, where σ_{inel} denotes the inelastic cross-section for 13 TeV collisions (80 mb for this analysis), and f_r represents the LHC revolution frequency.

4.3. ELECTRONS

Table 4.2: A summary of the electron triggers used in this thesis is shown. The L1 trigger threshold is shown in a bracket if it is required.

	trigger name	threshold [GeV]	LH identification	isolation
2015	HLT_e24_lhmedium_L1EM20VH	$E_T > 24(20)$	medium	-
	HLT_e60_lhmedium	$E_T > 60$	medium	-
	HLT_e120_lhloose	$E_T > 120$	loose	-
2016	HLT_e26_lhtight_nod0_ivarloose	$E_T > 26$	tight w/o d_0	loose
	HLT_e60_lhmedium_nod0	$E_T > 60$	medium w/o d_0	-
	HLT_e120_lhloose_nod0	$E_T > 120$	loose w/o d_0	-

algorithm, and some cell-level corrections [81–83] are not available online. The trigger sets for the 2016 run do not include the d_0 requirement because the requirement causes inefficiency when bremsstrahlung-aware refit is applied at the offline algorithm. The loose track only isolation is imposed on the lowest threshold trigger in the 2016 run, which is $p_{T,var}^{iso}/p_T < 0.10$.

Figure 4.8 shows the trigger efficiencies measured in $Z \rightarrow ee$ events for each year. the trigger for the 2015 (2016) run has greater than a 95% efficiency at $E_T > 50(60)$ GeV. The significant inefficiency in the 2016 data is observed at $E_T < 60$ GeV, which is mainly caused by the LH using only calorimeter related variables.

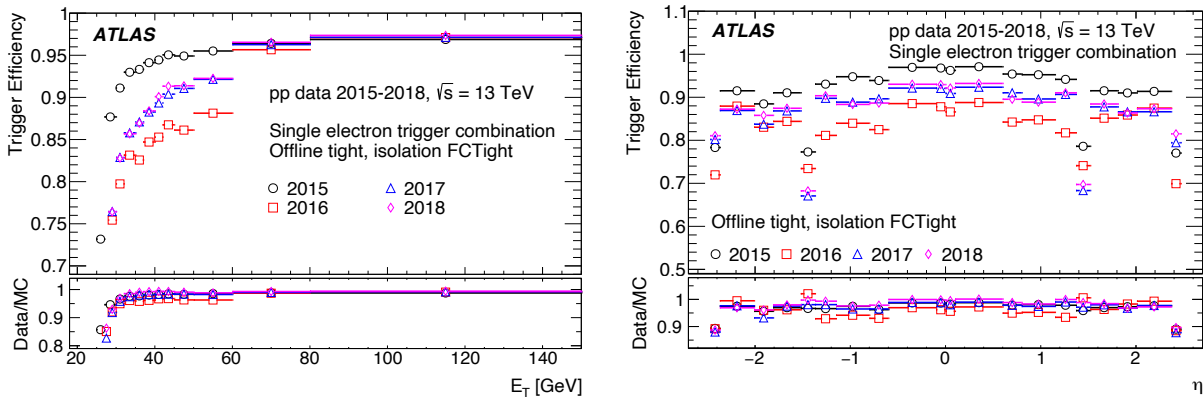


Fig. 4.8: Electron trigger efficiencies for each year as a function of p_T (left) and η are shown [84]. Three triggers shown in Table 4.2 for each year are combined by the logical “OR”. The efficiencies are given with respect to offline electrons required to be the tight identification and the “FixedCutTight” isolation. The bottom panel shows the ratio of the observed data to MC simulation efficiencies.

4.4 Muons

4.4.1 Reconstruction

A muon is reconstructed by a combined fit to the ID (Inner Detector) and MS (Muon Spectrometer) tracks. The MS track is reconstructed by the MDT, CSC, RPC, and TGC hits searched by an algorithm based on the Hough transform [85]. MS and ID tracks are combined with several algorithms. A first one is combined (CB) muon which is refitted with ID and MS hits. The hits used refitting are searched outside-in or inside-out pattern recognition. The former is the muon that is first reconstructed in the MS and the extrapolated inward and matched to an ID track. The latter one is inverse of the outside-in. A second type of reconstructed muon is the segment-tagged (ST) muon which is an ID track with at least one hit in the MDT or CSC chamber. The ST muon recovers reconstruction efficiencies for low p_T muons or muons on the edge of the MS coverage. The last one is calorimeter-tagged (CT) muon which is an ID track with calorimeter energy deposits agreed with a minimum-ionizing particle. The CT muons recover reconstruction efficiencies for ones in the crack region⁵⁾ ($|\eta| < 0.1$). A schematic illustration of the trajectories of the different sorts of muons and related detector segments is shown in Figure 4.9.

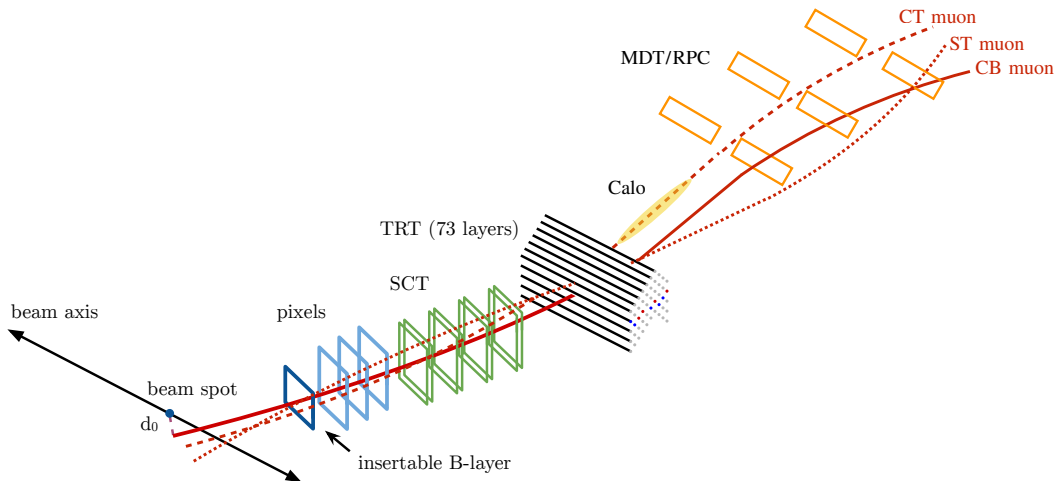


Fig. 4.9: A schematic illustration of muon paths (red lines) through detectors at the central region [77]. A muon goes through four pixel layers, four SCT layers, and several TRT drift tubes. A CB muon leaves hits on three MDT layers. A ST muon leaves hits on MDT layers. A CT muon goes through the crack region of the MS ($|\eta| < 0.1$) but tagged by calorimeter energy deposits.

4.4.2 Identification

A reconstructed muon is required to have $p_T > 7$ GeV and $|\eta| < 2.5$ [86]. Similar to electrons, two identification working points are used. “Medium” stands for muon reconstructed by using the CB algorithm imposed to have at least three hits in more than two MDT layers except for the $|\eta| < 0.1$ region. A

⁵⁾The region without a muon detector cell due to the calorimeter cabling service.

4.4. MUONS

q/p significance, $|q/p_{MS} - q/p_{ID}|$, where q is the charge and p_{MS} (p_{ID}) is the momentum of the muon measured in the MS (ID), are required to be less than seven. “Loose” muons include “Medium” ones, ST muons, and CT muons. Figure 4.10 shows the muon reconstruction efficiencies. The efficiency is almost 99% over most of the pseudorapidity range of $|\eta| < 2.5$ for $p_T > 5$ GeV. Adding to isolation requirement on tracks for electrons, “FixedCutTightTrackOnly” is defined as “FixedCutTight” except for the calorimeter requirement. The isolation efficiencies are almost 100%. Similar to electrons, two categories are defined as shown in Table 4.1.

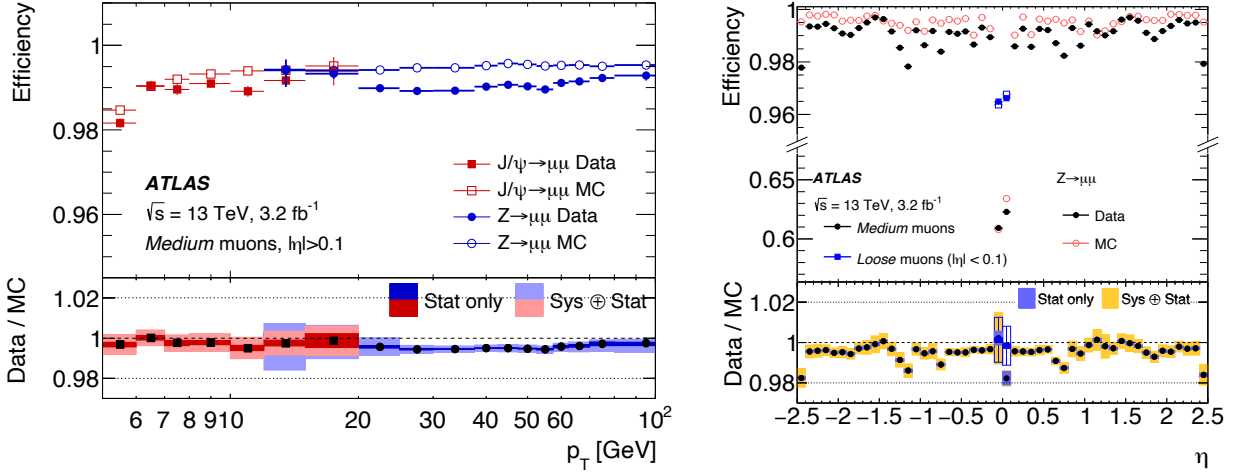


Fig. 4.10: Muon reconstruction efficiencies for p_T (left) and η (right) measured in $Z \rightarrow \mu\mu$ and $J/\Psi \rightarrow \mu\mu$ events are shown [86]. The efficiencies are shown as the product of a reconstruction efficiency and a “Medium” or “Loose” identification efficiency. The measured efficiencies from different sources, $Z \rightarrow \mu\mu$ and $J/\Psi \rightarrow \mu\mu$ events are consistent at overlap regions (10 – 20 GeV). The efficiencies are around 99% at most of the p_T ranges. The huge efficiency loss of “Medium” muons at the crack region ($|\eta| < 0.1$) is recovered by CT (calorimeter tagged) muon shown as “Loose” muons.

4.4.3 Calibration

Muon energy scale and resolution are simultaneously calibrated by $Z \rightarrow \mu\mu$ and $J/\Psi \rightarrow \mu\mu$ events. The invariant mass distribution for the MC simulation is fitted to the observed data using a binned maximum likelihood method which is parametrized by an energy scale and resolution of a given pair of electrons. A result of the calibration is shown in Figure 4.11. Corrected distribution has a better $m_{\mu\mu}$ description than the uncalibrated one. The uncertainties in the energy scale and resolution are estimated as a minimum of 0.05% for $|\eta| < 1$ to a maximum of 0.3% for $|\eta| \sim 2.5$ and a minimum of 2.3% for $|\eta| \sim 0$ to a maximum of 2.9% for $|\eta| \sim 2.5$, respectively.

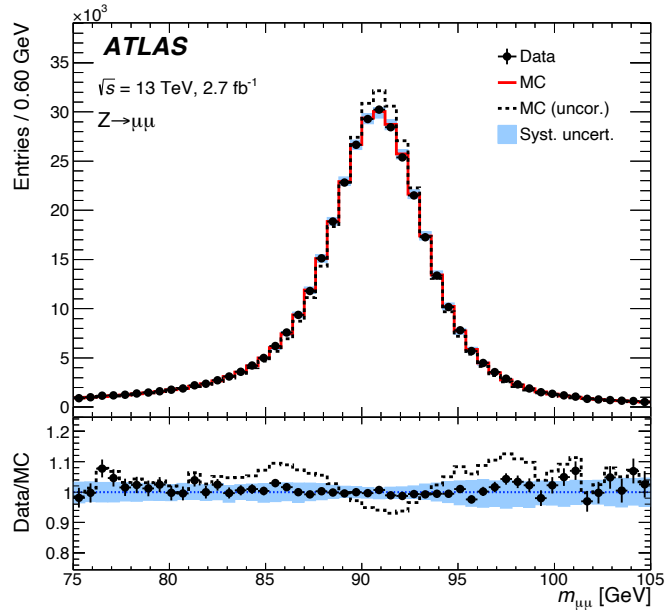


Fig. 4.11: A distribution for the invariant mass of the dimuon system ($m_{\mu\mu}$) with $Z \rightarrow \mu^+\mu^-$ events is shown [86]. A corrected $m_{\mu\mu}$ distribution (red line) describes distribution for the observed data (black dot) much better than an uncorrected $m_{\mu\mu}$ distribution (dashed line).

4.4.4 Trigger

As discussed in Section 3.3.6, the muon triggers consist of the ROI construction with muon spectrometers (MS) and the offline-like electron reconstruction around the ROI. The triggers used in this thesis are summarized in Table 4.3. The HLT muon is made up of the fast and precise reconstruction steps. The fast reconstruction uses part of MS and ID information around the ROI to reconstruct a muon candidate, and its momentum is estimated by predefined lookup tables. The precise reconstruction uses all MS and ID information and refines the muon track reconstructed by the fast reconstruction step.

The trigger efficiencies measured in $Z \rightarrow \mu\mu$ events are shown in Figure 4.12. The L1 inefficiency at the barrel region caused by the absence of detectors and it can be recovered by the E_T^{miss} trigger as introduced

Table 4.3: A summary of the electron triggers used in this thesis is shown. The L1 trigger threshold is shown in a bracket if it is required. The summation, $\sum_{\Delta R < X} p_T^{\text{trk}}$ stands for the scalar sum of p_T for all ID tracks inside a cone defined as $\Delta R < X$ except for the muon itself.

trigger name	threshold [GeV]	isolation
HLT_mu20_loose_L1MU15	$p_T > 20(15)$	$\sum_{\Delta R < 0.2} p_T^{\text{trk}}/p_T < 0.12$
HLT_mu24_loose	$p_T > 24$	$\sum_{\Delta R < \min(10 \text{ GeV}/p_T, 0.3)} p_T^{\text{trk}}/p_T < 0.16$
HLT_mu24_medium	$p_T > 24$	$\sum_{\Delta R < \min(10 \text{ GeV}/p_T, 0.3)} p_T^{\text{trk}}/p_T < 0.07$
HLT_mu26_medium	$p_T > 26$	$\sum_{\Delta R < \min(10 \text{ GeV}/p_T, 0.3)} p_T^{\text{trk}}/p_T < 0.07$
HLT_mu40	$p_T > 40$	-
HLT_mu50	$p_T > 50$	-

in Section 4.7.3. The HLT trigger efficiency with respect to the L1 is almost 100% despite the 1/100 rate reduction. The total trigger efficiency is approximately 70% at $p_T > 35$ GeV.

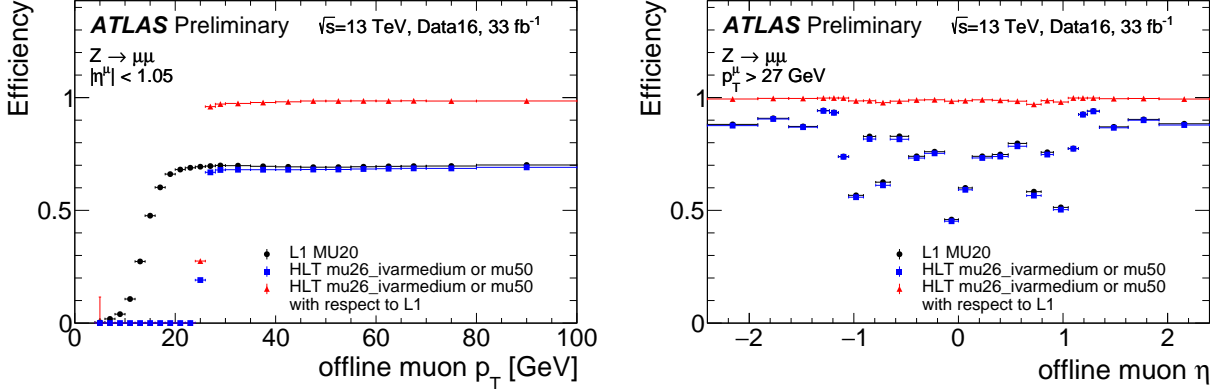


Fig. 4.12: Muon trigger efficiencies as a function of p_T (left) and η measured in the 2016 data with $Z \rightarrow \mu\mu$ events are shown [84]. Triggers shown in Table 4.2 are combined by the logical “OR”. The efficiencies are given with respect to offline “Medium” identified muon candidate. The trigger efficiency of the HLT mu26_ivarmedium is sharply turned on around its threshold, and it reached a plateau with a 70% efficiency. The efficiency losses come from L1 trigger inefficiency.

4.5 Jets

As discussed in Section 2.4, hadrons resulting in the parton shower and hadronization of a colored particle are reconstructed by calorimeters and trackers as a jet by *clustering*. Three sorts of jets are used in this thesis, two of them are reconstructed from topo-clusters described in Section 4.2, the other one is made from tracks described in Section 4.1.

4.5.1 Reconstruction

From both the theoretical and experimental points of view, the clustering algorithm must be *Infrared and Collinear safe* (IRC safe). Let a four-momentum be p_i and corresponding angular vector $\vec{\rho}_i = (y, \phi)$ are defined, where y is rapidity. The IRC safe stands for following conditions,

- Infrared safe (IR): $p_i + p_j = p_i$, where $p_j = 0$,
- Collinear safe (C): $p_i = p_j + p_k$, such that $|\vec{\rho}_j - \vec{\rho}_k| = 0$, $|p_i| = |p_j| + |p_k|$.

The ATLAS collaboration commonly uses anti- k_t algorithm [87, 88] which is a family of k_t sequential recombination satisfying IRC safe. The metric of k_t algorithm is $d_{ij}(k) = \min(p_{T,i}^{2k}, p_{T,j}^{2k})|\vec{\rho}_i - \vec{\rho}_j|^2/R^2$ and the beam distance $d_{iB}(k) = p_{T,i}^{2k}$. The parameter R is corresponding to a reference radius of a jet. The algorithm is as follows:

1. Define a list containing all reconstructed particles.
2. Search the minimum $d_{ij}(k)$ combination of particles over the list.
3. If $d_{ij}(k) < d_{iB}(k)$, remove p_i and p_j , and add new particle $p_{new} = p_i + p_j$, otherwise p_i is a jet.
4. Repeat until no particle left on the list.

The anti- k_t algorithm is a $k = -1$ case of the k_t sequential recombination.

A topo-cluster based anti- k_t algorithm with $R = 0.4$ is used to reconstruct single q/g jets, called small-R jets. A topo-cluster based anti- k_t algorithm with $R = 1.0$ is used to reconstruct W/Z jets, called large-R jets. Further discussions about large-R jets and identification procedures for hadronic W/Z candidates are in Chapter 5. Track based anti- k_t algorithm $R = 0.2$ is used to reconstruct single light quark or gluon jets, called track jets.

4.5.2 Calibration

Details on the large-R jets calibrations are described in Section 5.1, hence this section focuses on the small-R jets calibrations. The calibration chain of the jet energy scale for the small-R jets is composed of the origin correction, the jet area-based pileup correction, the MC-based calibration, the global sequential calibration, and the in-situ calibration. The MC-based and in-situ calibrations are almost identical to the one for large-R jets, and details about calibrations are described in Section 5.1.

Four-momenta of topo-clusters are pointing at the center of the detector coordinate, the origin correction reorients a small-R jet to primary vertex defined in Section 4.1. The η resolution improves roughly 0.06 to 0.045 at 20 GeV and 0.03 to 0.006 at 200 GeV.

The jet area-based pileup correction subtracts an energy expected to be in $\eta - \phi$ by the pileup contamination with respect to the number of vertices in the event N_{PV} and the average interaction per crossing μ . The N_{PV} and μ are sensitive to assess in-time and out-of-time pileup contributions, respectively. The corrected small-R jet p_T can be expressed as

$$p_T^{\text{corr.}} = p_T^{\text{reco.}} - \rho \times A - \alpha \times (N_{PV} - 1) - \beta \times \mu, \quad (4.1)$$

where ρ represents an average energy deposit per area evaluated with MC simulations in $|\eta| < 2$, A denotes an $\eta - \phi$ area of a given jet calculated with the ghost association technique [89], α and β are obtained from MC simulations in each p_T and η bins. The results of the correction are shown in Figure 4.13. The pileup dependencies are completely removed in the level of MC simulations.

The MC-calibration applies the inverse of an energy response ($E^{\text{reco.}}/E^{\text{truth}}$) as a function of $|\eta|$ as shown in Figure 4.14, and more details are discussed in Section 5.1.2. The global sequential calibration corrects residual dependence on its substructure. It exploits five variables related to the substructure, f_{Tile0} , f_{LAR3} , n_{trk} , W_{trk} , and n_{segments} represent the fraction of a jet energy measured in the first layer of the hadronic calorimeter, the fraction of a jet energy measured in the third layer of the electromagnetic calorimeter,

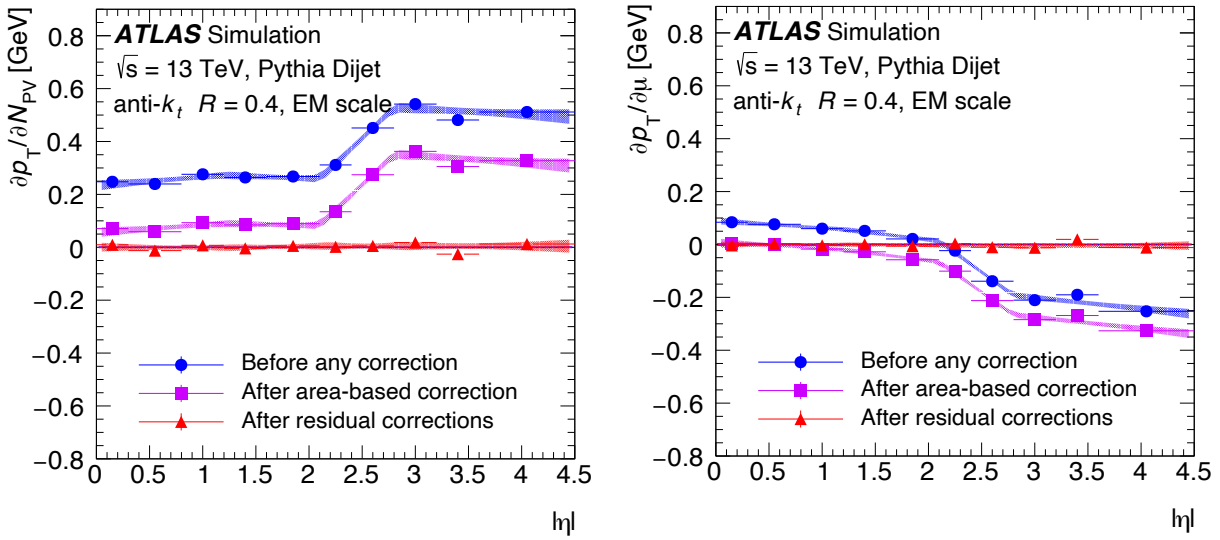


Fig. 4.13: Dependences of small-R jet p_T on N_{PV} (left) and μ (right) with respect to small-R jet $|\eta|$ are shown [90]. The flat distributions of the red points representing dependence after applying the correction indicate that the pileup dependencies are almost perfectly removed on average.

the number of ghost associated tracks with $p_T > 1$ GeV in association with a given jet, the average p_T -weighted transverse distance in the $\eta - \phi$ plane between the jet axis and the same tracks as n_{trk} , and the number of muon track segments. The dependence of the n_{trk} on p_T response is shown in Figure 4.14.

The results of the in-situ calibrations are shown in Figure 4.15 and technical details can be found in Section 5.1.3. The total uncertainty in the jet energy scale is about 4.5% at 20 GeV, 1% at 200 GeV, and 2% at 2 TeV. The dominant uncertainties are pileup and flavor response which is an uncertainty in different responses caused by origins of particles.

4.5.3 Identification

A reconstructed small-R jet is required to have $p_T > 20$ GeV for $|\eta| < 2.5$ or $p_T > 30$ GeV for $2.5 < |\eta| < 4.5$. A jet with $p_T < 60$ GeV for $|\eta| < 2.4$ is applied the *Jet Vertex Tagger* (JVT) [92] which based on likelihood-based algorithm in order to select only jets from the hard interaction. A reconstructed small-R jet containing b-hadron is identified using a multivariate algorithm (b-tagging) [93]. The weak boson tagging algorithms are described in Section 5.2.

Jet Vertex Tagger

The JVT is constructed from R_{pT} and corrJVF as a two-dimensional likelihood derived using the MC simulations and based on a k-nearest neighbor (kNN) algorithm [78]. The definitions of R_{pT} and corrJVF

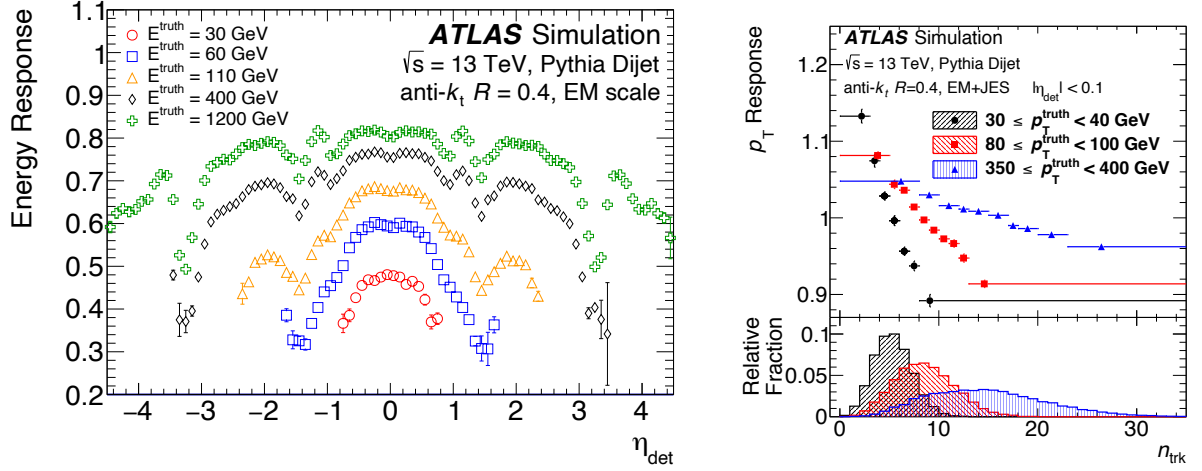


Fig. 4.14: The average energy response as a function of $|\eta|$ for jets with several truth energies (left) and the p_T responses for a n_{trk} variable in several truth jet energies (right) are shown [90]. For the left plot, the energy responses are better at higher jet energies due to the sampling nature of the calorimeter and worse at the transition region $|\eta| \sim 1.5$ and $|\eta| \sim 3.2$. For the right plot, jets with lower n_{trk} , i.e. jets contain many neutral particles have higher p_T responses because all of the constituents are calibrated to the EM-scale which is not stringently correct for the neutral hadrons.

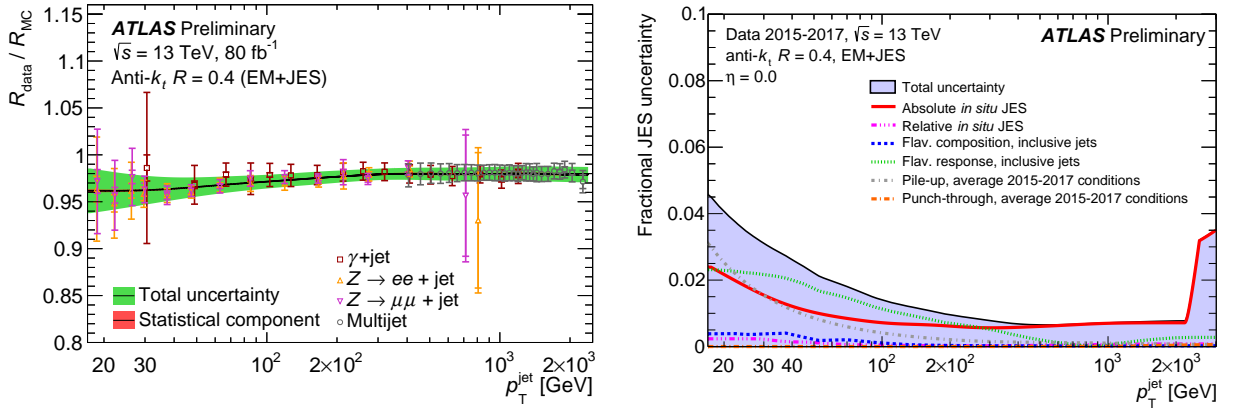


Fig. 4.15: A combination of jet energy responses measured in the observed data collected in 2015-2017 with γ +jets, $Z \rightarrow ee$ +jets, $Z \rightarrow \mu\mu$ +jets, and multijet (left) and its uncertainty breakdown (right) as a function of jet p_T are shown [91]. For the left plot, the measured energy responses with different events are consistent with each other at $R_{\text{data}}/R_{\text{MC}} = 0.96 - 0.97$. As for the right plot, the flavor response and absolute *in situ* JES are dominant. The former is evaluated by comparing the average jet responses for each jet flavor using PYTHIA and HERWIG, the latter represents the propagated uncertainties from each measurement.

are

$$R_{pT} = \frac{\sum_k p_{T,k}^{\text{track}}(\text{PV}_0)}{p_T^{\text{jet}}}, \quad (4.2)$$

$$\text{corrJVF} = \frac{\sum_m p_{T,m}^{\text{track}}(\text{PV}_0)}{\sum_l p_{T,l}^{\text{track}}(\text{PV}_0) + \frac{\sum_{n \geq 1} \sum_l p_{T,l}^{\text{track}}(\text{PV}_n)}{(k \cdot n_{\text{track}}^{\text{PU}})}}, \quad (4.3)$$

where $\sum_m p_{T,m}^{\text{track}}(\text{PV}_0, \text{PV}_n)$ is the scalar sum of the p_T of the tracks that are associated with the jet and originated from the primary vertex (PV_0) or pileup vertices (PV_n), k is a constant ($k = 0.01$) to suppress the pileup dependence, and $n_{\text{track}}^{\text{PU}}$ denotes the total number of pileup tracks in an event. The distributions for R_{pT} and corrJVF are shown in Figure 4.16. The R_{pT} and corrJVF have better discriminant powers in the low and high signal tagging efficiency regions, respectively.

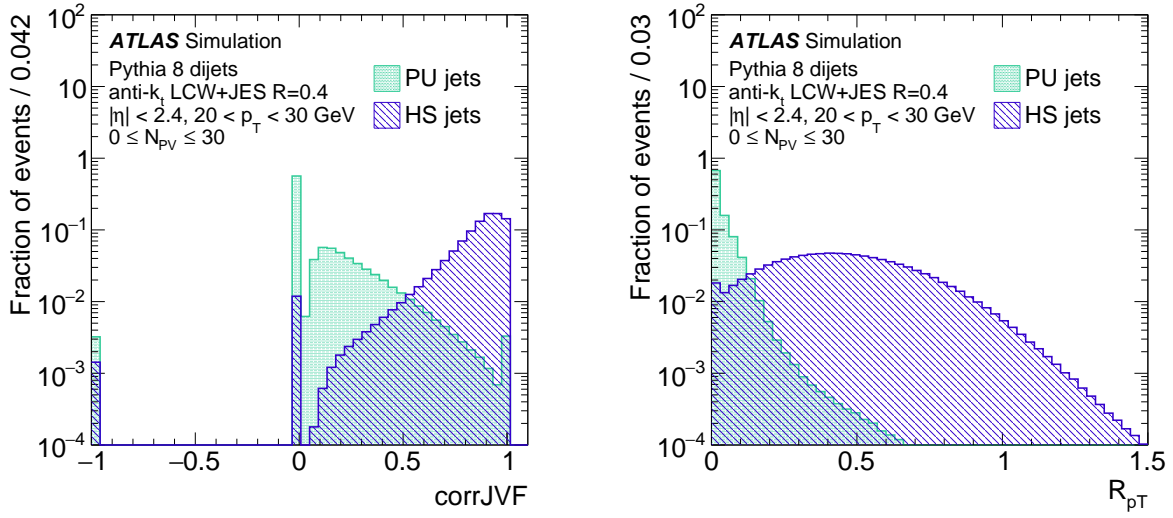


Fig. 4.16: Distributions for corrJVF (left) and R_{pT} (right) are shown [92]. The green filled and blue shaded histograms represent jets from pileup vertices and jets from the primary vertex, respectively.

b-tagging

The b-tagging used in this thesis is the MV2 which combines three algorithms, IP2D/IP3D [94], SV1 [95], and JETFITTER [96] by the boosted decision tree.

The IP2D (IP3D) is the algorithm based on likelihood discriminant evaluated by the signed transverse (and longitudinal) impact parameter significance: $d_0 \sin \theta / \sigma_{d_0}$ (and $d_0^{3D} \sin \theta / \sigma_{d_0}$), where θ denotes the angle between d_0 and jet axis, d_0^{3D} is d_0 calculated by the 3D closest point, and $\sigma(d_0)$ is the uncertainty in the d_0 .

The SV1 reconstructs single displaced secondary vertex in a jet. The algorithm starts from constructing all possible two-track vertices and reject tracks that are compatible with K_s or Λ , photon conversions or

hadronic interaction. The remains of the tracks are used to reconstruct an inclusive secondary vertex by removing outlier tracks from a χ^2 -fit.

The JETFITTER reconstructs the topology of weak b/c-hadron decay chains. An algorithm exploits Kalman filter to find which b/c-hadron decay chain is compatible with a topology of given tracks.

The MV2 combines outcomes of the above three algorithms by BDT. The output BDT score and its light jet rejection are shown in Figure 4.17. The MV2 output overwhelms individual JetFitter, SV1, and IP3D, and reduces light jet fractions to 1/380 at a 70% signal efficiency which is used in this analysis.

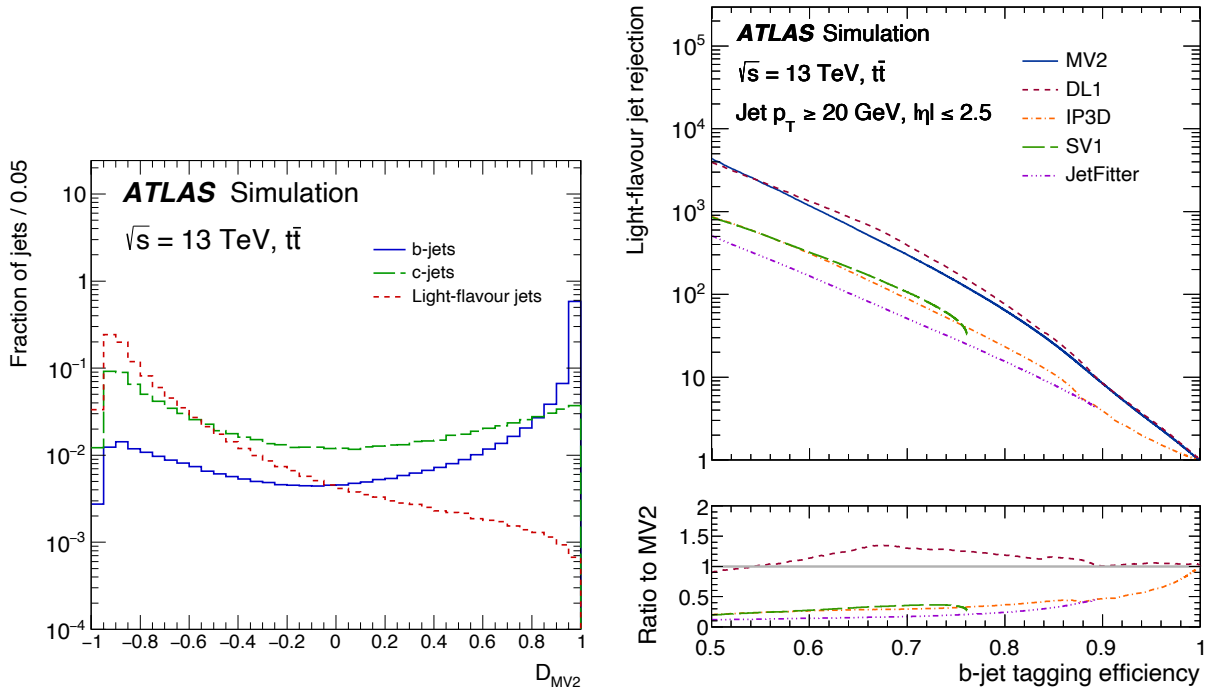


Fig. 4.17: The MV2 outputs (left) and light jet rejections as a function of b-jet tagging efficiency are shown [97]. The MV2 output has discrimination power for not only light jets but also c-hadron jets as shown in the left plot. The right plot represents the MV2 performed much better than its inputs, IP3D, SV1, and JETFITTER. Although the DL1 which uses deep neural network instead of BDT of MV2 has superior light-flavor jet rejection than that of MV2, we have chosen to use MV2 because the calibration for DL1 takes a longer time than that of MV2.

4.6 Overlap Removal

One topo-cluster or one track can be identified as more than one object from the above reconstruction criteria. Overlaps between objects are solved (*Overlap Removal*) by following the order of criteria:

1. Remove electron and jet if $\Delta R(\mu, e/\text{jet}) < 0.2/0.4$ and leave muon,
2. Remove jet if $\Delta R(e, \text{jet}) < 0.4$ and leave electron,

3. Remove small-R jet if $\Delta R(\text{small-R jet, large-R jet}) < 1.4$ and leave large-R jet.

The last criterion is used only for the merged analysis introduced in Section 6.3.

4.7 Missing Transverse Momentum

4.7.1 Reconstruction

The missing transverse momentum vector, \vec{E}_T^{miss} , is calculated as the negative vectorial sum of the transverse momenta of calibrated electrons, muons, jets, and *soft term*. The soft term is the energy depositions due to the underlying event and other types of soft radiation. It is reconstructed by ID tracks that are associated with the primary vertex but not used in any reconstructed objects [98], is referred to as track soft term (TST). Large-R jets and track jets are not used in the \vec{E}_T^{miss} calculation in order to avoid double-counting of energy. Also, reconstructed taus and photons are not included in the \vec{E}_T^{miss} calculation explicitly, but those are taken into account as hadronic jets. The track-based missing transverse momentum vector, \vec{p}_T^{miss} is the negative vectorial sum of the transverse momenta of all good-quality inner-detector tracks that are associated with the primary vertex.

4.7.2 Calibration

Systematic uncertainties associated with objects discussed above are propagated to the \vec{E}_T^{miss} calculation. The TST calibration is specifically performed for \vec{E}_T^{miss} with $Z \rightarrow ee$ events. Generally, the events do not include E_T^{miss} in the leading order of diagrams, so the parallel component of a TST momentum (\vec{p}_T^{soft}) along with the vectorial sum of reconstructed objects (\vec{p}_T^{hard}), $\vec{p}_{\parallel}^{\text{soft}}$ is balanced to \vec{p}_T^{hard} , and the perpendicular component ($\vec{p}_{\perp}^{\text{soft}}$) is to be $\vec{0}$. A schematic graph for the definitions is shown in Figure 4.18. Measured deviations are parametrized as three projected quantities, the parallel scale ($\langle E_{\parallel}^{\text{miss,SoftTerm}} \rangle$), the parallel resolution ($\sigma(E_{\parallel}^{\text{miss,SoftTerm}})$), and the transverse resolution ($\sigma(E_{\perp}^{\text{miss,SoftTerm}})$). The resolutions are defined as its root-mean-square. The transverse scale is turned out to have a negligible impact on analyses, thus it is not evaluated. The systematic uncertainties are calculated as the maximal disagreement between the observed data and various MC simulations. Figure 4.19 shows uncertainties for each component. The total uncertainty is at most 20% on the scale.

4.7.3 Trigger

At the L1, the E_T^{miss} is reconstructed by calorimeter towers at the ROI, and the muon is not included in the calculation. Therefore, the E_T^{miss} resolution is relatively coarser than the other triggers, which is typically ~ 50 GeV. Triggered events by the L1 E_T^{miss} trigger are examined by a more sophisticated method at the HLT. At the HLT, the E_T^{miss} reconstruction algorithms of *cell algorithm* and *jet-based algorithm* are used in this thesis. The former is based on measured cell energies in the electromagnetic and hadron calorimeter. An energy deposit at a cell is converted to momentum in the massless approximation, i.e.

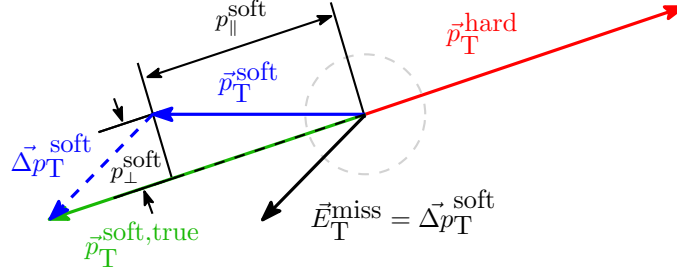


Fig. 4.18: A schematic graph of the TST projection for the calculation of the TST systematic uncertainties is shown [99].

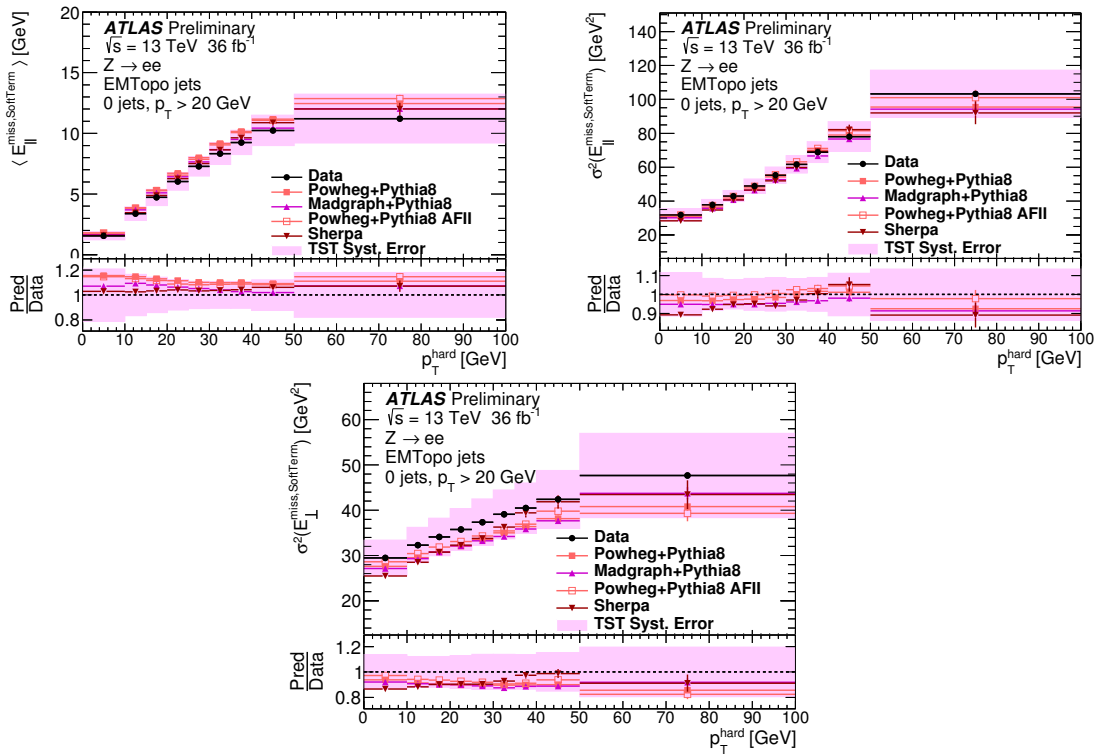


Fig. 4.19: Comparisons between the observed data and MC simulations for each the parallel scale (left), the parallel resolution (right), and the perpendicular resolution (bottom) as a function of p_T^{hard} are shown [99].

4.7. MISSING TRANSVERSE MOMENTUM

Table 4.4: A summary of the E_T^{miss} triggers used in this thesis is shown. The L1 trigger threshold is shown in a bracket if it is required.

trigger name	threshold [GeV]	reconstruction algorithm
HLT_xe70	$E_T > 70$	cell algorithm
HLT_xe90_mht_L1XE50	$E_T > 90(50)$	jet-based algorithm
HLT_xe110_mht_L1XE50	$E_T > 110(50)$	jet-based algorithm

$p_{x,i} = E_i \sin \theta_i \cos \phi_i$ and $p_{y,i} = E_i \sin \theta_i \sin \phi_i$, where i is a label of cell, E_i denotes energy of i -th cell, η_i and ϕ_i represents i -th cell coordinate with respect to center of the detector. A cell having an energy of $|E_i| > 2\sigma_i$ and $E_i > -5\sigma_i$ are considered, where σ_i is the averaged noise in the cell energy measurement. The norm of the vector sum of the momenta is used in the trigger decision. The latter algorithm (mht) is based on jets reconstructed with anti- k_t $R = 0.4$. The jets are calibrated in a similar way to the offline jet reconstruction as described in Section 4.5.2, area-based calibration and MC-based calibration. The norm of the vector sum of jet four-momenta is used in the trigger decision. The triggers used in this thesis are summarized in Table 4.4. The performance of the triggers is shown in Figure 4.20. The E_T^{miss} trigger plateau is around 200 GeV although the L1(HLT) trigger threshold is 50(90) GeV. This is caused by the coarse E_T^{miss} resolution at the L1.

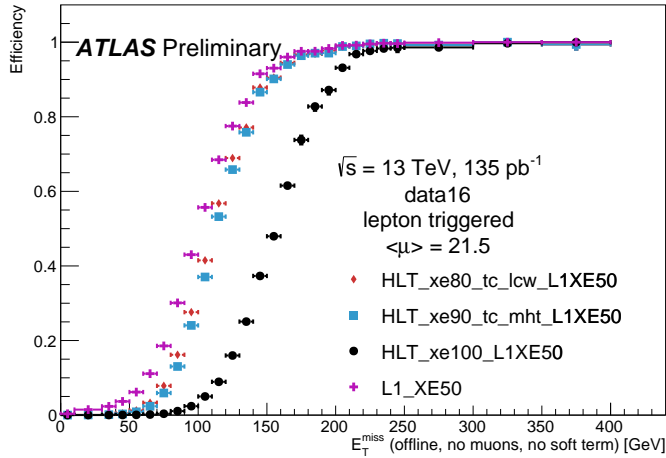


Fig. 4.20: The E_T^{miss} trigger efficiency with respect to single lepton triggered events corrected in 2016 [100] is shown. The blue square is the one which used in this thesis.

CHAPTER 5

Large-R Jet Calibration and Weak Vector Boson Identification

The previous chapter describes general reconstruction procedures for various physics objects. This chapter focuses on detailed accounts for large-R jet calibration techniques and weak vector boson identification criteria because the large-R jet is the most important object for the semileptonic VBS analysis. Section 5.1 describes a large-R calibration chain such as the groomings, the MC calibrations, and the in-situ calibrations. Baseline and advanced weak vector boson identification techniques are described in Sections 5.2.2 and 5.2.3, respectively.

5.1 Large-R Jet Calibration

The jet reconstruction and calibration chains are illustrated in Figure 5.1 and explanations of each step are given as follows. In the first step, the reconstruction for calorimeter energy clusters and jets have already been mentioned as the topo-clusters described in Section 4.2 and the k_t sequential recombination described in Section 4.5. The following sections introduce downstream procedures.



Fig. 5.1: An overview of the large-R jet reconstruction and calibration is shown. Reconstructed calorimeter energy clusters (topo-clusters) are clustered as an ungroomed jet by the anti- k_t $R = 1.0$ algorithm. The ungroomed jet is groomed by the trimming algorithm. Finally, it is calibrated by the MC and in-situ calibrations and then used in the semileptonic VBS analysis.

5.1.1 Grooming

Due to a large solid angle of a reconstructed large-R jet, it is severely contaminated by calorimeter noises, particles from pileup vertices, and soft radiations from the same bunch crossing as shown in Figure 5.2.

The removal of unnecessary energy deposits is achieved by *grooming*. There are several types of groomings such as “Mass drop/filtering” [101], “Pruning” [102], and “Trimming” [103]. For this study, the trimming algorithm is chosen from a study in Reference [104]. The trimming algorithm proceeds as

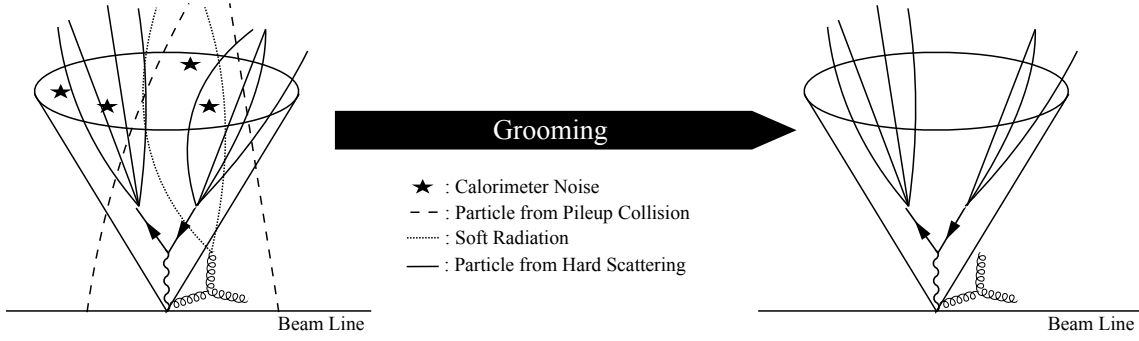


Fig. 5.2: An overview of a grooming technique is shown. The large area of a large-R jet significantly contains hits from undesired sources, pileup, soft radiation, and calorimeter noise. The trimming algorithm reclusters large-R jet with $k_t R = 0.2$ algorithm, and resultant jets satisfying $p_T^{R=0.2}/p_T^{R=1.0} < 0.05$ are trimmed.

follows: constituents of a Large-R jet are reclustered with the $k_t R = 0.2$ algorithm, and the reclustered $k_t R = 0.2$ jets are trimmed if those satisfy with a condition of $p_T^{R=0.2,i}/p_T^{R=1.0} < 0.05$, where i is an index of $R = 0.2$ k_T jets.

5.1.2 MC Calibration

The next step is for corrections of energy and angle with respect to MC simulations. This MC calibration is needed because the detectors cannot detect all particles within jets. In particular,

- hadrons passing through non-sensitive areas of the detector,
- Intrinsic energy loss by miss reconstruction in the detector,
- particles that cannot be reconstructed by calorimeters. (ν , μ , etc.)

The MC calibration exploits dijet samples generated by the PYTHIA 8 (v8.186) [55] with A14 set of tuned parameters [105] and NNPDF23LO PDF set. To restore the original four-momentum, the *truth jets* are defined as a reference. The truth jet is reconstructed in the same manner for reconstructed jets with particles having lifetime τ in the laboratory frame as $c\tau > 10$ mm. The calibration factor is defined as $R_E = \langle E_{\text{reco}}/E_{\text{truth}} \rangle$, where $\langle \rangle$ represents a mean obtained by fit to $E_{\text{reco}}/E_{\text{truth}}$ distribution with the Gaussian function. A correspondence between reconstructed and truth jets is matched by using ΔR . The correction factors for each E and m are represented as c_{JES} and c_{JMS} , respectively. Examples of correction factors are shown in Figure 5.3.

The c_{JMS} is evaluated after applying c_{JES} , pseudorapidity correction ($\Delta\eta$) only changes the polar angle. The corrected observables are denoted as

$$E_{\text{reco}} = c_{\text{JES}} E_0, \quad m_{\text{reco}} = c_{\text{JES}} c_{\text{JMS}} m_0, \quad \eta_{\text{reco}} = \eta_0 + \Delta\eta, \quad (5.1)$$

$$p_T^{\text{reco}} = c_{\text{JES}} \sqrt{E_0^2 - c_{\text{JES}}^2 m_0^2 / \cosh(\eta_0 + \Delta\eta)}. \quad (5.2)$$

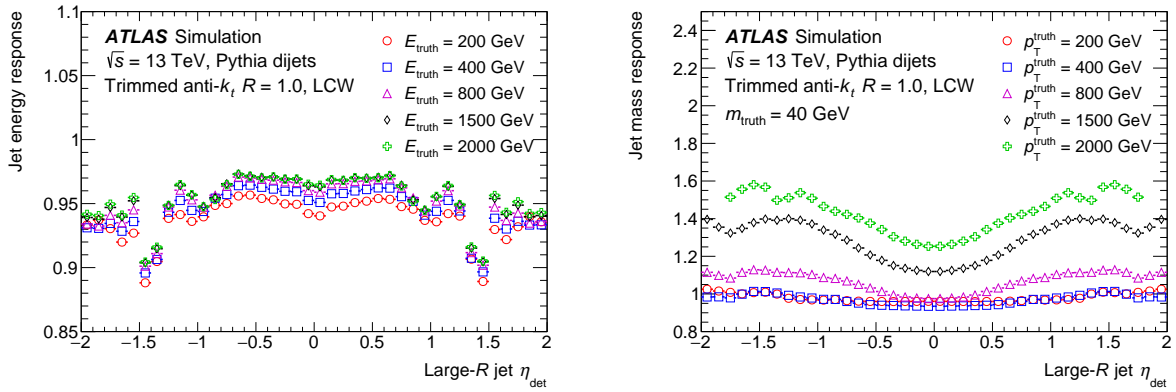


Fig. 5.3: The energy (left) and m (right) calibration factors for large-R jets with respect to η are shown [106]. The jet energy response is almost constant with respect to its energy, but explicit deficits are observed around jet $|\eta| \sim 1.4$ because of the transition regions of the calorimeter. The mass response is almost unity at $p_T = 200$ GeV but it increases in ~ 1.6 at $p_T = 2$ TeV because gluon radiation increases at higher energy.

5.1.3 *in-situ* Calibration

After applying the MC calibration, a four-momentum of a large-R jet reproduces a corresponding truth jet. Nevertheless, the MC calibration is based on detector simulations which have intrinsic differences from the observed data. The disagreements are corrected by *in-situ* techniques described in the following sections. The 2015-16 datasets are used for those calibrations. Details of the datasets and MC simulations used in those studies are shown in Reference [106].

Energy Scale Calibration

The energy calibration exploits the momentum conservation law on the transverse plane. Events for this calibration are required to be the back-to-back topology of a jet being calibrated (probe jet) and one or more well-calibrated objects (reference objects) such as γ , leptonically decaying Z boson, or small-R jets (multijets). Cartoons of each topology are shown in Figure 5.4. The processes for the reference objects have different large-R jet p_T ranges: γ +jet events cover low p_T ($\sim 150 < p_T < \sim 400$ GeV), Z+jet events cover medium p_T ($\sim 300 < p_T < \sim 1000$ GeV), and multijets events cover high p_T ($\sim 800 < p_T$ GeV) corresponding to those production cross-sections. The p_T of a probe jet (p_T^{probe}) is compared to the p_T of the sum of the reference objects (p_T^{ref}), which is intrinsically balanced from the momentum conservation law on the transverse plane. Thus the response ratios of the MC simulations to the observed data represent mismatches between those. Those ratios are applied to the observed data as a scale factor, and accompanied systematic uncertainties are considered in analyses.

Analyses are performed by selecting topology such as Figure 5.4¹⁾, and calculate a relative response

¹⁾The details of selection are described in Reference [107].

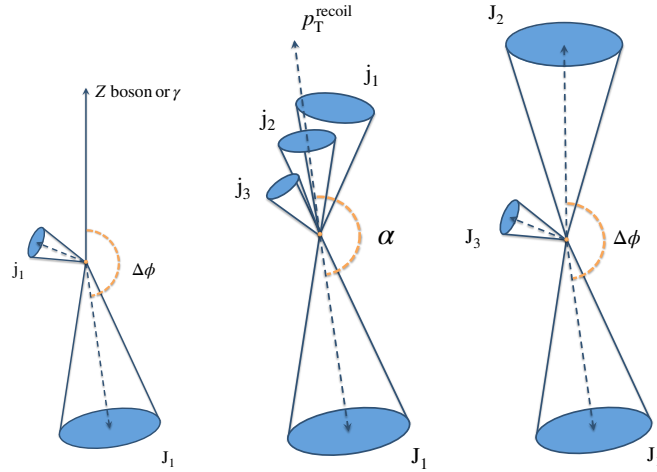


Fig. 5.4: Cartoons of topologies for Z/γ +jets (left), multijet (central), and dijet (right) are shown [106]. The capital j (J) and small j (j) denote a large-R jet and a small-R jet, respectively. The subscripts express the order of p_T . The $\Delta\phi$ or α is an angle between a large-R jet and recoil objects, Z , γ , the vector sum of small-R jets, or a large-R jet.

between the probe and reference jets defined as

$$R_{\text{rel}} = \left\langle \frac{p_T^{\text{probe}}}{p_T^{\text{ref}}} \right\rangle \sim \frac{2 + \langle \mathcal{A} \rangle}{2 - \langle \mathcal{A} \rangle}, \quad (5.3)$$

$$\mathcal{A} = \frac{p_T^{\text{probe}} - p_T^{\text{ref}}}{p_T^{\text{avg}}}, \quad (5.4)$$

where $p_T^{\text{avg}} = (p_T^{\text{probe}} + p_T^{\text{ref}})/2$, $\langle \rangle$ is the mean value of the \mathcal{A} distribution obtained by the Gaussian fit.

A representative R_{rel} distribution for each process is shown in Figure 5.5. The energy scales of the observed data for three different topologies are consistently 2-3% underestimated than that of the MC simulations, i.e. there are unidentified sources of energy loss at the ATLAS detector and/or unimplemented elements in the detector simulation. The several MC simulations agree within 1%. The difference between the observed data and the MC simulations is relatively small and consistent with that of small-R jets. The measurements of R_{rel} obtained by the different methods shown in Figure 5.5 are combined the same as the method described in Reference [108]. The result of the combination is shown in Figure 5.6. The combined p_T response in the observed data is around 3% lower than one for the MC simulation in the whole range. The total uncertainty is less than 1% below 1 TeV and 2% at 1 TeV. Thus the deviation is significant and the response ratio between the observed data and the MC simulation should be applied to data. The results performed here are the most reliable to date, however, since the tight time scale of the semileptonic VBS analysis performed in Chapter 6, this calibration is not applied. Instead, r_{trk} double ratio method introduced in Section 5.1.3 is used to estimate those systematic uncertainties.

5.1. LARGE-R JET CALIBRATION

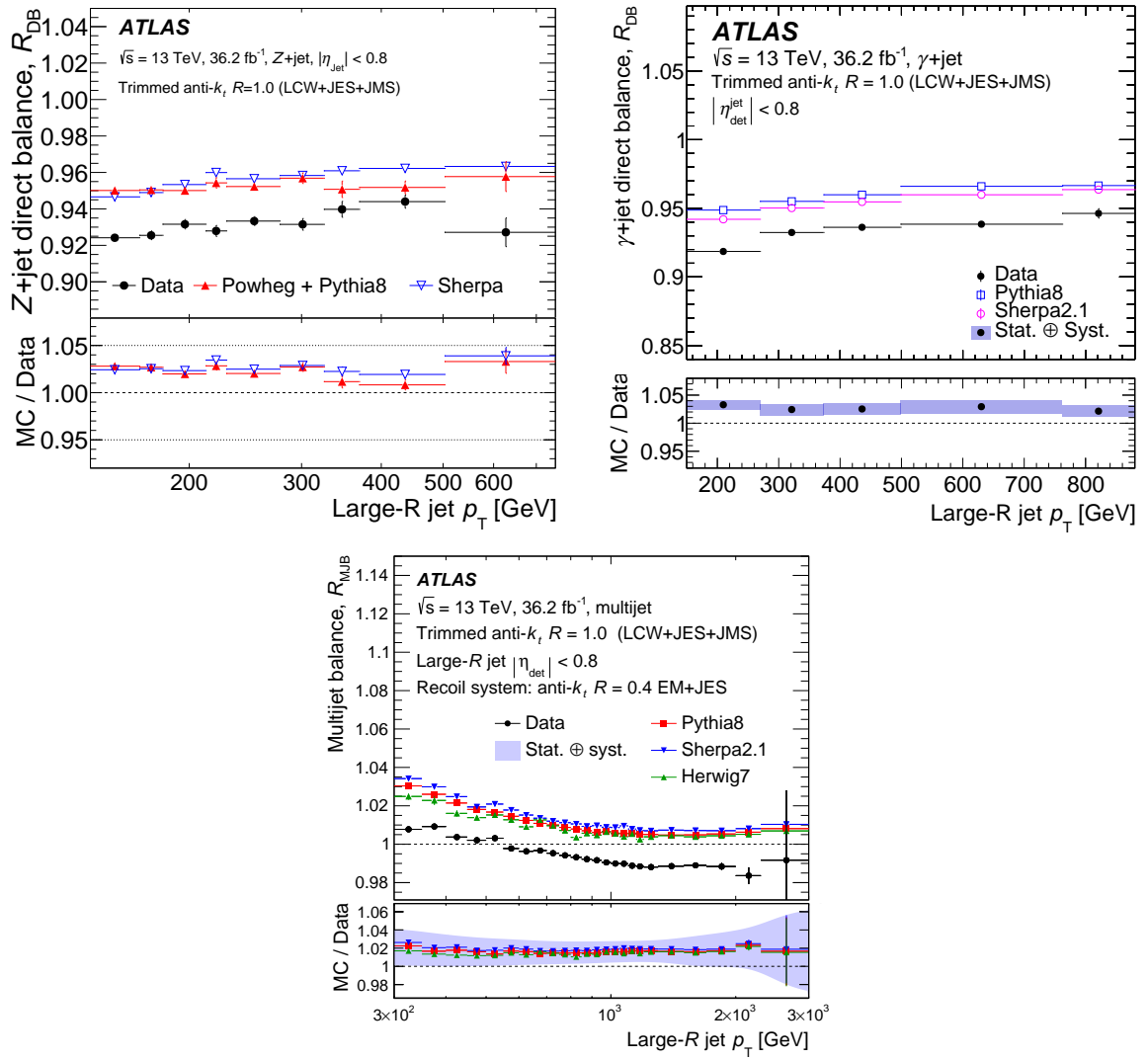


Fig. 5.5: R_{rel} distributions for Z jets (left), γ jets (right), and multijet (bottom) events are shown [106].

5.1. LARGE-R JET CALIBRATION

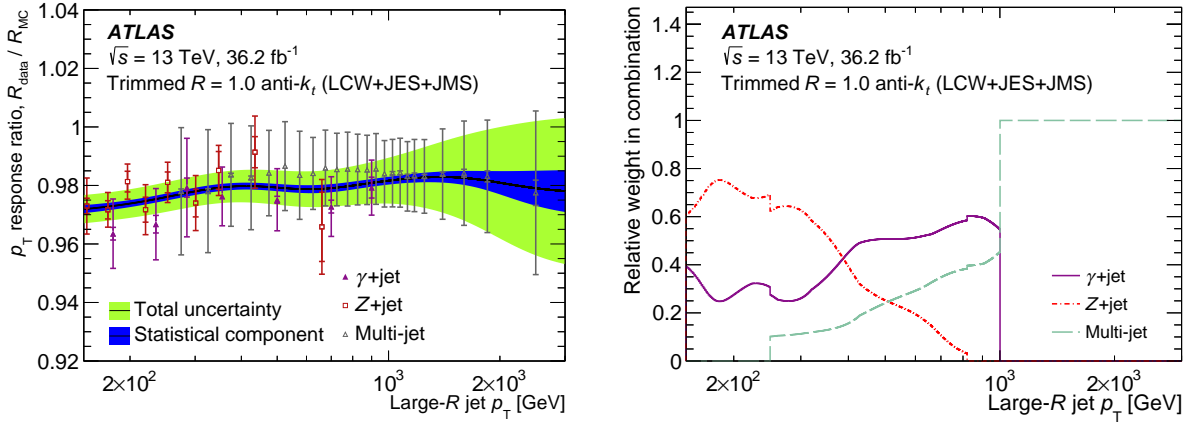


Fig. 5.6: The combined response ratio (left) and weights of each measurement in the combination (right) are shown [106]. The response ratio is at most 0.97 in the whole large-R jet p_T ranges. The three measurements from different topologies are consistent. The total uncertainty is less than 1% below 1 TeV and 2% at 1 TeV. The right plot represents that this combination is dominated by γ +jets, Z+jets, and multijet events at $p_T < 400$ GeV, $400 < p_T < 1000$ GeV, and $1000 < p_T$ GeV.

Energy Resolution Calibration

The energy resolution is calibrated with the dijet topology as shown in Figure 5.4. The width of the asymmetry \mathcal{A} distribution is represented as

$$\sigma(\mathcal{A}) = 2\sqrt{\left(\frac{\sigma(p_T^1 - p_T^2)}{p_T^1 + p_T^2}\right)^2 + \left(\frac{p_T^1 - p_T^2}{(p_T^1 + p_T^2)^2} \sigma(p_T^1 + p_T^2)\right)^2} \quad (5.5)$$

$$\sim \frac{\sqrt{\sigma(p_T^1)^2 + \sigma(p_T^2)^2}}{p_T^{\text{avg}}}, \quad (5.6)$$

where, p_T and $\sigma(p_T)$ represent p_T of jets and those errors, respectively. The jet-1 and jet-2 are assigned randomly to avoid any bias. The approximation of the second formula uses an assumption of $1 \gg \left(\frac{p_T^1 - p_T^2}{p_T^1 + p_T^2}\right)^2$.

In case that both the jet-1 and jet-2 are in the $|\eta| < 0.8$ region, i.e. both of them expected to have a similar energy resolution, Equation 5.5 is simplified as

$$\sigma(\mathcal{A}) \sim \frac{\sqrt{2\sigma(p_T^{\text{avg}})^2}}{p_T^{\text{avg}}} \rightarrow \frac{\sigma(p_T^{\text{avg}})}{p_T^{\text{avg}}} = \frac{\sigma(\mathcal{A})}{\sqrt{2}}. \quad (5.7)$$

For one where $|\eta| > 0.8$, a central jet $|\eta| < 0.8$ is exploited as a reference jet, this resolution is represented

as

$$\left(\frac{\sigma(p_T^{\text{forward}})}{p_T^{\text{avg}}}\right)^2 = \sigma(\mathcal{A})^2 - \left(\frac{\sigma(p_T^{\text{central}})}{p_T^{\text{avg}}}\right)^2 \quad (5.8)$$

$$= \sigma(\mathcal{A})^2 - \left(\frac{\sigma(\mathcal{A})}{\sqrt{2}}\right)^2, \quad (5.9)$$

$$\rightarrow \frac{\sigma(p_T^{\text{forward}})}{p_T^{\text{avg}}} = \sqrt{\sigma(\mathcal{A})^2 - \frac{\sigma(\mathcal{A})^2}{2}}, \quad (5.10)$$

where p_T^{central} and p_T^{forward} indicate p_T for jet in $|\eta| < 0.8$ and $|\eta| > 0.8$ regions, respectively. Therefore, the all things needed to measure the in-situ jet energy resolution is values of $\sigma(\mathcal{A})$.

In order to extract the pure response of $\sigma(\mathcal{A})$ avoiding non-Gaussian tails coming from pileup and out-of-cone particles, the extraction of $\sigma(\mathcal{A})$ is performed from the \mathcal{A} distribution by the sequential Gaussian fits:

1. Fit the asymmetry distribution for full range ($\mathcal{A} = [-1, 1]$),
2. Fit the asymmetry distribution within 2σ of iteration 1,
3. Fit the asymmetry distribution within 2σ of iteration 2.

An example of fits shown in Figure 5.7 represents the fits agree with the observed data for the core region for the \mathcal{A} distribution.

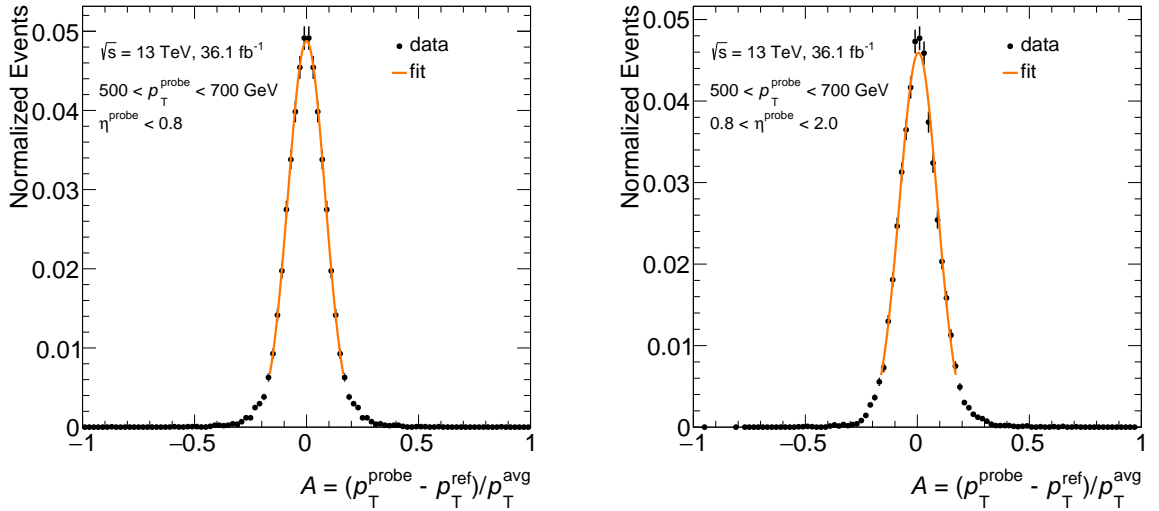


Fig. 5.7: The distribution of \mathcal{A} at $|\eta| < 0.8$ (left) and $|\eta| > 0.8$ (right) regions are shown. The results of fits (orange line) show good agreements with distributions for the observed data (black dots) avoiding non-Gaussian tails.

The evaluated $\sigma(\mathcal{A})$ values for the observed data, the MC simulation, and truth jets are plotted with respect to the large-R jet p_T as shown in Figure 5.8.

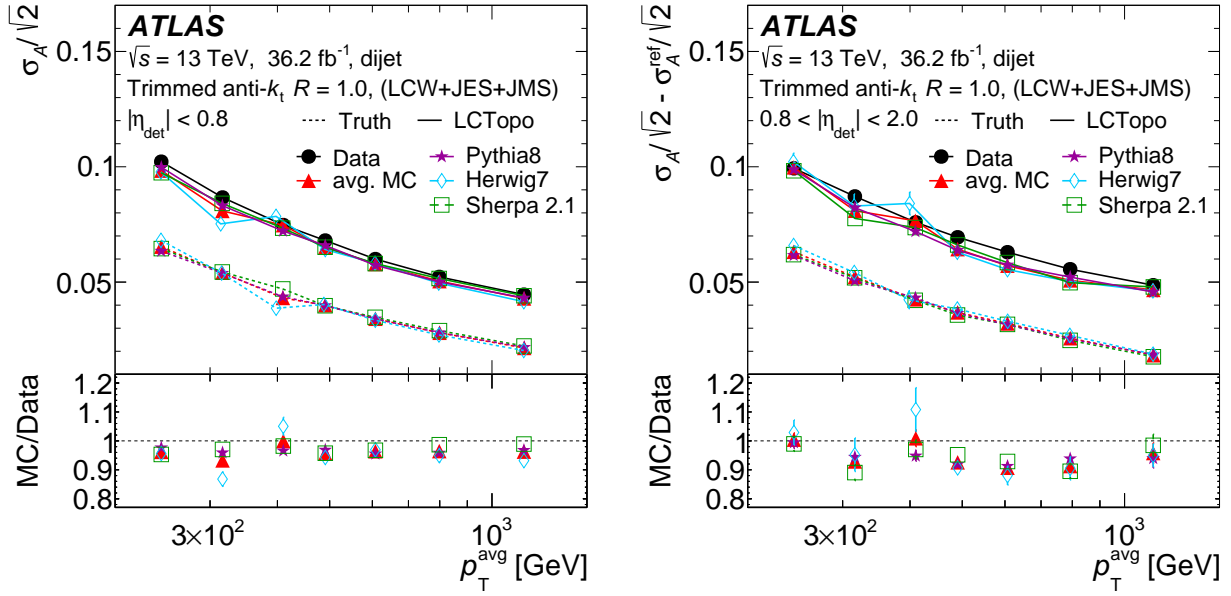


Fig. 5.8: The p_T dependence of $\sigma(\mathcal{A})$ at $|\eta| < 0.8$ (left) and $|\eta| > 0.8$ (right) regions are shown. The values of the observed data are shown in the black dots, the other colors indicate each MC simulation and an average of them. The dashed and solid lines stand for truth and reconstructed jets, respectively.

The $\sigma(\mathcal{A})$ values for the observed data and MC simulations include unbalancing sources deriving from out-of-cone effects and irreducible extra radiation. Since the sources are uncorrelated to the fluctuation of the detector resolution, those can be removed by the quadratic subtraction of a corresponding truth jet asymmetry $\mathcal{A}^{\text{truth}}$ from a reconstructed jet asymmetry $\mathcal{A}^{\text{reco}}$:

$$\mathcal{A}^{\text{subtracted}} = \sqrt{(\mathcal{A}^{\text{reco}})^2 - (\mathcal{A}^{\text{truth}})^2}. \quad (5.11)$$

The subtraction is performed after applying fits on graphs as shown in Figure 5.8 with the physical motivated function:

$$\frac{\sigma(p_T)}{p_T} = \frac{N}{p_T} \oplus \frac{S}{\sqrt{p_T}} \oplus C, \quad (5.12)$$

where fit variables N , S , and C refer to as noise, stochastic, and constant, corresponding to electronic and pileup noises, the sampling nature of the calorimeter, and signal losses due to the insensitive material, respectively. Subtracted asymmetry ($\mathcal{A}^{\text{subtracted}}$) values, i.e. the large-R jets p_T resolutions with respect to large-R jet p_T are shown in Figure 5.9. The resolutions are estimated as 6 (6)% at $p_T = 300$ GeV and 4 (4.5)% at $p_T = 1$ TeV for a jet in the $|\eta| < 0.8$ ($0.8 < |\eta| < 2.0$) region. The discrepancies between the observed data and MC simulations is at most 10%, which are small compared to the total uncertainty.

The total uncertainty in the jet energy resolutions and those decompositions are displayed as shown in Figure 5.10. The dominant uncertainties are the JES uncertainty propagated from the estimation at Section 5.1.3 at lower large-R jets p_T and the non-closure at higher large-R jets p_T . The non-closure is an uncertainty in this methodology, which is estimated by comparing a truth resolution $(p_T^{\text{jet}} - p_T^{\text{particle}})/p_T^{\text{particle}}$

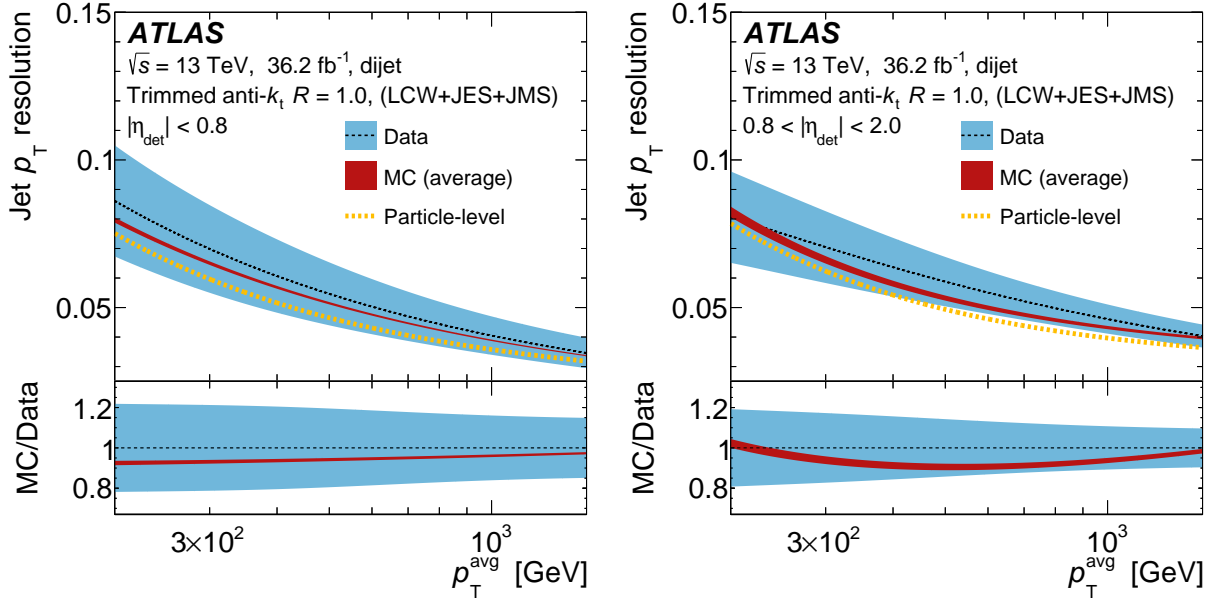


Fig. 5.9: The p_T dependences on jet p_T resolutions at $|\eta| < 0.8$ (left) and $|\eta| > 0.8$ (right) regions. The three lines represent the fit results with Equation 5.12 for the observed data (black dashed line), MC simulations (dark red line), and the particle-level (yellow dashed line) which is the resolutions directly calculated from ΔR -matched truth jet. The widths of lines denote statistical uncertainty in itself. Agreements with the MC simulations and Particle-level support validity of this method. The blue band stands for the combined systematic uncertainties.

and a JER estimated by this method, corresponding to the differences between the dark red line and dashed yellow lines in Figure 5.9. The total uncertainties are estimated as 16 (14)% at $p_T = 300$ GeV and 14 (10)% at $p_T = 1$ TeV for a jet in $|\eta| < 0.8$ ($0.8 < |\eta| < 2.0$). This is the first measurement of the large-R jet p_T resolution with an in-situ way.

Jet Substructure Variable Calibration

The large-R jets p_T , mass, and D_2 defined in Section 2.4 are calibrated by the *rTrk double ratio method* as follows. The quantity of r_{trk} is defined as $r_{\text{trk}} = X_{\text{calo}}/X_{\text{trk}}$ where X is a certain variable such as jet p_T , mass, or D_2 , X_{calo} and X_{trk} are quantities X calculated with the topo-clusters and tracks, respectively. The r_{trk} can be expanded as

$$r_{\text{trk}} = \frac{X_{\text{calo}}}{X_{\text{trk}}} = \frac{X_{\text{calo}}}{X_{\text{particle}}} \cdot \frac{X_{\text{particle}}}{X_{\text{charged-particle}}} \cdot \frac{X_{\text{charged-particle}}}{X_{\text{trk}}} \quad (5.13)$$

$$= R \cdot f_{\text{charge}}^{-1} \cdot R_{\text{trk}}^{-1}, \quad (5.14)$$

where X_{particle} and $X_{\text{charged-particle}}$ are quantities X calculated by truth particles and truth charged particles, respectively. $R = X_{\text{calo}}/X_{\text{particle}}$ refers to as calorimeter response, f_{charge}^{-1} is an inverse of charged particle fraction for a given jet, and $R_{\text{trk}}^{-1} = X_{\text{charged-particle}}/X_{\text{trk}}$ is an inverse of tracker response. On the assumptions of no correlation between R and $f_{\text{charge}}^{-1} \cdot R_{\text{trk}}^{-1}$, a relation $\langle r_{\text{trk}} \rangle \propto \langle R \rangle$, and a good charged

5.1. LARGE-R JET CALIBRATION

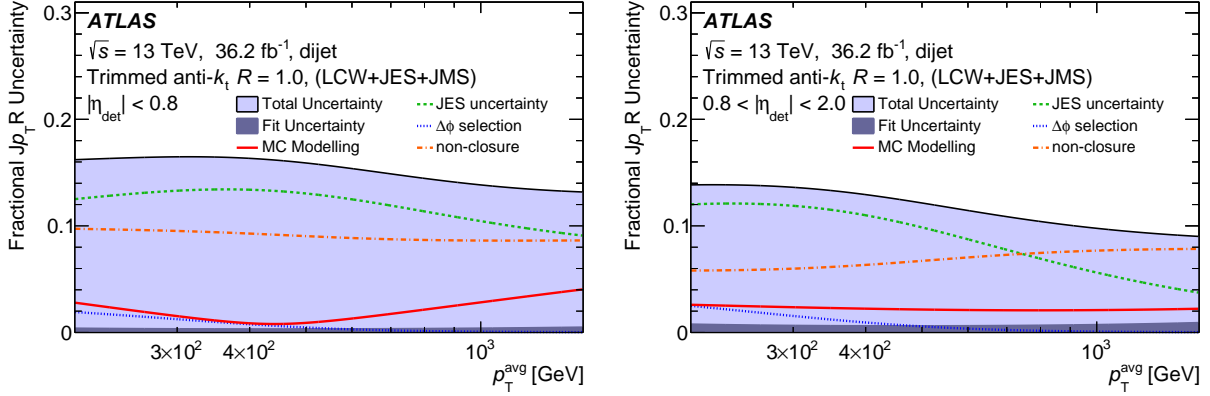


Fig. 5.10: The p_T dependence of uncertainty in jet p_T resolution at $|\eta| < 0.8$ (left) and $|\eta| > 0.8$ (right). An interpolation with a filter using a sliding Gaussian kernel is applied to all of the uncertainty dependencies with respect to large-R jets p_T .

particle counting and a momentum resolution ($k^{\text{MC}} \sim k^{\text{data}}$, where $k = f_{\text{charge}} R_{\text{trk}}$) hold, one can obtain the difference of response between the observed data and MC simulations:

$$\frac{\langle R^{\text{data}} \rangle}{\langle R^{\text{MC}} \rangle} = \frac{k^{\text{MC}}}{k^{\text{data}}} \frac{r_{\text{trk}}^{\text{data}}}{r_{\text{trk}}^{\text{MC}}} \sim \frac{r_{\text{trk}}^{\text{data}}}{r_{\text{trk}}^{\text{MC}}}. \quad (5.15)$$

Therefore, r_{trk} double ratio $r_{\text{trk}}^{\text{data}}/r_{\text{trk}}^{\text{MC}}$ is corresponding with the difference of response between the observed data and MC simulations. This method can be applied to generic types of jet substructure variables if the independence between R and $f_{\text{charge}}^{-1} \cdot R_{\text{trk}}^{-1}$ is guaranteed.

The uncertainty in this method (ϵ) is simply given as

$$\epsilon = \epsilon_{\text{Pythia}} \oplus \epsilon_{\text{Modeling}} \oplus \epsilon_{\text{Tracking}}, \quad (5.16)$$

where ϵ_{Pythia} is the difference of r_{trk} double ratios between the prediction of PYTHIA [55] and the observed data, $\epsilon_{\text{Modeling}}$ is the difference of r_{trk} double ratio between prediction of PYTHIA and HERWIG++ [56], and $\epsilon_{\text{Tracking}}$ is an uncertainty propagated from tracking uncertainties described in References [109] (resolution), [110] (efficiency within dense environments), and [111] (alignment). Figure 5.11 shows $\langle r_{\text{trk}} \rangle$ for large-R jets p_T , mass, and D_2 with respect to large-R jets p_T . Since the r_{trk} double ratios are compatible with unity within uncertainty, the scales predicted by the MC simulations are used in the semileptonic VBS analysis, and the uncertainties are propagated through the statistical treatment. A total uncertainty in the p_T scale is estimated as 2% (6%) at $p_T = 500$ GeV (3 TeV). A total uncertainty in the mass scale is estimated as 3% (6%) at $p_T = 500$ GeV (3 TeV). A total uncertainty in the D_2 scale is estimated as 2% (7%) at $p_T = 300$ GeV (3 TeV).

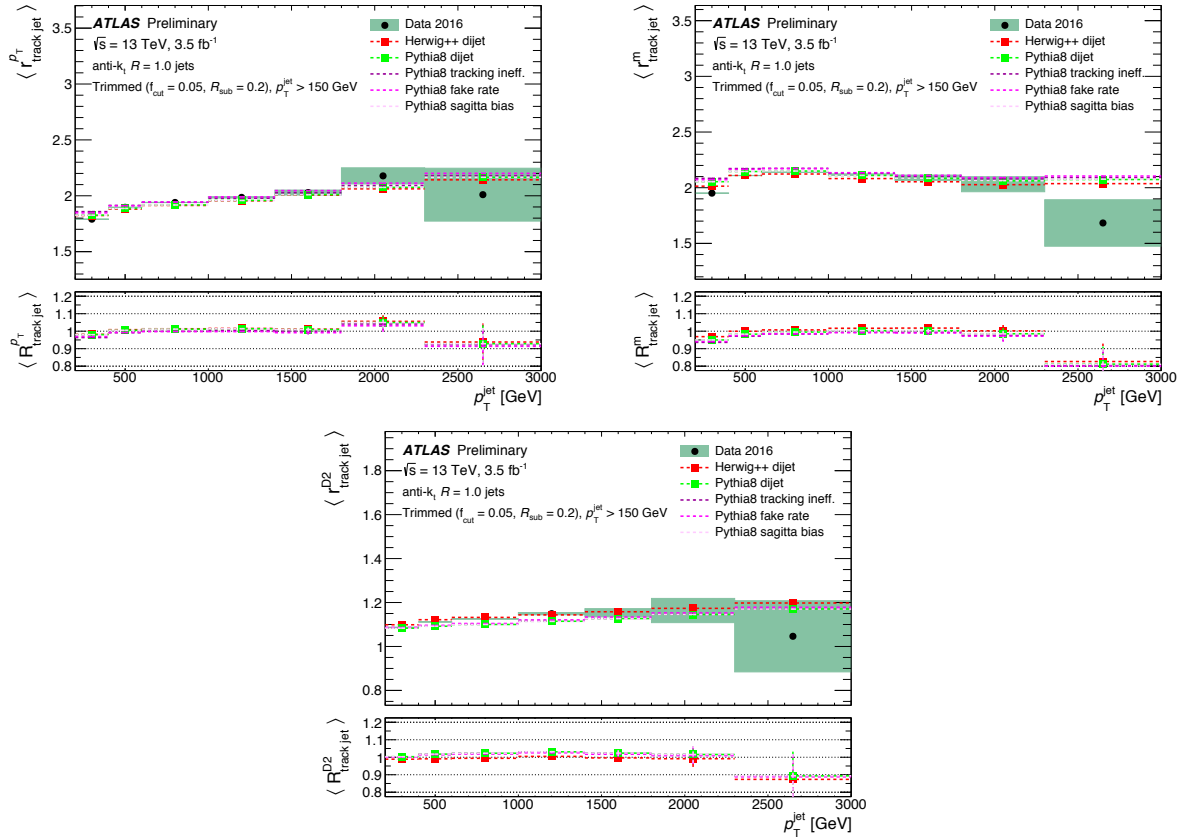


Fig. 5.11: The $\langle r_{\text{trk}} \rangle$ and its double ratio for large-R jets p_T (left), m (right) and D_2 (bottom) with respect to large-R jets p_T are shown [112]. The observed data and nominal MC simulation (PYTHIA) are shown in black and green dots, respectively. The systematic variation of an MC simulator (HERWIG++) is shown in red dots. Three variations to evaluate tracking uncertainties are shown in dashed lines.

5.2 Weak Vector Boson Identification

The reconstruction with a large-R jet significantly increases the signal efficiency of highly Lorentz boosted boson jets, whereas it drastically adds backgrounds from q/g jets since there is no difference in four-momentum level between them. The D_2 and invariant mass for large-R jets discussed in Section 2.4 are used to identify boson jets from q/g jets. A D_2 is calculated from topo-clusters for a given jet. As for a jet invariant mass, a dedicated reconstruction technique, *Track Assisted Mass* is exploited for reconstruction as introduced in Section 5.2.1. Two different types of identification approach are introduced in Section 5.2.2 for cut-based taggers, and in Section 5.2.3 for machine learning based taggers. The 2015-16 ATLAS dataset is used for those studies. The MC simulations used in those studies are shown in Reference [107].

5.2.1 Track Assisted Mass

For the energy (or momentum) resolutions, in principle, a calorimeter energy resolution improves for higher energy jets as shown in Figure 5.9 because calorimeter energy resolution relies on the number of counted photons produced by scintillator proportion to the energy for a given jet, whereas a track momentum resolution becomes worse due to almost straight curvature at higher p_T . As for the angle resolution, a cell in calorimeters is much larger than the one of silicon detectors for tracking, hence tracks have much better angle resolutions.

Since Large-R jets are used for highly Lorentz boosted jets, particles inside the jets are very close to each other not enough to separate with the calorimeter due to its size of cells. A schematic graph of this situation is shown in Figure 5.12.

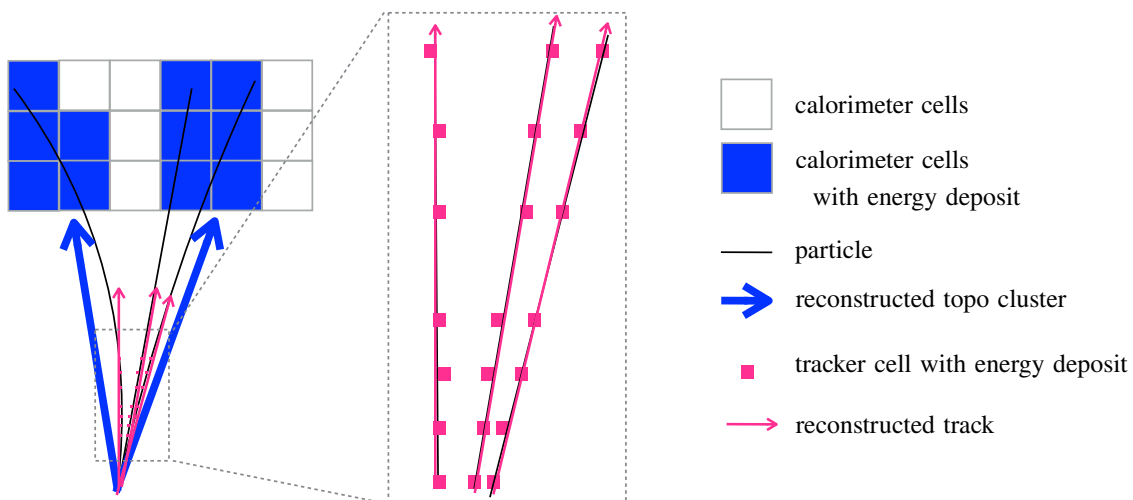


Fig. 5.12: A schematic graph for three charged particles into the calorimeter through the tracker. One of them is isolated, and the other ones are very close to each other. An isolated one is reconstructed as a single topo-cluster and a single track, whereas the other ones are reconstructed as a single topo-cluster and double tracks.

A simple solution is that one uses an energy for a calorimeter jet (reconstructed from topo-cluster) and an angle for a track jet for a given jet. In general, a mass of a track jet is lower than the one for a truth jet by missing neutral particles in a given jet. The neutral particle fraction is correlated to the $p_T^{\text{calo}}/p_T^{\text{track}}$ where p_T^{calo} and p_T^{track} stand for p_T for given calorimeter and track jets, respectively. As a result, a strong correlation between $p_T^{\text{calo}}/p_T^{\text{track}}$ and mass emerges for a given track jet m^{track} as shown in Figure 5.13.

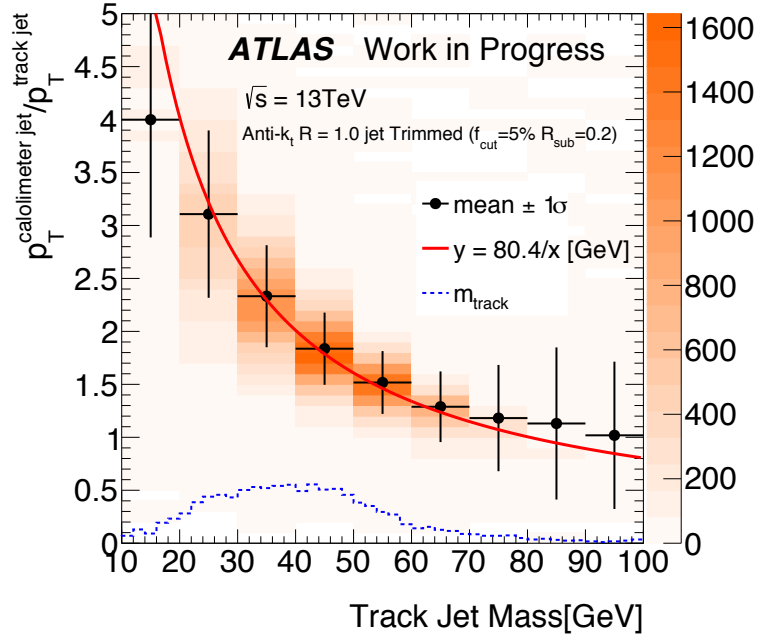


Fig. 5.13: A population for W jets on the m^{track} and $p_T^{\text{calo}}/p_T^{\text{track}}$ plane. A median for the W jets population for each m^{track} bin (black marker with RMS as error bar) is compatible with the $80.4/x$ curve (red line).

The correlation shown in Figure 5.13 implies that the track assisted (TA) mass has potential to be a better resolution than the mass of a calorimeter jet (calo mass). The TA mass is defined as

$$m^{\text{TA}} = \frac{p_T^{\text{calo}}}{p_T^{\text{track}}} \cdot m^{\text{track}}, \quad (5.17)$$

where m^{TA} represents the track assisted mass. Correspondences between a calorimeter jet and tracks are mapped by the *ghost association technique*²⁾ [89].

The TA mass resolution is better than that of the calo mass at $p_T > 1$ TeV as shown in Figure 5.14, however, ones at $p_T < 1$ TeV are worse. This is because a track p_T resolution is worse at a lower p_T range as mentioned already. A simple solution to improve resolutions at low p_T ranges is combining the

²⁾Large-R jet constituents (topo-clusters) and tracks with an artificial four-momentum, $(p_T, \eta, \phi, E) = (0, \eta_{\text{trk}}, \phi_{\text{trk}}, 0)$, are simultaneously clustered with anti- k_t $R = 1.0$ algorithm (the tracks are not affected to the jet reclustering because of zero momentum). Then the tracks included in the reclustered jet are judged as to be associated tracks.

track assisted mass and the calo mass with the linear combination:

$$m^{\text{comb}} = \frac{\sigma_{\text{calo}}^{-2}}{\sigma_{\text{calo}}^{-2} + \sigma_{\text{track}}^{-2}} m^{\text{calo}} + \frac{\sigma_{\text{track}}^{-2}}{\sigma_{\text{calo}}^{-2} + \sigma_{\text{track}}^{-2}} m^{\text{track}}, \quad (5.18)$$

where m^{comb} is referred to as combined mass, and σ_{calo} and σ_{track} stand for those resolutions as shown in Figure 5.14. The combined mass has almost the same or better resolution than that of the calo mass in the whole p_T range as shown in Figure 5.14. The combined mass resolution improves approximately 30% (50%) compared to the one of the calo mass.

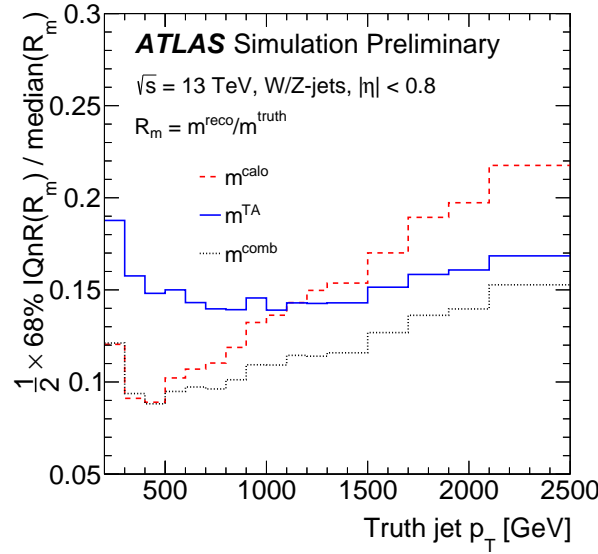


Fig. 5.14: The mass resolution for a calorimeter jet (m^{calo}), a track assisted mass (m^{TA}), and a combined mass (m^{comb}) are shown. The resolution (y-axis) is defined with the median of a mass response ($R_m = m^{\text{reco.}}/m^{\text{truth}}$) and the 68% inter quantile range (IQnR). The m^{calo} has better mass resolution below $p_T = 1$ TeV, whereas m^{TA} has better resolution at above $p_T = 1$ TeV. The m^{comb} has the same or a better resolution than m^{calo} at the whole p_T range except a few bins at low p_T . This reverse feature is because R_m does not perfectly behave as Gaussian, and then the linear combination becomes a non-ideal combination.

5.2.2 Two-Variable-Tagger

In this section, the combined mass (hereafter “mass”) defined in the previous section are used to construct weak vector boson identification algorithm together with the D_2 . The cut-based tagger consists of rectangular cuts on the D_2 and mass. This tagger is used in the semileptonic VBS analysis described in Chapter 6.

Firstly, the description of MC simulated events for the D_2 and mass is confirmed in the observed data by $t\bar{t}$ events as shown in Figure 5.15. The 2015-16 dataset and MC simulations for the $t\bar{t}$ and single top-quark production, W/Z +jets events are used in the comparisons. The samples are the same ones

used in the semileptonic VBS analysis described in Section 6.2. Both of the distributions describe the observed data well within systematic uncertainties.

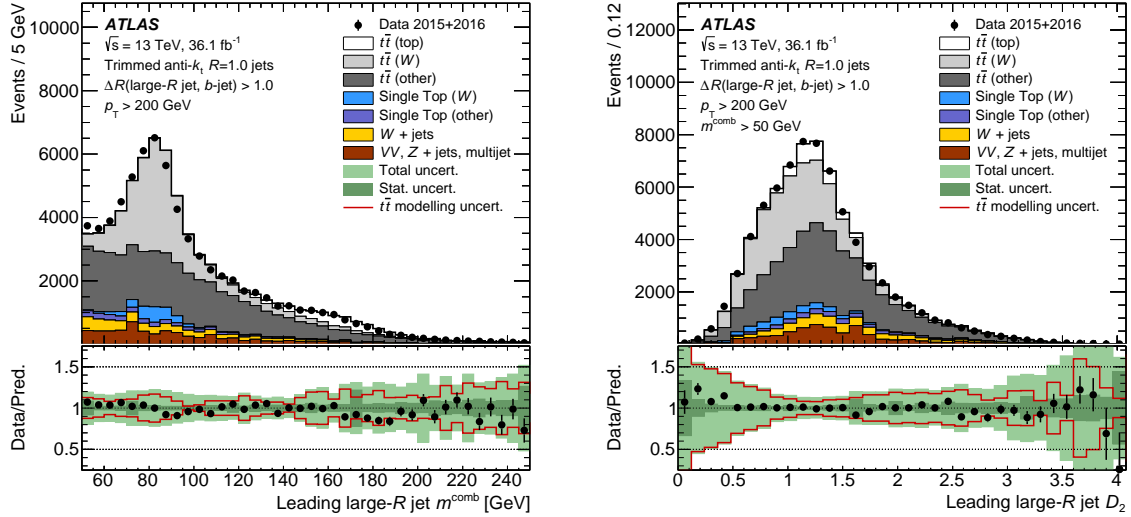


Fig. 5.15: Comparisons between the observed data and MC simulations for large-R jets mass (left) and D_2 (right) in $t\bar{t}$ enhanced region are shown. The dominant systematic uncertainty is theoretical uncertainties for $t\bar{t}$ shape [107].

Secondly, the thresholds of rectangular cuts are defined. There is ambiguity for cut thresholds on a two-dimensional space for the D_2 and mass. In this study, a q/g background jets rejection at fixed signal efficiencies (50, 80%) is assigned as a metric, and scanning over full ranges of D_2 upper cuts and mass sideband cuts with respect to jet p_T are performed. p_T dependent cut thresholds are intended to consider p_T dependencies of D_2 and mass. This study exploits MC simulated events only. The signal W or Z jets are obtained from $W' \rightarrow WZ \rightarrow q\bar{q}q\bar{q}$ events made by the high-mass sequential standard model [113]. The resonance masses are set from 400 GeV to 5 TeV to obtain the p_T range for W/Z jets from 200 GeV to 2.5 TeV. The background q/g jets are generated by multijet processes which are modeled using the leading order of Feynman diagrams by the PYTHIA 8 (v8.186) event generator the same as MC calibration. Both of the signal and background are fragmented by the PYTHIA 8 (v8.186) event generator with the NNPDF23LO PDF set.

As the final step, the chosen mass cut thresholds for each p_T bin are fitted by the physically inspired function form $m_J = \sqrt{(A/p_T + B)^2 + (C \cdot p_T + D)^2}$, where A , B , C , and D represent fit constants. The first term corresponds to an opening angle between two quarks, the second term corresponds to the detector resolution. The one for the D_2 is fitted by fourth-order polynomial functions. Figure 5.16 shows a W jet population on the p_T and D_2 or p_T and mass space, and Figure 5.17 shows the cut functions for each variable. The cut thresholds are optimized for each W and Z boson jets case, separately.

The two-variable-tagger achieved approximately a 95% (98.7%) background rejection at a 50% signal efficiency at a p_T range of $200 \leq p_T \leq 500$ GeV ($1000 \leq p_T \leq 1500$ GeV) as shown in Figure 5.21.

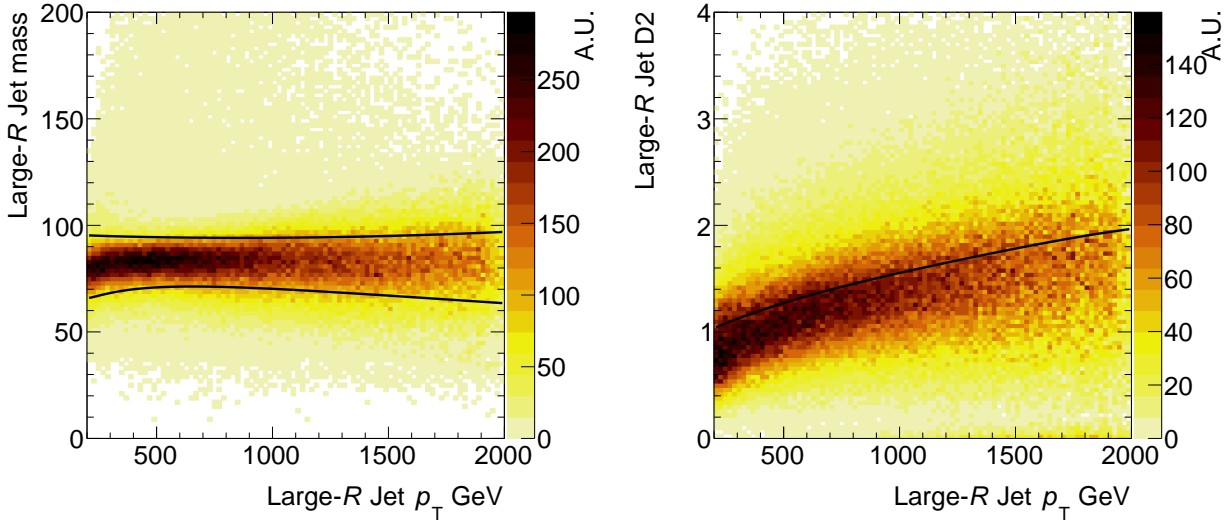


Fig. 5.16: A W jet population on the p_T and mass space (left) and the p_T and D_2 space (right) are shown. The black lines stand for 50% working point thresholds.

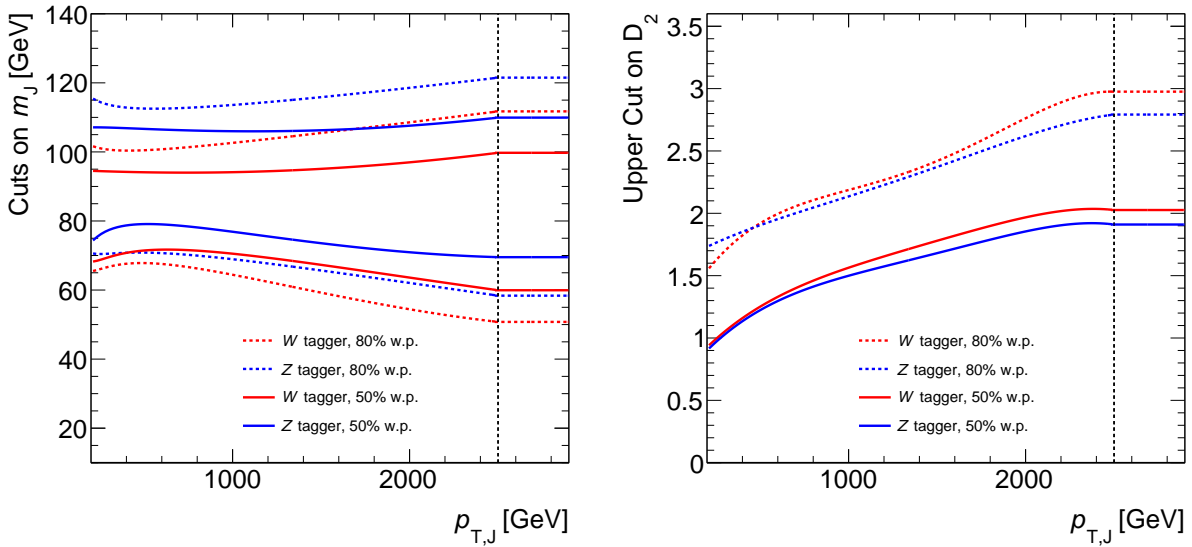


Fig. 5.17: The thresholds of the mass window cuts (left) and the upper cut on D_2 (right) with respect to p_T of a large-R jet are shown. The red and blue (dashed) lines represent 50% (80%) cut thresholds for W and Z boson-tagging. Above the vertical dashed line on $p_T = 2500$ GeV, the cut thresholds become constants because there is not enough statistics above $p_T = 2500$ GeV in MC simulated events to define cut thresholds.

5.2.3 Jet-Substructure-Based Machine Learning Tagger

In this section, advanced machine learning taggers are described. The two-variable-tagger works well but there is a potential to improve its performance because two variables are too little to grasp a full internal structure of a jet containing $O(100)$ hadrons. Machine learning approaches by using $O(10)$ variables are developed to get a better discrimination power. Boosted Decision Tree (BDT) and Deep Neural Network (DNN) are separately tested as representative machine learning algorithms. Candidates for the input variables are summarized in Table 5.1 and a concise explanation for those variables is as follows.

Table 5.1: A summary of jet substructure variables studied along with an indication of the tagger topology to which the observable is applicable is shown. In the case of the energy correlation observables, the angular exponent β is set to 1.0 and for the N-subjettiness observables, the winner-take-all [114] configuration is used.

Observable	Variable	References
Calibrated jet kinematics	p_T, mass	[115]
Energy correlation function	e_3, C_2, D_2	[116, 117]
N-subjettiness	$\tau_1, \tau_2, \tau_{21}$	[118, 119]
Fox–Wolfram moment	R_2^{FW}	[120]
Splitting measures	$z_{\text{cut}}, \sqrt{d_{12}}$	[121, 122]
Planar flow	\mathcal{P}	[123]
Angularity	α_3	[124]
Aplanarity	A	[125]
KtDR	KtDR	[126]

Energy correlation function

The definition of energy correlation function is shown in Equation 2.43. The energy correlation ratio is defined as $D_2 = e_3 / (e_2)^3$ and $C_2 = e_3 / (e_2)^2$.

N-subjettiness

The N-subjettiness is designed to find out the number of subjets for a given jet (symbol J), N-subjettiness value is small when a given jet has N subjets, where $N \in 0, 1, 2$. The definition of 0/1/2-subjettiness

(τ_0, τ_1, τ_2) are defined as

$$\tau_0 = \sum_{i \in J} p_{T,i} \Delta R_{ij}, \quad (5.19)$$

$$\tau_1 = \frac{1}{\tau_0} \sum_{i \in J} p_{T,i} \Delta R_{i\alpha_1}, \quad (5.20)$$

$$\tau_2 = \frac{1}{\tau_0} \sum_{i \in J} p_{T,i} \min(\Delta R_{i\alpha_1}, \Delta R_{i\alpha_2}), \quad (5.21)$$

where ΔR_{XY} stands for the angle between X and Y , α_1 and α_2 are the first and second leading constituent in the jet, respectively. N-subjettiness ratio: $\tau_{21} = \tau_2/\tau_1$ is also a candidate for the machine learning tagger.

Fox–Wolfram moment

The Fox–Wolfram moment is variable exploiting Legendre polynomials,

$$H_l = \sum_{i,j} \frac{p_i p_j}{E^2} P_l(\cos \theta_{ij}), \quad (5.22)$$

where E is the energy of a given jet, p_i and p_j are absolute values of the momentum for an i and j -th particle, P_l is the l -th Legendre polynomial. A back-to-back jet pair in its rest frame has $H_l \sim 1$ for even l and $H_l \sim 0$ for odd l . The ratio $R_2^{FW} = H_2/H_0$ is used in this analysis.

Splitting measures

The splitting scale is the most straight forward definition for defining the number of subjects in a given jet. Firstly, it reclusters a given jet with k_t ($R=0.2$) algorithm and stops the algorithm when the number of subjects is equal to two. Then the splitting scale is defined as

$$\sqrt{d_{ij}} = \min(p_{T,i}^2, p_{T,j}^2) \frac{\Delta R_{ij}^2}{R^2}, \quad (5.23)$$

where ΔR_{ij} is an angle between i and j , R is a radius for a given jet. The z_{cut} is a similar variable to $\sqrt{d_{12}}$ defined as

$$\sqrt{d_{cut}} = \min(p_{T,i}^2, p_{T,j}^2) \Delta R_{ij}^2, \quad (5.24)$$

$$z_{cut} = \frac{d_{cut}}{d_{cut} + m_J}, \quad (5.25)$$

where m_J is the invariant mass of a given jet.

Planar flow

The planar flow exploits a shape tensor defined as

$$I_w^{kl} = \frac{1}{m_j} \sum_i E_i \frac{p_{i,k} p_{i,l}}{E_i}, \quad (5.26)$$

$$\mathcal{P} = \frac{4\det(I_w)}{\text{tr}(I_w)^2}, \quad (5.27)$$

where l and k stand for l and k -th components of its transverse momentum (x or y in the ATLAS coordinate system), E is the energy of an i -th constituent, and m_j is the invariant mass of a given jet.

Angularity

The angularity is a simple variable related to angles for a pair of constituents in a given jet:

$$\alpha_3 = \frac{1}{m_j} \sum_i E_i \sin^3 \theta_i (1 - \cos \theta_i)^{-2}, \quad (5.28)$$

where θ stands for an angle between a given jet and an i -th constituent, m_j and E denote the mass and energy for a given jet, respectively.

Aplanarity

The aplanarity is calculated in the rest frame for a given jet:

$$S^{\alpha\beta} = \frac{\sum_i p_i^\alpha p_i^\beta}{\sum_i p_i^2}, \quad (5.29)$$

$$A = \frac{3\lambda_3}{2}, \quad (5.30)$$

where p_i is the magnitude of the momentum for an i -th constituent. p_i^α and p_i^β stand for $\alpha, \beta = x, y, z$ projected momentum for an i -th constituent. λ_3 stands for the smallest eigenvalue.

KtDR

The KtDR is the simplest variable among input candidates which is the angle between a pair of k_t $R = 0.2$ reclustering subjects the same as the splitting scale.

The machine learning approaches are particularly useful in case that input variables are not the same variables (100% correlated nor anti-correlated) nor fully independent (0% correlated), otherwise those are enough to be analyzed by simple cut-based analyses. In order to check correlations between those candidate variables, linear correlation coefficients between candidate variables are evaluated as shown in Figure 5.18. Almost all pairs of variables have correlations, in particular, there are strong correlations

5.2. WEAK VECTOR BOSON IDENTIFICATION

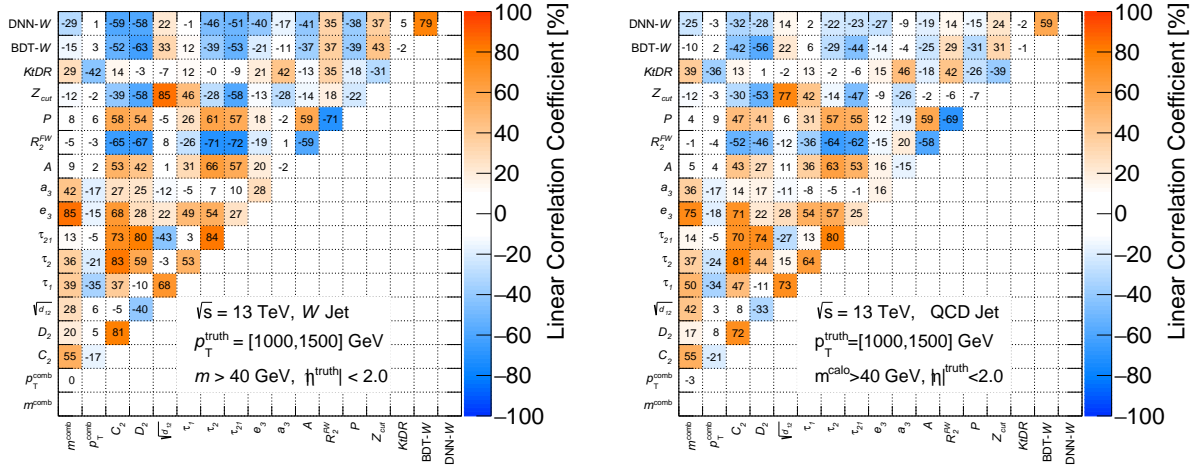


Fig. 5.18: Linear correlation coefficients between input variables for signal W boson jets (left) and background q/g jets (right) are shown. 100% (-100%) means completely correlated (anti-correlated).

between z_{cut} and $\sqrt{d_{12}}$, e_3 and mass, τ_{21} and τ_2 , τ_{21} and D_2 , τ_2 and D_2 , and τ_2 and C_2 . Those pairs of variables are expected to have strong correlations because those definitions are similar. However, those linear correlation coefficients are at most around 80%, and it indicates that inputting those two variables are still meaningful. Therefore, those variables are left as a candidate for input variables.

Trainings are performed with the same MC simulation samples as the two-variable-tagger optimization described in Section 5.2.2. The samples are split into 70% and 30% in statistics, and the former is used in trainings, and the latter is used in testing those performances. In order to choose an input variable set for the BDT and DNN, an optimization study is performed for each. In terms of computer intensity for trainings, fewer input variables are desired. A DNN training takes longer than that of BDT, therefore, different optimization strategies are taken. As for BDTs, one variable which gives the largest increase in a background rejection at a fixed signal efficiency (50%) is sequentially added into input variable sets as shown in Figure 5.19. A BDT with the least input variables having a background rejection consistent with the one having the highest background rejection within statistical fluctuation are chosen as the best BDT. The chosen BDT are inputted 11 variables (D_2 , mass, p_T , $KtDR$, τ_{21} , α_3 , τ_1 , \mathcal{P} , R_2^{FW} , A , C_2). As for DNNs, several test groups of similar variables are defined as shown in Table 5.2, then DNNs are trained for each group as an input set. The same as the case of the BDT, a DNN with the least input variables having a background rejection consistent with the one having the highest background rejection within statistical fluctuation is chosen as the best DNN. The group 8 is chosen as the best DNN which are inputted 12 variables (D_2 , mass, p_T , $KtDR$, τ_{21} , α_3 , \mathcal{P} , R_2^{FW} , A , C_2 , z_{cut} , $\sqrt{d_{12}}$).

Both BDT and DNN hyperparameters³⁾ are optimized by grid scans with the same metric as the input variable optimization, the background rejection at 50% signal efficiency⁴⁾. Chosen hyperparameters are shown in Tables 5.3 and 5.4.

The output distributions for the BDT and DNN are shown in Figure 5.20. The BDT and DNN distribu-

³⁾Hyperparameters are parameters given before training.

⁴⁾Details on the hyperparameter optimizations are summarized in Reference [127].

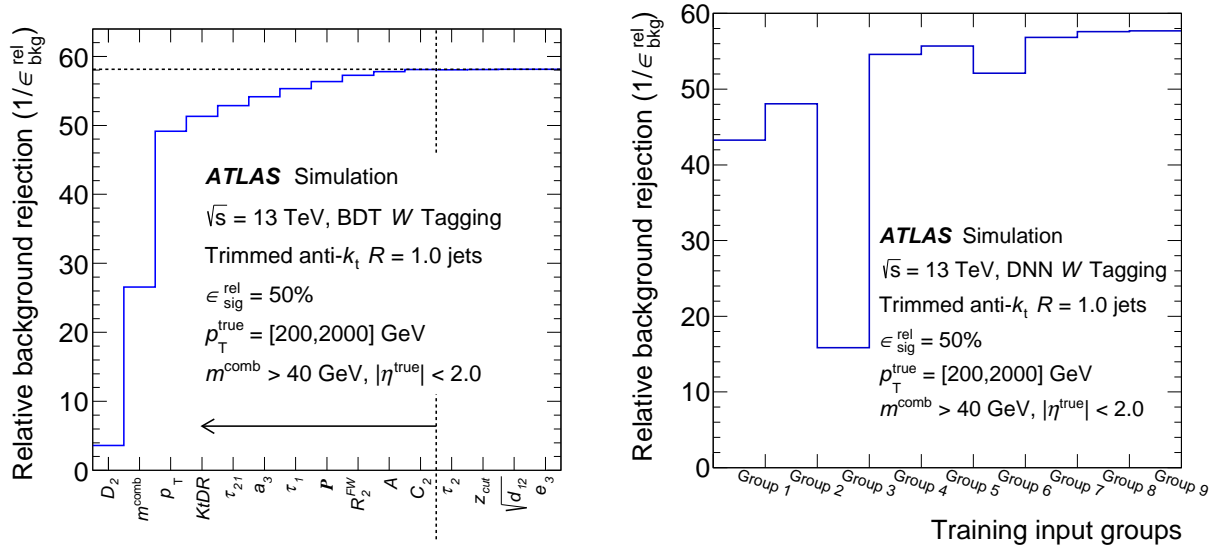


Fig. 5.19: Background rejections for the BDT (left) and DNN (right) taggers are shown. A variable set up to C_2 variable are chosen for the BDT. As for DNN, the Group 8 is chosen.

Table 5.2: A summary of the set of observables that were tested for W boson for the various DNN input observable groups as well as the chosen sets for DNN and BDT as input observables using Figures 5.19 is shown.

Observable	DNN Test Groups									Chosen Inputs	
	1	2	3	4	5	6	7	8	9	BDT	DNN
mass	○	○		○	○	○	○	○	○	○	○
p_T	○	○			○	○		○	○	○	○
e_3	○	○				○			○	○	○
C_2			○	○	○		○	○	○	○	○
D_2			○	○	○		○	○	○	○	○
τ_1	○	○					○		○	○	○
τ_2	○	○					○		○	○	○
τ_{21}			○	○	○		○	○	○	○	○
R_2^{FW}			○	○	○	○	○	○	○	○	○
\vec{p}			○	○	○	○	○	○	○	○	○
a_3			○	○	○	○	○	○	○	○	○
A			○	○	○	○	○	○	○	○	○
z_{cut}			○	○	○		○	○	○	○	○
$\sqrt{d_{12}}$		○					○	○	○	○	○
KtDR		○					○	○	○	○	○

Table 5.3: Brief explanations of the BDT parameters and the chosen parameters are shown.

Setting Name	Description	Chosen Value
BoostType	Type of boosting technique	GradientBoost
NTrees	Number of trees in the forest	500
MaxDepth	Max depth of the decision tree allowed	20
MinimumNodeSize	Minimum fraction of training events required in a leaf node	1.0%
Shrinkage	Learning rate for GradientBoost algorithm	0.5
UseBaggedBoost	Use only a random (bagged) subsample of all events for growing the trees in each iteration	True
BaggedSampleFraction	Relative size of bagged event sample to the original size of the data sample	0.5
SeparationType	Separation criterion for node splitting	GiniIndex
nCuts	Number of grid points in the variable range used in finding optimal cut in node splitting	500

Table 5.4: A summary of the chosen DNN parameters and architecture is shown.

Setting name	Chosen value or architecture	Reference
Used framework	Keras	[128]
Layer type	Dense	[128]
Number of hidden layers	4	[128]
Activation function	rectified linear unit (relu)	[129]
Learning rate	0.0001	[130]
L1 Regulariser	0.001	[129]
NN weight initialization	Glorot uniform	[131]
Batch size	200	[129]
Batch normalization	Yes	[132]
Number of epochs	100	[128]
Architecture	16, 14, 9, 6	-

tions have similar shapes. As shown in Figure 5.18, those have considerably strong correlations, 79% for W jets and 59% for q/g jets. Moreover, correlations between those machine learning outputs and input variables are also similar. The correlation to the D_2 is the most strong which is expected because the D_2 is the most powerful single discriminator.

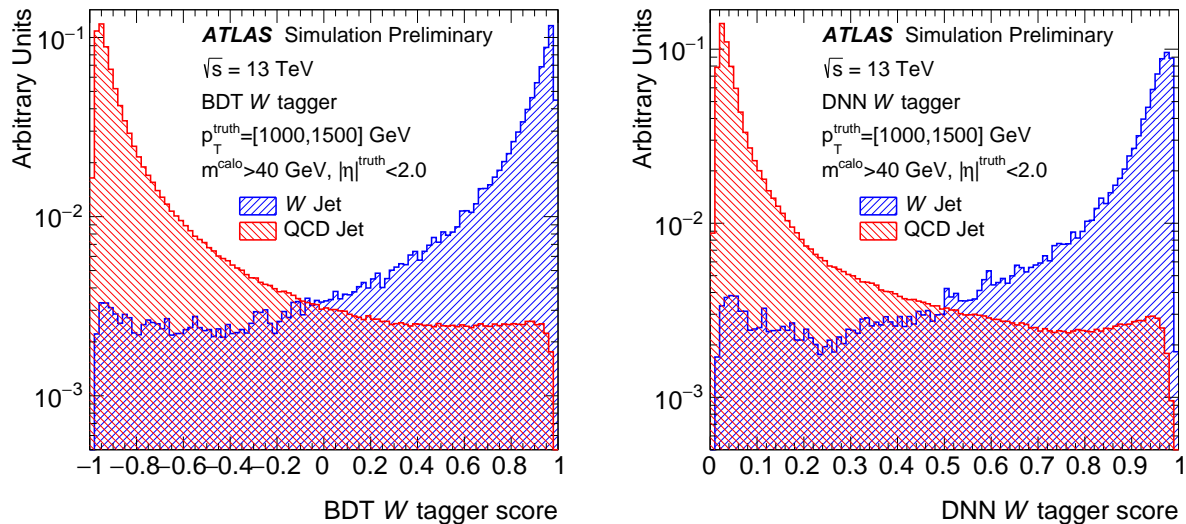


Fig. 5.20: Output distributions for the BDT (left) and DNN (right) taggers. The blue and red shaded areas represent W boson and q/g jets distributions, respectively.

Background rejections are compared to the two-variable-tagger by ROC curves⁵⁾ as shown in Figure 5.21. Background rejections for the BDT and DNN taggers are almost the same, and those are superior to the one for the two-variable-tagger by approximately 20%. Those are the first constructions of weak vector boson identification techniques with large- R jets by machine learning approach, and those performances are the best among weak vector boson identification techniques ever built at that time [107].

While those great performances, those have undesired strong correlations to jet mass as shown in Figure 5.22. Before the cut of BDT or DNN taggers, a mass distribution for the background q/g jet has an exponentially decreasing shape with respect to the large- R jet mass. After cuts of the BDT or DNN taggers, the mass distribution for the background q/g jet is very similar to the one for signal. This indicates that analyses cannot use mass-sidebands as background control regions. Since the profiling of nuisance parameters at mass-sidebands by the simultaneous likelihood fit are essential for most of the analyses including the semileptonic VBS analysis, this tagger is not used in the semileptonic VBS analysis.

A decorrelation technique exploiting adversarial neural network is being developed in [133], this technique achieved a drastic decrease in correlation between the mass and neural network output. Implementation of such a new algorithm is the future prospects for the next generation of analysis.

⁵⁾ROC curve: A 2-dimensional graph for sets of signal efficiency and a background efficiency or rejection obtaining from scanning over the various cut thresholds.

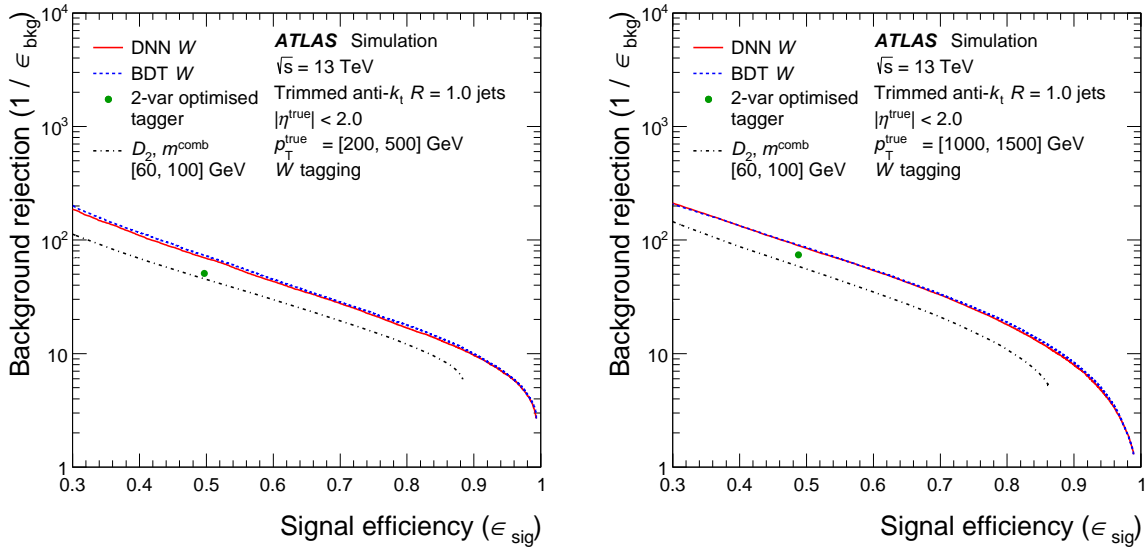


Fig. 5.21: The performance comparisons of the W taggers in a low- p_T (left) and high- p_T (right) bin are shown. The performance is evaluated with the same p_T distribution for signal and background; W jets are weighted to match p_T distributions of the multijet background samples.

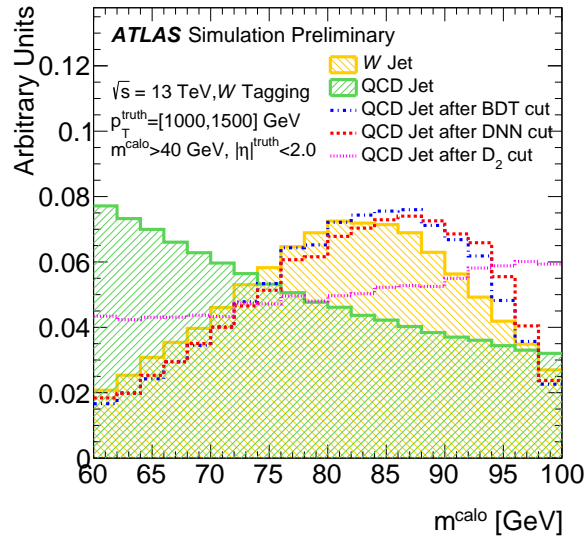


Fig. 5.22: Calorimeter mass distributions showing the signal before selection and the background both before selection, with a selection only on D_2 , with a selection on the BDT discriminant, and the DNN discriminant in the case of W boson tagging in $1000 < p_T < 1500$ GeV are shown.

CHAPTER 6

Search for Semileptonic Vector Boson Scattering

In this chapter, the main body of this thesis, search for the SM semileptonic VBS is described. The introductions to the signals and backgrounds are described in Section 6.1. The dataset and MC simulations used in this analysis are explained in Section 6.2. Sections 6.3 and 6.4 describe event selections to improve the signal purity of the dataset. The SM background estimation methods are explained in Section 6.5. Sections 6.6, 6.7 and 6.8 describe the definition of fiducial volume performed the cross-section measurement for the semileptonic VBS, systematic uncertainties, and the setup for the likelihood fit. Finally, the results of the likelihood fit are described in Section 6.9.

6.1 Experimental Signature of Semileptonic VBS and Backgrounds

The experimental signature of the VBS processes is characterized by two bosons and two forward jets, which is illustrated in Figure 6.1.

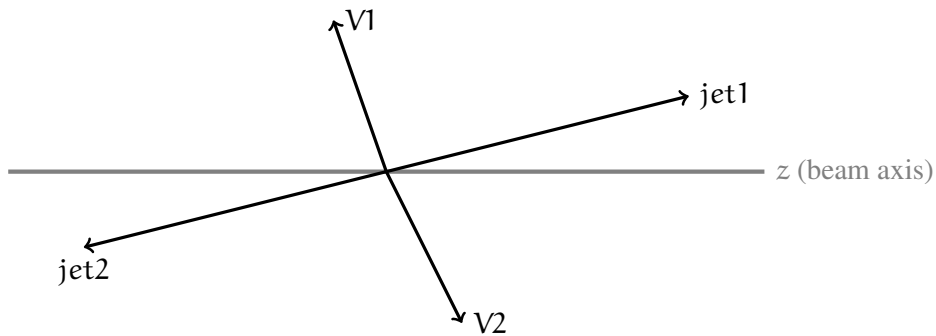


Fig. 6.1: A schematic diagram of a typical VBS topology in the experimental system.

Two forward jets are tagged by requiring the highest invariant mass of a pair of small-R jets (is referred to as m_{jj}^{tag} in short), and a central diboson system is reconstructed by two small-R or one large-R, and leptons and/or E_T^{miss} .

Multiple processes can be contributed to the topology, the production of $VVjj$ having only electroweak-interaction vertices ($EWVVjj$), and having two strong-interaction vertices ($QCDVVjj$). Representative Feynman diagrams are shown in Figure 6.2. $EWVVjj$ composes of two processes, the VBS processes which are actual scatterings of two vector bosons, and the rest of the diagrams (non-VBS) which two vector bosons do not scatter each other. The non-VBS processes cannot separate in a gauge-invariant

way [134] and those inflict a non-negligible contribution to a total cross-section, therefore, it is included in the signal definition.

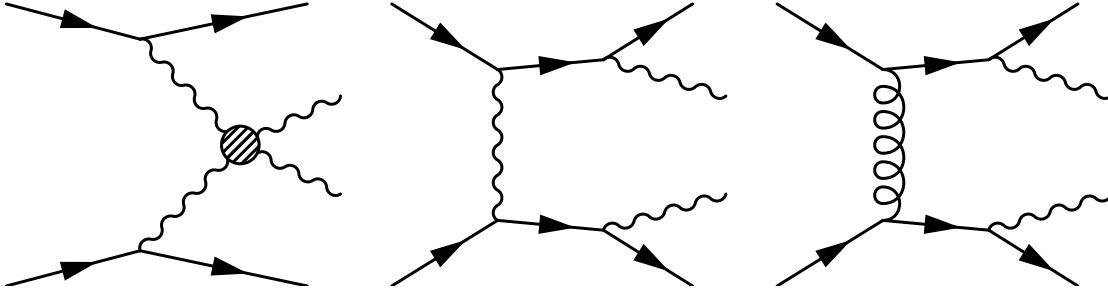


Fig. 6.2: Representative Feynman diagrams of the VBS processes (left), the electroweak productions of the non-VBS processes (center), and the strong productions of the non-VBS processes (right) are shown. The wavy, curled, and straight lines represent W/Z bosons, a gluon, and quarks, respectively. The dashed circle can be replaced with the VBS interactions as shown in Figure 2.1.

Three semileptonic decay channels for VV system are explored as a Z boson decaying into a pair of neutrinos, $Z \rightarrow \nu\nu$;¹⁾ a W boson decaying into a charged lepton (an electron or muon, denoted by ℓ) and a neutrino, $W \rightarrow \ell\nu$; and a Z boson decaying into a pair of light charged leptons, $Z \rightarrow \ell\ell$. In all cases, the other vector boson V is required to decay into a pair of quarks, $V \rightarrow qq$, leading to $ZV \rightarrow \nu\nu qq$, $WV \rightarrow \ell\nu qq$, and $ZV \rightarrow \ell\ell qq$ final states. These processes overlap in the fiducial region of the measurement because of the geometrical acceptance of the detector for leptons and jets. The decay channels are selected as 0-, 1- and 2-lepton final states, where the 1-lepton (2-lepton) final state receives the only contribution from $WV \rightarrow \ell\nu qq$ ($ZV \rightarrow \ell\ell qq$) processes, and the 0-lepton final state receives about equal contributions from $WV \rightarrow \ell\nu qq$ (missing one charged lepton) and $ZV \rightarrow \nu\nu qq$ processes.

Adding to the $QCDVVjj$, several SM processes having relatively high cross-sections can fake the signal topology. Representative Feynman diagrams of backgrounds at tree level are shown in Figure 6.3. The main source of background for this study is the single W or Z boson production in association with jets (referred to as W +jets and Z +jets, or collectively V +jets). The V +jets are different final states from the signals, but those fake signals by additional jets produced from gluon radiation and pileup collisions. The second largest background is the top quark pair production processes ($t\bar{t}$). The $t\bar{t}$ production is exactly the same final state to the signals, and it can be identified by tagging two b -hadrons with the b -tagging. There are minor contributions from single top quark production (single top) containing t -channel, s -channel, and t -channel in association with a W boson. Those are differentiated to the signals by using topology and the b -tagging.

¹⁾To simplify the notation, antiparticles are not explicitly labeled in this thesis.

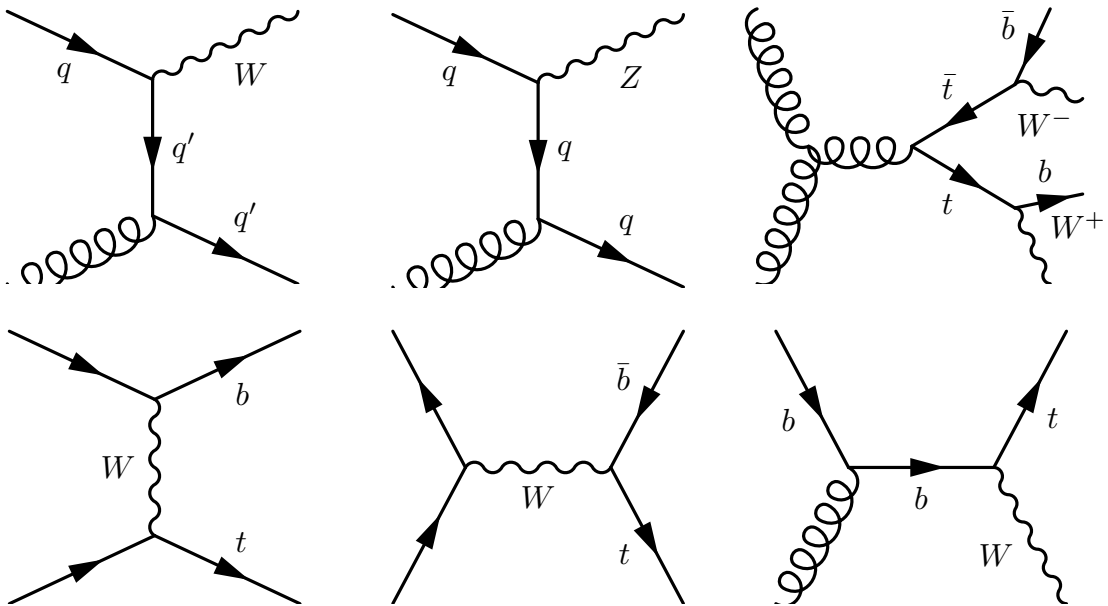


Fig. 6.3: Feynman diagrams of W^+ jets (top left), Z + jets (top center), $t\bar{t}$ (top right), single top produced via t-channel (bottom left), s-channel (bottom center), and t-channel in association with a W boson (bottom right) are shown.

6.2 Experimental Datasets and Monte-Carlo Simulations

This section describes the experimental datasets and MC simulations. In Section 6.2.1, the history of data taking, corresponding integrated luminosities and pileup conditions, and triggers are shown. A summary of event generators used for MC simulations is described in Section 6.2.3.

6.2.1 Experimental Datasets

The dataset used in this study is collected with the ATLAS detector in 2015 and 2016 pp collisions at $\sqrt{s} = 13$ TeV. Data collection histories and the distribution of the mean number of interactions per crossing ($\langle \mu \rangle$)²⁾ are shown in Figure 6.4. In the 2015 (2016) runs, the ATLAS experiment recorded an integrated luminosity of 3.9 fb^{-1} (35.6 fb^{-1}) out of 4.2 fb^{-1} (38.5 fb^{-1}) delivered by the LHC, which corresponds to a data taking efficiency of 92%. The inefficiencies are due to *warm start*: when the collisions become stable, the tracking detectors are turned on a ramp of the high-voltages and turning on the preamplifiers for the pixel system. Further quality requirements are imposed on the data to ensure all detectors worked correctly. The efficiencies for each detector are shown in Table 6.1. Overall, the efficiency is 87.1 (93)% for the 2015 and 2016 data takings, and the main source of inefficiencies are the IBL and toroid turned off in a few runs. Furthermore, saturation in the specific cell of the electromagnetic

²⁾The mean number of interactions per crossing denotes the mean of the Poisson distribution of the number of interactions per crossing calculated for each bunch from the instantaneous luminosity (L_{bunch}) as $\mu = L_{\text{bunch}} \sigma_{\text{inel}} / f_{\text{r}}$, where σ_{inel} denotes the inelastic cross-section for 13 TeV collisions (80 mb for this analysis), and f_{r} represents the LHC revolution frequency.

calorimeter are observed and it is not implemented in MC simulations. It is removed by the run-by-run veto with an efficiency of 98%. The total integrated luminosity used in this analysis is 35.5 fb^{-1} .

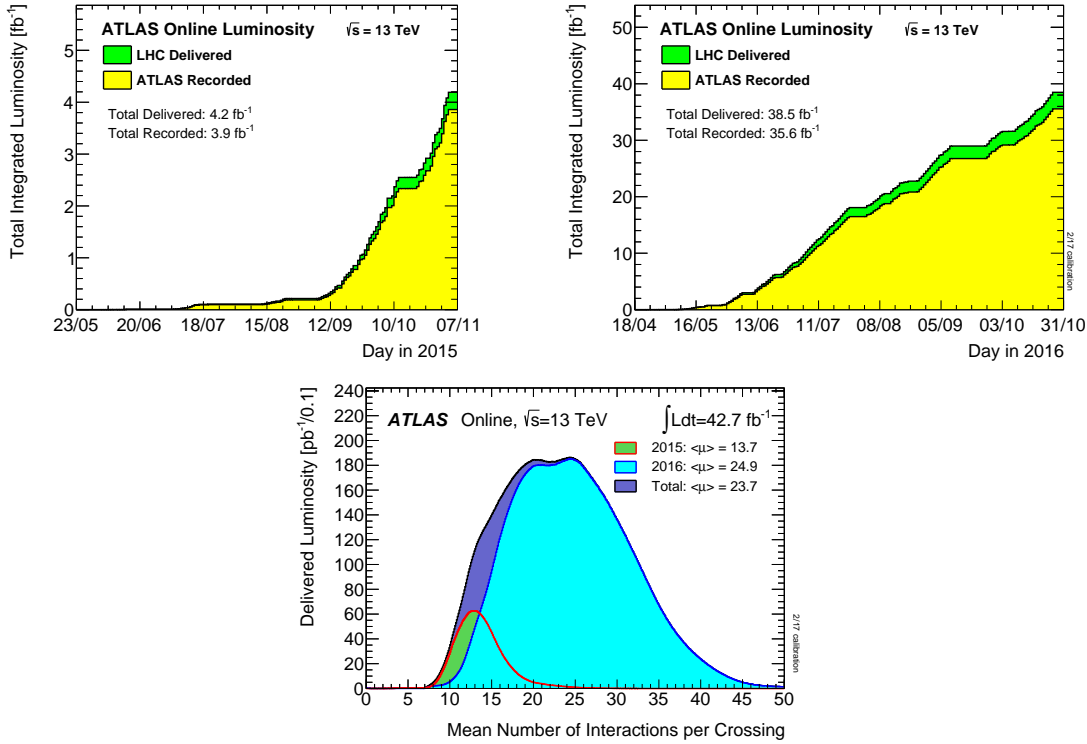


Fig. 6.4: Accumulated integrated luminosity plots for the years of 2015 (left) and 2016 (right) are shown. The green and yellow histograms are corresponding to the LHC delivered luminosity and ATLAS recorded luminosity. In the bottom plot, distributions for the number of interactions per crossing in runs for 2015 (green), 2016 (light blue), and its total (deep blue) are shown.

The datasets are categorized by data taken periods summarized in Table 6.2. Since the categorization corresponding to the proton collision conditions which are deeply related to the trigger strategy, trigger sets used in this analysis are chosen with respect to those data taken periods.

6.2.2 Trigger selection

Different trigger sets are used in each 0-, 1-, and 2-lepton channel with respect to those final states. For the 0-lepton analysis, only the unrescaled E_T^{miss} triggers are used. The thresholds are varied between 70 – 110 GeV with respect to different collision conditions. For the 1- and 2-lepton analyses, the unrescaled single lepton triggers with the lowest momentum threshold at that time are used. The thresholds are 20 – 140 GeV for the various requirements. In order to compensate for a relatively lower efficiency of the muon trigger due to the insensible detector regions as described in Section 4.12, the E_T^{miss} triggers³⁾ is collectively used at $p_T(\mu\nu) > 150 \text{ GeV}$ for the 1-lepton channel. Since the trigger

³⁾Luckily, the muons are not included in the E_T^{miss} calculation at the trigger level.

6.2. EXPERIMENTAL DATASETS AND MONTE-CARLO SIMULATIONS

Table 6.1: Good data quality efficiencies of each detector for each year in a unit of % are shown [135]. The relatively large inefficiency of the pixel detector shown in 2015 is because of the IBL being turned off for two runs. The toroid inefficiencies in 2015 and 2016 are caused by turning off for some runs.

year	Inner Detector			Calorimeter		Muon Spectrometer				Magnet		total
	Pixel	SCT	TRT	LAr	Tile	MDT	RPC	CSC	TGC	Solenoid	Toroid	
2015	93.5	99.4	98.3	99.4	100	100	100	100	100	100	97.8	87.1
2016	98.9	99.9	99.7	99.3	98.9	99.8	99.8	99.9	99.9	99.1	97.2	93

Table 6.2: Naming of periods and corresponding luminosities [136] are shown for each year. The run numbers are associated with each proton fill. The integrated luminosities represent the ones delivered by the LHC.

Year	Period	Date Taking Period	Corresponding Run Numbers	Integrated Luminosity[/pb]
2015	D1-D6	Aug.12 - Aug.23	276073-276954	105
	E1-E5	Sep.06 - Sep.20	278727-279928	501
	F1-F3	Sep.20 - Sep.26	279932-280422	353
	G1-G4	Sep.26 - Oct.06	280423-281075	821
	H1-H3	Oct.06 - Oct.12	281130-281411	616
	J1-J6	Oct.20 - Nov.03	282625-284484	1620
	total			
2016	A1-A10	Apr.22 - May.27	296939-300287	764
	B1-B5	May.27 - Jun.06	300345-300908	2231
	C1-C4	Jun.11 - Jun.21	301912-302393	3222
	D1-D8	Jun.24 - Jul.10	302737-303560	5852
	E1-E3	Jul.10 - Jul.16	303638-303892	2253
	F1-F3	Jul.16 - Jul.25	303943-304494	3729
	G1-G7	Aug.01 - Aug.21	305291-306714	4618
	I1-I5	Aug.24 - Sep.09	307124-308084	6235
	K1-K3	Sep.24 - Oct.03	309311-309759	2561
	L1-L11	Oct.06 - Oct.26	310015-311481	6942
total				38407

efficiencies are not reached up to 100% at 150 GeV, trigger efficiency scale factors are applied as shown in Figure 6.5.

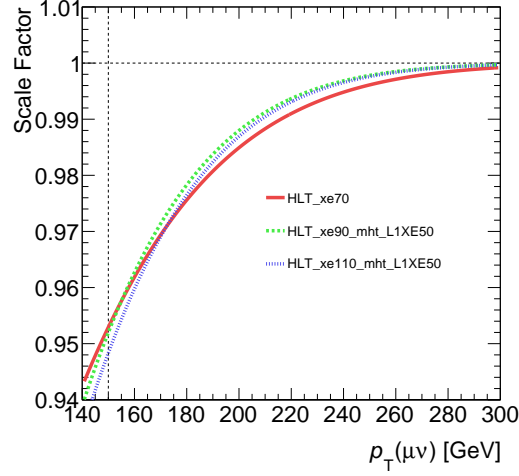


Fig. 6.5: The trigger scale factors for the E_T^{miss} triggers used in this analysis are shown. The E_T^{miss} trigger are used above $p_T(\mu\nu) = 150$ GeV (vertical dashed line).

The triggers used in the 0-, 1-, and 2-lepton channels are summarized in Tables 6.3, 6.4, and 6.5.

Table 6.3: A list of triggers used in the 0-lepton channel analysis is shown. The xe or XE stands for E_T^{miss} , the mht stands for an E_T^{miss} reconstruction technique described in Section 4.7.3 and Reference [137]. The numbers corresponding to E_T^{miss} thresholds. HLT_xe110_mht_L1XE50 stands for passing L1 trigger with a threshold of $E_T^{\text{miss}} > 50$ GeV and HLT trigger with a threshold of $E_T^{\text{miss}} > 110$ GeV using the mht E_T^{miss} reconstruction technique.

Year	Period	MET triggers
2015	whole period	HLT_xe70
2016	A-D3	HLT_xe90_mht_L1XE50
	D4-E4, F2-L11	HLT_xe110_mht_L1XE50

6.2.3 Monte-Carlo Simulations

The expected signal and background processes are simulated by the Monte-Carlo method (MC) implemented by the several dedicated simulation programs explained in the following subsections.

6.2. EXPERIMENTAL DATASETS AND MONTE-CARLO SIMULATIONS

Table 6.4: A list of triggers used in the 1-lepton channel is shown. the lhtight, lhmedium, and lhloose stand for passing tight, medium, and loose likelihood-based identification requirements, respectively. iloose, ivarloose, and ivarmedium stand for isolation requirements described in Section 4.3.4. More details are described in Reference [137].

Year	Period	Electron channel	Muon channel	
			$p_T (\mu\nu) < 150$ GeV	$p_T (\mu\nu) > 150$ GeV
2015	whole period	HLT_e24_lhmedium_L1EM20VH HLT_e60_lhmedium HLT_e120_lhloose	HLT_mu20_iloose_L1MU15 HLT_mu40	HLT_xe70
	A	HLT_e26_lhtight_nod0_ivarloose HLT_e60_lhmedium_nod0 HLT_e140_lhloose_nod0	HLT_mu24_ivarloose HLT_mu40	HLT_xe90_mht_L1XE50
2016	B-D3	the same as above	HLT_mu24_ivarmedium HLT_mu50	the same as above
	D4-	the same as above	HLT_mu26_ivarmedium HLT_mu50	HLT_xe110_mht_L1XE50

Table 6.5: A list of triggers used in the 2-lepton channel analysis is shown. Notations are the same as Table 6.4.

Year	Period	Electron channel	Muon channel
2015	whole period	HLT_e24_lhmedium_L1EM20VH HLT_e60_lhmedium HLT_e120_lhloose	HLT_mu20_iloose_L1MU15 HLT_mu40
	A	HLT_e26_lhtight_nod0_ivarloose HLT_e60_lhmedium_nod0 HLT_e140_lhloose_nod0	HLT_mu24_ivarloose HLT_mu40
2016	B-D3	the same as above	HLT_mu24_ivarmedium HLT_mu50
	B-D3	the same as above	HLT_mu26_ivarmedium HLT_mu50

Electroweak $VVjj$ Simulation

The $EWVVjj$ production is modeled using the MADGRAPH5_aMC@NLO v2.3.3 [38] event generator with the NNPDF30LO PDF set [53]. The parton shower and hadronization are implemented with the PYTHIA 8.186 [55] using the A14 set of tuned parameters for the underlying events [105]. The $EWVVjj$ samples are generated with two on-shell V bosons, with one V boson decaying leptonically ($Z \rightarrow \ell\ell$ with $\ell = e, \mu, \tau$, $Z \rightarrow \nu\nu$, $W \rightarrow \ell\nu$ with $\ell = e, \mu, \tau$), and the other V boson decaying hadronically. For the $WWjj$ processes, all charge combinations are included (W^+W^+ , W^+W^- , and W^-W^-). For each sample, all of the purely-electroweak tree-level diagrams (i.e. $\mathcal{O}(\alpha_{EW}^6)$ diagrams) that contribute to the final state are included. The non-VBS diagrams are greatly suppressed by the event selection in this analysis. In particular, for the processes including a Wtb vertex are not considered as $EWVVjj$ signal, and their contribution is removed by requiring that the VBS tagging jets (a pair of jets originating from spectator quarks which coming directly from partonic quarks) are not to be b-tagging ones (b-veto). For EWK $WWjj$ production, the electroweak $t\bar{t}$ process shows a significant contribution ($\sim 70\%$). Such a contribution is negligible in the signal region due to b-veto and high m_{jj}^{tag} requirements.

Anomalous Quartic Gauge Coupling Signal Simulation

Given a large number of operators that could modify the quartic vertices considered in this analysis, only a few representative ones are considered as L_{S0} , L_{M0} , and L_{T0} . Corresponding couplings are represented as f_{S0}/Λ^4 , f_{M0}/Λ^4 , and f_{T0}/Λ^4 . MC samples are produced for those three exclusive operators and for all six final states. The coupling strength of each operator is determined based on the expected sensitivity as summarized in Table 6.6. Similar to the VBS signal samples, the aQGC samples are modeled by using the MADGRAPH5_aMC@NLO v2.3.3 [38] event generator connected with the PYTHIA 8 [55] for the fragmentation tuned by the NNPDF30LO PDF set [53] is used.

Table 6.6: The aQGC couplings for the benchmark signal samples used in this analysis are shown.

	f_{S0}/Λ^4	f_{M0}/Λ^4	f_{T0}/Λ^4
coupling constant [TeV $^{-4}$]	50	1	5

Background Simulation

The main source of background for this study is the $V+$ jets process. The $V+$ jets events are generated by the SHERPA 2.2.1 [138] event generator. The W/Z production in association with at most two jets are calculated at the next leading order (NLO), and three and four jets processes are calculated at the leading order (LO) using the COMIX [139] and OPENLOOPS [140] programs. The $t\bar{t}$ events are produced by the POWHEG-BOX v2 [141] event generator with the CT10 PDF set in the matrix-element calculations. The third largest background is the $QCDVVjj$ process which is a production of a pair of vector bosons in association with a pair of jets having one or more QCD-induced vertices. The $QCDVVjj$ process

is generated by the SHERPA 2.2.1 [138] the same as the V+jets events generation. The rest of the backgrounds are significantly less contribution than the above backgrounds, the single top events are generated by the POWHEG-BOX v1 [142–144] event generator. All leptonically decaying vector bosons decay all lepton flavors (e, μ, τ). For all processes including W and top quarks, spin correlations are preserved. The top quark mass is set to 172.5 GeV. The EVTGEN v1.2.0 program [145] is used for decaying bottom or charm hadrons for the POWHEG-BOX samples. The parton showers, fragmentation, and pileup collision in the same bunch crossing are simulated using the PYTHIA 6.428 [146] with the CTEQ6L1 [54] PDF set with the corresponding Perugia 2012 tune (P2012) for all samples except ones generated with the SHERPA 2.2.1 which is predefined the dedicated shower programs.

All processes are normalized using the latest theoretical predictions for their cross-sections. Cross-sections for the V+jets production are calculated with up to the next-to-next-to-leading-order (NNLO) QCD correction. Cross-sections for QCDVVjj are calculated at the NLO including the LO contribution with two additional partons [138, 147]. A cross-section for $t\bar{t}$ events is calculated at the NNLO in QCD, including resummation of next-to-next-to-leading logarithmic (NNLL) soft-gluon terms [148, 149]. A cross-section for the single top production is calculated by the NLO in QCD [150], including the NNLL correction only for the Wt process [151].

A summary of the MC simulations is shown in Figure 6.7.

Table 6.7: A summary of MC simulations used in this thesis is shown.

Process	Generator	$\sigma \times \text{BR}$ [pb]
$\text{EWVVjj} \rightarrow \nu\nu q\bar{q}/l\nu q\bar{q}/llq\bar{q} + \text{jj}$	MADGRAPH5_aMC@NLO v2.3.3 +PYTHIA 8	2.22
$\text{aQGC VVjj} \rightarrow \nu\nu q\bar{q}/l\nu q\bar{q}/llq\bar{q} + \text{jj}$	MADGRAPH5_aMC@NLO v2.3.3 +PYTHIA 8	-
$W+\text{jets} \rightarrow l\nu + \text{jets}$	SHERPA 2.2.1	6.63×10^4
$Z+\text{jets} \rightarrow ll/\nu\nu + \text{jets}$	SHERPA 2.2.1	1.93×10^4
$t\bar{t} \rightarrow l\nu q\bar{q}bb/l\nu l\nu bb$	POWHEG-BOX v2 + PYTHIA 6	452
Single top $\rightarrow l\nu b$	POWHEG-BOX v1 + PYTHIA 6	4.14
$\text{QCDVVjj} \rightarrow \nu\nu q\bar{q}/l\nu q\bar{q}/llq\bar{q} + \text{jets}$	SHERPA 2.2.1	82.7

Generated MC events are simulated with a detailed detector simulation [152] by the GEANT4 [153]. In- and out-of-time additional collisions are simulated by the PYTHIA 8.186 and overlaid in the same and neighboring bunch crossing (pileup). All MC simulations are reweighted to match the pile-up condition in the observed data.

6.3 Event Selection

In order to enhance a signal purity, selections are imposed by making use of the VBS signal topology. The events are preselected first as described in Section 6.3.1, then specific event selections are applied

for each 0-, 1-, and 2-lepton channel described in Sections 6.3.2, 6.3.3, and 6.3.2.

6.3.1 Preselection

Common jet selection criteria are applied to all categories, $p_T > 20$ GeV for $|\eta| < 2.5$ and $p_T > 30$ GeV for $2.5 < |\eta| < 4.5$ for small-R jets. Large-R jets are required to have $p_T > 200$ GeV for $|\eta| < 2.0$. Events are split by a p_T of a hadronically decaying vector boson V_{had} . Events having one or more qualified large-R jets are categorized as *merged*, otherwise *resolved*. For resolved channels, candidates for the tagging jets⁴⁾ are selected by choosing a small-R jets pair with the highest invariant mass (m_{jj}^{tag}), then a jet pair which has a minimum value of $\min(|m_W - m_{jj}|, |m_Z - m_{jj}|)$ ⁵⁾ from the remaining jets is chosen as a candidate for hadronically decaying W/Z boson (V_{had}). In merged channels, forward jets are selected first in the same way as the resolved case, then a large-R jet which has a minimum value of $\min(|m_W - m_J|, |m_Z - m_J|)$ where m_J is invariant mass of a large-R jet is chosen as a V_{had} . The distribution of m_J is shown in Figure 6.6.

Before categorizations, the events are applied to the lower cut on 400 GeV for a m_{jj}^{tag} . The distribution of m_{jj}^{tag} is shown in Figure 6.6. The cut value 400 GeV is chosen to have enough signal and background statistics on the MC simulations to effectively train the BDT which is introduced in Section 6.4.1. Then events are categorized in 0-, 1-, 2-lepton channels by the number of charged leptons, then those subcategories are analyzed separately as discussed below in turn.

6.3.2 0-lepton

Events passed E_T^{miss} triggers are required further E_T^{miss} cut (greater than 200 GeV) and no lepton with $p_T > 7$ GeV in an event. The E_T^{miss} cut threshold is determined to maximize the bin-by-bin accumulated significance of the m_T distribution. In the 0-lepton channel, the QCD-induced multijet background is significant, so the multijet event suppressing cuts, an angle between track-based \vec{p}_T^{miss} and calorimeter-based \vec{E}_T^{miss} to be smaller than $\pi/2$ ($\Delta\phi(\vec{E}_T^{\text{miss}}, \vec{p}_T^{\text{miss}}) < \pi/2$), the smallest angle between small-R jets and \vec{E}_T^{miss} to be greater than $\pi/6$ ($\min[\Delta\phi(\vec{E}_T^{\text{miss}}, \text{small-R jet})] > \pi/6$), and the angle between \vec{E}_T^{miss} and V_{had} momentum to be greater than $\pi/9$ ($\Delta\phi(\vec{E}_T^{\text{miss}}, \vec{V}_{\text{had}}) > \pi/9$) are simultaneously applied. The thresholds for the multijet event suppressing cuts are determined that the multijet events are to be negligible.

6.3.3 1-lepton

Events are imposed to have exactly one ‘tight’ lepton with $p_T > 27$ GeV, no ‘medium’ lepton with $p_T > 7$ GeV, and E_T^{miss} greater than 80 GeV. The E_T^{miss} cut threshold is determined to maximize the bin-by-bin accumulated significance of the m_{VV} distribution. In the 1-lepton channel, the $t\bar{t}$ process shows non-negligible contamination, so events that have b-jets are rejected.

⁴⁾ A pair of jets originating from spectator quarks which coming directly from partonic quarks.

⁵⁾ $m_W = 80.385$ GeV and $m_Z = 91.187$ GeV are used in this study.

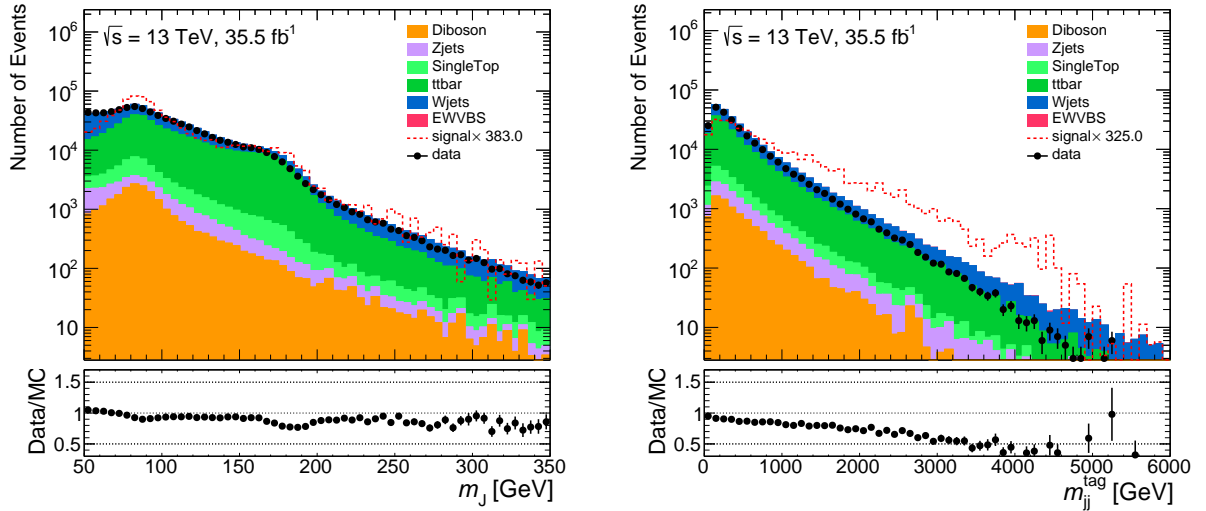


Fig. 6.6: The m_{jj}^{tag} (left) and large-R jet mass (right) distributions for events required to pass the 1-lepton trigger set and having exactly one lepton, one large-R jet, and large-R jet mass greater than 50 GeV are shown. For the left plot, the ratio of the observed data to the MC simulation is wavy because the in-situ large-R jet mass calibration is not imposed, and it is covered by the systematic uncertainty. The first and second peak of the large-R jet mass distribution derived by W boson and top-quark masses. The signal has also the second peak because of electroweak $t\bar{t}$ contamination as described in Section 6.2.3. For the right plot, the predictions of the MC simulations are quite overshooting the observed data, especially at the high m_{jj}^{tag} region. The deviation will be calibrated by m_{jj}^{tag} reweighting as described in Section 6.5.1.

6.3.4 2-lepton

Two ‘loose’ leptons with $p_T > 20$ GeV in which one ‘tight’ lepton with $p_T > 28$ GeV are required. The invariant mass of pair of the leptons satisfying $83 < m_{ee} < 99$ GeV for electrons and $-0.0117 \times p_T^{\mu\mu} + 85.63 < m_{\mu\mu} < 0.0185 \times p_T^{\mu\mu} + 94$ GeV for muons. Cut values are chosen to take into account invariant mass resolutions shown in Reference [154].

6.3.5 Signal Regions and Control Regions

Further categorization criteria are applied either to enhance the signal purity as a signal region (SR) or to enhance the purity of each background component as a control region (CR). As for the SR, invariant mass of V_{had} to be close to boson mass poles, $64 < m_{jj} < 106$ GeV is required for resolved (resolved SR), or large-R jets p_T dependent mass window cuts are applied as shown in Figure 5.17 (merged SR). Merged regions are subdivided with D_2 cut thresholds into the high-purity SR (HP SR) and low-purity SR (LP SR). The HP SR is defined as passing a 50% signal efficiency cut threshold on D_2 . The LP SR is defined as failing a 50% signal efficiency cut threshold but passing an 80% signal efficiency cut threshold on D_2 . The thresholds are shown in Figure 5.17. The HP SR has the best signal purity and shows the primary sensitivity. The LP SR recovers signal efficiency for transversely polarized W/Z bosons because those decay products tend to have asymmetric momentum in the experimental frame,

6.3. EVENT SELECTION

and this leads to a fuzzy 2-prong structure having a D_2 value between the longitudinally polarized W/Z boson jets and background q/g jets. Additionally, the LP SR also works as a CR of backgrounds. V_{had} mass sidebands of the SR are exploited as V +jets CRs since the backgrounds are expected not to have hadronically decaying V bosons, the mass of V_{had} must not have a resonant structure. Those are referred to as VCR , ZCR or WCR depending on channels. The HP and LP CRs are also prepared the same as in the SR. $t\bar{t}$ CRs having one or more b-tagged jets are set only for the 1-lepton channel referred to as $TopCR$.

The ordering of the above categorization is organized as shown in Figure 6.7.

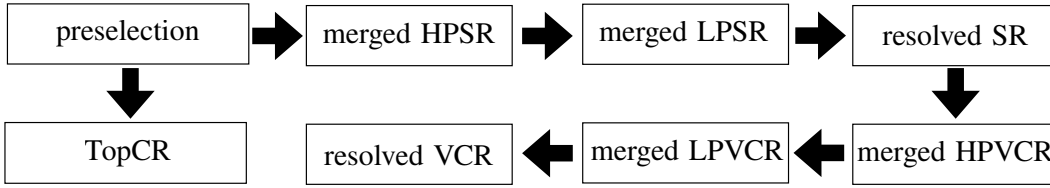


Fig. 6.7: The ordering of the categorization is illustrated. The events passed the preselection are subsequently imposed on criteria in the ordering of allows if those do not pass the previous criteria.

A schematic diagram of the SR and CR definitions and compositions of each signal and background is shown in Figure 6.8. A summary of signal event selections is shown in Table 6.8.

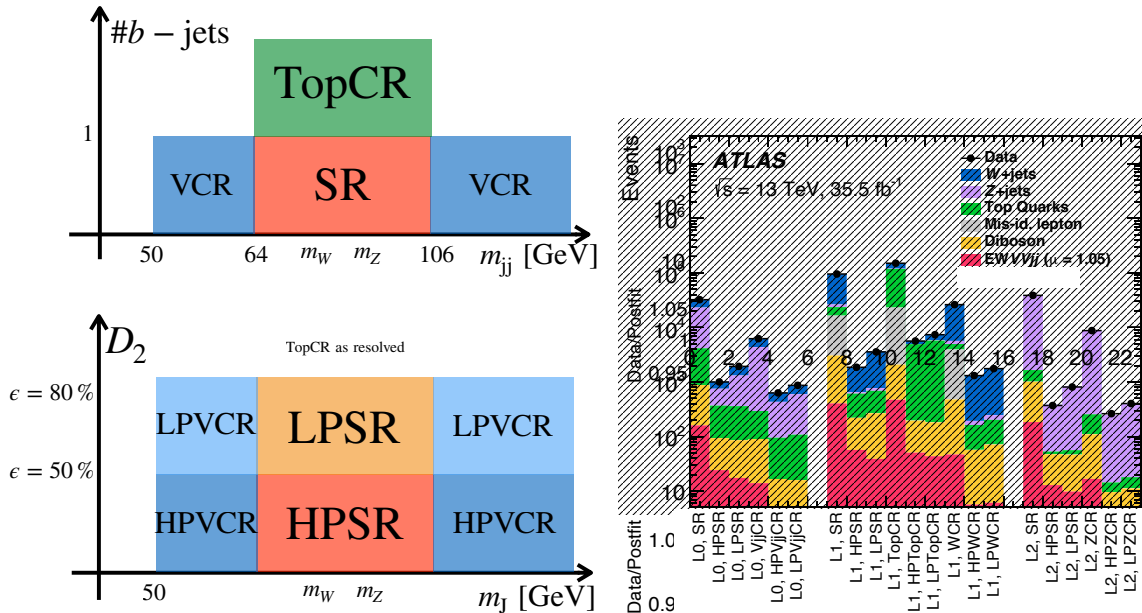


Fig. 6.8: A schematic diagram of SR/CR definitions for resolved (top left) and merged (bottom left) are shown. A plot for event yields in each signal and control region (right) is shown. The labels L0, L1, and L2 stand for the 0-, 1-, and 2-lepton channels, respectively. The labels ‘HP SR’, ‘LP SR’, and ‘SR’ stand for the high-purity merged, low-purity merged, and resolved signal regions, respectively.

6.4 Multivariate Analysis

The SRs defined in the previous section achieved to extract quite high purity signal regions, however, those are not sufficient to observe the EWV ν processes with enough significance to claim an evidence. Therefore, events in the SRs are further processed by the Boosted Decision Tree (BDT) to utilize the whole kinematical information about events including those higher order of correlations as much as possible. The BDT is chosen among machine learning algorithms because of the reasonable training speed and implementability on ROOT [155] based analysis codes through the Toolkit for Multivariate Data Analysis (TMVA [78]). The BDT is trained with simulation events with optimizing the input variable set and hyperparameters of the BDT as described in Sections 6.4.1 and 6.4.2. Output distributions of the BDT are exploited as discriminant variables for the statistical tests described in Section 6.8 are shown in Section 6.4.3.

6.4.1 Training Setup

The BDT is trained with MC simulated events. Extended signal regions are set by removing m_{jj}^{tag} requirement for 0- and 1-lepton channels and additionally removing W/Z-tagger requirements for 1-lepton to acquire enough training statistics. Two subdivided samples of equal size are used for the training separately and applying conversely⁶⁾, then the output distributions are merged with each other. This way utilizes full statistics of the MC simulated samples in the training but avoids any overtrainings⁷⁾.

Hyperparameters of the BDT are optimized at the merged region for each channel separately, and those are applied in both the merged and resolved regions. The considered hyperparameter set is the same one as shown in Table 5.3. The optimizations are performed at the merged regions because those have fewer statistics than that of resolved ones, hence, the chosen hyperparameter sets are safer against overtrainings at resolved regions compared to the inverse case. The chosen hyperparameter sets are shown in Table 6.9.

6.4.2 Input Variables

Input variable set is intended to be formed by variables having higher separation powers between the signal and backgrounds but not to have similar variables which have large redundancy, also distributions of chosen variables for simulated samples have to show good agreement with distributions for the observed data from an aspect of reliability of this measurement. Most of the variables are chosen related to the kinematics of tree-level four-momenta which characterize the signal topology. Additionally, the q/g separating variables related to the internal structure of jets and the number of jets are considered because of most of the backgrounds induced by the QCD interactions which tend to produce outgoing gluons. The optimization is done for each lepton channel and resolved or merged, separately.

⁶⁾Samples are divided into A and B for the even and odd number of events, respectively. Then each subsample A and B is used for training and get BDT_A and BDT_B . The $\text{BDT}_{A(B)}$ is applied to subsample B(A) to create the templates.

⁷⁾A machine learning algorithm learns statistical fluctuation on the training sample, which can be a cause of bias in the measurements.

Table 6.8: A summary of the event selection in the 0-, 1- and 2-lepton channels is shown.

Selection	0-lepton	1-lepton	2-lepton
Trigger	E_T^{miss} triggers	Single-electron triggers Single-muon or E_T^{miss} triggers	Single-lepton triggers
Leptons	0 'loose' leptons with $p_T > 7$ GeV	1 'tight' lepton with $p_T > 27$ GeV 0 'loose' leptons with $p_T > 7$ GeV	2 'loose' leptons with $p_T > 20$ GeV ≥ 1 lepton with $p_T > 28$ GeV
E_T^{miss}	> 200 GeV	> 80 GeV	–
$m_{\ell\ell}$	–	–	$83 < m_{ee} < 99$ GeV $-0.0117 \times p_T^{\mu\mu} + 85.63 < m_{\mu\mu} < 0.0185 \times p_T^{\mu\mu} + 94$ GeV
Small-R jets		$p_T > 20$ GeV if $ \eta < 2.5$, and $p_T > 30$ GeV if $2.5 < \eta < 4.5$	
Large-R jets		$p_T > 200$ GeV, $ \eta < 2$	
$V_{\text{had}} \rightarrow J$ $V_{\text{had}} \rightarrow jj$		V boson tagging, $\min(m_J - m_W , m_J - m_Z)$ $64 < m_{jj} < 106$ GeV, jj pair with $\min(m_{jj} - m_W , m_{jj} - m_Z)$, leading jet with $p_T > 40$ GeV	
Tagging-jets		$j \notin V_{\text{had}}$, not b-tagged, $\Delta R(J, j) > 1.4$ $\eta_{\text{tag}, j_1} \cdot \eta_{\text{tag}, j_2} < 0$, $m_{jj}^{\text{tag}} > 400$ GeV, $p_T > 30$ GeV	
Num. of b-jets	–	0	–
Multijet removal	$p_T^{\text{miss}} > 50$ GeV $\Delta\phi(E_T^{\text{miss}}, \vec{p}_T^{\text{miss}}) < \pi/2$ $\min[\Delta\phi(E_T^{\text{miss}}, \text{small-R jet})] > \pi/6$ $\Delta\phi(E_T^{\text{miss}}, \vec{V}_{\text{had}}) > \pi/9$	–	–

Table 6.9: A summary of the BDTG algorithm parameters for 0/1/2-lepton channels is shown.

BDTG parameter	0-lepton	1-lepton	2-lepton
NTrees	400	800	400
MaxDepth	4	4	4
Shrinkage	0.1	0.3	0.1
MinNodeSize	5 %	5 %	15 %
nCuts	20	20	20
UseBaggedBoost	True	True	True
BaggedSampleFraction	0.5	0.5	0.5
SeparationType	GiniIndex	GiniIndex	GiniIndex

Candidates for the input variables into the BDT are listed in Table 6.10. The small-R jets are labeled in decreasing p_T as ‘ j_1 ’ and ‘ j_2 ’ for a V_{had} candidate, and as ‘tag, j_1 ’ and ‘tag, j_2 ’ for the tagging-jets. The invariant mass and transverse momentum of the reconstructed VV ($VVjj$) system are denoted by m_{VV} (m_{VVjj}) and p_T^{VV} (p_T^{VVjj}), respectively. In those calculations, the momentum of a neutrino from $W \rightarrow l\nu$ decay ($\vec{p}_\nu = (p_{T,\nu}, p_{z,\nu})$) is obtained by requiring W mass (m_W) constraint on a lepton ($p_l^\mu = (p_{T,l}, p_{z,l}, m_l)$) and a neutrino system. The W mass squared is expressed as

$$m_W^2 = \left(E_l + \sqrt{p_{T,\nu}^2 + p_{z,\nu}^2} \right)^2 - \left((p_{T,\nu} + p_{T,l})^2 + (p_{z,\nu} + p_{z,l})^2 \right) \quad (6.1)$$

$$= m_l^2 + 2E_l \sqrt{p_{T,\nu}^2 + p_{T,l}^2} - 2p_{T,\nu} p_{T,l} - 2p_{z,\nu} p_{z,l}, \quad (6.2)$$

$$(6.3)$$

In order to solve the unknown $p_{z,\nu}$, a quadratic equation on $p_{z,\nu}$ is formed as

$$0 = 4p_{T,l}^2 \cdot p_{z,\nu}^2 - 4 \left(m_W^2 + 2p_{T,\nu} p_{T,l} \right) p_{z,l} \cdot p_{z,\nu} - \left(m_W^2 + 2p_{T,\nu} p_{T,l} \right)^2 + 4E_l^2 p_{T,\nu}^2, \quad (6.4)$$

where an approximation that the lepton mass can be ignored compared to its momentum is assumed. The $p_{T,\nu}$ is assumed to be E_T^{miss} , and then $p_{z,\nu}$ is obtained by solving the quadratic formula. In this study, the smaller real component of the solutions is chosen because it is slightly close to the true value. Angular variables are also considered, such as the pseudorapidity gap between the tagging-jets ($\Delta\eta_{jj}^{\text{tag}}$) and between the small-R V_{had} jets ($\Delta\eta_{jj}$), the angular separation between the lepton and neutrino from the W boson decay ($\Delta R(\ell, \nu)$) in the 1-lepton channel, and the azimuthal angle between the directions of \vec{E}_T^{miss} and the large-R jet ($\Delta\phi(\vec{E}_T^{\text{miss}}, J)$) in the merged category of the 0-lepton channel. A topological variable named boson centrality is also used, and it is defined as $\zeta_\nu = \min(\Delta\eta_-, \Delta\eta_+)$, where $\Delta\eta_- = \min[\eta(V_{\text{had}}), \eta(V_{\text{lep}})] - \min[\eta_{\text{tag},j_1}, \eta_{\text{tag},j_2}]$ and $\Delta\eta_+ = \max[\eta_{\text{tag},j_1}, \eta_{\text{tag},j_2}] - \max[\eta(V_{\text{had}}), \eta(V_{\text{lep}})]$. The variable ζ_ν has large values when the tagging-jets have a large separation in η and the two boson candidates lie between the tagging-jets in η . Variables sensitive to the quark–gluon jet separation are also included, such as the width of the small-R jets (w) [156], and the number of tracks associated with the jets ($n_{\text{tracks}}^{\text{jet}}$). The number of track jets $n_{j,\text{track}}$ and the number of additional small-R jets other than the V_{had} jets and tagging-jets $n_{j,\text{extr}}$ are also found to be useful for the BDTs. In the 1-lepton channel, the

pseudorapidity of the lepton (η_ℓ) is also considered.

In order to quantify which variable has affected BDT outputs the most, those are ranked by that importance, *variable importance* which is defined as how often the variable used to split decision tree node by weighting the separation gain-squared and the number of events on each node. The ranks are displayed in Table 6.10. For both the resolved and merged regions, the kinematical variables related to the forward jet pair and the central diboson system are highly ranked. That is expected because those kinematics reflect the most significant differences of the Feynman diagrams between the signal and backgrounds, and those four-momenta can be measured with better resolutions than the other variables. One of the q/g jets separation variable w^{tag,j_1} is relatively highly ranked at resolved regions, which is guessed because the resolved regions contain much V+jets backgrounds than the merged regions, and the second, third, and fourth jets of V+jets events tend to be gluon jets since representative Feynman diagrams of V+jets events contain only one quark.

In order to check the inputs having no large redundancies, linear correlation coefficients are evaluated as shown in Appendix C. Basically, most of the pairs of variables have weak correlations, i.e. which are worth inputting into the BDT. Several pairs of input variables have strong correlations, which are quantitatively understood. The distributions of input variables of the BDTs are compared between the observed data and MC simulations as shown in Appendix B. In general, each of them is found to be in good agreement. Additionally, modelings of correlations between pairs of input variables are checked as shown in Appendix C. Most of the correlations between pairs of input variables in the observed data are reproduced by the MC simulations. Summarizing the above, The correlations between input variables are well understood, and the input variables are well modeled by the MC simulations including those correlations, hence, the machine learning approach introduced in this analysis is thought to be well controlled.

6.4.3 Output Variables

The output BDT distributions for each channel are shown in Figures 6.9, 6.10, 6.11. Those range over approximately between -1 to $+1$, and the signal purity monotonic increases at higher BDT output values. The BDT outputs have much better discriminating power than that of a signal variable such as m_{VV} , for example, the expected significance by a likelihood fit with BDT outputs is 2.5 standard deviations, whereas that with m_{VV} is 1.5 standard deviations. Therefore, the approach to exploit the BDT algorithm has a huge importance on this analysis.

Table 6.10: Variables used in the BDT trainings in the resolved (left) and merged (right) categories of each lepton channel analysis are shown. The numbers in cells represent the rankings by the variable importance.

Variable	resolved			Variable	merged		
	0-lepton	1-lepton	2-lepton		0-lepton	1-lepton	2-lepton
m_{jj}^{tag}	1	–	2	m_{jj}^{tag}	1	–	1
$\Delta\eta_{jj}^{\text{tag}}$	–	–	9	$\Delta\eta_{jj}^{\text{tag}}$	–	–	6
p_T^{tag,j_1}	12	8	–	p_T^{tag,j_2}	5	3	8
p_T^{tag,j_2}	10	11	8	m_J	3	–	–
$\Delta\eta_{jj}$	8	9	4	$D_2^{(\beta=1)}$	7	–	4
$p_T^{j_1}$	13	–	–	E_T^{miss}	2	–	–
$p_T^{j_2}$	4	2	5	$\Delta\phi(\vec{E}_T^{\text{miss}}, J)$	4	–	–
w^{j_1}	5	7	7	η_ℓ	–	4	–
w^{j_2}	7	5	6	$n_{j,\text{track}}$	6	–	–
$n_{\text{tracks}}^{j_1}$	–	12	14	ζ_V	–	2	2
$n_{\text{tracks}}^{j_2}$	–	15	16	m_{VV}	–	–	3
w^{tag,j_1}	6	6	1	p_T^{VV}	–	–	5
w^{tag,j_2}	9	13	12	m_{VVjj}	–	1	–
$n_{\text{tracks}}^{\text{tag},j_1}$	–	14	15	p_T^{VVjj}	–	–	7
$n_{\text{tracks}}^{\text{tag},j_2}$	–	16	11	w^{tag,j_1}	8	–	–
$n_{j,\text{track}}$	11	–	3	w^{tag,j_2}	9	–	–
$n_{j,\text{extr}}$	3	–	–				
E_T^{miss}	2	–	–				
η_ℓ	–	3	–				
$\Delta R(\ell, \nu)$	–	10	–				
ζ_V	–	4	10				
m_{VV}	–	–	13				
m_{VVjj}	–	1	–				

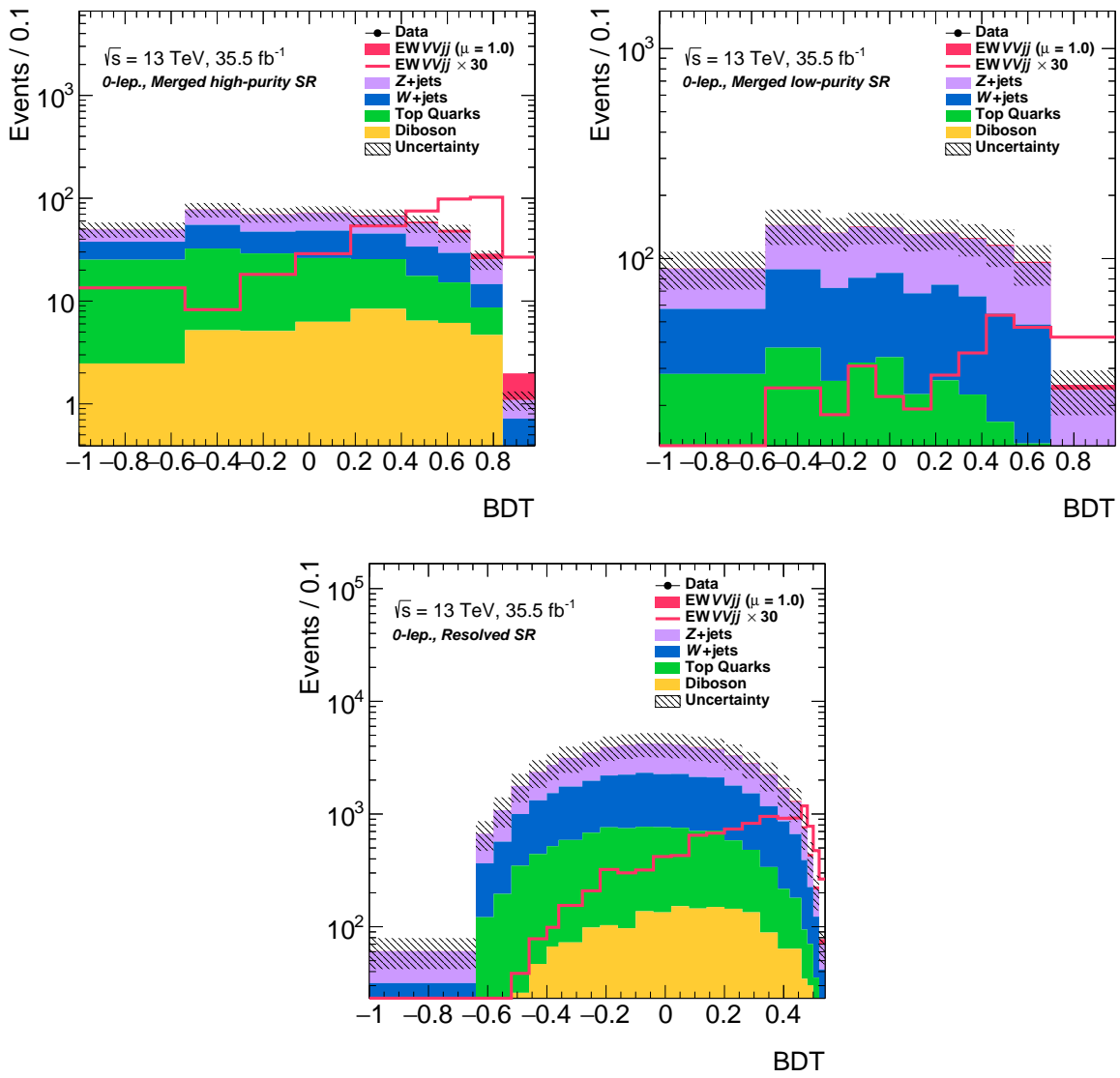


Fig. 6.9: BDT response distributions in the 0-lepton SRs, merged HP (top left), merged LP (top right) and resolved (bottom) are shown.

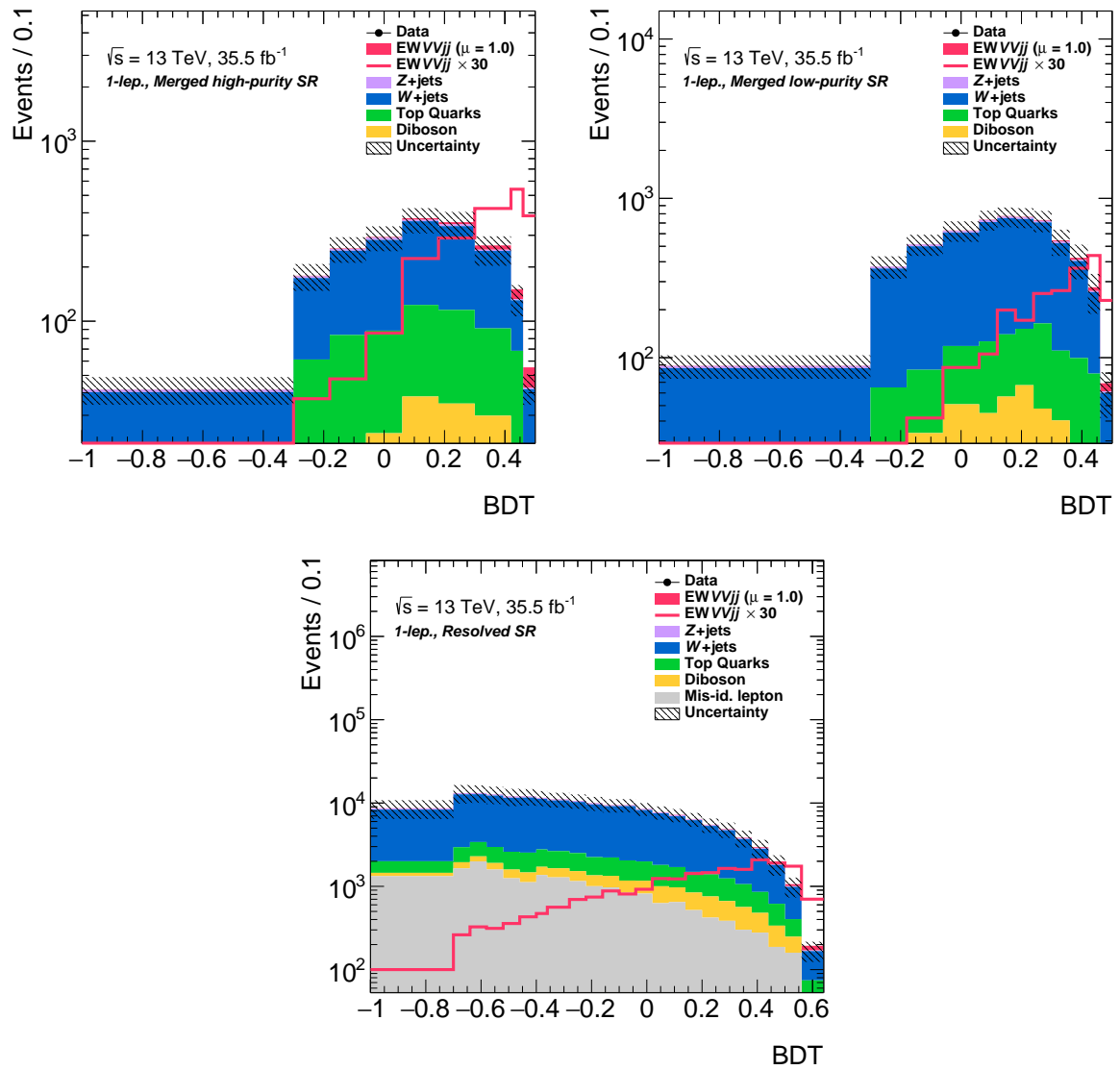


Fig. 6.10: BDT response distributions in the 1-lepton SRs, merged HP (top left), merged LP (top right) and resolved (bottom) are shown.

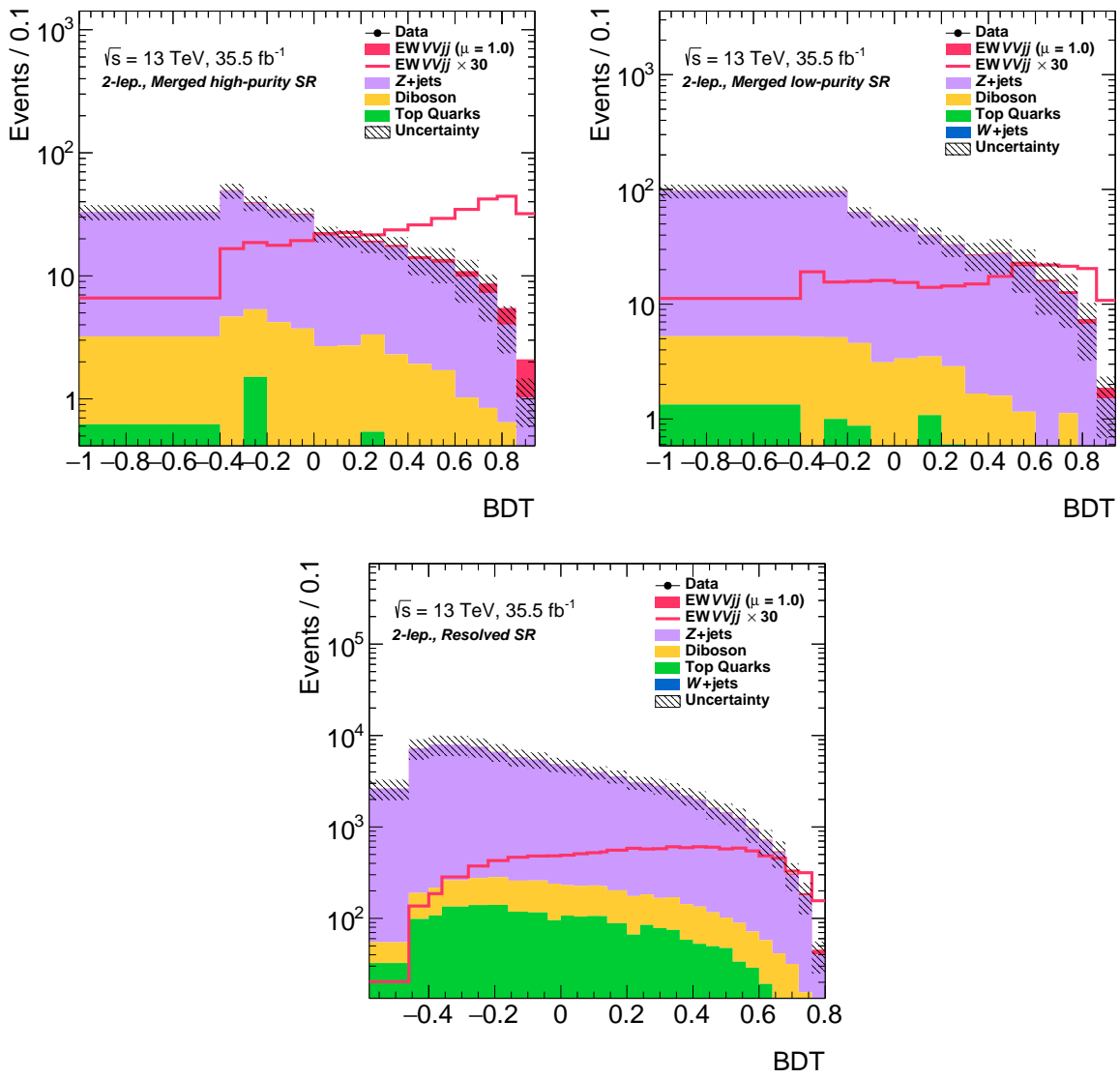


Fig. 6.11: BDT response distributions in the 2-lepton SRs, merged HP (top left), merged LP (top right) and resolved (bottom), are shown.

6.5 Background Modeling and Estimation

Background templates for statistical tests are made by the MC simulations except for the QCD dijet background estimation as described in Section 6.2. This section describes dedicated corrections for V+jets samples and QCD multijet estimation method in Sections 6.5.1 and 6.5.2, respectively. An estimation way for the interference between QCDV+jets and EWV+jets is also shown in Section 6.5.3.

6.5.1 V+jets background

There is a known issue related to modeling of m_{jj}^{tag} distribution in SHERPA2.2.1 which overshoots the observed data as shown in Figure 6.12. Authors of SHERPA suspect that it presumably relies on the tuning of QCD parameters, therefore, it is planned to retune in the next version of SHERPA, SHERPA2.7. However, the releasing takes considerable time, hence, in-situ m_{jj}^{tag} shape corrections are performed in this analysis as shown below.

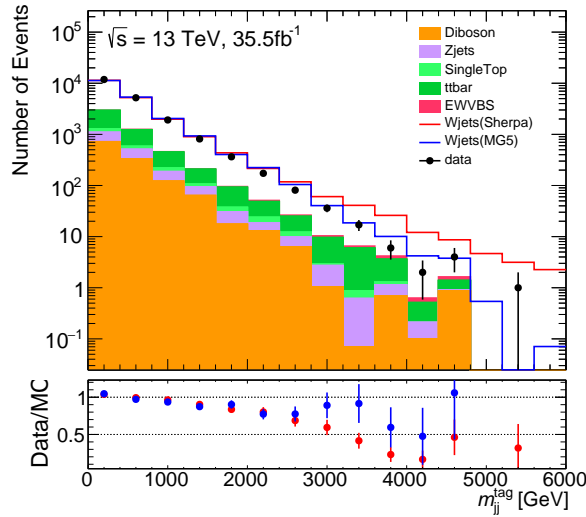


Fig. 6.12: Comparisons of m_{jj}^{tag} distributions between the observed data and SHERPA2.2.1 or MADGRAPH5_aMC@NLO v2.3.2 at merged WCR region except for the m_{jj}^{tag} cut. The prediction of MADGRAPH5_aMC@NLO performs better modeling than that of SHERPA2.2.1, however, it have been generated much fewer statistics in timescale of this analysis, SHERPA2.2.1 has been chosen as the nominal sample.

The correction goes as follows, a fit is performed to a ratio of the observed data to the MC simulations for m_{jj}^{tag} after normalizing its scale at each 1-lepton WCR for W+jets and the 2-lepton ZCR for Z+jets by a linear function, and it is applied to each W+jets and Z+jets SHERPA sample as an event-by-event weight with respect to m_{jj}^{tag} . Distributions for Non-V+jets MC simulated samples are subtracted from the distribution for the observed data to obtain pure V+jets event shapes. The number of events for non-V+jets MC is at most 10%. The same reweighting functions are applied to the 0-lepton channel.

6.5. BACKGROUND MODELING AND ESTIMATION

However, deviations are found in VCR of the 0-lepton channel after reweighting due to phase-space differences between the 0- and 1- or 2-lepton channels caused by different event selections. An additional reweighting is applied only for the 0-lepton channel ($c(m_{jj}^{\text{tag}})$) which is a ratio of the 1- or 2-lepton channel to the 0-lepton channel on the m_{jj}^{tag} distributions. The total weight represents as

$$w(m_{jj}^{\text{tag}}) = \frac{N^{\text{data}} - N^{\text{non-}W+\text{jetsMC}}}{N^{W+\text{jetsMC}}} \times c(m_{jj}^{\text{tag}}), \quad (6.5)$$

$$c(m_{jj}^{\text{tag}}) = N_{W+\text{jets}(Z+\text{jets})\text{MC}}^{1\text{lep}(2\text{lep})} / N_{W+\text{jets}(Z+\text{jets})\text{MC}}^{0\text{lep}}, \quad (6.6)$$

where N^X stands for the number of events for the X sample, non- $W+\text{jetsMC}$ denotes the sum of the MC simulated samples other than the $W+\text{jets}$ sample.

The correction factor measurements are performed at subdivided WCR and ZCR by additional m_{Vhad} binnings, $m_{\text{Vhad}} = 50, 60, 70$ and $100, 150, 200, 300$ GeV in order to account for m_{Vhad} dependences on the m_{jj}^{tag} mismodelings. The correction factor estimations for representative m_{Vhad} subdivided WCR regions are shown in Figure 6.13.

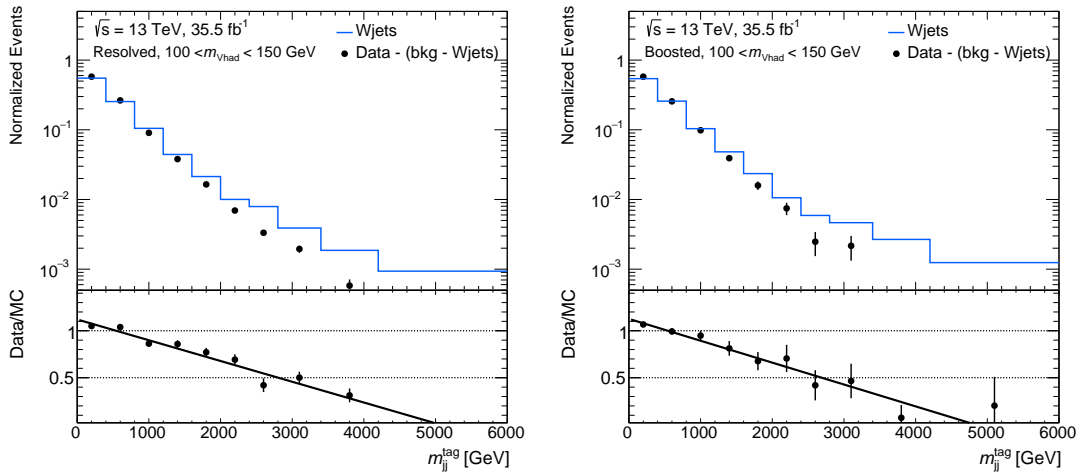


Fig. 6.13: Fits of m_{jj}^{tag} slope at a particular m_{Vhad} bin of the resolved (left) and merged (right) WCR are shown.

The measured correction factors ($w(m_{jj}^{\text{tag}})$) are obtained by interpolating to the SR mass window ($m_{\text{Vhad}} \sim [70, 100]$ GeV) by the linear fittings as shown in Figure 6.14. The correction factors commonly used in this study are summarized in Table 6.11.

Sanity checks by comparing distributions between the observed data and the SHERPA samples after applying the correction factors are performed as shown in Figure 6.15. Distributions are consistent with the observed data after applying correction factors, which indicate that the reweighting functions are correctly estimated in the regions.

Figure 6.16 shows the m_{jj}^{tag} correction weights as a function of m_{jj}^{tag} for the $W+\text{jets}$ and $Z+\text{jets}$ processes

6.5. BACKGROUND MODELING AND ESTIMATION

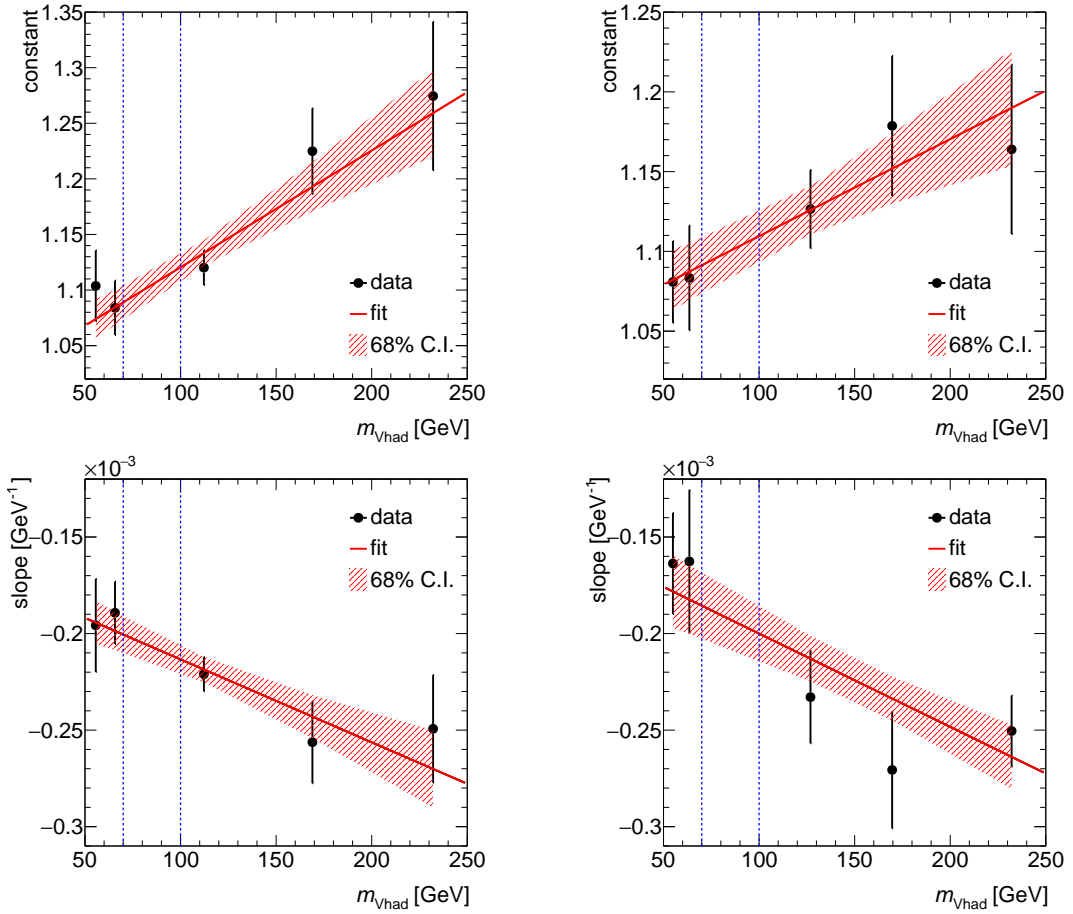


Fig. 6.14: Constants (top) and slopes (bottom) of the reweighting functions as a function of m_{Vhad} for resolved (left), for merged (right) regions are shown. The red band represents the 68% confidence interval of the linear fit. Regions surrounded by the blue lines roughly correspond to the SR, and the constants and slopes at the center of those blue lines are used for the m_{jj}^{tag} reweighting.

Table 6.11: A summary of coefficients for the estimated m_{jj}^{tag} reweighting functions for the W +jets process is shown.

	W+jets		Z+jets	
	Resolved	Merged	Resolved	Merged
p_0 (constant)	1.10(4)	1.10(2)	1.17(7)	1.17(4)
p_1 (slope) [GeV^{-1}]	$-2.1 \times 10^{-4}(2)$	$-1.9 \times 10^{-4}(3)$	$-2.50 \times 10^{-4}(6)$	$-2.7 \times 10^{-4}(2)$

Table 6.12: A summary of coefficients for the estimated additional m_{jj}^{tag} reweighting functions ($c(m_{jj}^{tag})$) for the W +jets and Z +jets processes is shown.

	W+jets		Z+jets	
	Resolved	Merged	Resolved	Merged
p_0 (constant)	0.77(5)	0.79(7)	0.82(4)	0.75(4)
p_1 (slope) [GeV^{-1}]	$2.6 \times 10^{-4}(5)$	$2.3 \times 10^{-4}(6)$	$1.9 \times 10^{-4}(3)$	$3.0 \times 10^{-4}(4)$

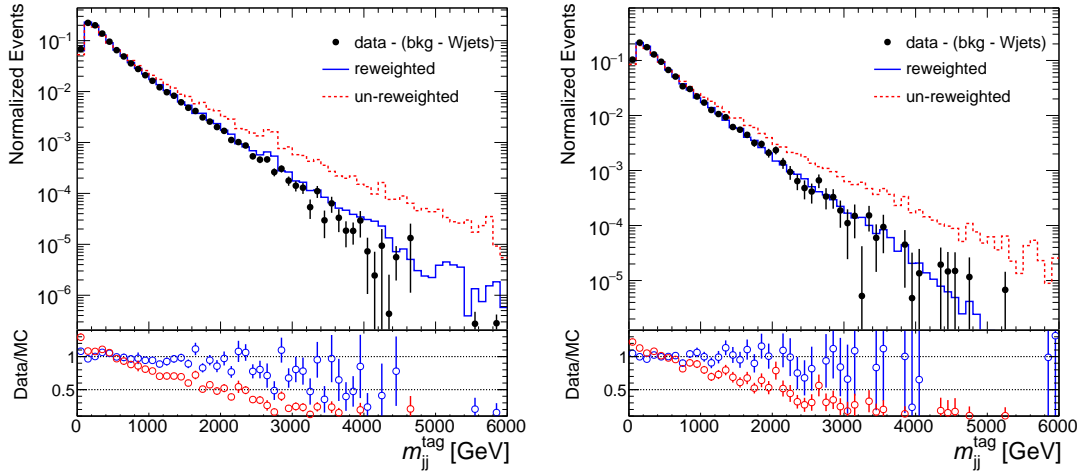


Fig. 6.15: The m_{jj}^{tag} distributions before and after m_{jj}^{tag} reweighting for the resolved WCR (left) and merged WCR (right) are shown. The histograms for the observed data are subtracted by distributions for the MC simulations other than the W +jets sample.

for the merged and resolved regions. The uncertainty band includes only the statistical uncertainty deter-

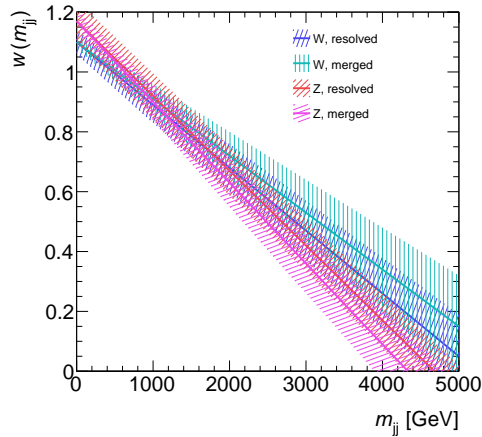


Fig. 6.16: m_{jj}^{tag} correction weights as a function of m_{jj}^{tag} for the W +jets and Z +jets processes in the merged and resolved regions are shown. The uncertainty band includes only the statistical uncertainty determined from the fit. For the illustration, the uncertainties in a pair of parameters are correlated 100% positively.

mined from the fit. All of the reweighting functions are consistent within the uncertainty, which implies that the mismodeling does not depend on p_T of V_{had} . To be conservative, the differences between m_{jj}^{tag} distributions before and after the reweighting are taken as a 1σ of the systematic uncertainty.

6.5.2 QCD multijet background

While the $V+jets$ process after the m_{jj} reweighting and the $t\bar{t}$ process are well modeled in the MC simulations, the QCD multijet processes, which could contribute to the SRs due to leptons produced in and after the hadronization or misidentified leptons referred to as *fake*, are not well described by the MC simulations in terms of a scale nor shape. The fake mainly arises from two origins, a first fake is from a pair creation from γ , which dominates high p_T electron fakes. A second fake is due to semileptonic decay of heavy flavor in jets, which dominates low p_T muon fakes. Schematic diagrams for those fakes are illustrated in Figure 6.17.

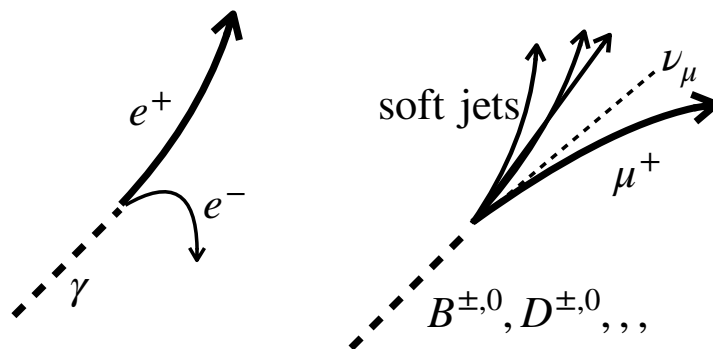


Fig. 6.17: . A schematic diagram of a representative electron fake is shown in the left. Asymmetric decay of γ cannot be reduced by the electron isolation cut, hence it can fake an electron. A schematic diagram of a representative muon fake is shown in the right. B and D mesons that produced from b- and c-quarks arising from the fragmentation can decay leptonically. This is the main source of μ fakes.

The multijet background in the 1-lepton resolved region is estimated by the observed data using a *fake factor* method. The multijet background in the 0-lepton channel is suppressed using multijet removal cuts (Section 6.3), and in the 2-lepton analysis, the contribution from multijet is found to be negligible.

Fake Factor Method

The fake factor method derives fake factors by conceptually the same as the ABCD method. The regions correspond to ABCD are determined by the number of jets and the identification or isolation requirement for the lepton. Dedicated single jet control regions are defined, which are required to be only one jet in the events, but the other selections are the same as the SRs. Each region is then further divided into two subregions, $CR_{\text{single jet}}$ and $CR_{\text{single jet}}^{\text{inv}}$ with the different lepton identification or isolation criterion as shown in Table 6.13. For the definitions of $CR_{\text{single jet}}$ and $CR_{\text{single jet}}^{\text{inv}}$ for the muon channel at the $p_T(\mu\nu) < 150$ GeV region, muon triggers listed in Table 6.4 which require isolation requirements are applied the same as SRs. The isolation requirement for the region is tightened to prevent bias by those triggers. For the $p_T(\mu\nu) > 150$ GeV region is using E_T^{miss} trigger, the isolation bias is not a concern.

Table 6.13: Identification and isolation requirements for the single jet control regions are shown. The electron identification categories, TightLH and MediumLH, and the muon isolation variable $p_{T,var}^{iso}$ have already been explained in Sections 4.3 and 4.4, respectively.

	$CR_{single\ jet}^{sig}$	$CR_{single\ jet}^{inv}$
electron	pass TightLH	pass MediumLH and fail TightLH
muon ($p_T(l\nu) > 150\ GeV$)	$p_{T,var}^{iso}/p_T < 0.06$	$0.06 < p_{T,var}^{iso}/p_T < 0.15$
muon ($p_T(l\nu) < 150\ GeV$)	$p_{T,var}^{iso}/p_T < 0.06$	$0.06 < p_{T,var}^{iso}/p_T < 0.07$

A fake factor is defined as

$$f = \frac{N_{event}(CR_{single\ jet}^{sig})}{N_{event}(CR_{single\ jet}^{inv})}, \quad (6.7)$$

where $N_{event}(X)$ stands for the number of events in a X region.

Fake rates have the dependence on lepton η and p_T , thus the fake factors are derived with the binning as shown in Table 6.14. Additional binnings on E_T^{miss} are applied for the electron channel because of

Table 6.14: Binnings for each electron and muon channel for evaluating fake factors are summarized.

channel	p_T [GeV]	$ \eta $	E_T^{miss} [GeV]
electron	27-115		0, 60, 75, ∞
	115-135	0, 1.37, 1.52, 2.47	0, 38, 52, ∞
	135-155		0, 26, 43, ∞
	155-190		0, 25, 45, ∞
	190,300,400,600, ∞	inclusive	inclusive
muon	27, 42, 59, 76, 99, ∞	0, 1.05, 1.5, 2.5	inclusive

dependencies on the fake factors for the E_T^{miss} are observed. For the muon channel, a fake factor is estimated in two different regions with $p_T(\mu\nu) < 150\ GeV$ and $p_T(\mu\nu) > 150\ GeV$ to account for the different isolation requirements. In order to remove non-multijet contributions, electroweak events in the $CR_{single\ jet}^{inv}$ region are subtracted by using the MC simulations. Evaluated fake factors are shown as a function of lepton p_T in Figure 6.18 for the region of $p_T(l\nu) > 150\ GeV$.

Validity of the estimation is checked at a validation region (VR) required to be the leading jet p_T smaller than 40 GeV (the SR requires greater than 40 GeV) and loosen E_T^{miss} cut greater than 30GeV (the SRs requires $E_T^{miss} > 80\ GeV$) as shown in Figure 6.19. As expected, electron fakes are populated at high p_T , whereas muon fakes are populated low p_T . Overall, the estimated multijet background and the other backgrounds reproduce the observed data at the VR. The considerable discrepancies arise from the fewer statistics can be covered by systematic uncertainties, and it is found to be negligible impact to this measurement.

6.5. BACKGROUND MODELING AND ESTIMATION

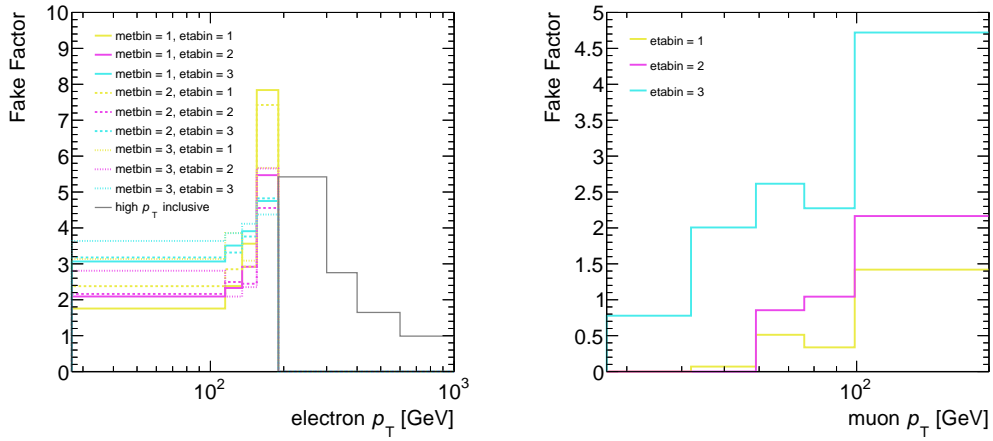


Fig. 6.18: Fake factors for the electron (left) and muon (right) channels. The bin numbers correspond to the binning defined in Table 6.14 by the ascending order.

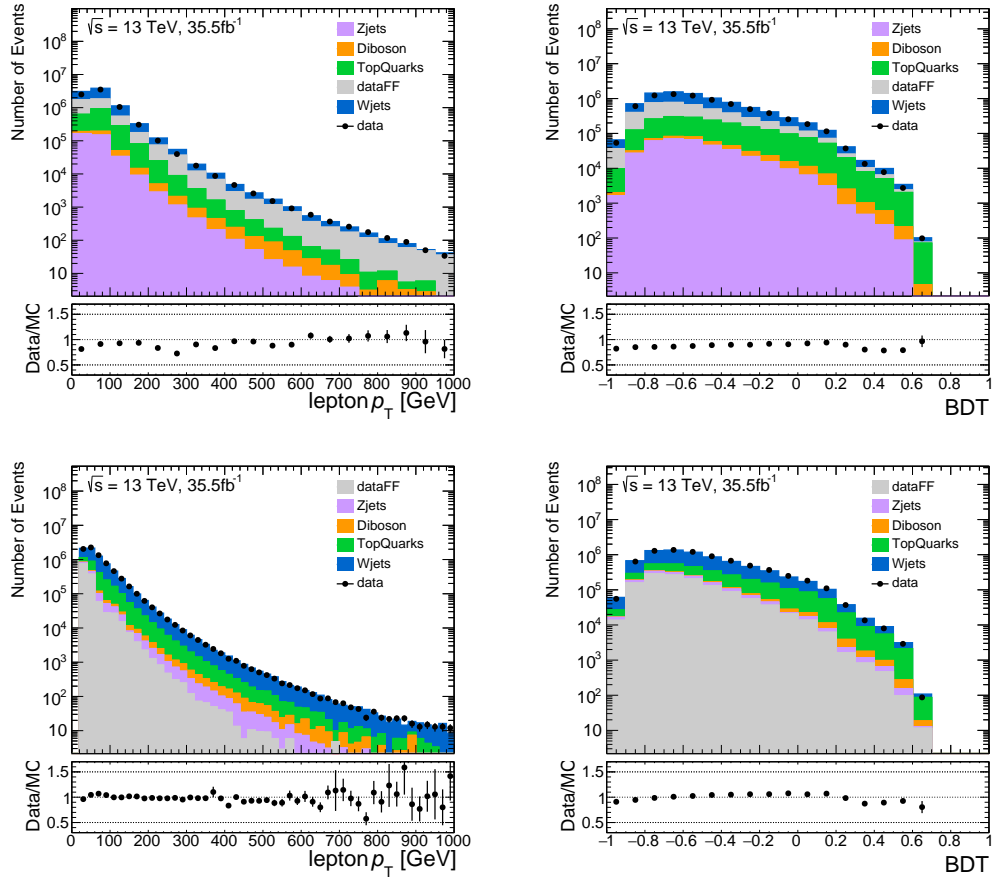


Fig. 6.19: Distributions of lepton p_T (top left) and BDT output (top right) for the electron channel, and lepton p_T (bottom left) and BDT output (bottom right) for the muon channel at the VR. The systematic uncertainties shown in Section 6.7.2 are not displayed in these plots. The gray histograms (labeled dataFF) represents the estimated multijet background by the fake factor method. The sum of predictions are approximately compatible with the observed data.

6.5.3 Interference between QCDVVjj and EWVVjj

The common final state between QCDVVjj and EWVVjj processes implies that the existence of interference which is the cross term of the matrix element. The matrix element squared $|M|^2$ for the VVjj final state at the LO is given by

$$|M|^2 = |M_{EW} + M_{QCD}|^2 = |M_{EW}|^2 + |M_{QCD}|^2 + 2 \times \text{Re}(M_{EW} \cdot M_{QCD}^*), \quad (6.8)$$

where $|M_{EW}|^2$ is the amplitude of the EWVVjj with the eighth order of electroweak coupling constant α referred to as *EWK*, $|M_{QCD}|^2$ is the amplitude of the QCDVVjj with the fourth-order of α and fourth-order of QCD coupling constant α_s referred to as *QCD*, and $\text{Re}(M_{EW} \cdot M_{QCD}^*)$ is the amplitude of the interference term between those referred to as *INT*. The INT term is estimated in the dedicated MC simulations which include the INT term only generated by the MADGRAPH5_aMC@NLO event generator the same as signal production. The detector simulation is not considered in this estimation to reduce computation time. The cross-sections evaluated the simulations are summarized in Table 6.15, and the relative contributions of the INT term compared to the EWK term are found to be around $O(1)\%$. This contribution is sufficiently small, thus the INT term is included as a systematic uncertainty associated with the signal prediction.

Table 6.15: Total cross-sections for each final state. σ_{QCD} , σ_{EWK} , and σ_{INT} stand for cross-sections for QCDVVjj,EWVVjj, and interference term, respectively.

Final state	σ_{QCD} [pb]	σ_{EWK} [pb]	σ_{INT} [pb]
WW \rightarrow lvqq	211.4	1.75	-0.20
WZ \rightarrow lvqq	2.90	0.24	0.0045
WZ \rightarrow vvqq	1.92	0.14	0.0046
WZ \rightarrow llqq	0.533	0.041	0.0015
ZZ \rightarrow vvqq	0.810	0.031	0.00096
ZZ \rightarrow llqq	0.223	0.0092	0.00032

Figure 6.20 shows m_{jj}^{tag} distributions of the INT term and the EWK term, for each VVjj production process after fiducial selection at the truth level which described in Section 6.6. The ratio plots show the relative contribution of the INT term, $(N_{INT} + N_{EWK})/N_{EWK}$, as a function of m_{jj}^{tag} . The largest impact on the signal prediction is found to be at most 6% in the resolved regions and at most about 10% in the merged regions. The ratio $(N_{INT} + N_{EWK})/N_{EWK}$ as a function of m_{jj}^{tag} is then used as systematic uncertainty associated with the signal prediction for each VVjj production process in this study.

6.5. BACKGROUND MODELING AND ESTIMATION

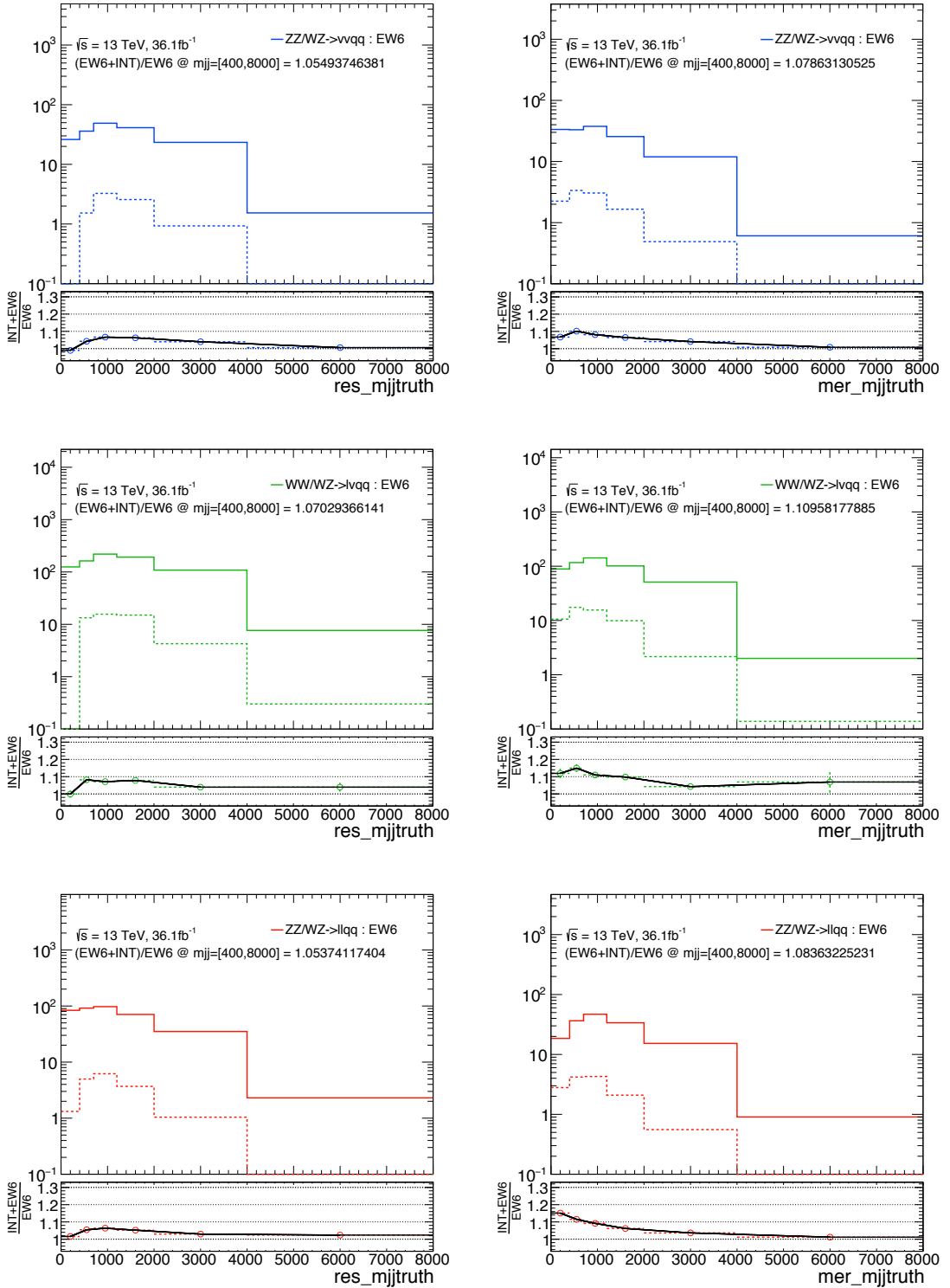


Fig. 6.20: m_{jj}^{tag} distributions for the EWK process (solid line) and the INT term (dashed line) for the resolved (left), and the merged (right) regions. The first row is for the $\nu\nu qq$ final state, and the second row is for the $\ell\nu qq$ final state, and the third row is for the $\ell\ell qq$ final state. Fiducial event selections as described in Section 6.6 are applied. In the ratio plots beneath, the black line shows the interpolation of $(N_{\text{INT}} + N_{\text{EWK}})/N_{\text{EWK}}$ as a function of m_{jj}^{tag} .

6.6 Fiducial Volume Definition and Measurement Procedure

Besides the search for the $EWV\bar{V}jj$ processes, a measurement of cross-section in a particular fiducial volume is performed simultaneously. Section 6.6.1 presents definitions of the fiducial volume where the cross-section measurement performed. The methodology of this measurement is introduced in Section 6.6.2.

6.6.1 Fiducial Volume Definition

The fiducial volume of this measurement is defined by using stable final state particles⁸⁾. Leptons produced in the decay of a hadron or its descendants are not considered in the charged lepton requirement of the fiducial volume. The fiducial selection is summarized in Table 6.16 and details are given below.

A charged lepton is required to have $p_T > 7$ GeV and $|\eta| < 2.5$. Jets are formed from all final state particles except prompt⁹⁾ leptons, prompt neutrinos, and prompt photons using the anti- k_t algorithm. A small-R jet is required to satisfy $p_T > 20$ GeV for $|\eta| < 2.5$ or $p_T > 30$ GeV for $2.5 < |\eta| < 4.5$. Jets within $\Delta R(j, e/\mu) = 0.2$ are rejected. Jets containing a b-hadron identified by the MC event record are labeled as b-jets. A large-R jet is required to be with $p_T > 200$ GeV and at $|\eta| < 2.0$, and those are groomed by the trimming algorithm as for reconstruction level algorithm described in Section 5.1.1. No D_2 requirement is applied to large-R jets. The selections of hadronically decaying bosons and tagging-jets follow the same steps and applies the same criteria for reconstruction level as shown in Table 6.16. The number of leptons is required to be zero, one, and two for the 0-, 1-, and 2-lepton channels, respectively. Events having any leptons more than the above are vetoed. For the 0-lepton channel, the transverse momentum of the neutrino system corresponding to the E_T^{miss} is imposed on $p_T^{\nu\nu} > 200$ GeV. For the 1-lepton channel, a lepton is required to be $p_T > 27$ GeV, and events are required to have $p_T^{\nu} > 80$ GeV and excluding any b-jets. For the 2-lepton channel, the leading (subleading) lepton is required to be $p_T > 28$ (20) GeV, and the invariant mass of the lepton pair is required to be within $83 < m_{\ell\ell} < 99$ GeV.

The predicted cross-section for $EWV\bar{V}jj$ is calculated in the fiducial volume as shown in Table 6.17. The contribution of each process to each fiducial volume is summarized in Table 6.18.

6.6.2 Cross-Section Measurement Procedure

The evaluation of the fiducial cross-section is performed by scaling the measured signal-strength μ defined as

$$\mu = \frac{(\sigma_{EWV\bar{V}jj} \times \text{BR}(V\bar{V} \rightarrow \text{semileptonic}))_{\text{obs}}}{(\sigma_{EWV\bar{V}jj} \times \text{BR}(V\bar{V} \rightarrow \text{semileptonic}))_{\text{SM}}}, \quad (6.9)$$

where $\sigma_{EWV\bar{V}jj}$ and $\text{BR}(V\bar{V} \rightarrow \text{semileptonic})$ stand for the cross-section for the $EWV\bar{V}jj$ processes and the branching fraction for the semileptonic decay of $V\bar{V}$, obs and SM denote observed and standard

⁸⁾ Particles having lifetime τ in the laboratory frame as $c\tau > 10$ mm. More details are described in Reference [157].

⁹⁾ Outgoing particles of a Feynman diagram

6.6. FIDUCIAL VOLUME DEFINITION AND MEASUREMENT PROCEDURE

Table 6.16: Fiducial volume definitions used for the measurement of the EWVj processes are shown.

Object selection	
Leptons	$p_T > 7 \text{ GeV}, \eta < 2.5$
Small-R jets	$p_T > 20 \text{ GeV}$ if $ \eta < 2.5$, and $p_T > 30 \text{ GeV}$ if $2.5 < \eta < 4.5$
Large-R jets	$p_T > 200 \text{ GeV}, \eta < 2.0$
Event selection	
Leptonic V	0-lepton Zero leptons, $p_T^{VV} > 200 \text{ GeV}$
	1-lepton One lepton with $p_T > 27 \text{ GeV}, p_T^V > 80 \text{ GeV}$
	2-lepton Two leptons, with leading (subleading) lepton $p_T > 28$ (20) GeV $83 < m_{\ell\ell} < 99 \text{ GeV}$
Hadronic V	Merged One large-R jet with the minimum of $\min(m_J - m_W , m_J - m_Z)$ $64 < m_J < 106 \text{ GeV}$
	Resolved Two small-R jets with the minimum of $\min(m_{jj} - m_W , m_{jj} - m_Z)$ $p_T^{j1} > 40 \text{ GeV}, p_T^{j2} > 20 \text{ GeV}$ $64 < m_{jj} < 106 \text{ GeV}$
Tagging-jets	Two small-R non-b jets with the highest m_{jj}^{tag} satisfying with $\eta_{\text{tag},j_1} \cdot \eta_{\text{tag},j_2} < 0$ $m_{jj}^{\text{tag}} > 400 \text{ GeV}, p_T^{\text{tag},j_{1,2}} > 30 \text{ GeV}$
Number of b-jets	0-lepton –
	1-lepton 0
	2-lepton –

Table 6.17: Summary of predicted fiducial cross-sections in six fiducial categories. The unit of values is in fb.

$\sigma_{EWVVj}^{\text{fid,SM}}$	0-lepton	1-lepton	2-lepton
Resolved	9.22 ± 0.18	16.37 ± 0.35	6.01 ± 0.03
Merged	4.1 ± 0.13	6.08 ± 0.48	1.2 ± 0.06
Total	13.32 ± 0.22	22.45 ± 0.41	7.21 ± 0.03
		42.98 ± 0.46	

Table 6.18: Predicted contributions of six different samples in six fiducial categories.

Channels	ZZllqq	ZZvvqq	ZWllqq	ZWvvqq	WZlvqq	WWlvqq
0-lepton Merged	0	13.6%	0	26.6%	13.0%	46.7%
1-lepton Merged	0.42%	0	0.93%	0	20.3%	78.4%
2-lepton Merged	30.7%	0	69.3%	0	0	0
0-lepton Resolved	0	14.3%	0	31.0%	12.0%	42.6%
1-lepton Resolved	0.09%	0	0.45%	0	17.5%	81.9%
2-lepton Resolved	27.9%	0	72.1%	0	0	0

model expectation quantities, respectively.

Then, the fiducial cross-section is evaluated:

$$\sigma_{EWVVjj}^{\text{fid,obs}} = \mu_{EWVVjj}^{\text{obs}} \cdot \sigma_{EWVVjj}^{\text{fid,SM}}, \quad (6.10)$$

where $\sigma_{EWVVjj}^{\text{fid,SM}}$ is the expected fiducial cross-section in the region, $\mu_{EWVVjj}^{\text{obs}}$ will be obtained in Section 6.8.

This simple projection works on the assumption that there is no new physics effect that could bring sizable kinematic changes in both the background and signal. Hence, the new physics signals leading to an enhancement for EWVVjj signal-strength can be observed in this method in an unbiased way.

6.7 Systematic Uncertainties

This section describes the systematic uncertainties considered in this study. Uncertainties are categorized into three parts, uncertainties related to signals, backgrounds, and the experiment. Each of them is explained in the following subsections, Sections 6.7.1, 6.7.2, and 6.7.3, respectively.

6.7.1 Systematic Uncertainties in Signal Prediction

The following uncertainties are considered as signal prediction uncertainties:

1. Parton Distribution Function (PDF),
2. Parton shower modeling,
3. ISR/FSR modeling,
4. Interference between EWVVjj and QCDVVjj.

The signal modeling uncertainty in the PDF is estimated by using the uncertainties associated with the NNPDF23LO set and the acceptance difference with alternative PDF sets: CT10 and MMHT2014LO. Those uncertainties are adding in quadrature, and the PDF uncertainty is estimated to be 3–5% depending on the SRs and CRs. The parton shower uncertainty is estimated by varying relevant parameters in the A14-NNPDF tune [105] in the PYTHIA, which ranges around 1-5%. The effect of the QCD scale uncertainty is estimated by varying the factorization (μ_F) and renormalization scales (μ_R) independently by a factor of two with the constraint $0.5 \leq \mu_F/\mu_R \leq 2$, which is approximately 1-3%. A summary of the magnitude of uncertainties above is shown in Table 6.19. Also, Both the shape and scale for the INT term evaluated in Section 6.5 are included as an uncertainty.

Table 6.19: A summary of uncertainties associated with the signal prediction in the six fiducial categories is shown.

Channels	QCD-scale	PDF choice	Parton shower model
0-lepton Merged	1.83%	4.58%	4.09%
1-lepton Merged	3.23%	5.62%	6.01%
2-lepton Merged	1.75%	4.34%	2.30%
0-lepton Resolved	1.47%	4.96%	3.38%
1-lepton Resolved	1.60%	5.25%	2.34%
2-lepton Resolved	2.44%	5.37%	2.46%

6.7.2 Systematic Uncertainties in Background Prediction

The overall normalization factors are determined by the VCR and TopCR for $V+$ jets and $t\bar{t}$ processes, respectively. Thus only systematic uncertainties related to shapes of the final discriminant (m_{jj}^{tag} or BDT) are taken into account for those. Backgrounds that have no pure CR, the diboson and single- t processes are considered both shape and scale uncertainties.

$V+$ jets: The m_{jj}^{tag} reweighting systematic uncertainty introduced in Section 6.5.1 has the largest impact on this study. A subdominant uncertainty is a matrix element and a parton shower variation estimated by comparing between the nominal event generator of SHERPA and an alternative event generator of MADGRAPH5_aMC@NLO. The m_{jj}^{tag} reweighting is applied to SHERPA samples only in the evaluation of the systematic uncertainties. Other uncertainties, QCD-scale, parton shower model, and PDF choice are found to be negligible in this measurement. Additional normalization uncertainty for $V+$ jets in the 0-lepton channel is considered to take into account for the acceptance difference between the 0- and 1-(2-)lepton channels because there is no pure $V+$ jets control region in the 0-lepton channel. The additional uncertainty is estimated using the ratio of the event yield in each signal region of the 0-lepton channel to that in the 1-(2-)lepton channel, and by comparing this ratio obtained from the nominal MC simulation (SHERPA) with the ratio from an alternative sample (MADGRAPH5_aMC@NLO). The uncertainties are estimated as 8% (14%) for the $W+$ jets process in the merged (resolved) signal region, and 22% (42%) for the $Z+$ jets process in the merged (resolved) region.

$t\bar{t}$: Shape difference given by matrix element is derived by comparing predictions between the nominal event generator of POWHEG-BOX and an alternative event generator of MADGRAPH5_aMC@NLO 2.2.2, a parton shower variation is evaluated by comparing nominal sample PYTHIA 6.428 using the P2012 tune to HERWIG++ 2.7.1 using the UEEE5 underlying-event tune [56]. Also, additional uncertainties derived by the factorization and renormalization scales doubled or halved samples are considered. Those uncertainties are estimated as 5-30% in total.

diboson: A normalization uncertainty for the QCD scale is estimated by varying the factorization and renormalization scales from one-half to two with the constraint $0.5 \leq \mu_F/\mu_R \leq 2$. The PDF uncertainty is evaluated from the uncertainties associated with the nominal PDF set NNPDF30NNLO, also including the differences to alternative PDF sets, CT10NNLO [158] and MMHT2014NNLO [159]. The normalization uncertainty for diboson normalization is around 30% in total. A shape uncertainty is

estimated by comparing samples generated by the nominal event generator of SHERPA and an alternative event generator of POWHEG-BOX. The uncertainty is estimated as 2-30%.

single-top: A normalization uncertainty is assigned 20% to this background estimated by Reference [160]. Due to its tiny fraction, shape uncertainty is ignored.

multijet: Two uncertainties associated with the fake factor method are considered. A first uncertainty is for the electroweak subtraction. The twice of the electroweak subtraction factor is conservatively assigned as the uncertainty. A second uncertainty is a difference in other electron or muon identification working points in the calculation of the E_T^{miss} reconstruction.

All of the above uncertainties and those inverses are considered as $+1\sigma$ and -1σ in the likelihood fits introduced in Section 6.8.

6.7.3 Experimental Systematic Uncertainties

Luminosity uncertainty measured by the LUCID [66] is 2.1% for the sum of 2015 and 2016 datasets. This uncertainty is applied to both signals and backgrounds whose normalization factors relied on MC simulations.

All the lepton trigger efficiencies are almost 100%, therefore, those uncertainties are negligible. Modelings of the electron and muon reconstruction, identification, and isolation efficiencies are studied with a tag-and-probe method using $Z \rightarrow \ell\ell$ events in the observed data and MC simulations at $\sqrt{s} = 13$ TeV as shown in Sections 4.3.3 and 4.4.3. Small corrections are applied to MC simulations associated with the 1% order of uncertainty in both the energy scale and resolution.

Uncertainties in a small-R jet are estimated by *in-situ* techniques as described in Section 4.5.2. For central jets ($|\eta| < 2.0$), the total uncertainty in the jet energy scale ranges from about 6% for jets with $p_T = 25$ GeV, to about 2% for jets with a p_T of 1 TeV. An uncertainty in the jet energy resolution is 10-20% for jets with a $p_T = 20$ GeV to less than 5% for jet with $p_T > 200$ GeV. Leptons and jets uncertainties are propagated to uncertainty in E_T^{miss} including jet soft term. b-tagging uncertainties derived *in-situ* way by $t\bar{t}$ events mainly, an uncertainty in the difference between tagging efficiency measured on the observed data and the MC simulations as described in Section 4.5.3.

Uncertainties in a large-R jet are derived by the r_{trk} double ratio method described in Section 5.1.3 and Reference [107]. uncertainties in p_T , mass, and D_2 have considerable impacts on this study. The magnitudes are the order of 2-5%. Resolution uncertainties in p_T , mass, and D_2 assigned to be 20%, 20%, and 15%, respectively. Those values are not measured and are thought to be well conservative from several aspects [161].

6.8 Statistical Analysis and Interpretation

This section represents the statistical setup for the extraction of signal-strength and standard deviation against the null-hypothesis. The statistical interpretation relies on the profile likelihood test statistic [162] which implemented with the RooFit [163] and RooStats [164] packages.

6.8.1 Methodology

The likelihood function is given by

$$L(\mu, \vec{\nu}, \vec{\theta}) = \left(\prod_{n_i \in \text{bins}} P(n_i | \mu, \vec{\nu}, \vec{s}(\vec{\theta}), \vec{b}(\vec{\theta})) \right) \times G(\vec{\theta} | \vec{\theta}_0), \quad (6.11)$$

$$P(n_i | \mu, \vec{\nu}, \vec{s}(\vec{\theta}), \vec{b}(\vec{\theta})) = \frac{(\mu s_i(\vec{\theta}) + \sum_{k \in \text{bkgs}} \nu_k b_{ki}(\vec{\theta}))^{n_i}}{n_i!} e^{-(-\mu s_i(\vec{\theta}) - \sum_{k \in \text{bkgs}} \nu_k b_{ki}(\vec{\theta}))}, \quad (6.12)$$

where μ and ν_k are the freely adjustable normalization factors for the signal and the k -th background, respectively. ν_k for the backgrounds not having dedicated control region (QCDVVjj, single top) are fixed to unity. θ_i represents each systematic uncertainty, and those initial values are set at $\vec{\theta}_0$. s_i and b_{ki} are the expected numbers of signal and k -th background events in certain i -th bin. $G(\vec{\theta} | \vec{\theta}_0)$ is a constraint term for systematic uncertainties given by the Gaussian distribution on the nuisance parameters with a unity of expected value and with 1σ of uncertainty as to the standard deviation. θ and ν are referred to as nuisance parameters (NP).

The *parameter of interest* that this likelihood fit focuses on is signal-strength μ which has already been defined in Equation 6.9. A *test statistic* used to perform the hypothesis test is the *log-likelihood ratio*:

$$t = -2 \ln \Lambda = -2 \ln \left(\frac{L(\mu, \vec{\hat{\nu}}, \vec{\hat{\theta}})}{L(\hat{\mu}, \vec{\hat{\nu}}, \vec{\hat{\theta}})} \right). \quad (6.13)$$

The numerator stands for the conditional likelihood estimator, which is maximized with all the parameters varied including μ , and corresponding nuisance parameters are represented as $\vec{\hat{\nu}}, \vec{\hat{\theta}}$. The denominator stands for the unconditional likelihood estimator, which is maximization without the fixed value of μ , and corresponding the signal-strength and nuisance parameters are represented as $\hat{\mu}, \vec{\hat{\nu}}, \vec{\hat{\theta}}$. After each maximization, nuisance parameters are fixed at a certain value, this is referred to as *profiled*.

The compatibility between a hypothesis and the observed dataset with t_{obs} is evaluated by p -value or Z standard deviation (with a unit of σ), which are calculated by the distribution of the t as follows,

$$p = \int_{t_{\text{obs}}}^{\infty} f(t | \mu) dt, \quad (6.14)$$

$$Z = \Phi^{-1}(1 - p), \quad (6.15)$$

where Φ^{-1} is the inverse of the cumulative distribution of the Gaussian distribution. A given alter-

native hypothesis is excluded if the p-value is sufficiently small, or $Z[\sigma]$ is sufficiently higher. The 3σ corresponds to 99.7% is the typical value in which physicists claim evidence of alternative hypothesis. One undesirable feature of the p-value is that alternative hypothesis: $H_0, \mu \neq 0$ is excluded even if null hypothesis: $H_0, \mu = 0$ is excluded. To deal with this issue, CL_{s+b} and CL_b are defined which are p-value under the alternative hypothesis and p-value under null hypothesis, respectively. The $CL_s = CL_{s+b}/CL_b$ [165] is used as an alternative metric. CL_s cannot be small when the experimental dataset does not exclude an alternative hypothesis nor a null hypothesis.

In this study, a null-hypothesis is equivalent to standard model prediction except for the EWVj contribution, an alternative hypothesis is the full SM prediction. The definition of CL_s is used to claim the existence of the EWVj processes. Obtained μ_{obs} is translated to the fiducial cross-section measurement as explained in Section 6.6.

The distribution of the t can be estimated by the *toy-simulation* or *asymptotic formulas* [166]. The asymptotic formulas are adopted in this analysis due to its low computational intensity.

From the result of Reference [167], the test statistics t distributed as

$$t_\mu = \frac{(\mu - \hat{\mu})^2}{\sigma^2} + \mathcal{O}(1/\sqrt{N}), \quad (6.16)$$

where $\hat{\mu}$ follows a Gaussian distribution with a mean as μ' and standard deviation as σ , N is the size of the data sample. The $\hat{\mu}$ and σ can be estimated by using the covariance matrix of the likelihood function parameters $(\mu, \vec{v}, \vec{\theta})$. The second term of Equation 6.16 can be neglected under the assumption of large sample size, in which case the inverse of the covariance matrix is written as

$$V_{ij}^{-1} = -E \left[\frac{\partial^2 \ln L}{\partial \theta_i \partial \theta_j} \right]. \quad (6.17)$$

σ and $\hat{\mu}$ can be obtained by the covariance matrix.

6.8.2 Setup

All CRs and SRs are fitted simultaneously with the discriminators for each region as summarized in Table 6.20. In the VCRs, m_{jj}^{tag} are used in order to constrain the m_{jj}^{tag} reweighting systematic uncertainty which makes the largest impact on this analysis. Since the $t\bar{t}$ MC simulations describe the observed data well in the regions of this analysis, the TopCR is not binned by any variables to avoid complexity. The binnings of the discriminators are optimized to maximize significance with a constraint on those statistical uncertainties not to exceed 5% without consideration of systematic uncertainties.

All systematic uncertainties explained in Section 6.7 are included in the likelihood fit as nuisance parameters $(\vec{\theta})$. Summaries of normalization factors and shape systematic uncertainties are shown in Appendix D. The normalization factors for each background component are divided into two by resolved and merged so as to absorb different degrees of cross-section discrepancies between expectations and the observed data in the V_{had} momentum.

Table 6.20: The distributions used in the likelihood fit for the signal regions and control regions for all the categories in each channel. “One bin” denotes that a single bin without any shape information is used in the corresponding fit region.

Region		Discriminant		
		Merged high-purity	Merged low-purity	Resolved
0-lepton	SR	BDT	BDT	BDT
	VjjCR	m_{jj}^{tag}	m_{jj}^{tag}	m_{jj}^{tag}
1-lepton	SR	BDT	BDT	BDT
	WCR	m_{jj}^{tag}	m_{jj}^{tag}	m_{jj}^{tag}
	TopCR	One bin	One bin	One bin
2-lepton	SR	BDT	BDT	BDT
	ZCR	m_{jj}^{tag}	m_{jj}^{tag}	m_{jj}^{tag}

6.9 Results

This section describes the results of the likelihood fit introduced in the previous section. The validity of the fit is confirmed by several aspects; the expected event yields are compared with the observed ones in Section 6.9.1; m_{jj}^{tag} distributions after the fit discussed in Section 6.9.2; BDT output distributions after the fit discussed in Section 6.9.3; BDT input distributions after the fit discussed in Section 6.9.4; nuisance parameter pulls, constraints, and correlations in Section 6.9.5; and impacts of nuisance parameters on the signal-strength in Section 6.9.6. At the end of the chapter, the extracted signal-strength and fiducial cross-sections are disclosed in Section 6.9.7.

6.9.1 Event Yields

The numbers of observed and estimated events in the SRs are summarized in Table 6.21. The most significant backgrounds are the W/Z +jets, W +jets, and Z +jets processes for the 0-, 1-, 2-lepton channels, respectively. The $t\bar{t}$ process is the second dominant background among leptonic channels. The contributions from the diboson and single top productions are minor.

The numbers of observed and estimated events in the SRs and CRs are illustrated in Figure 6.21. All the observed event yields in each region are compatible with the SM expectations. In most of the regions, overall normalization factors for each background component are lower than unity. From a summary of normalization factors after the fit as shown in Table 6.22, this tendency is turned out to be originated from the V +jets and $t\bar{t}$ processes. For the V +jets normalization factor, it is known that the predicted V +jets cross-sections are overestimated in the high m_{jj}^{tag} and/or merged regions, the same observation is reported in other analyses, for example in Reference [168]. The lower normalization factors for the $t\bar{t}$ process are also expected by the same reason to the V +jets process¹⁰⁾.

¹⁰⁾There is no clear reason for that, however, it might be accounted for the higher order QCD corrections or the difficulty of the forward jet modelings.

6.9. RESULTS

Table 6.21: Numbers of observed and predicted events for the signal and background processes in the each 0-, 1-, 2-lepton signal region, obtained from signal-fits to the signal and control regions. The signal yields are calculated after the fit with the observed signal-strength of 1.05 applied. The uncertainties combine statistical and systematic contributions. Backgrounds that have negligible contributions are ignored in this table. The – in 1-lepton channel represents no multijet estimation is considered in the region. The fit constrains the background estimate towards the observed data, which reduces the total background uncertainty by correlating those uncertainties from the individual backgrounds.

Channel	Sample	Resolved	Merged HP	Merged LP	
0-lepton	Background	W + jets	9200 ± 1300	259 ± 27	582 ± 56
		Z + jets	$19\,000 \pm 1400$	383 ± 29	955 ± 69
		Top quarks	3280 ± 480	277 ± 28	276 ± 32
		Diboson	720 ± 120	69 ± 12	68 ± 14
		Total	$32\,100 \pm 2000$	988 ± 50	1881 ± 96
	Signal	$W(\ell\nu)W(qq')$	56 ± 22	8.0 ± 3.2	5.4 ± 2.2
		$W(\ell\nu)Z(qq)$	12.0 ± 4.7	2.1 ± 0.8	1.6 ± 0.6
		$Z(\nu\nu)W(qq')$	66 ± 25	9.0 ± 3.5	7.4 ± 2.9
		$Z(\nu\nu)Z(qq)$	27 ± 10	5.1 ± 2.0	3.1 ± 1.2
		Total	161 ± 35	24.3 ± 5.2	17.5 ± 3.9
	SM	$32\,300 \pm 2000$	1012 ± 50	1898 ± 96	
	Data	32 299	1002	1935	
	Channel	Sample	Resolved	Merged HP	Merged LP
	1-lepton	Background	W + jets	$69\,100 \pm 1900$	1201 ± 65
Z + jets			2770 ± 370	39 ± 3	83 ± 6
Top quarks			7100 ± 1100	394 ± 56	422 ± 63
Diboson			2660 ± 600	163 ± 35	229 ± 57
Multijet			$13\,400 \pm 1600$	–	–
Total		$95\,100 \pm 2800$	1797 ± 93	3560 ± 130	
Signal		$W(\ell\nu)W(qq')$	330 ± 120	45 ± 17	34 ± 13
		$W(\ell\nu)Z(qq)$	78 ± 29	11 ± 4	5 ± 2
		Total	410 ± 130	57 ± 18	39 ± 13
SM		$95\,500 \pm 2800$	1854 ± 95	3600 ± 130	
Data	95 366	1864	3571		
Channel	Sample	Resolved	Merged HP	Merged LP	
2-lepton	Background	Z + jets	$37\,090 \pm 310$	331 ± 14	775 ± 24
		Top quarks	645 ± 99	5.8 ± 0.9	9.9 ± 2.7
		Diboson	830 ± 170	34.6 ± 7.6	36.7 ± 8.2
		Total	$38\,570 \pm 370$	371 ± 16	821 ± 25
	Signal	$Z(\ell\ell)W(qq')$	138 ± 53	8.6 ± 3.3	7.0 ± 2.7
		$Z(\ell\ell)Z(qq)$	46 ± 18	4.3 ± 1.7	2.9 ± 1.1
		Total	185 ± 56	12.9 ± 3.7	9.8 ± 2.9
	SM	$38\,760 \pm 370$	384 ± 17	831 ± 25	
	Data	38 734	371	810	

Table 6.22: A summary of normalization factors obtained from the fit to the observed data is shown.

Channel	resolved	merged
W+jets	0.93 ± 0.07	0.86 ± 0.06
Z+jets	0.93 ± 0.05	0.80 ± 0.04
$t\bar{t}$	0.67 ± 0.10	0.83 ± 0.01

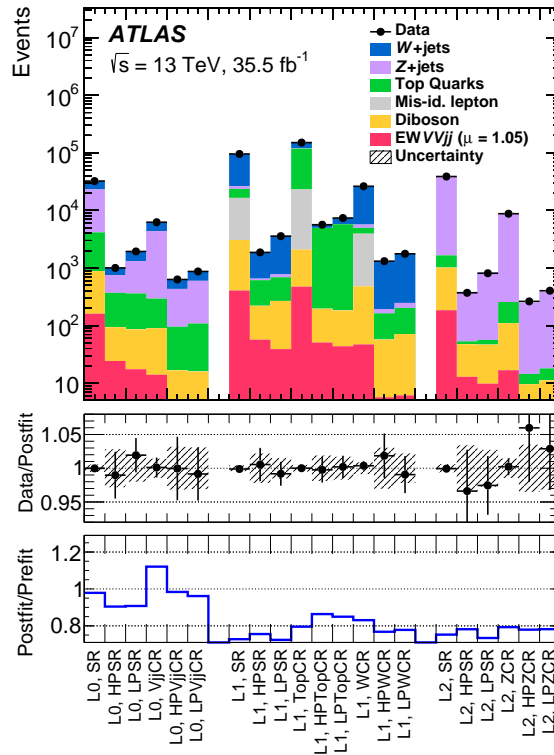


Fig. 6.21: Comparisons of the observed data and expected background event yields in each signal or control region. The labels L0, L1, and L2 stand for the 0-, 1- and, 2-lepton channels, respectively. The labels ‘HP SR’, ‘LP SR’, and ‘SR’ stand for the high-purity merged, low-purity merged and resolved signal regions, respectively. The middle pane shows the ratios of the observed data to the post-fit signal and background predictions. The bottom pane shows the ratios of the post-fit and pre-fit background predictions.

6.9.2 m_{jj}^{tag} Distributions at CR after Fitting

The scale and systematic uncertainties associated with the dominant background, the $V+$ jets process are corrected and constrained at $V_{jj}CR$, WCR , and ZCR for 0-, 1-, and 2-lepton channels. Figures 6.22, 6.23, and 6.24 show the m_{jj}^{tag} distributions after the fit. All the predicted distributions nicely agree with the observed data, which represent that the $V+$ jets backgrounds are well controlled by the fit.

6.9.3 BDT Output Distributions at SR after Fitting

The most important distribution to extract the signal-strength is the BDT output at the SR because the observed signal-strength is the most directly correlated to those plots. In order to guarantee the observed signal-strength obtained by the likelihood fit, the observed distributions of the BDT outputs in SRs used in the likelihood fit are compared with the predictions as shown in Figures 6.25, 6.26, and 6.27 for the 0-, 1-, and the 2-lepton channels, respectively. The observed data distributions are well reproduced by the predicted contributions from bins of low BDT output dominated background events to bins of high BDT output dominated signal events. There are minor undershooting and overshooting in the last bin of the BDT distribution for the merged HP signal region in the 1-lepton channel and several last bins of the BDT distribution for the merged HP signal region in the 2-lepton channel, respectively. Those tendencies are within statistical fluctuations and are reflected on the observed values of the signal-strength discrepancy between three leptonic channels as shown in Section 6.9.7. The ratios of the post-fit and pre-fit background predictions are generally flat, which implies that the nominal BDT shapes are compatible with the observed data.

6.9.4 BDT Input Distributions at SR after Fitting

The likelihood fit was performed with BDT distributions at SRs and prediction, and the observed data are compatible with predictions as shown in Section 6.9.3. However, it is possible that upper and lower deviations for two different BDT input distributions after the likelihood fit are canceled in the BDT output distributions. In this case, scales of background components might be misaligned and, consequently, the observed signal-strength might be wrong. In order to check the modeling of BDT input distributions after the likelihood fit, BDT input distributions for the predictions after the likelihood fit are compared to the observed data. Figures 6.28, 6.29, and 6.30 show selected plots in signal regions of BDT inputs that are most discriminating for each 0-, 1-, and 2-lepton channel. All other input distributions are shown in Appendix B. Overall, predictions are fairly compatible with the observed data. The total uncertainty shown as black shaded bands are much reduced by the fit, in particular, the total uncertainties in the distributions of m_{jj}^{tag} variable are at most less than 10%, whereas those are 50% before the fit. A slight overshooting and undershooting of expectations are observed for the m_{VVjj} variable in the 1-lepton channel and p_T^{j2} in the 2-lepton channel, respectively. Those tendencies are within statistical fluctuations and are reflected on those BDT outputs.

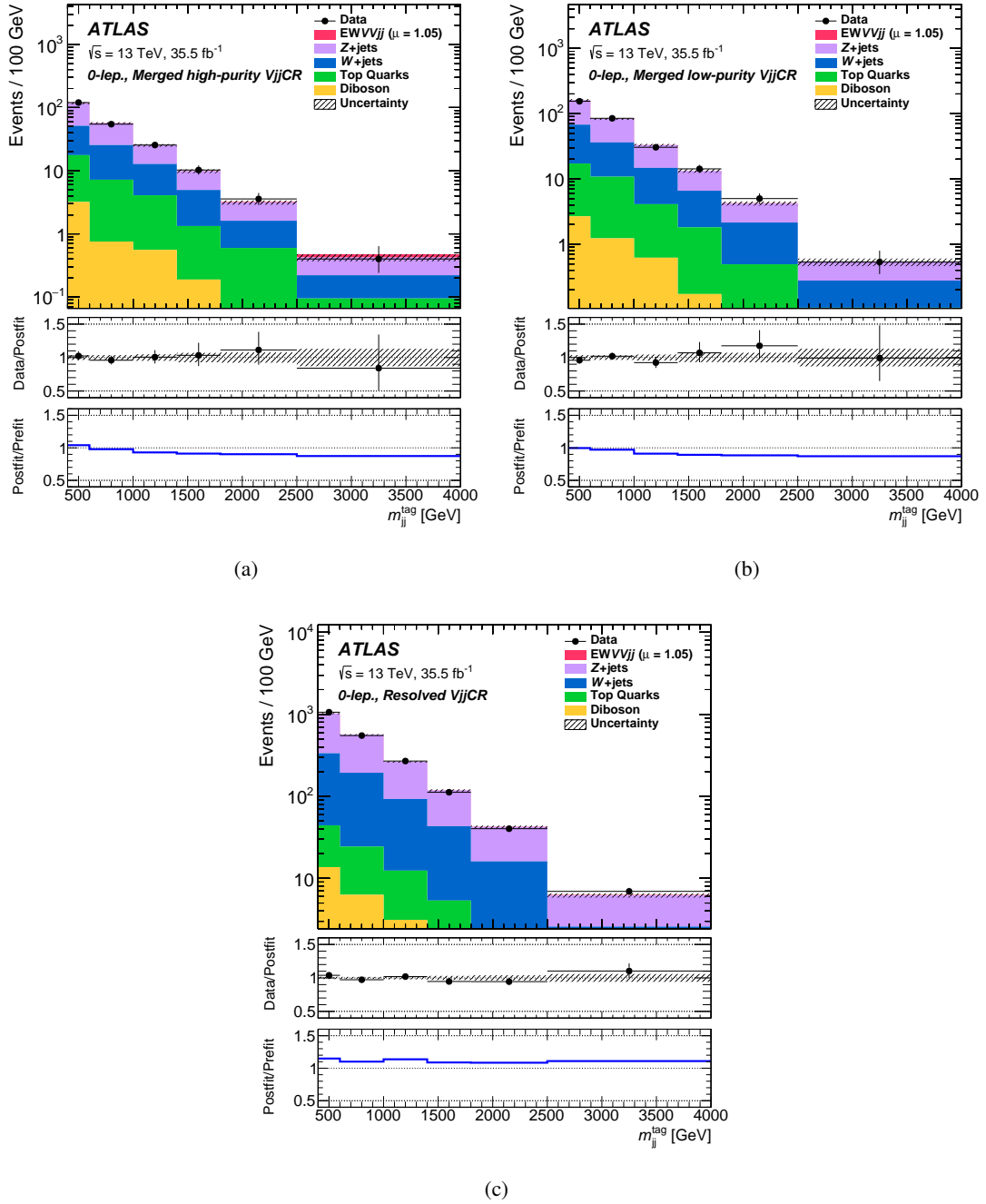


Fig. 6.22: Comparisons of the observed data and expected background distributions of m_{jj}^{tag} of the side-band control regions in the 0-lepton channel: (a) high-purity and (b) low-purity merged signal regions; (c) the resolved signal region. The background contributions after the global likelihood fit are shown as filled histograms. The signal is shown as a filled histogram on top of the fitted backgrounds normalized to the signal yield extracted from the observed data ($\mu = 1.05$), but it is not visible due to its small contribution. The middle pane shows the ratios of the observed data to the post-fit signal and background predictions. The uncertainty in the total prediction, shown as bands, combines statistical and systematic contributions. The bottom pane shows the ratios of the post-fit and pre-fit background predictions.

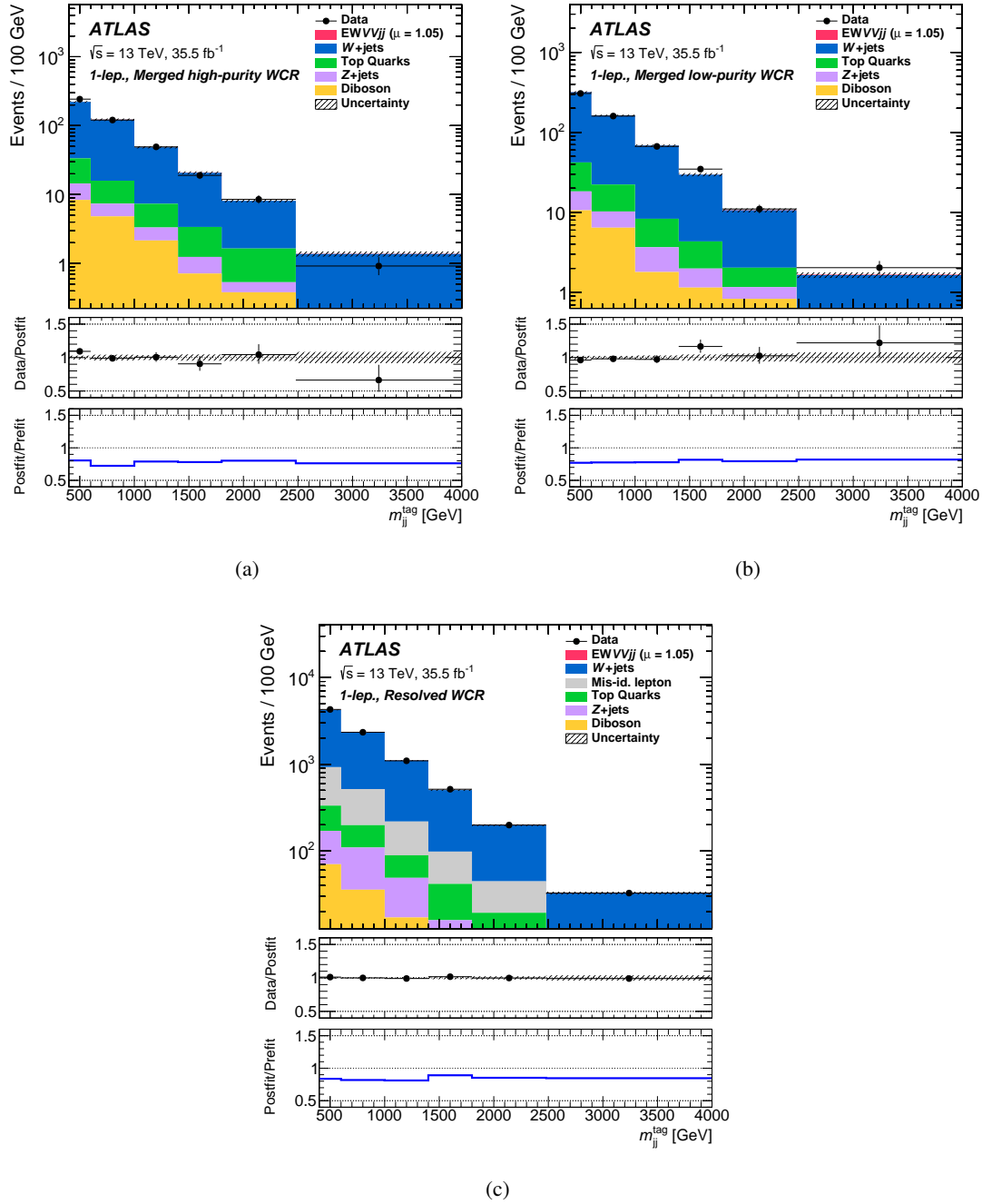


Fig. 6.23: Comparisons of the observed data and expected background distributions of m_{jj}^{tag} of the $W+$ jets control regions in the 1-lepton channel: (a) high-purity and (b) low-purity merged signal regions; (c) the resolved signal region. The background contributions after the global likelihood fit are shown as filled histograms. The signal is shown as a filled histogram on top of the fitted backgrounds normalized to the signal yield extracted from the observed data ($\mu = 1.05$), but it is not visible due to its small contribution. The middle pane shows the ratios of the observed data to the post-fit signal and background predictions. The uncertainty in the total prediction, shown as bands, combines statistical and systematic contributions. The bottom pane shows the ratios of the post-fit and pre-fit background predictions.

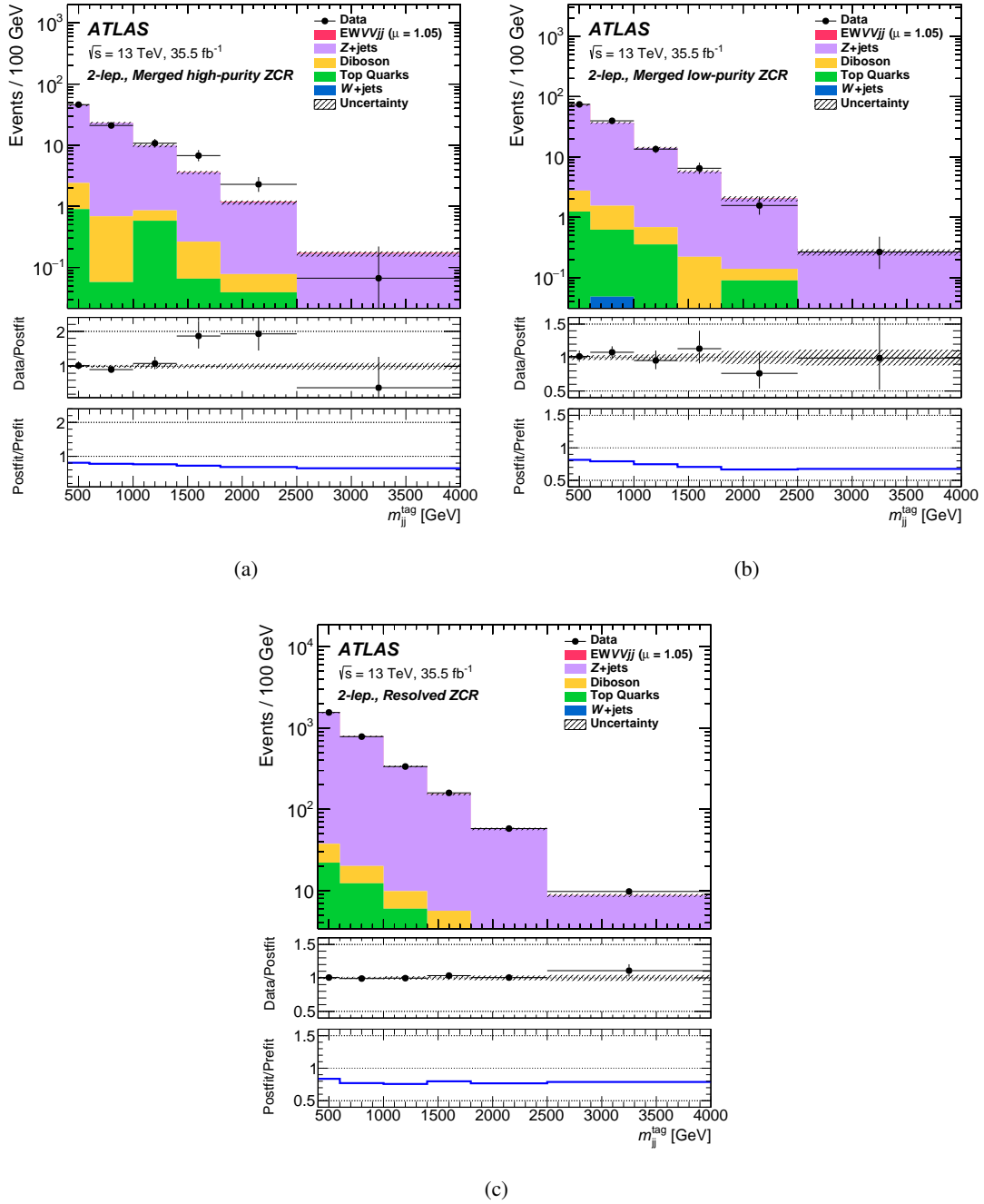


Fig. 6.24: Comparisons of the observed data and expected background distributions of m_{jj}^{tag} of the Z + jets control regions in the 2-lepton channel: (a) high-purity and (b) low-purity merged signal regions; (c) the resolved signal region. The background contributions after the global likelihood fit are shown as filled histograms. The signal is shown as a filled histogram on top of the fitted backgrounds normalized to the signal yield extracted from the observed data ($\mu = 1.05$), but it is not visible due to its small contribution. The middle pane shows the ratios of the observed data to the post-fit signal and background predictions. The uncertainty in the total prediction, shown as bands, combines statistical and systematic contributions. The bottom pane shows the ratios of the post-fit and pre-fit background predictions.

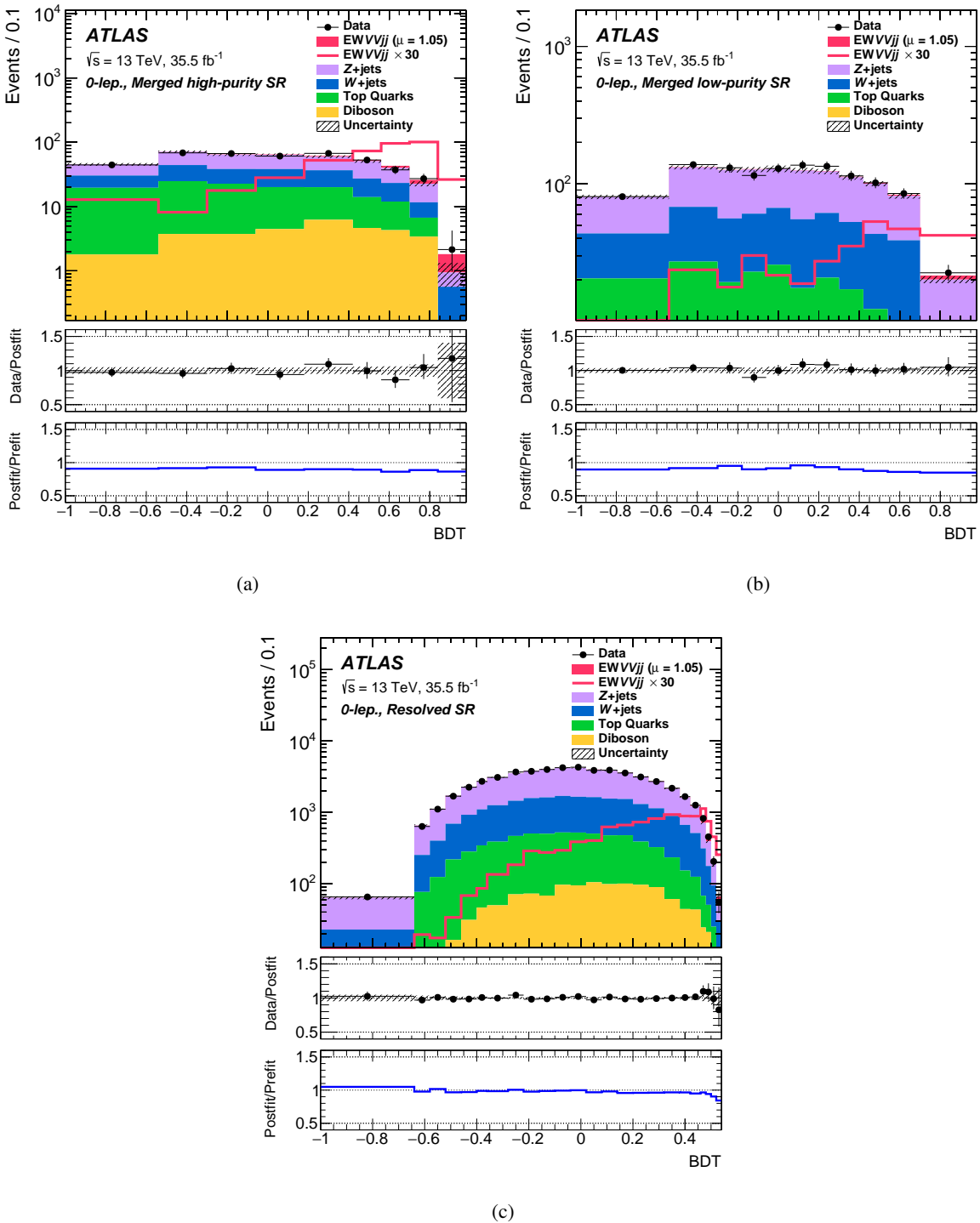


Fig. 6.25: Comparisons of the observed data and expected distributions of the BDT outputs of the 0-lepton channel signal regions: (a) high-purity and (b) low-purity merged signal regions; (c) the resolved signal region. The background contributions after the likelihood fit are shown as filled histograms. The signal is shown as a filled histogram on top of the fitted backgrounds normalized to the signal yield extracted from the observed data ($\mu = 1.05$), and unstacked as an unfilled histogram, scaled by the factor of 30. The entries in overflow are included in the last bin. The middle pane shows the ratios of the observed data to the post-fit signal and background predictions. The uncertainty in the total prediction, shown as bands, combines statistical and systematic contributions. The bottom pane shows the ratios of the post-fit and pre-fit background predictions.

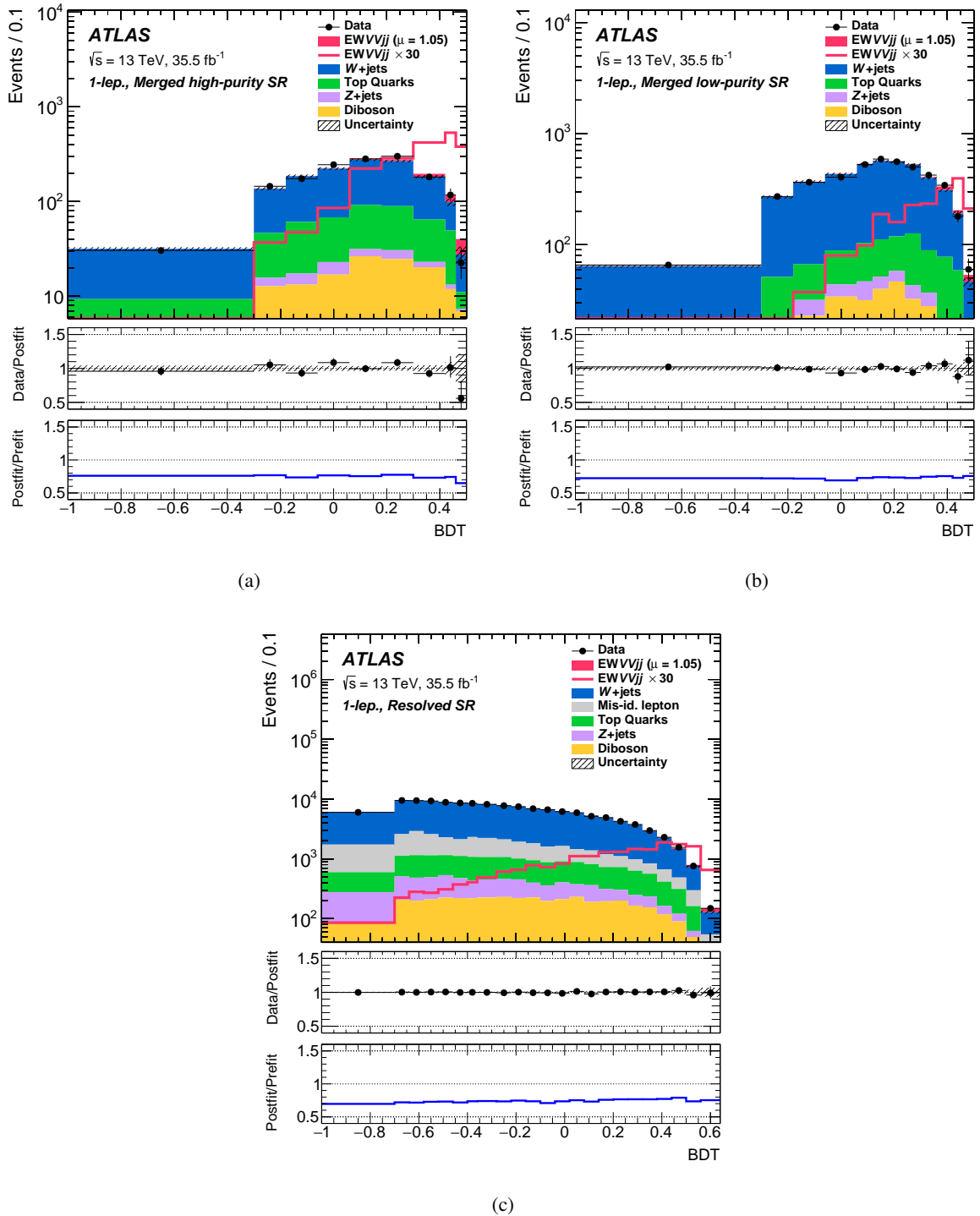


Fig. 6.26: Comparisons of the observed data and expected distributions of the BDT outputs of the 1-lepton channel signal regions: (a) high-purity and (b) low-purity merged signal regions; (c) the resolved signal region. The background contributions after the likelihood fit are shown as filled histograms. The signal is shown as a filled histogram on top of the fitted backgrounds normalized to the signal yield extracted from the observed data ($\mu = 1.05$), and unstacked as an unfilled histogram, scaled by the factor of 30. The entries in overflow are included in the last bin. The middle pane shows the ratios of the observed data to the post-fit signal and background predictions. The uncertainty in the total prediction, shown as bands, combines statistical and systematic contributions. The bottom pane shows the ratios of the post-fit and pre-fit background predictions.

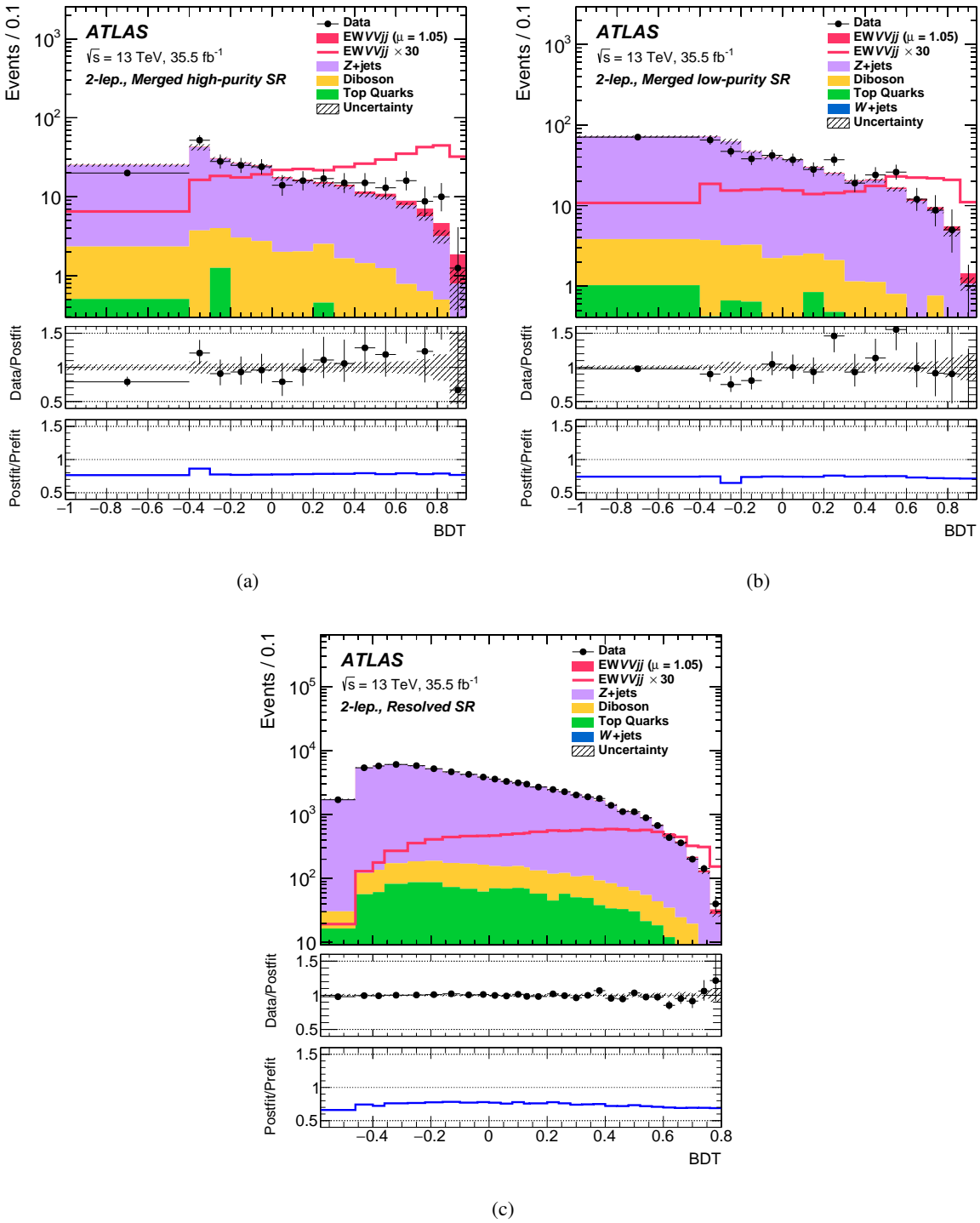


Fig. 6.27: Comparisons of the observed data and expected distributions of the BDT outputs of the 2-lepton channel signal regions: (a) high-purity and (b) low-purity merged signal regions; (c) the resolved signal region. The background contributions after the likelihood fit are shown as filled histograms. The signal is shown as a filled histogram on top of the fitted backgrounds normalized to the signal yield extracted from the observed data ($\mu = 1.05$), and unstacked as an unfilled histogram, scaled by the factor of 30. The entries in overflow are included in the last bin. The middle pane shows the ratios of the observed data to the post-fit signal and background predictions. The uncertainty in the total prediction, shown as bands, combines statistical and systematic contributions. The bottom pane shows the ratios of the post-fit and pre-fit background predictions.

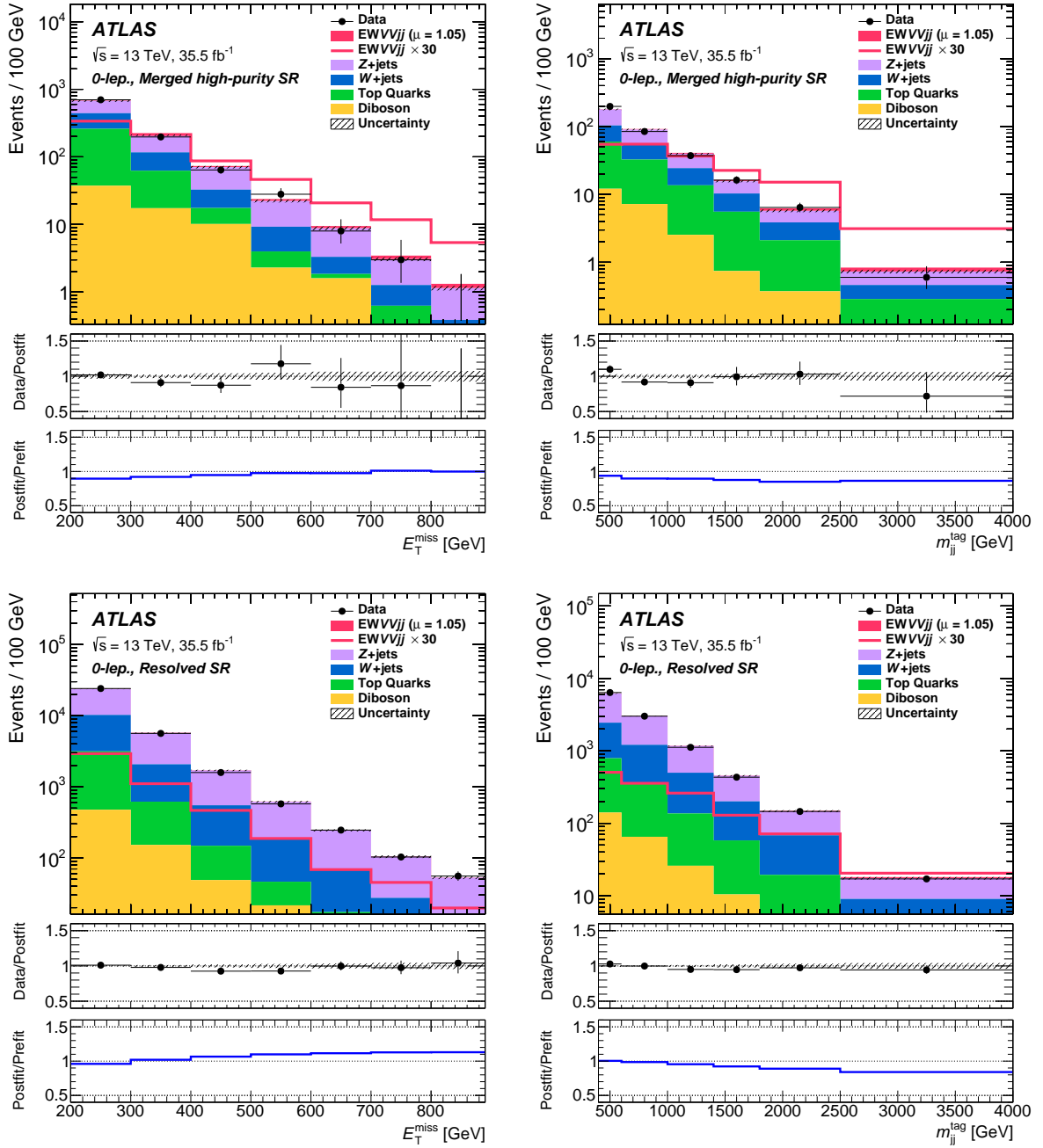


Fig. 6.28: The distributions for E_T^{miss} (left), m_{jj}^{tag} (right), in the 0-lepton merged HP (top) and 0-lepton resolved (bottom) signal regions. The background contributions after the likelihood fit are shown as filled histograms. The signal is shown as a filled histogram on top of the fitted backgrounds normalized to the signal yield extracted from the observed data ($\mu = 1.05$), and unstacked as an unfilled histogram, scaled by the factor of 30. The size of the combined statistical and systematic uncertainty for the sum of the fitted signal and background is indicated by the hatched band. The middle pane shows the ratios of the observed data to the post-fit signal and background predictions. The bottom pane shows the ratios of the post-fit and pre-fit background predictions.

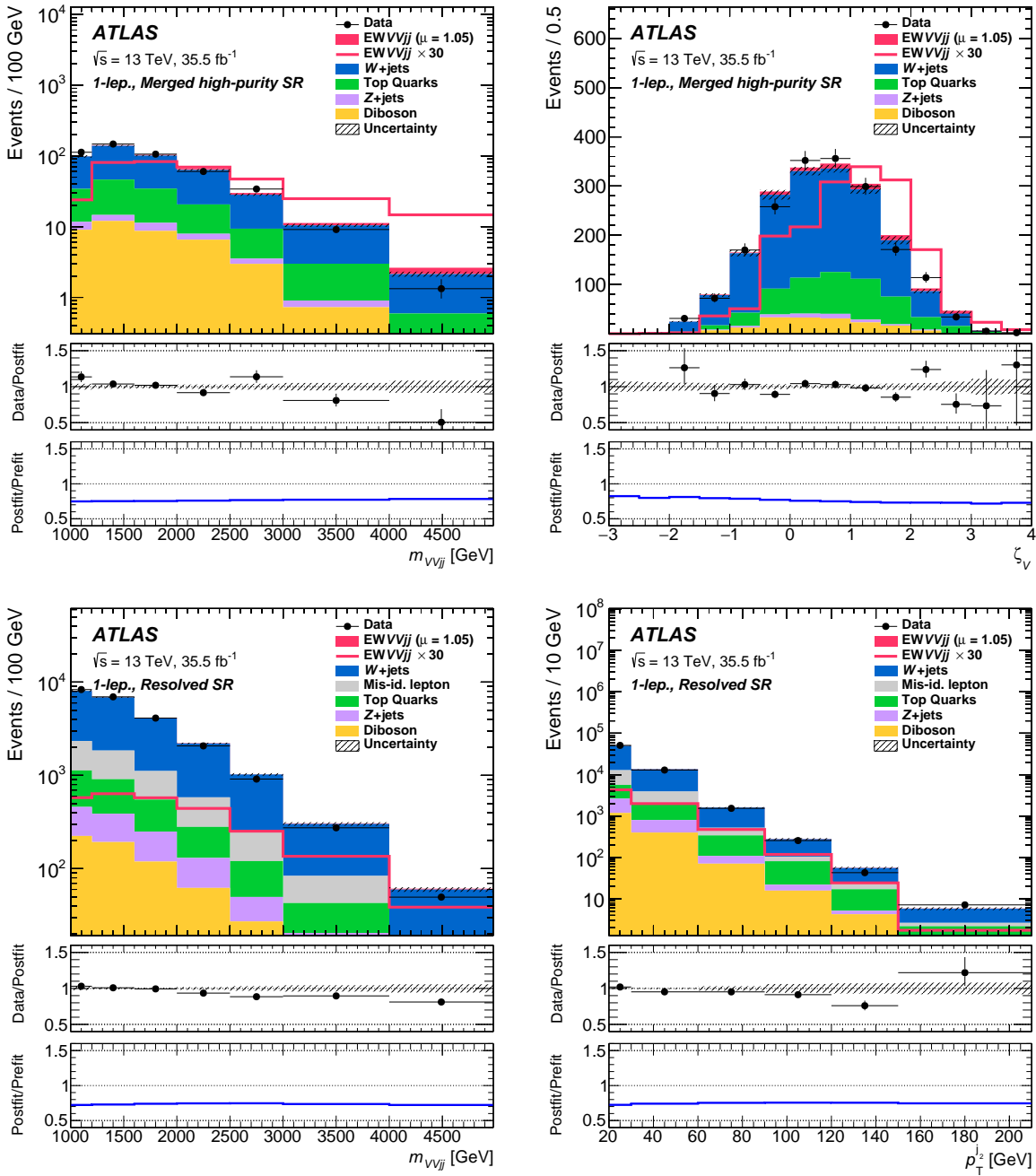


Fig. 6.29: The distributions for $m_{\nu\nu_{jj}}$ (left), ζ_V (top right), and p_T^{j2} (bottom right), in the 1-lepton merged HP (top) and 1-lepton resolved (bottom) signal regions. The background contributions after the likelihood fit are shown as filled histograms. The signal is shown as a filled histogram on top of the fitted backgrounds normalized to the signal yield extracted from the observed data ($\mu = 1.05$), and unstaked as an unfilled histogram, scaled by the factor of 30. The size of the combined statistical and systematic uncertainty for the sum of the fitted signal and background is indicated by the hatched band. The middle pane shows the ratios of the observed data to the post-fit signal and background predictions. The bottom pane shows the ratios of the post-fit and pre-fit background predictions.

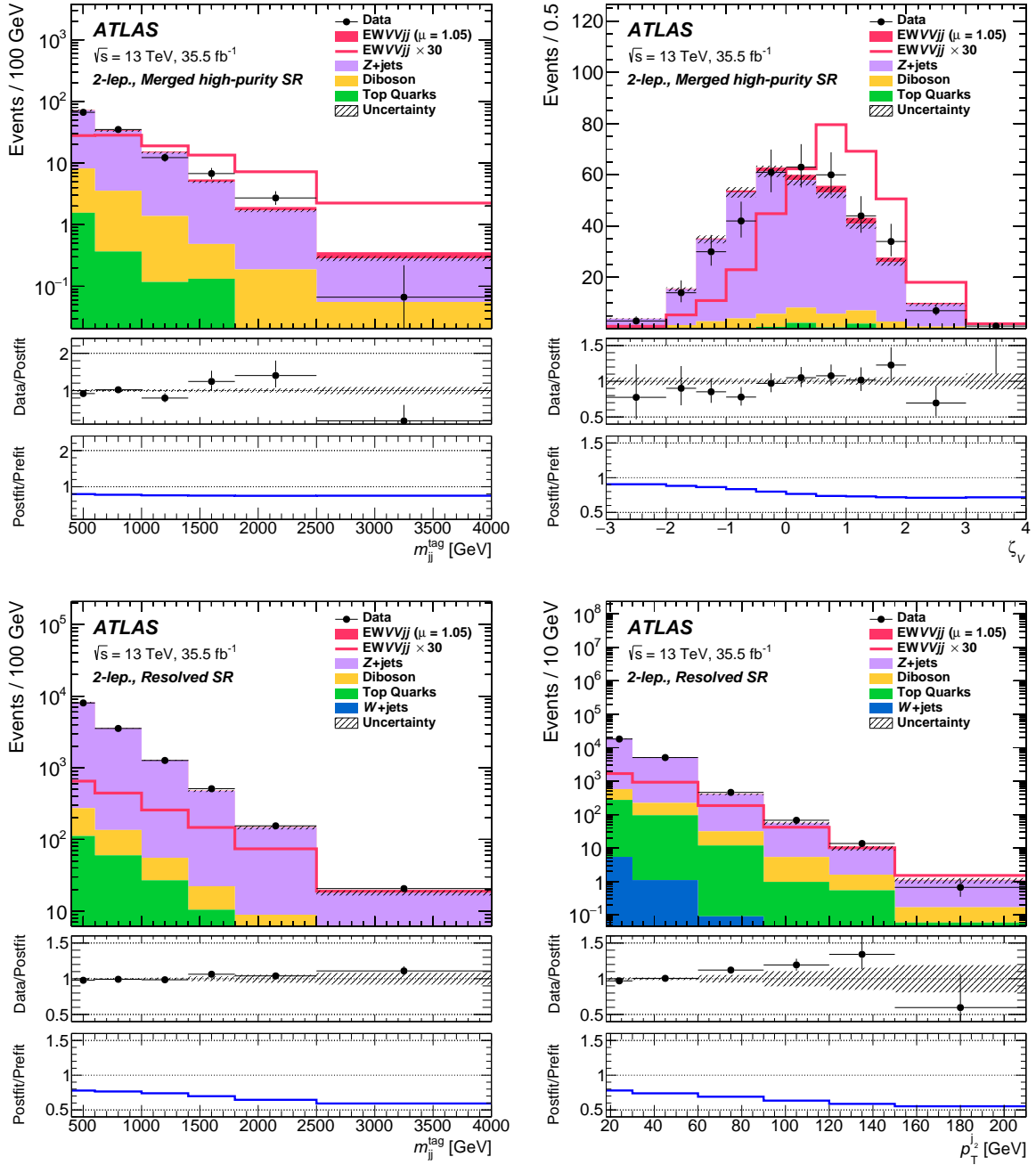


Fig. 6.30: The distributions for m_{jj}^{tag} (top left), ζ_V (top right), and p_T^{j2} (bottom right), in the 2-lepton merged HP (top) and 2-lepton resolved (bottom) signal regions. The background contributions after the likelihood fit are shown as filled histograms. The signal is shown as a filled histogram on top of the fitted backgrounds normalized to the signal yield extracted from the observed data ($\mu = 1.05$), and unstacked as an unfilled histogram, scaled by the factor of 30. The size of the combined statistical and systematic uncertainty for the sum of the fitted signal and background is indicated by the hatched band. The middle pane shows the ratios of the observed data to the post-fit signal and background predictions. The bottom pane shows the ratios of the post-fit and pre-fit background predictions.

6.9.5 Nuisance Parameter Pulls, Constraints, and Correlations

Although the BDT output and input distributions are compatible with the observed data as shown in Sections 6.9.3 and 6.9.4, observed signal-strength might be wrong because of unreasonable nuisance parameter *pulls* and *constraints*. The pulls defined as $(\hat{\theta} - \theta)/\Delta\theta$, where $\Delta\theta$ represents the magnitude of prior uncertainty, and θ and $\hat{\theta}$ denote pre- and post-fit nuisance parameters, respectively. The constraints represent how much the prior uncertainties are constrained by the observed data by the fit. Figure 6.31 shows the pulls and constraints as black dots and error bars, respectively. If the prior nuisance parameters are perfectly given, pulls for systematic uncertainty (normalization factor) and constraints are zero (unity) and 1σ . Deviations from the zero (unity) of the pull for systematic uncertainty (normalization factor) represent that the expectation does not describe the observed data well. Since the prior uncertainties are evaluated in an inclusive phase-space in order to apply to arbitrary analyses, the uncertainty in particular phase-space can be smaller. This leads to smaller constraints than 1σ .

All of the pulls are within 1σ of the prior uncertainties except for `SysZjetNorm0LepMerged`, `SysZjetNorm0LepResolved`, and `SysMET_SoftTrk_ResoPara`. The first two ones are the normalization uncertainties for Z+jets in the 0-lepton channel to account for the phase-space difference between the 0-lepton and 2-lepton channels. The last one is the uncertainty associated with E_T^{miss} soft term evaluation. These three nuisance parameters have small impacts on the signal-strength as shown in Section 6.9.6, thus those do not twist the measurement of signal-strength at all. Another discrepancy is observed in the nuisance parameter of `SysVVNorm` which is the normalization uncertainty for the QCD induced diboson process. This nuisance parameter is pulled down by approximately 1σ by mainly the 2-lepton channel where the diboson process is the second largest one. This overestimating is consistently observed in one of the measurements of the VBS processes with $WZ \rightarrow l\nu ll$ channel using the same generator for the diboson process, thus this pull is most likely caused by mismodelings of the event generator.

Understandings of correlation between nuisance parameters are also important because unexpected correlations might be some clues to twisted fit results. A correlation matrix displayed correlations between nuisance parameters from the fit with the observed data are shown in Figure 6.32. No unexpected correlations are observed.

In summary, most of the nuisance parameters are not pulled nor constrained, and a few pulled and constrained nuisance parameters are well understood or not worrisome, and no unexpected correlations are observed, therefore, the likelihood fit performed in this analysis is thought to be surely valid.

6.9. RESULTS

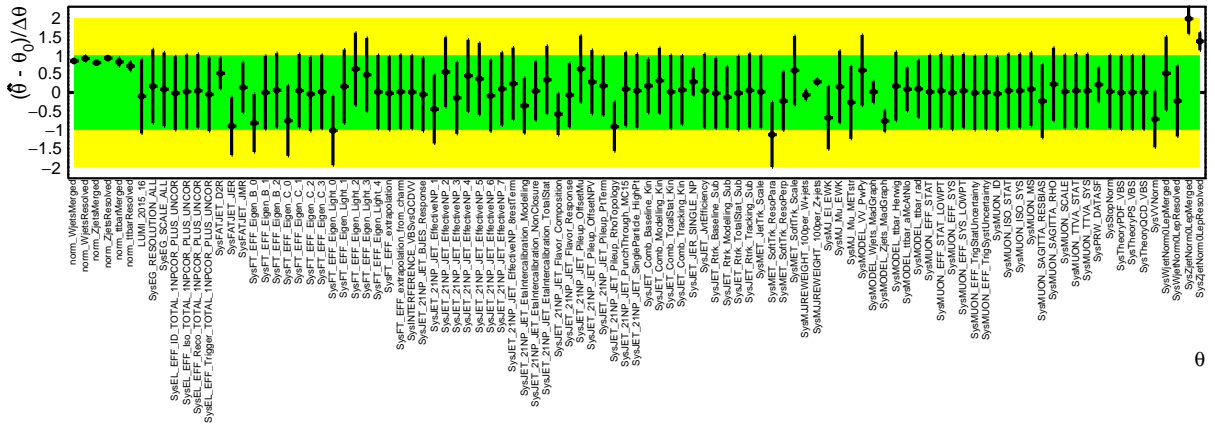


Fig. 6.31: Nuisance parameter pulls from the fit with the observed data are shown. Entries of normalization factors (begin with norm.) represent values of normalization factors and those errors as shown in Figure 6.22.

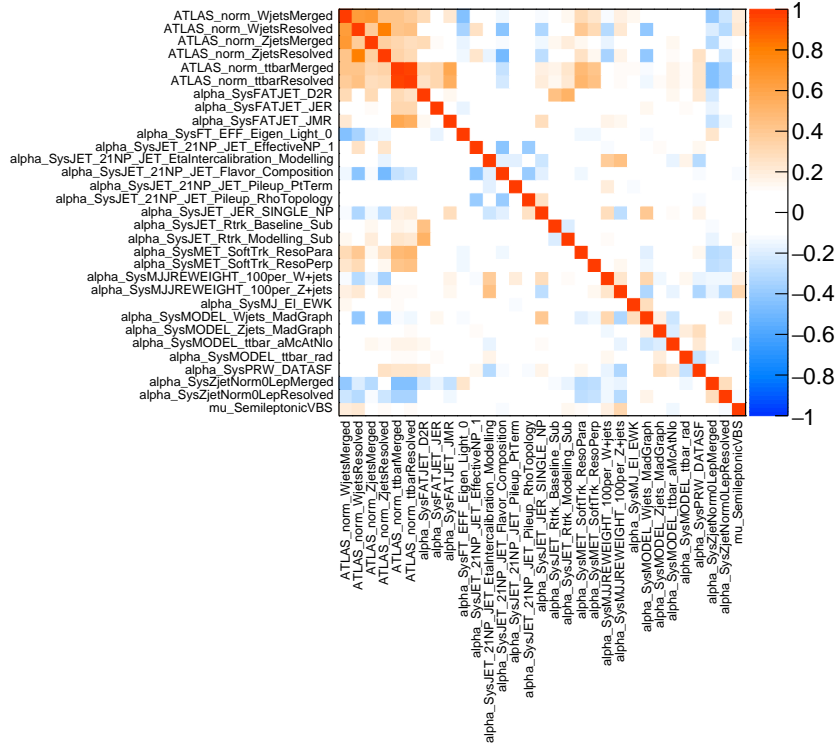


Fig. 6.32: A correlation matrix of nuisance parameters from the fit with the observed data is shown. Only nuisance parameters which are greater than 20% are shown.

6.9.6 Impacts of Nuisance Parameters

In order to understand where a limitation to the precision of the signal-strength measurement comes from, the impacts of systematic uncertainties on the measurement of the signal-strength after the fit are studied. The relative uncertainties in the post-fit signal-strength value from the leading sources of systematic uncertainty are shown in Figure 6.33. The systematic uncertainty having the largest impact is the m_{jj}^{tag} reweighting uncertainty for the Z +jets process by approximately 13%, and the second and third impact are the diboson background normalization and the m_{jj}^{tag} reweighting uncertainty for the W +jets process, respectively. The m_{jj}^{tag} reweighting uncertainties are expected to be highly ranked because of those very large prior uncertainties. Although those are highly ranked as both of them have impacts by more than 100% on the pre-fit signal-strength value before the fit, both of them are well constrained by m_{jj}^{tag} distributions of VCR. The m_{jj}^{tag} reweighting uncertainty for the Z +jets process is larger than that of the W +jets process because the Z +jets process has fewer statistics than the W +jets process. Uncertainties associated with the diboson process are also expected to be highly ranked because no dedicated CRs for it are defined, and its shape is similar to the one of the signal. A summary of the impacts grouped by similar ones is shown in Table 6.23. 1σ of the total uncertainty shifts signal-strength in approximately 40% and the one of the quadratic sum of systematic uncertainties shifts signal-strength by approximately 35%. This implies that the accuracy of this measurement is dominated by systematic uncertainties. As mentioned above, uncertainties related to the V +jets process (m_{jj}^{tag} reweighting uncertainties and statistical uncertainties) are dominant, and the subdominant uncertainties are uncertainties for diboson and large- R jets.

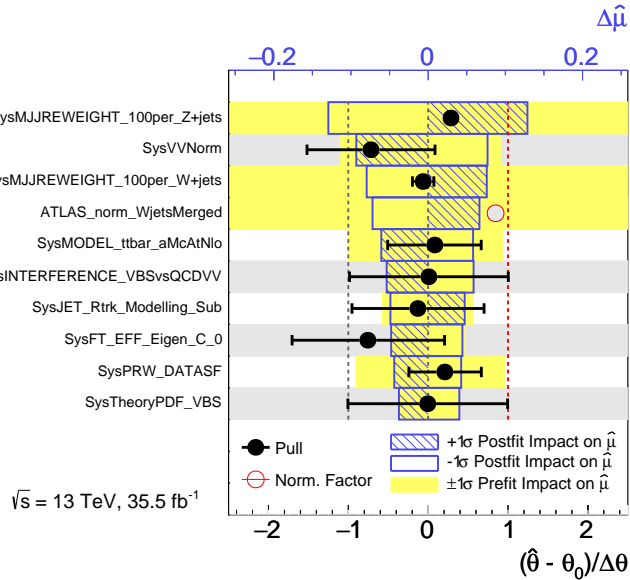


Fig. 6.33: Pre-fit (yellow) and post-fit (blue) nuisance parameter impacts on the signal-strengths are shown. The impacts are ranked by the order of $\Delta\hat{\mu} = \hat{\mu}_\chi - \hat{\mu}_0$, where $\hat{\mu}_0$ is a signal-strength obtained by the nominal fit, and $\hat{\mu}_\chi$ is a signal-strength obtained by a fit fixing the nuisance parameter X on plus or minus 1σ . The black and red dots denote pulls and normalization factors. The naming convention is summarized in Appendix D.

Table 6.23: The symmetrized impacts of uncertainty on post-fit signal-strength ($\Delta\hat{\mu}$). The floating normalizations include uncertainties in normalization scale factors for the Z+jets, W+jets, and top quark contributions.

Uncertainty source	$\Delta\hat{\mu}$
Total uncertainty	0.41
Statistical	0.20
Systematic	0.35
Theoretical and modeling uncertainties	
Floating normalizations	0.09
Z + jets	0.13
W+ jets	0.09
$t\bar{t}$	0.06
Diboson	0.09
Multijet	0.04
Signal	0.07
MC statistics	0.17
Experimental uncertainties	
Large-R jets	0.08
Small-R jets	0.06
Leptons	0.02
E_T^{miss}	0.04
b-tagging	0.07
Pileup	0.04
Luminosity	0.03

6.9.7 The Observed Signal-Strength and Fiducial Cross-Sections

Since no incomprehensible features are found in the detailed inspections of the likelihood fit as described in the previous sections, the observed signal-strength is reported as follows. The observed signal-strength of the semileptonic VBS signals is obtained as

$$\mu_{EWVVjj}^{\text{obs}} = 1.05_{-0.40}^{+0.42} = 1.05 \pm 0.20(\text{stat.})_{-0.34}^{+0.37}(\text{syst.}),$$

where stat and syst represent the statistical and the sum of systematic uncertainties, respectively. The background-only hypothesis is excluded in the observed data with a significance of 2.7 standard deviations compared with 2.5 standard deviations expected. Since 1σ of the total uncertainty covers $\mu = (\sigma_{\text{obs.}}/\sigma_{\text{pred.}}) = 1$, this measurement is consistent with the SM, in other words, there is no BSM observed.

Figure 6.34 shows the measured signal-strength from the combined fit with a single signal-strength fit parameter, and from a fit where each lepton channel has its own signal-strength parameter. The signal-strength values for the 0- and 2-lepton channels are greater than equal ~ 2 , and the one for the 1-lepton channel is 0.33, hence the combined signal-strength among three channels is 1.05. The probability that the signal-strengths measured in the three lepton channels are compatible is 36%.

The $-2\ln(\Lambda)$ values scan for the signal-strength μ is illustrated in Figure 6.34. As shown in the figure, the predicted log-likelihood functions for statistical errors and for the total errors are consistent with the observed ones. The values at $\mu = 0$ represent significance against the null-hypothesis, which correspond to 2.7 and 2.5 standard deviations for the observed and expected measurements, respectively. Arbitrary upper limits can be calculated by the likelihood curves, for instance, the 2σ upper limit is approximately $\mu = 1.9$.

The fiducial cross-sections for the EWVVjj processes are measured in the merged and resolved fiducial phase-space regions described in Section 6.6 and inclusively. The merged HP SR and LP SR are combined to form one single merged fiducial phase-space region. The systematic uncertainties in the measured fiducial cross-sections include contributions from experimental systematic uncertainties, theory modeling uncertainties in the backgrounds, theory modeling uncertainties in the shapes of signal kinematic distributions, and luminosity uncertainties. The measured and the SM predicted fiducial cross-sections for the EWVVjj processes are summarized in Table 6.24, where the measured values are obtained from two different simultaneous fits. In the first fit, two signal-strength parameters are used, one for the merged category (both HP and LP), and the other one for the resolved category; whereas in the second fit, a single signal-strength parameter is used. The measured values are obtained from a simultaneous fit where each lepton channel has its own signal-strength parameter, and in each lepton channel, the same signal-strength parameter is applied to both the merged and resolved categories. The predictions are from the MADGRAPH5_aMC@NLO 2.4.3 event generator at the LO only, and no higher-order corrections are included; the theoretical uncertainties due to the PDF, missing higher-order corrections, and parton shower modeling are estimated as described in Section 6.7. The measured fiducial cross-sections are consistent with the SM predictions.

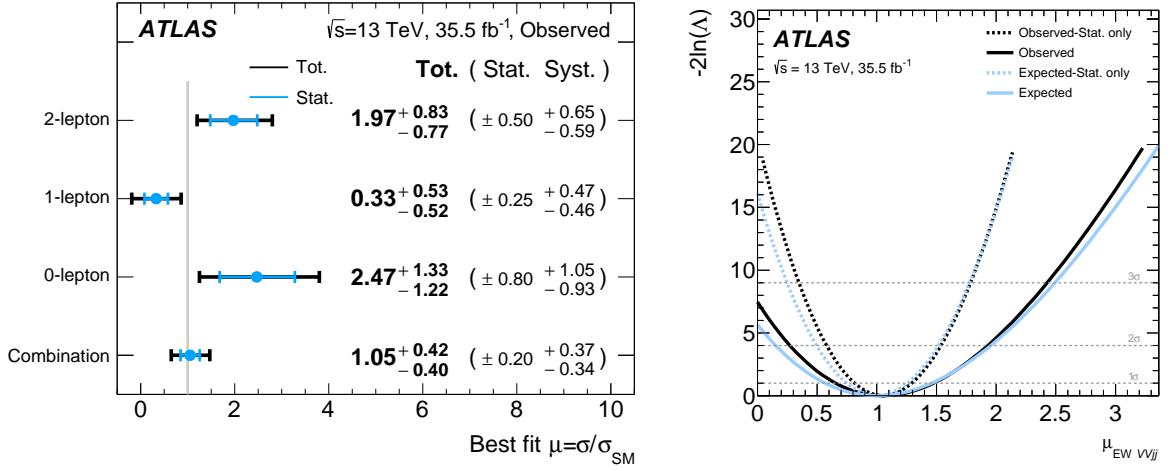


Fig. 6.34: The fitted values of the signal-strength parameter $\mu_{EW VVjj}^{obs}$ for the 0-, 1-, and 2-lepton channels and their combination (left) and scan of the negative log-likelihood, $-2 \ln \Lambda$, for the signal-strength of the EW $VVjj$ production (right) are shown. In the left plot, the individual $\mu_{EW VVjj}^{obs}$ values for the lepton channels are obtained from a simultaneous fit with the signal-strength parameter for each of the lepton channels floating independently. The probability that the signal-strengths measured in the three lepton channels are compatible is 36%. In the right plot, the solid upper black (lower blue) line represents the observed (expected) value including all systematic uncertainties, whereas the dashed upper black (lower blue) line is for the observed (expected) value without systematic uncertainties (lower and upper refer here to the position of the lines in the legend).

Table 6.24: Summary of predicted and measured fiducial cross-sections for EW $VVjj$ production. The three lepton channels are combined. For the measured fiducial cross-sections in the merged and resolved categories, two signal-strength parameters are used in the combined fit, one for the merged category and the other one for the resolved category; whereas for the measured fiducial cross-section in the inclusive fiducial phase-space, a single signal-strength parameter is used. For the SM predicted cross-section, the error is the theoretical uncertainty (theo.). For the measured cross-section, the first error is the statistical uncertainty (stat.), and the second error is the systematic uncertainty (syst.).

Fiducial phase-space	Predicted $\sigma_{EW VVjj}^{fid,SM}$ [fb]	Measured $\sigma_{EW VVjj}^{fid,obs}$ [fb]
Merged	11.4 ± 0.7 (theo.)	12.7 ± 3.8 (stat.) $^{+4.8}_{-4.2}$ (syst.)
Resolved	31.6 ± 1.8 (theo.)	26.5 ± 8.2 (stat.) $^{+17.4}_{-17.1}$ (syst.)
Inclusive	43.0 ± 2.4 (theo.)	45.1 ± 8.6 (stat.) $^{+15.9}_{-14.6}$ (syst.)

CHAPTER 7

Interpretation with Effective Field Theory

Since the measurement performed in the previous chapter is consistent with the SM prediction, the obtained results are interpreted to limits on coefficients of the EFT (effective field theory) operators. The theoretical backgrounds of the EFT have already been introduced in Section 2.3. Hereafter, technical implementation of the EFT interpretation of this study and its results are explained. Section 7.1 describes an overview of the interpretation, Section 7.2 introduces the statistical treatment to obtain the limits, and the obtained limits on coefficients of the EFT operators are summarized and compared to the latest published limits in Section 7.3.

7.1 Setup for EFT interpretation

A cross-section for aQGC is given by the integration of matrix element squared over the Lorentz-invariant phase-space of the Lagrangian shown in Equation 2.17:

$$\sigma_{\text{EFT}} = \sigma_{\text{SM}} + \left(\sum_i \left(\frac{f_i}{\Lambda^4} \right)^2 s_i^{\text{PureEFT}} \right) + \left(\sum_i \frac{f_i}{\Lambda^4} s_{i,\text{SM}}^{\text{INT}} \right) + \left(\sum_{i<j} \frac{f_i}{\Lambda^4} \frac{f_j}{\Lambda^4} s_{i,j}^{\text{INT}} \right), \quad (7.1)$$

where σ and s stand for cross-section and cross-section divided by f_x/Λ^4 or $(f_x/\Lambda^4)^2$, i and j denote operators listed in Equation 2.18 to 2.35. The first term represents the pure SM contribution. The second and third terms are referred to as quadratic term (*QUAD*) and interference term (*INT*), which are contributions from the pure EFT operator and an interference between the EFT and the SM operator, respectively. The last term denotes an interference between EFT operators. In this search, the last term is ignored for simplicity and for consistency to the previous results on aQGC searches [26–33, 169, 170].

As discussed in Section 6.2.3, the MC simulations are prepared for fixed coefficients of f_{S0}/Λ^4 , f_{M0}/Λ^4 , and f_{T0}/Λ^4 as shown in Table 6.6. The cross-sections for each sample are obtained by the MADGRAPH5_aMC@NLO v2.3.3 event generator as shown in Section 6.2.3. Samples with different coefficients are imitated by scaling the generated samples with respect to parabolic functions because Equation 7.1 denotes that σ_{EFT} is a parabolic function of the coefficients $(\frac{f_i}{\Lambda^4})$ after ignoring the last term. The cross-sections for each coefficient are evaluated by the MC simulations which are not applied to any detector simulation nor reconstruction procedures. The parabolic functions are obtained by fitting the cross-sections with respect to coefficients as shown in Figure 7.1.

The shapes (mainly discussing about m_{VV}) for the imitated samples are not stringently correct because scaling by coefficients $(\frac{f_i}{\Lambda^4})$ should be applied linearly for the INT term and quadratically for the pure

7.1. SETUP FOR EFT INTERPRETATION

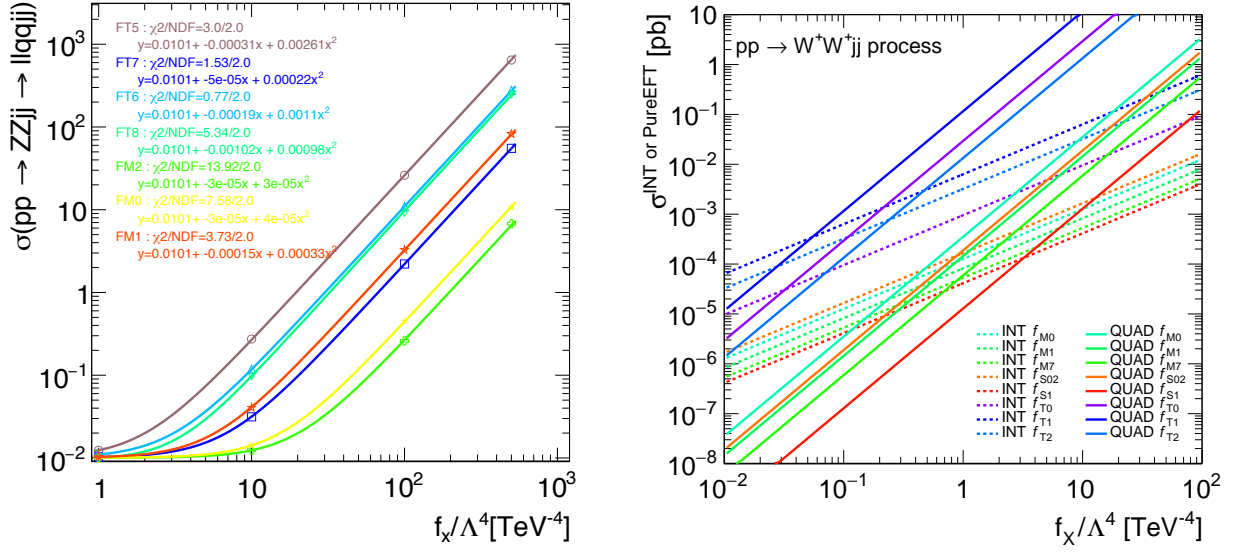


Fig. 7.1: Cross-sections as a function of couplings are shown in the left plot. Markers and liens stand for the calculated cross-sections and obtained parabolic functions, respectively. Cross-sections as a function of couplings for each INT (dashed line) and QUAD (solid line) component are shown in the right plot. Colors indicate sorts of operators.

EFT term by definition. However, coefficients expected to be limited by this analysis, $\mathcal{O}(1)$, $\mathcal{O}(1)$, and $\mathcal{O}(0.1)$ for L_S , L_M , and L_T , respectively, have the leading contributions by the QUAD terms as shown in Figure 7.1. Furthermore, the signal-to-noise ratio is drastically improved at high m_{VV} phase-space which is dominated by the QUAD term as shown in Figure 7.2. Therefore, the imitated samples are adequate approximations for the fully calculated aQGC samples.

From studies with simulation, operators having similar Lorentz structure, each L_S , L_M , or L_T , have very similar kinematical shapes as shown in Figure 7.3. Whereas apparent differences between L_S , L_M , and L_T operators are confirmed, which are the polarization states of weak bosons as shown in Figure 7.4. Hence, samples for L_{S1} are imitated by L_{S0} , samples for L_{M1} to L_{M7} are imitated by L_{M0} , and samples for L_{T1} to L_{T7} are imitated by L_{T0} .

7.1. SETUP FOR EFT INTERPRETATION

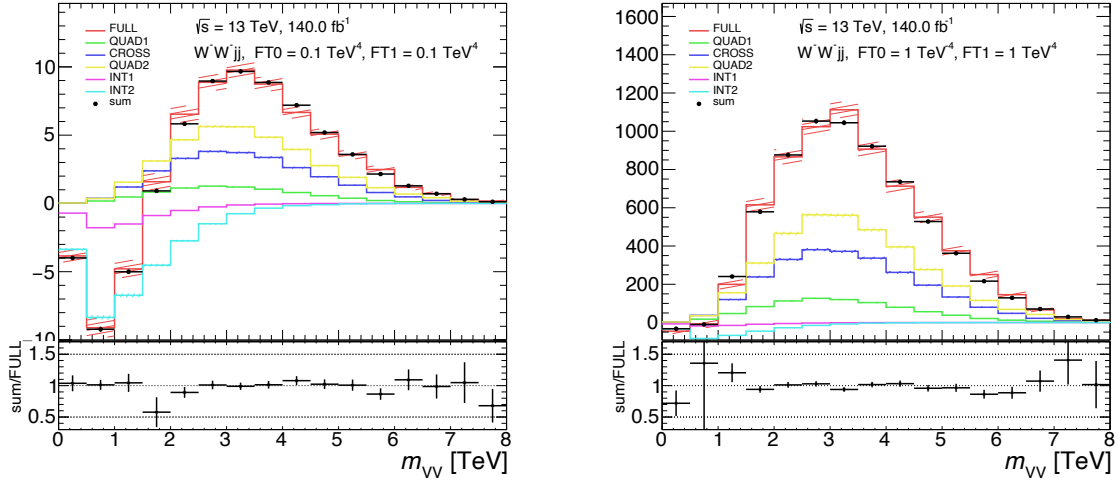


Fig. 7.2: m_{VV} distributions for L_{T0} quadratic term (QUAD1: green), L_{T1} quadratic term (QUAD2: yellow), L_{T0} interference term (INT1: magenta), L_{T1} interference term (INT2: cyan), those cross term (CROSS: blue), and simulating all of them at the same time (sum: black) with coefficient values of $f_{T0}/\Lambda^4 = 0.1 \text{ TeV}^{-4}$ and $f_{T1}/\Lambda^4 = 0.1 \text{ TeV}^{-4}$ (left) and coefficient values of $f_{T0}/\Lambda^4 = 1 \text{ TeV}^{-4}$ and $f_{T1}/\Lambda^4 = 1 \text{ TeV}^{-4}$ (right). To check whether the decomposition to five elements works well, generation with a full contribution (FULL: red) is compared to a sum of five elements (sum: black dot). the bottom plots show the ratios of the sum to FULL.

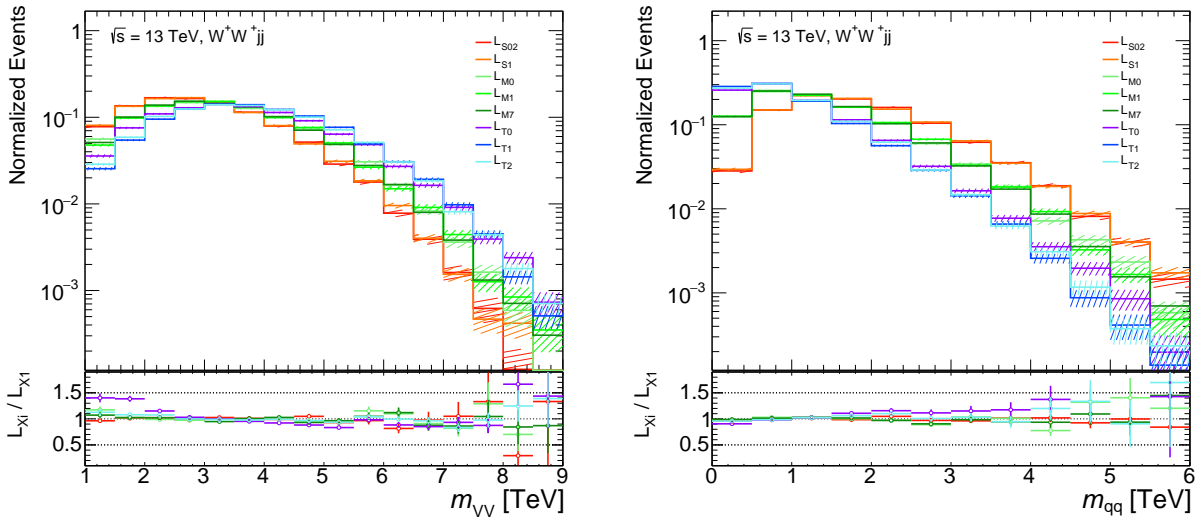


Fig. 7.3: Invariant masses of a diboson pair (left) and invariant mass of a spectator quark pair (right) shapes for different operators are shown. Red-ish, green-ish, and blue-ish colors represent $L_S, L_M,$ and L_T operators, respectively. Histograms only include events for QUAD terms.

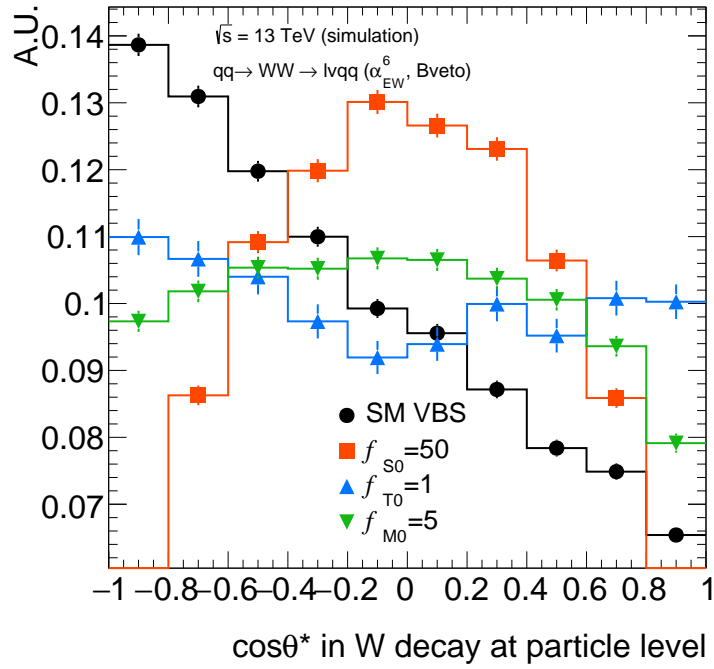


Fig. 7.4: Distributions for the angle between a decay product and original W momentum at the W rest frame ($\cos \theta^*$) for the $WW \rightarrow lvqq$ processes. The red, blue, and green lines show $f_{S0}/\Lambda^4 = 50 \text{ TeV}^{-4}$, $f_{T0}/\Lambda^4 = 1 \text{ TeV}^{-4}$, and $f_{M0}/\Lambda^4 = 5 \text{ TeV}^{-4}$, respectively. In principle, $\cos \theta^*$ for longitudinally polarized vector bosons follow $1 - \cos^2 \theta^*$, whereas $\cos \theta^*$ for transversely polarized vector bosons follow $(1 \pm \cos \theta^*)^2$, so this plot indicates that the L_{S0} operator tends to generate longitudinally polarized vector bosons, the L_{T0} operator tends to generate transversely polarized vector bosons (equal contributions from left- and right-hand polarization), and the L_{M0} is in between those.

7.2 Statistical Test

aQGC events populate at higher m_{VV} because the coefficient is constrained by the cut-off scale Λ as shown in Equation 7.1. EFT interpretations are performed by fitting on m_{VV} instead of the BDT discriminant used in the EWV ν jj measurement at the same signal regions except for the resolved signal region where no signals are expected. Figure 7.6 shows m_{VV} distributions used for the statistical tests.

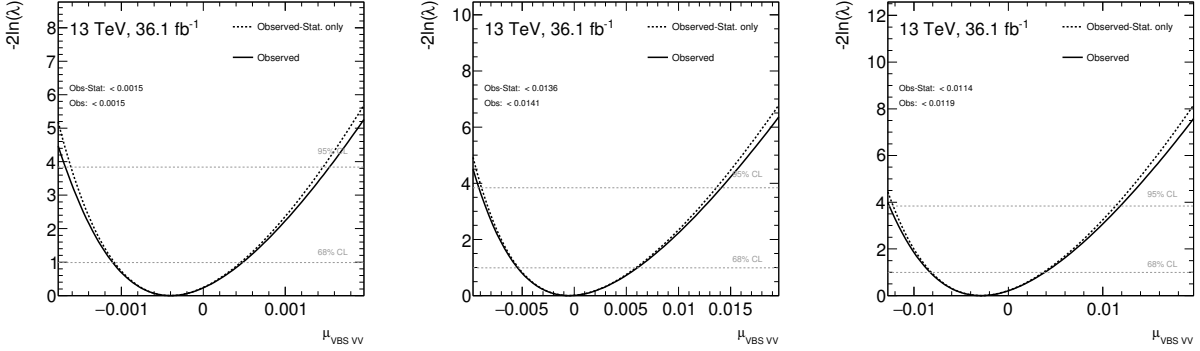


Fig. 7.5: Log-likelihood curves for L_{S0} (left), L_{M0} (center), and L_{T0} (right) are shown. The dashed curve only includes statistical uncertainty, the solid curve includes both the statistical and systematic uncertainties. Since no excess over the SM prediction is observed, curves have local minimum at $\mu_{VBS \nu\nu} \sim 0$ ($\mu_{VBS \nu\nu}$ stands for signal-strength for each operator). Horizontal dashed lines guide for the confidence limits based on the χ^2 distribution with two degrees of freedom.

Fits are performed for each three operator with the same strategy discussed in Section 6.7. The log-likelihood ($-2 \ln \lambda$) distributions with respect to aQGC strength μ for each signal are shown in Figure 7.5. From the plots, systematic uncertainties are known to be negligible. This is because the high tail of m_{VV} has quite large statistical uncertainty in the observed data due to fewer statistics. A μ value at crossing the 95% C.L line and the likelihood curve are used to calculate upper limits on the coefficients.

7.3 Limits on Coefficient of Operators

Limits are set with respect to 95% C.L. by comparing Figures 7.1 and 7.5, which are summarized in Figure 7.7 and Table 7.1. The obtained limits are better by the order of one than that of the full-leptonic analysis. The obtained limits are the most stringent to date¹⁾, i.e. these results clearly represent that the semileptonic final states has the best sensitivity to most of the BSM theories related to the VBS topology at present.

¹⁾The obtained limits on the coefficients are comparable to the ones from Reference [34].

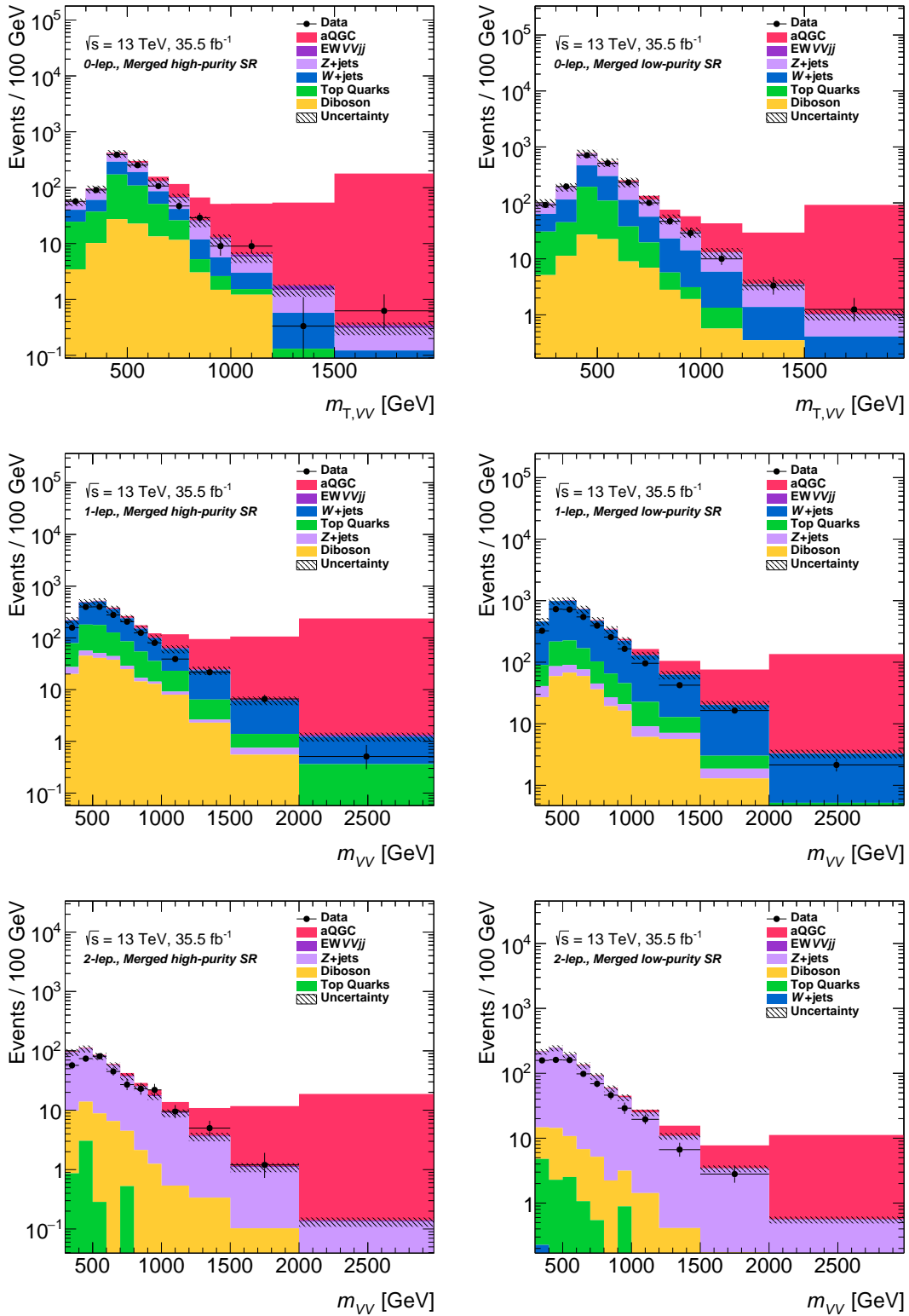


Fig. 7.6: m_{VV} distribution at boosted signal region for 0-lepton HP (top left), 0-lepton LP (top right), 1-lepton HP (middle left), 1-lepton LP (middle right), 2-lepton HP (bottom left), and 2-lepton LP (bottom right) before the fit. Since the normalization factors obtained by the fit are not applied, histograms for MC simulations have approximately 10-20% greater than the observed data. histograms for MC simulations match the observed data when the fit is performed to obtain limits.

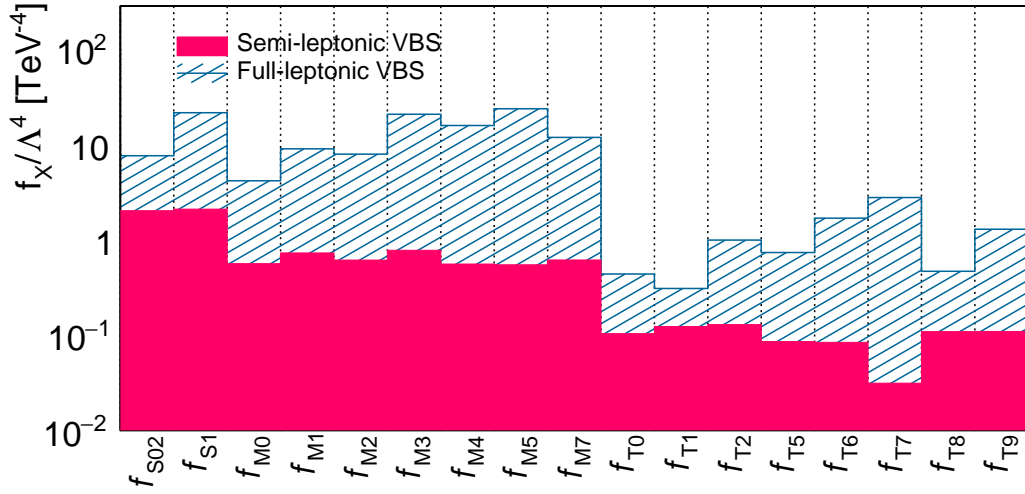


Fig. 7.7: 95% C.L. limits on the coefficient of EFT operators are summarized. The blue shaded histogram is the limits obtained by the full-leptonic VBS analyses [21, 24, 50, 51], the magenta filled histogram is the limits calculated by this study.

Table 7.1: Comparison between current best limits on the coefficient for dimension-8 EFT operators by leptonic searches and limits obtained from this study are shown.

Operator	Full-leptonic analyses	Semileptonic VBS	Reference
	Observed Limit [TeV ⁻⁴]	Observed Limit [TeV ⁻⁴]	
L _{S02}	[-7.7, 7.7]	[-1.89, 2.04]	[21]
L _{S1}	[-21.6, 21.8]	[-1.81, 2.12]	[21]
L _{M0}	[-4.2, 4.2]	[-0.63, 0.57]	[50]
L _{M1}	[-8.7, 9.1]	[-0.45, 0.73]	[21]
L _{M2}	[-8.2, 8.0]	[-0.57, 0.62]	[24]
L _{M3}	[-21, 21]	[-0.42, 0.78]	[24]
L _{M4}	[-15, 16]	[-0.64, 0.56]	[24]
L _{M5}	[-25, 24]	[-0.65, 0.55]	[24]
L _{M7}	[-12, 12]	[-0.56, 0.62]	[21]
L _{T0}	[-0.46, 0.44]	[-0.12, 0.10]	[51]
L _{T1}	[-0.28, 0.31]	[-0.09, 0.12]	[21]
L _{T2}	[-0.89, 1.00]	[-0.09, 0.13]	[21]
L _{T5}	[-0.70, 0.74]	[-0.15, 0.09]	[24]
L _{T6}	[-1.60, 1.70]	[-0.15, 0.08]	[24]
L _{T7}	[-2.60, 2.80]	[-0.59, 0.03]	[24]
L _{T8}	[-0.47, 0.47]	[-0.11, 0.11]	[24]
L _{T9}	[-1.30, 1.30]	[-0.11, 0.11]	[24]

CHAPTER 8

Conclusions

The standard model predicts that the electroweak symmetry breaking completely changed the vacuum structure at the early universe and, consequently, masses of elementary particles were generated. Thanks to enough center-of-mass energy of the LHC to generate two on-shell electroweak bosons, the most important process to examine the electroweak symmetry breaking, vector boson scattering can be studied at the LHC. This thesis presents the first search for the EWVj processes and anomalous quartic gauge couplings with the semileptonic final states at the ATLAS detector with an integrated luminosity of 35.5 fb^{-1} corresponding to data collected in 2015 and 2016.

The sensitivities of the studies for both the SM and aQGC are drastically improved by the large-R jet reconstruction and the corresponding boosted weak vector boson identification techniques. The combined mass reconstruction algorithm, which utilizes accurate track angle resolutions and great calorimeter energy resolutions achieves improvement in 30% (50%) mass resolution compared to the mass of a calorimeter jet. The two-variable-tagger that is a boson identification algorithm combining discriminant powers of the combined mass and D_2 with optimized rectangular cuts, which achieves approximately a 95% (98.7%) rejection at a 50% signal efficiency at a p_T range of $200 \leq p_T \leq 500 \text{ GeV}$ ($1000 \leq p_T \leq 1500 \text{ GeV}$). Systematic uncertainties associated with the combined mass and D_2 scales are evaluated by the r_{trk} double ratio method, which are relatively 3% (6%) for the combined mass at a large-R p_T of $\sim 500 \text{ GeV}$ (3 TeV) and 2% (6%) for D_2 at a large-R jet p_T of 300 GeV (3 TeV).

The main sources of background for the semileptonic VBS analysis are the V+jets and $t\bar{t}$ processes. It is eliminated by making use of the signal event topology expected from Feynman diagrams. Further eliminations of those backgrounds are achieved by using the BDT discriminant, and it is directly used as an input of profile binned likelihood fits.

The leading pre-fit uncertainty is the modeling of the V+jets process by the MC simulations having an impact by more than 100% on the signal-strength value, and it is drastically decreased to 13% by the simultaneous fit utilizing m_{jj}^{tag} distributions as inputs of CRs.

An excess of the observed data over the expected background from the SM without EWVj processes is observed with the observed (expected) significance of 2.7 (2.5) standard deviations. The measured signal-strength is $\mu_{\text{EWVj}}^{\text{obs}} = 1.05_{-0.40}^{+0.42} = 1.05 \pm 0.20(\text{stat.})_{-0.34}^{+0.37}(\text{syst.})$. The fiducial cross-section of EWVj is measured to be $\sigma_{\text{EWVj}}^{\text{fid,obs}} = 45.1 \pm 8.6(\text{stat.})_{-14.6}^{+15.9}(\text{syst.}) \text{ fb}^{-1}$.

Since the measurement of EWVj processes is consistent with the SM, the results are interpreted as limits on coefficients of the dimension-8 EFT operators. Given limits on coefficients, f_{S0} to f_{S2} , f_{M0} to f_{M7} , and f_{T0} to f_{T9} are the most stringent to date.

CHAPTER 9

Prospect for Future Measurement

The ATLAS detector has collected an integrated luminosity of 140 fb^{-1} from 2015 to 2018 (Run2). The LHC is scheduled to reboot in 2021 and lasts until 2023, and a possibility of one year extension is being discussed. A corresponding integrated luminosity is pessimistically expected to be 300 fb^{-1} until 2023, 400 fb^{-1} with an extension year. There is an option to increase the center-of-mass energy to 14 TeV.

This chapter describes future prospects for the semileptonic VBS analysis. In order to assess expected sensitivity with future accumulated datasets, Section 9.1 describes the results of simple luminosity projections and possible improvements in the analysis. When the $EWV\bar{V}jj$ processes are observed with the semileptonic final states with adequate significance, for example 5 standard deviations, one of the most fascinating observable is the boson polarization from the aspects of both the SM measurement and aQGC search. A new methodology to identify the weak boson polarization with large-R jets are introduced in Section 9.2.

9.1 Expected Sensitivity

The measurement performed in this thesis as shown in Section 6.1 is projected by scaling ratios of those integrated luminosities. Figure 9.1 shows the expected sensitivities in expected integrated luminosities. The center-of-mass energy is conservatively assumed to be 13 TeV.

The measurement performed in this thesis has an observed (expected) sensitivity of 2.7 (2.5) standard deviations. With the full Run2 dataset which has already been collected, expected sensitivity increases in 3.9 standard deviations. Furthermore, it reached to 4.8 and 5.1 standard deviations for the datasets collected by the end of 2023 and 2024, respectively. Thus the measurement expected to be reached around 5 standard deviations without any improvement except the luminosity increasing.

As mentioned in Section 6.9.6, the uncertainty in the measurement of the SM $EWV\bar{V}jj$ processes is already systematic dominant. Hence, adding to increasing in integrated luminosities, improvements on sensitivity are possibly saturated by the systematic uncertainties. Majority of impacts on the signal-strength come from statistics in the MC simulations, modeling of the $V+$ jets processes by the MC simulations, and experimental uncertainty in large-R jet. The MC statistics will increase in a factor of 4 for the ongoing full Run2 analysis and it naively causes decreasing of its uncertainty in a factor of 2. For the $V+$ jets MC simulation, an improved version of SHERPA (SHERPA3) is expected to drastically eliminate the mismodeling of m_{jj}^{tag} , and it removes m_{jj} reweighting and related systematic uncertainties at all. The large-R jet uncertainty will decrease in half by systematic uncertainties estimated with in-situ way as

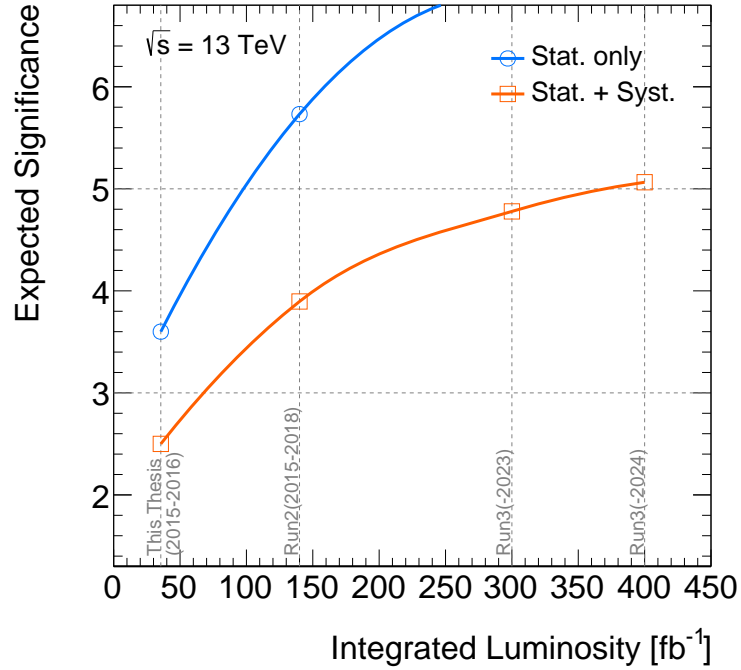


Fig. 9.1: Expected sensitivities with (orange) and without (blue) systematic uncertainties at integrated luminosities of 140,300, and 400 fb⁻¹ are shown.

described in Section 5.1.3. By those improvements, the observation with 5 standard deviations in the full Run2 dataset might be possible. In Run3 and awaiting the HL-LHC¹⁾, therefore, detailed inspections of VBS processes become main topics.

9.2 Polarization-Sensitive Large-R jets Observable

As shown in Section 9.1, it is clear that the EWVj processes in the semileptonic final states will have been discovered within several years, and it allows us to perform property measurements. The W polarization state is essential information for understanding electroweak symmetry breaking with the EWVj processes because the unitarity violation explained in Section 2.2 occurs only in the $V_L V_L \rightarrow V_L V_L$ scattering. Also, the polarization of outgoing bosons separates types of EFT operators (F_S, F_M , and F_T) as shown in Figure 7.4. Furthermore, sensitivities on several new physics searches [171, 172] related to the weak vector bosons can be improved by optimizations with polarization information.

The W boson polarization state has already measured in both hadronic and leptonic decay in 2017[173]. However, the measurements with large-R jet have never been performed. This section shows a construction of a polarization-sensitive variable, and its discriminant power is validated by measuring W boson polarization in $t\bar{t}$ events with the 2016 dataset. The same samples listed in Section 6.2 are used in this analysis.

¹⁾HL-LHC stands for High-Luminosity LHC which is the last run period for the LHC scheduled in between 2027 and 2040.

9.2.1 Polarization-Sensitive Variables

Since the polarization is defined by its spin direction with respect to the particle momentum, a direction of its decay product with spin is sensitive to the polarization.

The decay of W boson is represented as

$$\frac{1}{\sigma} \frac{d\sigma}{d \cos \theta^*} = \frac{3}{4} (1 - \cos^2 \theta^*) fr_0 + \frac{3}{8} (1 - \cos \theta^*)^2 fr_L + \frac{3}{8} (1 + \cos \theta^*)^2 fr_R, \quad (9.1)$$

where θ^* is an angle between the W boson momentum and its decay product of down-type fermion in the W boson rest frame. fr_0 , fr_R , and fr_L are fractions of longitudinal, right-handed, and left-handed, respectively. It is assumed that fermions from a W boson decay are massless.

From Equation 9.1, $\cos \theta^*$ for longitudinally polarized W boson distributes as $1 - \cos^2 \theta^*$, $\cos \theta^*$ for transversely polarized W boson distributes as $(1 \pm \cos \theta^*)^2$. This θ^* is the most fundamental quantities in the leading order of Feynman diagram, therefore, it is the most straight forward observable for the measurement of a polarization state of a W boson.

A Lorentz boosted W boson is reconstructed with the large-R jet that merges two jets originated from decay products of W boson. The two jets are identified from a large-R jet by *exclusive-kt* algorithm. The algorithm reclusters large-R jets with $R = 1.0$ k_T algorithm, and the two subjets before the last merging are assigned as two subjets from decay products. The exclusive kt algorithm employs kt clustering because the clustering algorithm tends to reconstruct two balanced subjets, whereas the anti- k_t algorithm tends to reconstruct two quite unbalanced subjets.

The last ambiguity to reconstruct $\cos \theta^*$ is which subjet is assigned as a down type quark. Several quantities of subjet are tested (the number of tracks in subjet, p_T of subjet, etc), and the c -tagging score is turned out to be the most effective. The c -tagging is the same algorithm as b -tagging introduced in Section 4.5.3 except the MV2 training with c -hadron jets as a signal. The b -hadron (light-flavor) jet efficiency is 25% (5%) at c -hadron jet efficiency of 41%. Details on c -tagging are described in Reference [174]. A subjet with the lower c -tagging score is likely a down-type quark in the $W \rightarrow cs$ decay and completely random in the $W \rightarrow ud$ decay. Since the W decays cs and ud almost equally, the algorithm works.

9.2.2 Template of $\cos \theta^*$ Distribution for Purely Polarized W boson

A measurement of the fraction of polarization state of the W boson in $t\bar{t}$ events needs templates on the assumptions of purely longitudinal, left-handed, and right-handed states. Pure polarization state simulations are made by reweighting SM prediction of $\cos \theta^*$ distribution at particle-level. Figure 9.2 shows $\cos \theta^*$ distribution of $t\bar{t}$ events and its 3-components(fr_0 , fr_R , and fr_L) fit. The reweighting factors are calculated by the fraction (fr_0 , fr_R , and fr_L). A comparison of each fraction between the analytic NNLO calculation and fit results is shown in Table 9.1. The fit results agree with the NNLO calculation well.

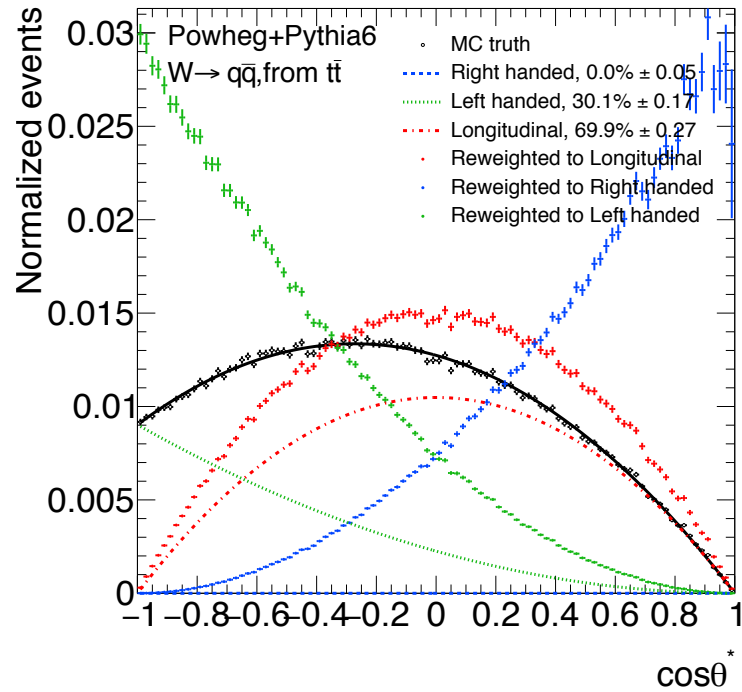


Fig. 9.2: $\cos \theta^*$ distributions for tree-level quarks from W boson decay are shown. The black marker shows the SM prediction by the POWHEG event generator. The black line is the best fit function obtained by a 3-components (fr_0 , fr_R , and fr_L) fit. The red, green, and blue markers represent $\cos \theta^*$ distributions after reweighting to each pure polarization state.

Table 9.1: Comparisons between the NNLO calculation and the fit result are shown.

	fr_0	fr_L	fr_R
NNLO calc.[175]	0.687(5)	0.311(5)	0.0017(1)
Fit result	0.699(3)	0.301(2)	0.0000(5)

Figure 9.3 shows the $\cos \theta^*$ distribution after the detector simulation and the reconstruction chain to be compared to the observed data. The distribution is smeared by both detector resolutions and reconstruction procedures, but there is still discriminant power among purely polarized templates.

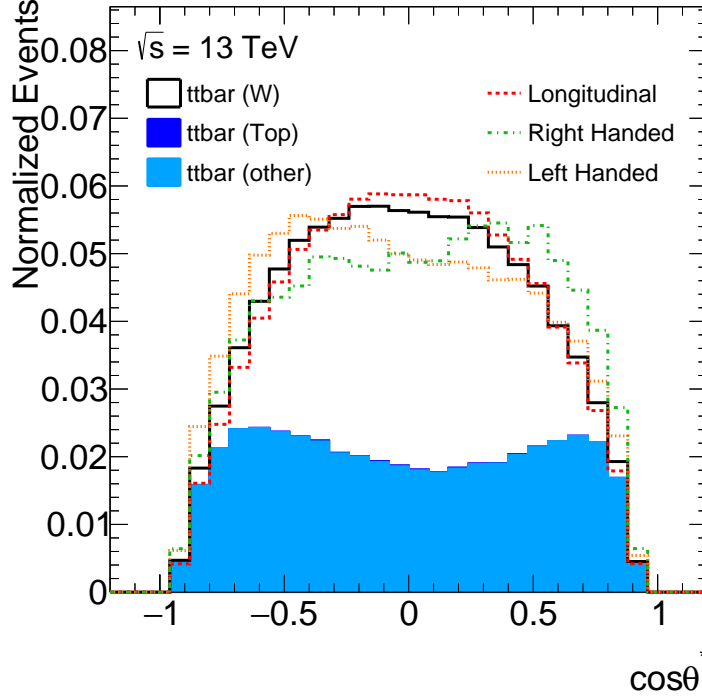


Fig. 9.3: The $\cos \theta^*$ distribution at the reconstruction level. $t\bar{t}$ events are shown in each case, a large-R jet matched to $W \rightarrow q\bar{q}$ (white), a large-R jet matched to $t \rightarrow W\bar{b} \rightarrow q\bar{q}\bar{b}$ (deep blue), and others (light blue).

9.2.3 Event Selection

To check whether the reconstructed $\cos \theta^*$ works for the observed data, $t\bar{t}$ events are utilized. The $t\bar{t} \rightarrow l\nu b q \bar{q} \bar{b}$ final state is selected to obtain W boson jets and enhance the purity of the $t\bar{t}$ process.

The single lepton triggers shown in Section 6.2.2 are also required in this study. Events are required to have exactly one lepton with $p_T > 30$ GeV, and events with extra leptons with $p_T > 20$ GeV are rejected. The electron is identified with the “tight” working point described in Section 4.3. One small-R jet is required with $p_T > 25$ GeV with $\Delta R(\text{small} - \text{R jet}, \text{lepton}) < 1.5$. A large-R jet that is used to test $\cos \theta^*$ is required to be $p_T > 200$ GeV within $\Delta\phi(\text{large} - \text{R jet}, \text{lepton}) > 2.3$. For the neutrino, $E_T^{\text{miss}} > 20$ GeV and $E_T^{\text{miss}} + M_T^W > 60$ GeV are required. To veto a large-R jet which contains two quarks from the W boson and one b -jet from the top-quark decay, the b -tagged small-R jet is required to be outside of large-R jet ($\Delta R(\text{b-jet}, \text{large} - \text{R jet}) > 1.5$). The schematic graph of the selected topology is shown in Figure 9.4.

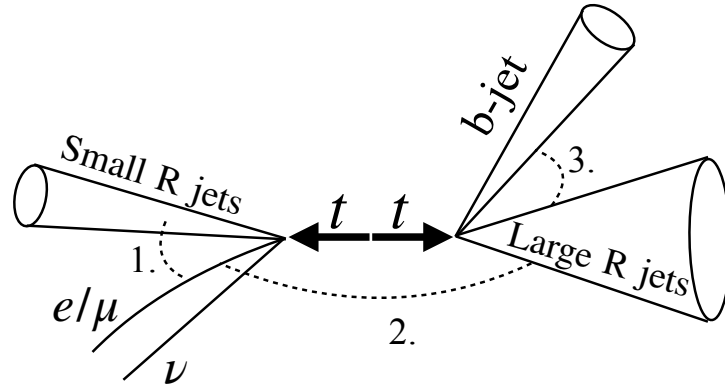


Fig. 9.4: A schematic graph of a selected topology for $t\bar{t}$ events is shown. Three angular cuts, 1.: $\Delta R(\text{small-R jet, lepton}) < 1.5$, 2.: $\Delta\phi(\text{large-R jet, lepton}) > 2.3$, and 3.: $\Delta R(\text{b-jet, large-R jet}) > 1.5$ are applied.

Selected events are used for comparisons between the observed data and the MC simulations for large-R jet mass and $\cos\theta^*$ distributions as shown in Figure 9.5.

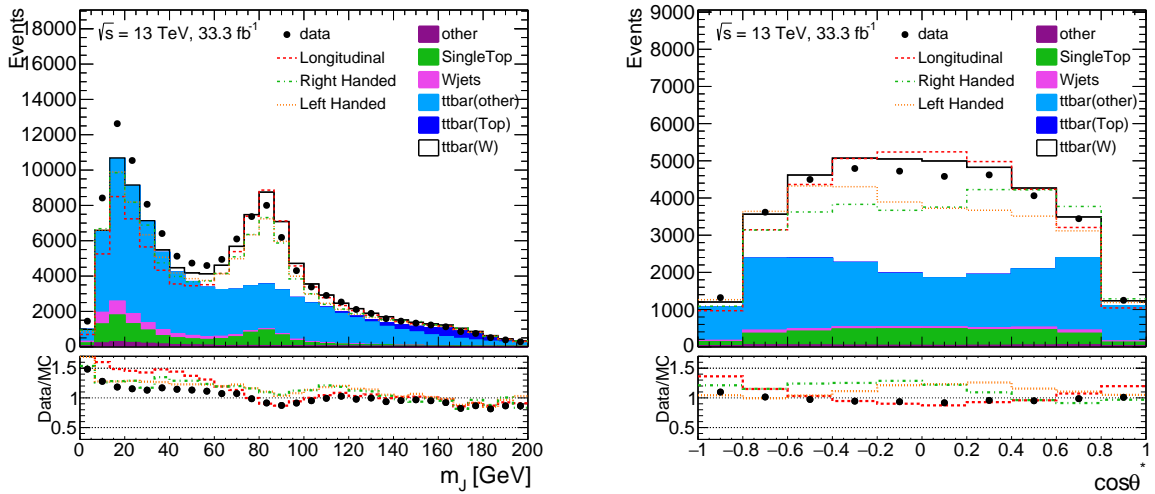


Fig. 9.5: Comparisons between data and MC simulated events for large-R jet mass (left) and $\cos\theta^*$ (right) distributions. The discrepancy at the lower region most likely comes from multi-jets events.

In-situ calibration for large-R jet mass is not applied, so the peak of W jet mass for the observed data is slightly shifted from the peak for the MC simulated events. Moreover, multi-jet events make some discrepancies at lower masses. To obtain pure W jet events, the mass cut on $60 < m_j < 100\text{GeV}$ is applied. Large-R jets with higher $|\cos\theta^*|$ indicate that W decays with unbalance p_T and having a large decay angle between quarks. Then those invariant mass becomes small because of leaking jet constituents from a given jet cone. Therefore, MC simulated events undershoot the observed data at high $|\cos\theta^*|$.

9.2.4 Results

The obtained $\cos \theta^*$ distribution (Figure 9.5) for the observed data is fitted by templates for the assumption of three purely polarized W bosons. A χ^2 fit is performed, and Figure 9.6 shows the χ^2 distribution. The total fraction is fixed to unity ($fr_0 + fr_R + fr_L = 1$). Any systematic uncertainties are considered in this fit. The χ^2 distribution is subtracted by the value of minimum, and the confidence intervals are calculated based on χ^2 probability with two degrees of freedom as shown in Figure 9.6. The result is summarized in Table 9.2.

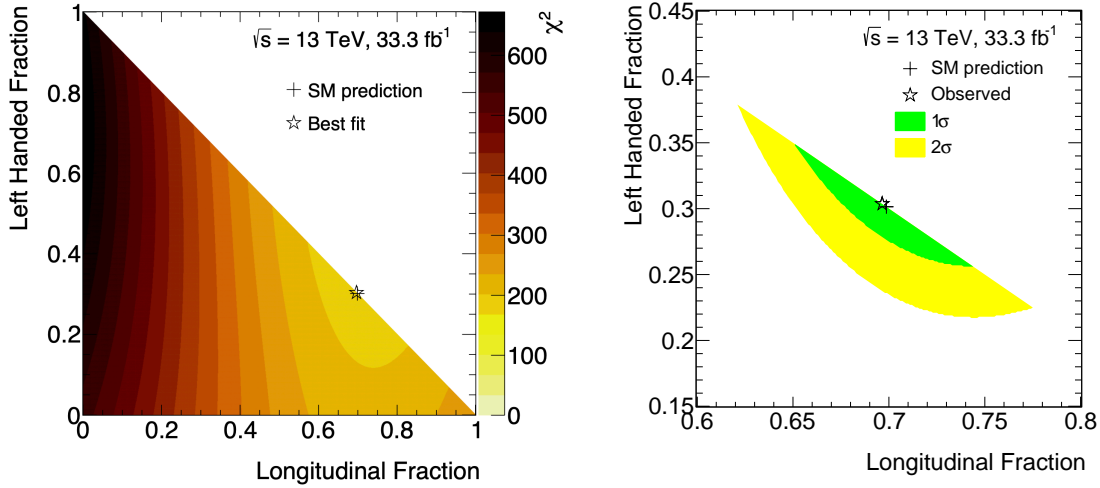


Fig. 9.6: The χ^2 distribution with respect to each template fraction for $\cos \theta^*$ distribution (left) and the confidence interval for the measurement (right) are shown. Only statistical uncertainty is considered.

Table 9.2: A comparison of polarization fractions of the W boson between the SM prediction and observed values is shown.

	fr_0	fr_L	fr_R
Observed	0.70(5)	0.30(5)	0.00(7)
SM prediction	0.699(3)	0.301(2)	0.0000(5)

The observed longitudinal and transverse polarization fractions are compatible with the SM prediction. A precision of longitudinal (left-handed) polarization fraction arise from statistical uncertainty is absolutely 5 (5)%, which is comparable to the one of leptonic final state 1.2 (1.2)%. This result is the first proof that the reconstructed $\cos \theta^*$ works as a polarization discriminator for a large-R jet. This opens the window of the weak boson polarization measurement at the high-energy regime including the semileptonic VBS, i.e. measurements on the Run3 and succeeding HL-LHC become much meaningful, and those lead to deeper understandings of the SM and more stringent tests of BSMs.

Appendices

APPENDIX A

Matrix Elements of W^+W^- scattering

The matrix elements for the W^+W^- scattering introduced in Section 2.2 are explicitly shown as

$$\begin{aligned}\mathcal{M}_1 &= (\epsilon_1 \cdot \epsilon_2)(\epsilon_3 \cdot \epsilon_4)(t - u) \\ &\quad + 4[(\epsilon_1 \cdot \epsilon_2)\{(\epsilon_3 \cdot \mathbf{k}_4)(\epsilon_4 \cdot \mathbf{k}_2) - (\epsilon_3 \cdot \mathbf{k}_2)(\epsilon_4 \cdot \mathbf{k}_3)\} \\ &\quad\quad + (\epsilon_3 \cdot \epsilon_4)\{(\epsilon_1 \cdot \mathbf{k}_3)(\epsilon_2 \cdot \mathbf{k}_4) - (\epsilon_1 \cdot \mathbf{k}_4)(\epsilon_2 \cdot \mathbf{k}_3)\} \\ &\quad\quad - (\epsilon_2 \cdot \mathbf{k}_1)\{(\epsilon_1 \cdot \mathbf{k}_3)(\epsilon_4 \cdot \mathbf{k}_3) - (\epsilon_1 \cdot \epsilon_4)(\epsilon_3 \cdot \mathbf{k}_4)\} \\ &\quad\quad - (\epsilon_1 \cdot \mathbf{k}_2)\{(\epsilon_2 \cdot \mathbf{k}_4)(\epsilon_3 \cdot \mathbf{k}_4) - (\epsilon_2 \cdot \epsilon_3)(\epsilon_4 \cdot \mathbf{k}_3)\}],\end{aligned}\tag{A.1}$$

$$\begin{aligned}\mathcal{M}_2 &= (\epsilon_1 \cdot \epsilon_3)(\epsilon_2 \cdot \epsilon_4)(s - u) \\ &\quad - 4[(\epsilon_1 \cdot \epsilon_3)\{(\epsilon_2 \cdot \mathbf{k}_3)(\epsilon_4 \cdot \mathbf{k}_2) + (\epsilon_2 \cdot \mathbf{k}_4)(\epsilon_4 \cdot \mathbf{k}_3)\} \\ &\quad\quad + (\epsilon_2 \cdot \epsilon_4)\{(\epsilon_1 \cdot \mathbf{k}_2)(\epsilon_3 \cdot \mathbf{k}_4) - (\epsilon_1 \cdot \mathbf{k}_4)(\epsilon_3 \cdot \mathbf{k}_2)\} \\ &\quad\quad - (\epsilon_1 \cdot \mathbf{k}_3)\{(\epsilon_3 \cdot \mathbf{k}_4)(\epsilon_2 \cdot \mathbf{k}_4) + (\epsilon_2 \cdot \epsilon_3)(\epsilon_4 \cdot \mathbf{k}_2)\} \\ &\quad\quad - (\epsilon_3 \cdot \mathbf{k}_1)\{(\epsilon_1 \cdot \mathbf{k}_4)(\epsilon_2 \cdot \mathbf{k}_4) + (\epsilon_1 \cdot \epsilon_2)(\epsilon_4 \cdot \mathbf{k}_2)\}],\end{aligned}\tag{A.2}$$

$$\mathcal{M}_3 = (\epsilon_1 \cdot \epsilon_2)(\epsilon_3 \cdot \epsilon_4) + (\epsilon_1 \cdot \epsilon_3)(\epsilon_2 \cdot \epsilon_4) - 2(\epsilon_1 \cdot \epsilon_4)(\epsilon_2 \cdot \epsilon_3),\tag{A.3}$$

$$\mathcal{M}_4 = (\epsilon_1 \cdot \epsilon_2)(\epsilon_3 \cdot \epsilon_4),\tag{A.4}$$

$$\mathcal{M}_5 = (\epsilon_1 \cdot \epsilon_3)(\epsilon_2 \cdot \epsilon_4).\tag{A.5}$$

The notation follows as described in Section 2.2.

APPENDIX B

BDT Input Modeling for Semileptonic VBS Analysis

Distributions of all input variables used in the BDT training for each channel are shown in this section. The distributions are applied nuisance parameters obtained from the global likelihood fit.

B.1 0-lepton channel

BDT input variable distributions for 0-lepton channel are shown in Figure B.1,B.2, ,B.3 for the merged high-purity regions, Figure B.4,B.5, ,B.6, for the merged low-purity regions, Figure B.7,B.8, B.9,B.10, for the resolved regions. MC predictions are applied post-fit values of the nuisance parameters.

B.2 1-lepton channel

BDT input variable distributions for 1-lepton channel are shown in Figure B.11,B.12, for merged signal region, Figure B.13,B.14, for resolved signal region. MC predictions are applied post-fit values of nuisance parameter.

B.3 2-lepton channel

BDT input variable distributions for 2-lepton channel are shown in Figure B.15,B.16, B.17,B.18 for merged, B.19,B.20, Figure B.21,B.22, B.23 for resolved.

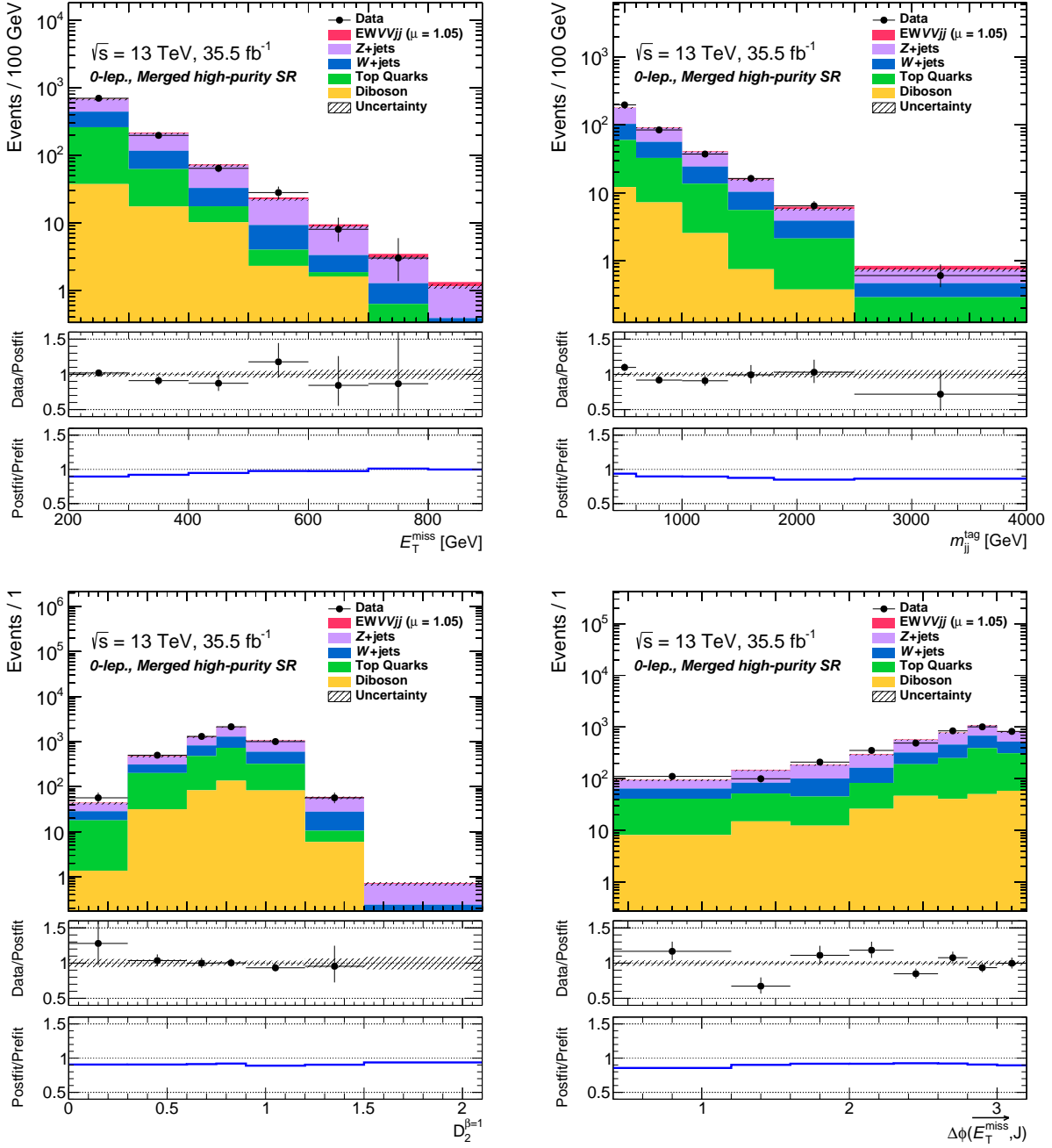


Fig. B.1: Distributions of variables used in the BDT training in the merged high-purity region for the 0-lepton channel applying post-fit uncertainties are shown.

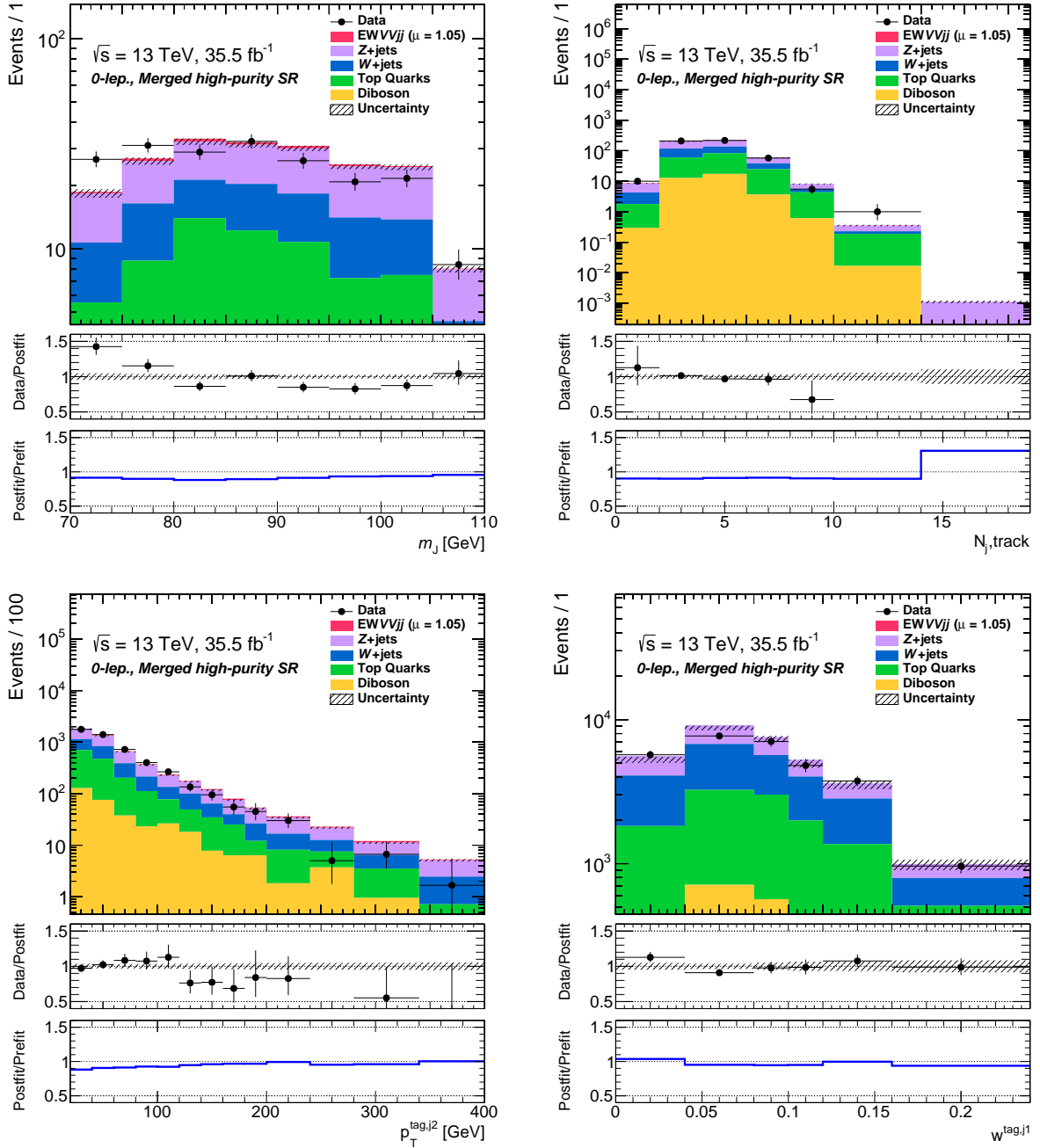


Fig. B.2: Distributions of variables used in the BDT training in the merged high-purity region for the 0-lepton channel applying post-fit uncertainties are shown.

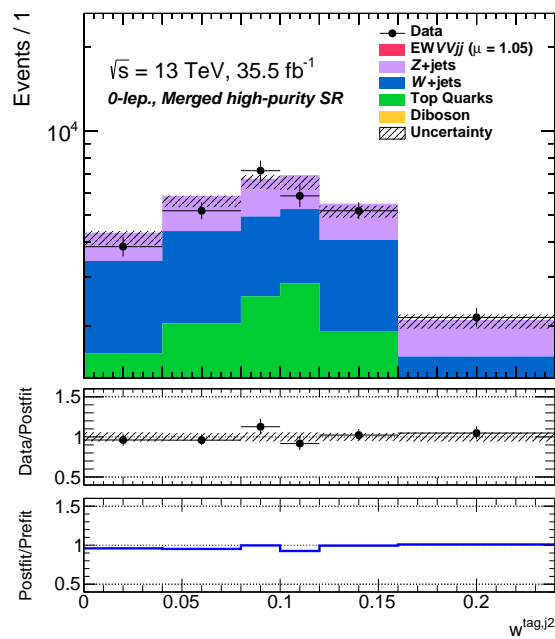


Fig. B.3: A distribution of variable used in the BDT training in the merged high-purity region for the 0-lepton channel applying post-fit uncertainties is shown.

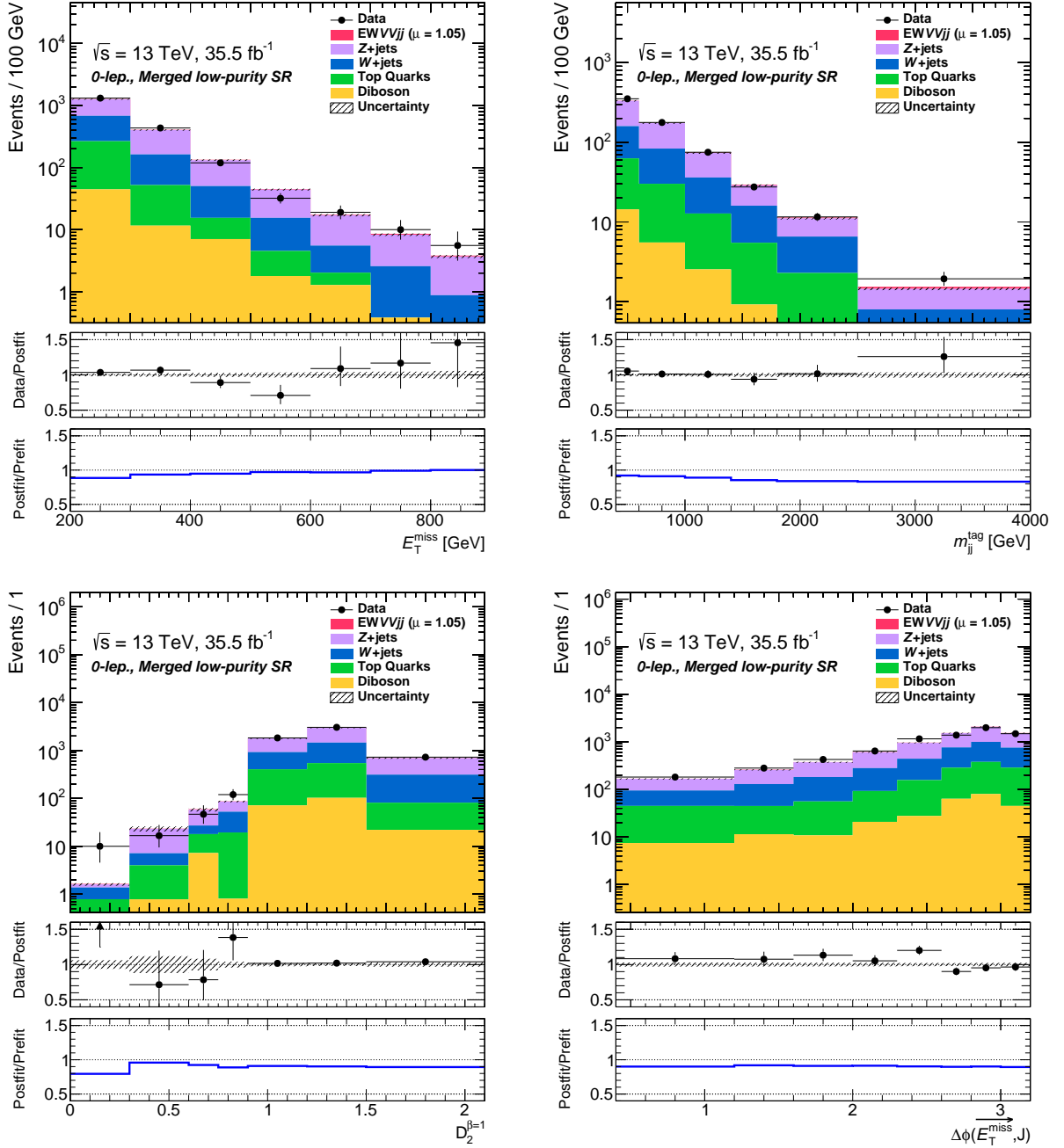


Fig. B.4: Distributions of variables used in the BDT training in the merged low-purity region for the 0-lepton channel applying post-fit uncertainties are shown.

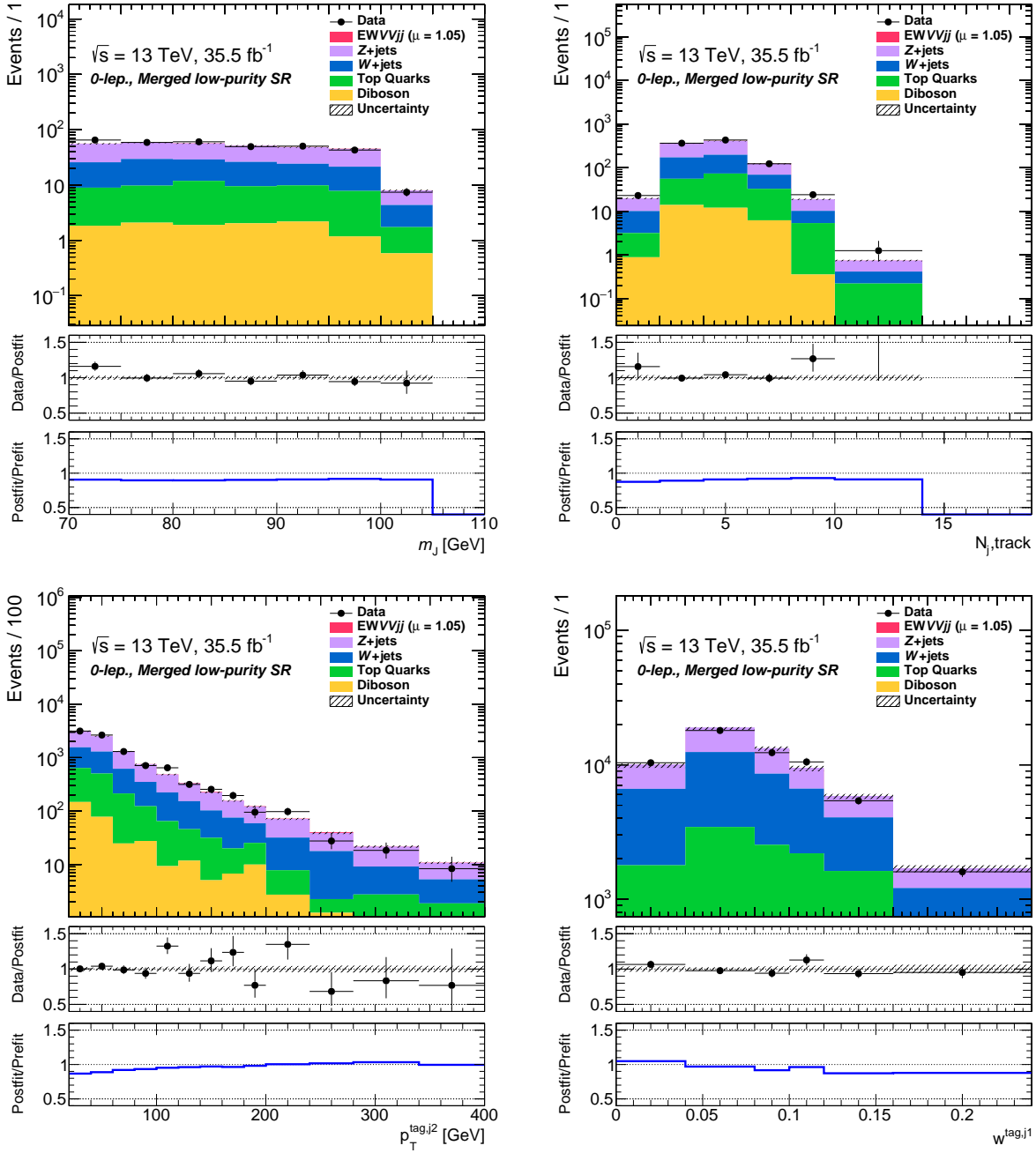


Fig. B.5: Distributions of variables used in the BDT training in the merged low-purity region for the 0-lepton channel applying post-fit uncertainties are shown.

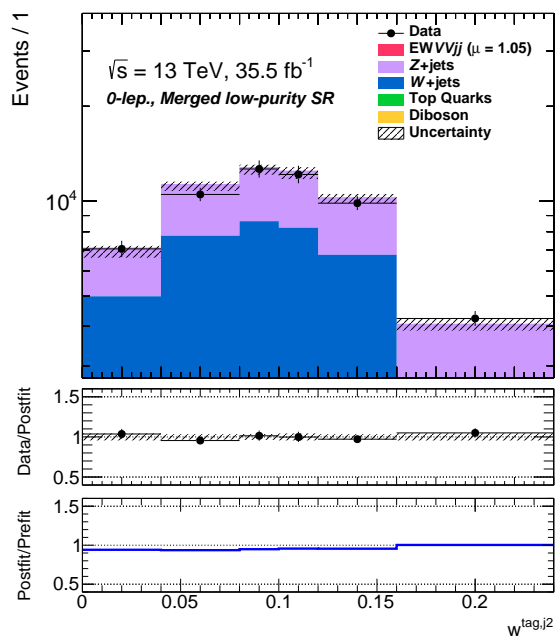


Fig. B.6: A distribution of variable used in the BDT training in the merged low-purity region for the 0-lepton channel applying post-fit uncertainties is shown.

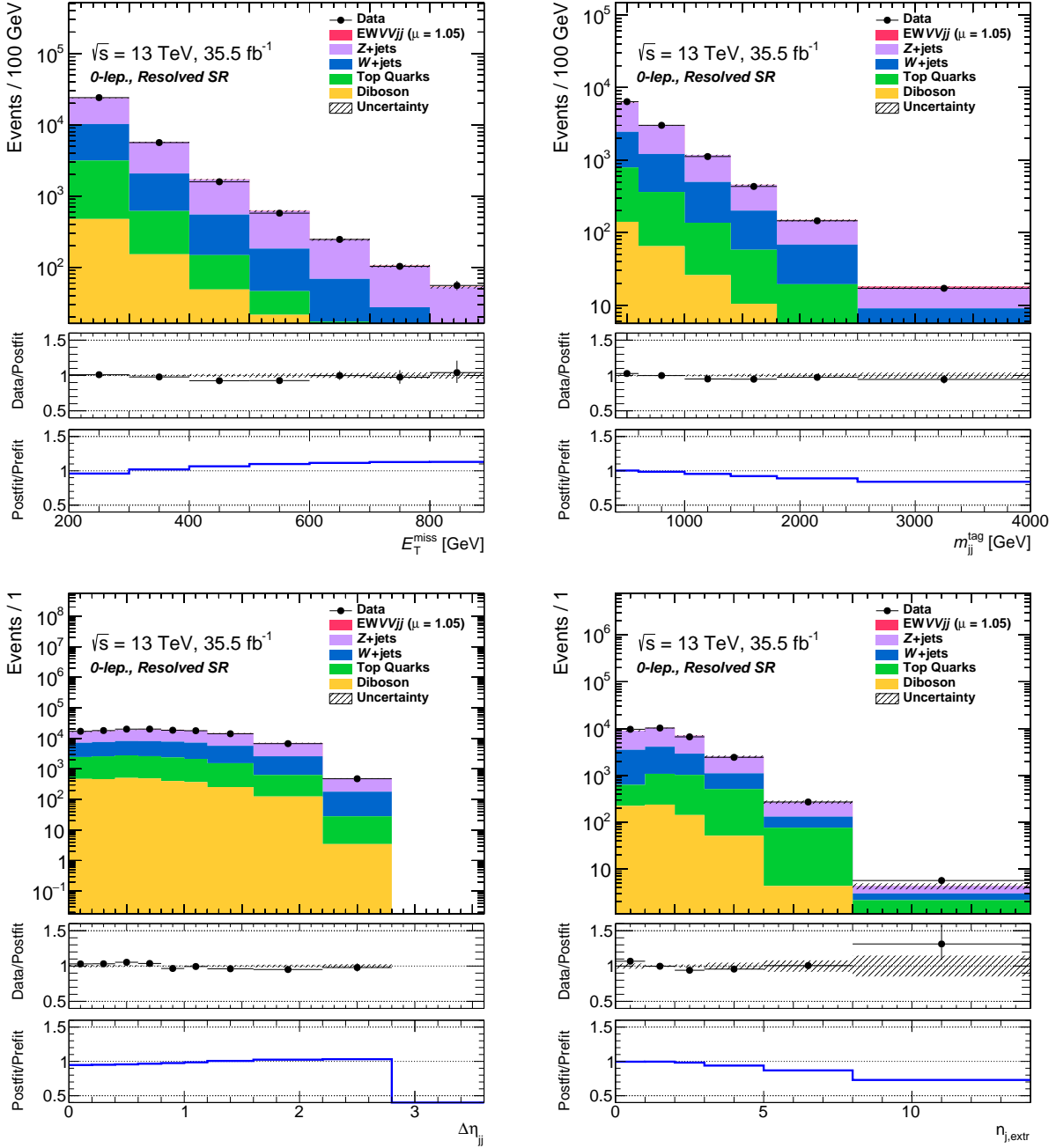


Fig. B.7: Distributions of variables used in the BDT training in the resolved region for the 0-lepton channel applying post-fit uncertainties are shown.

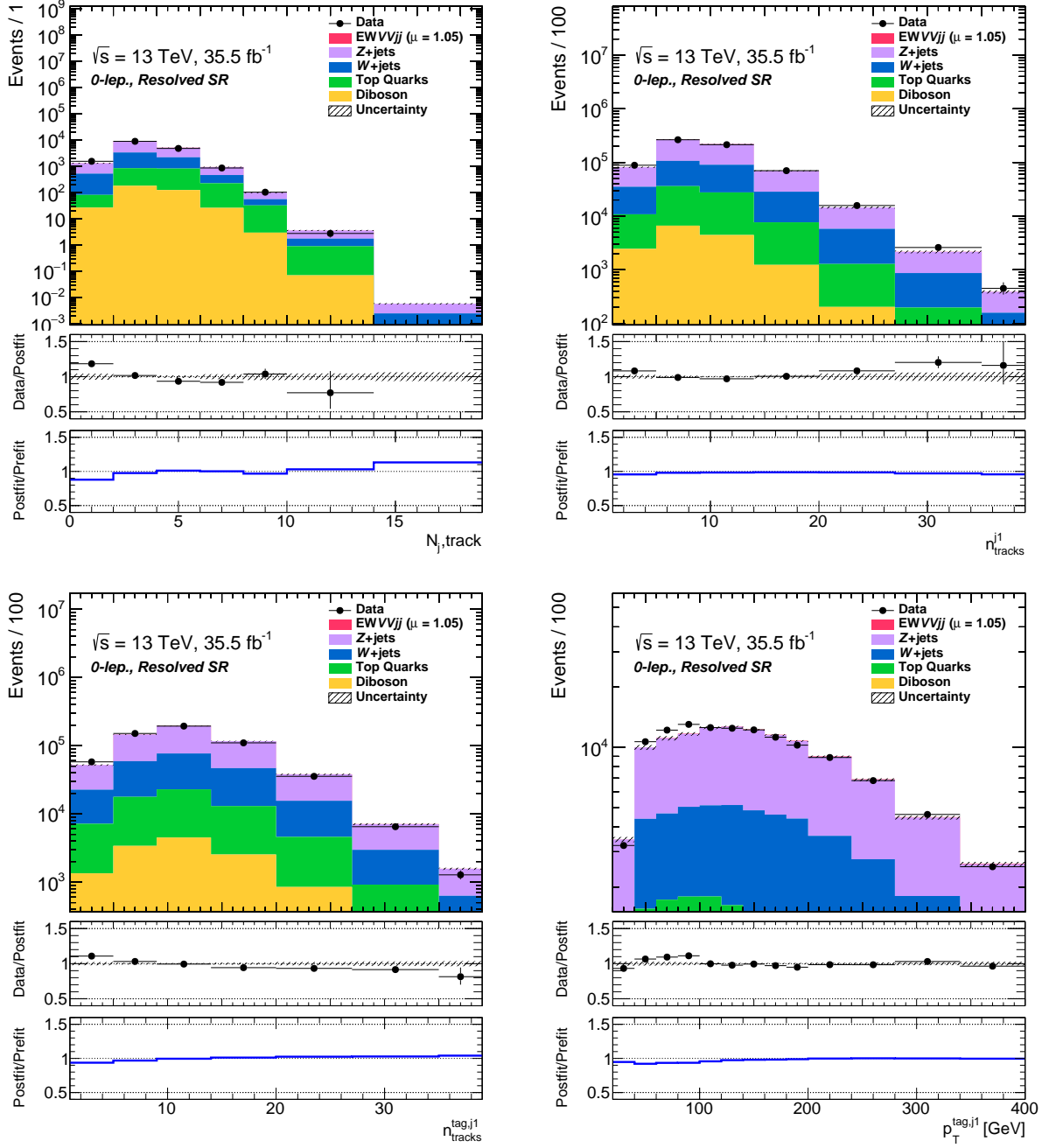


Fig. B.8: Distributions of variables used in the BDT training in the resolved region for the 0-lepton channel applying post-fit uncertainties are shown.

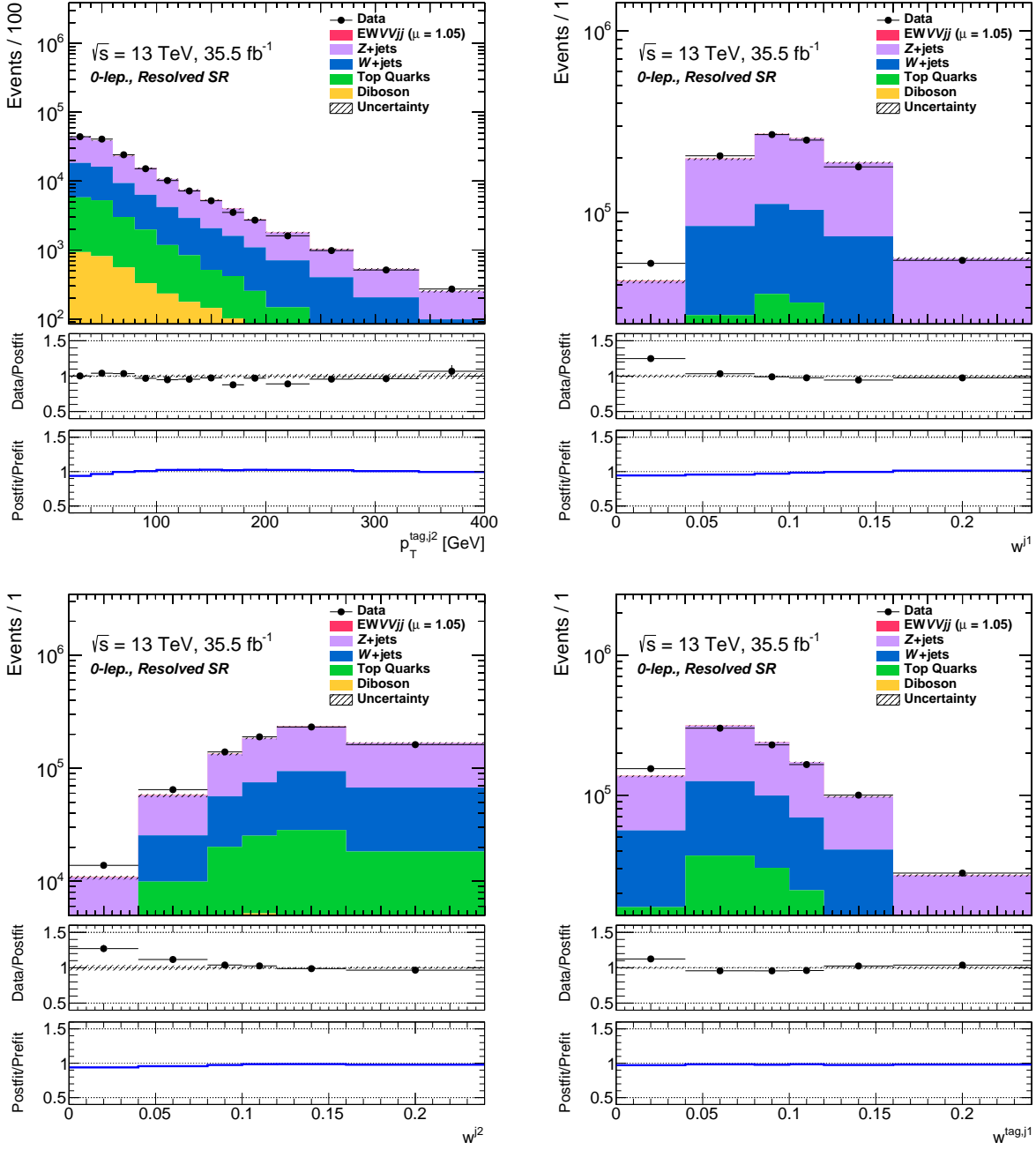


Fig. B.9: Distributions of variables used in the BDT training in the resolved region for the 0-lepton channel applying post-fit uncertainties are shown.

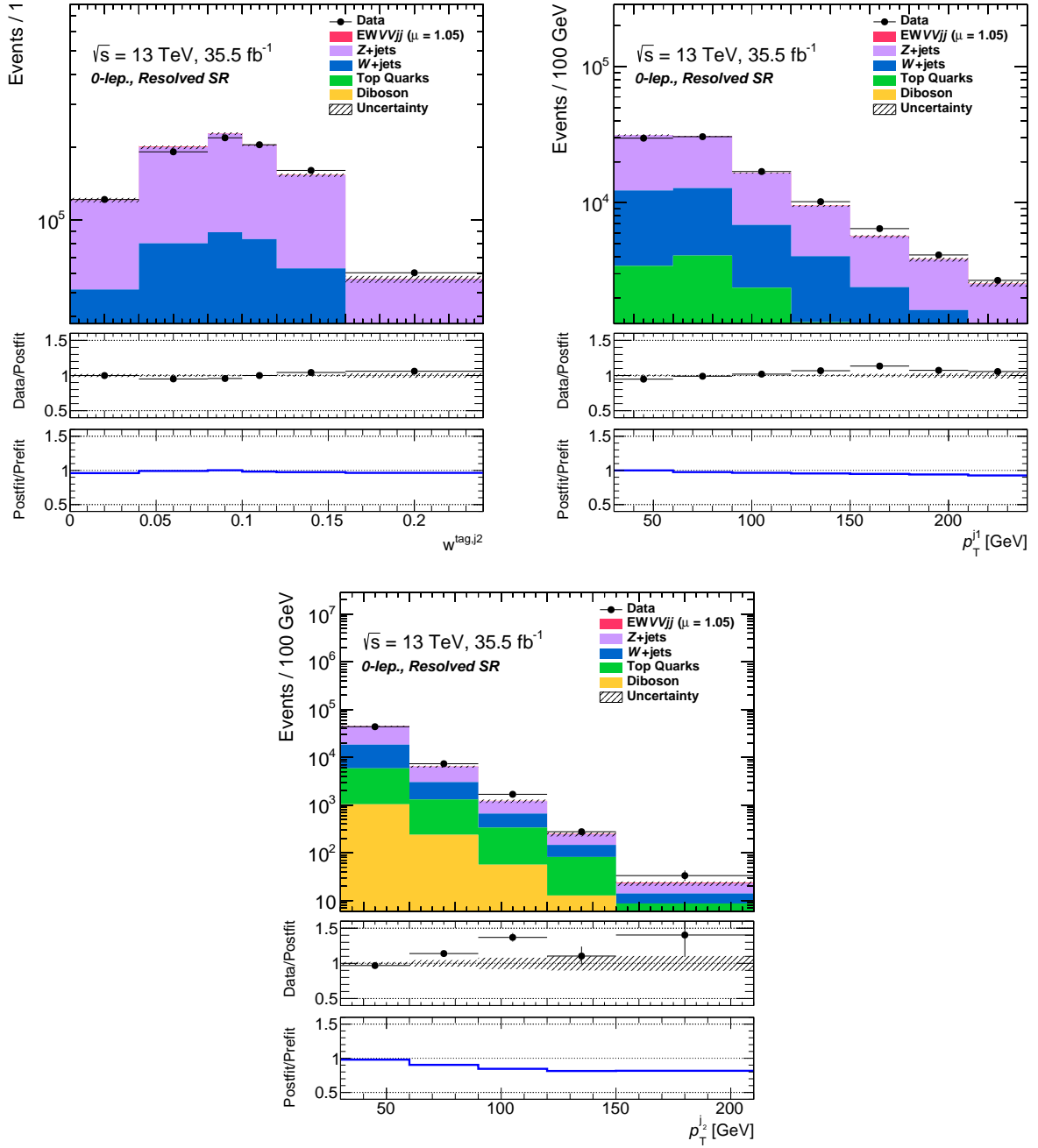


Fig. B.10: Distributions of variables used in the BDT training in the resolved region for the 0-lepton channel applying post-fit uncertainties are shown.)

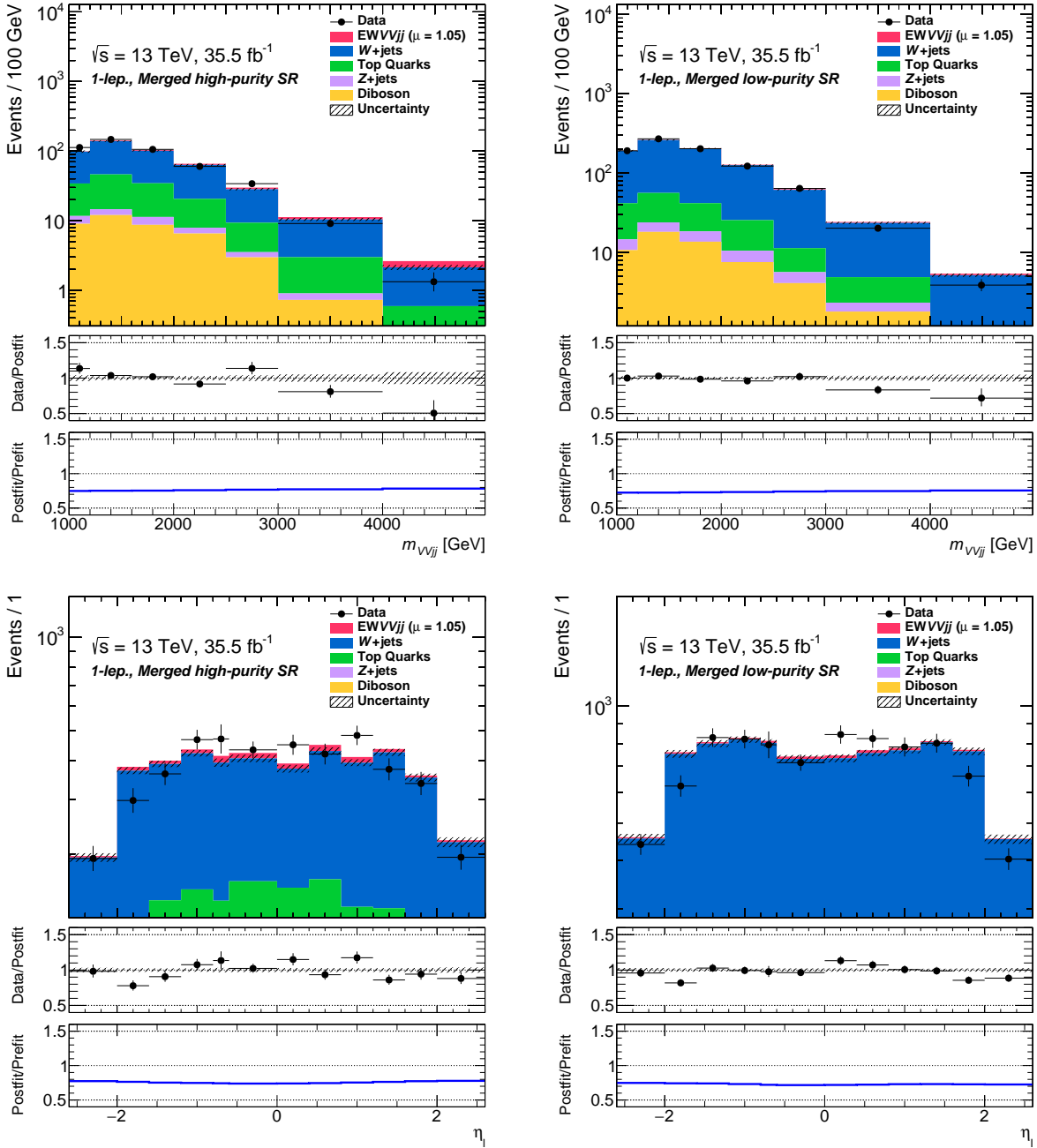


Fig. B.11: Distributions of variables used in the BDT training in the merged region for the 1-lepton channel applying post-fit uncertainties are shown.

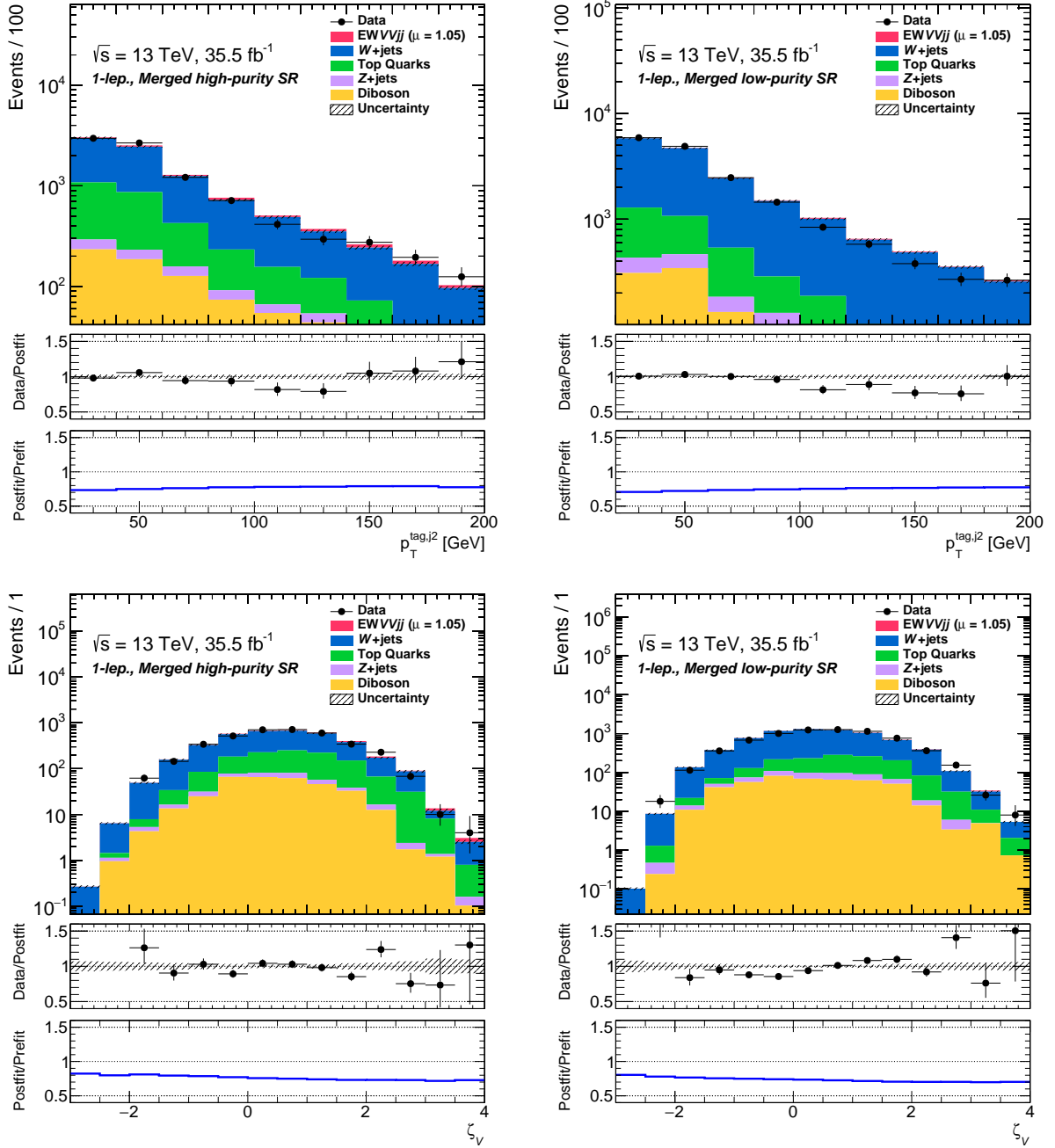


Fig. B.12: Distributions of variables used in the BDT training in the merged region for the 1-lepton channel applying post-fit uncertainties are shown.

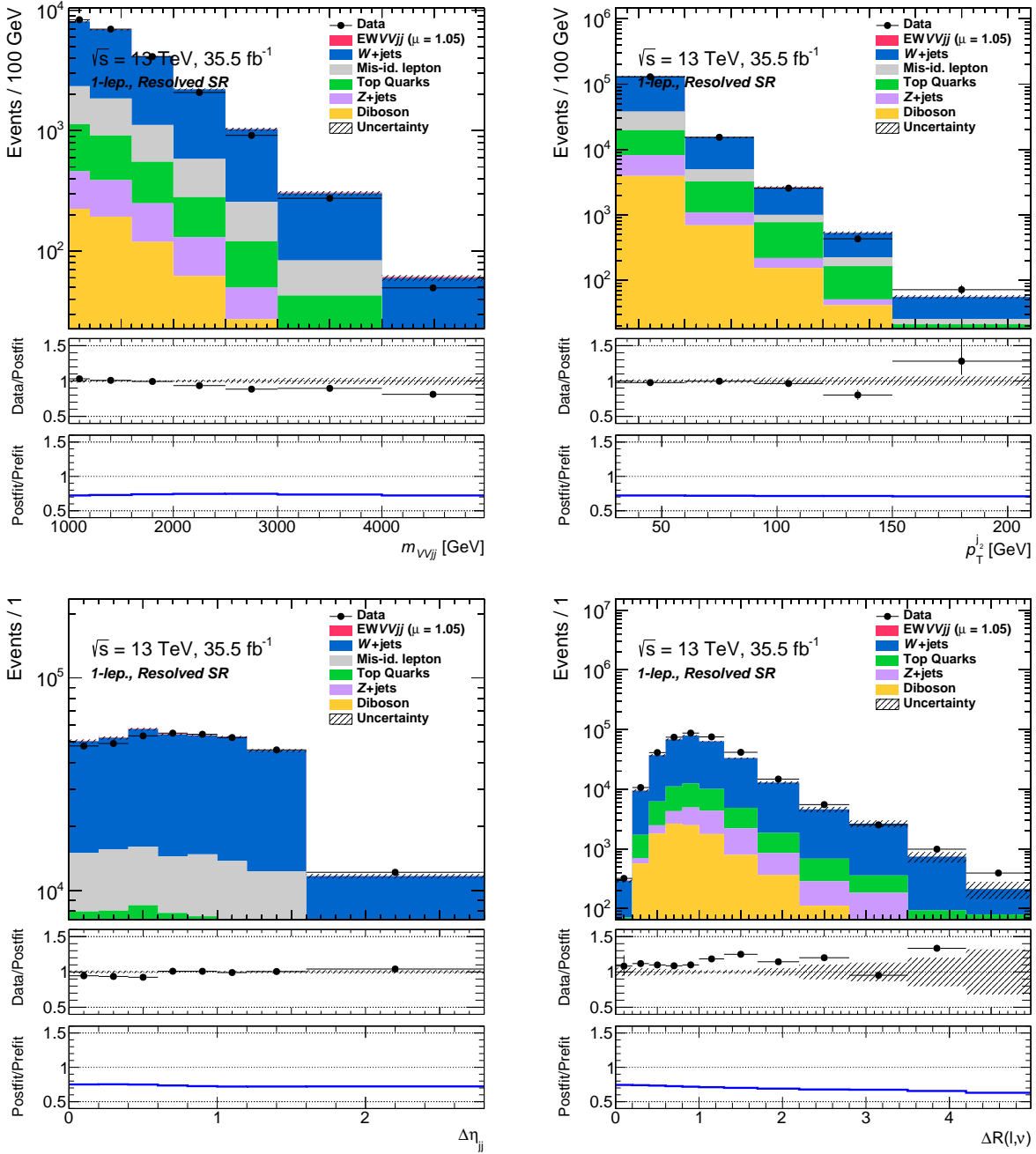


Fig. B.13: Distributions of variables used in the BDT training in the resolved region for the 1-lepton channel applying post-fit uncertainties are shown.

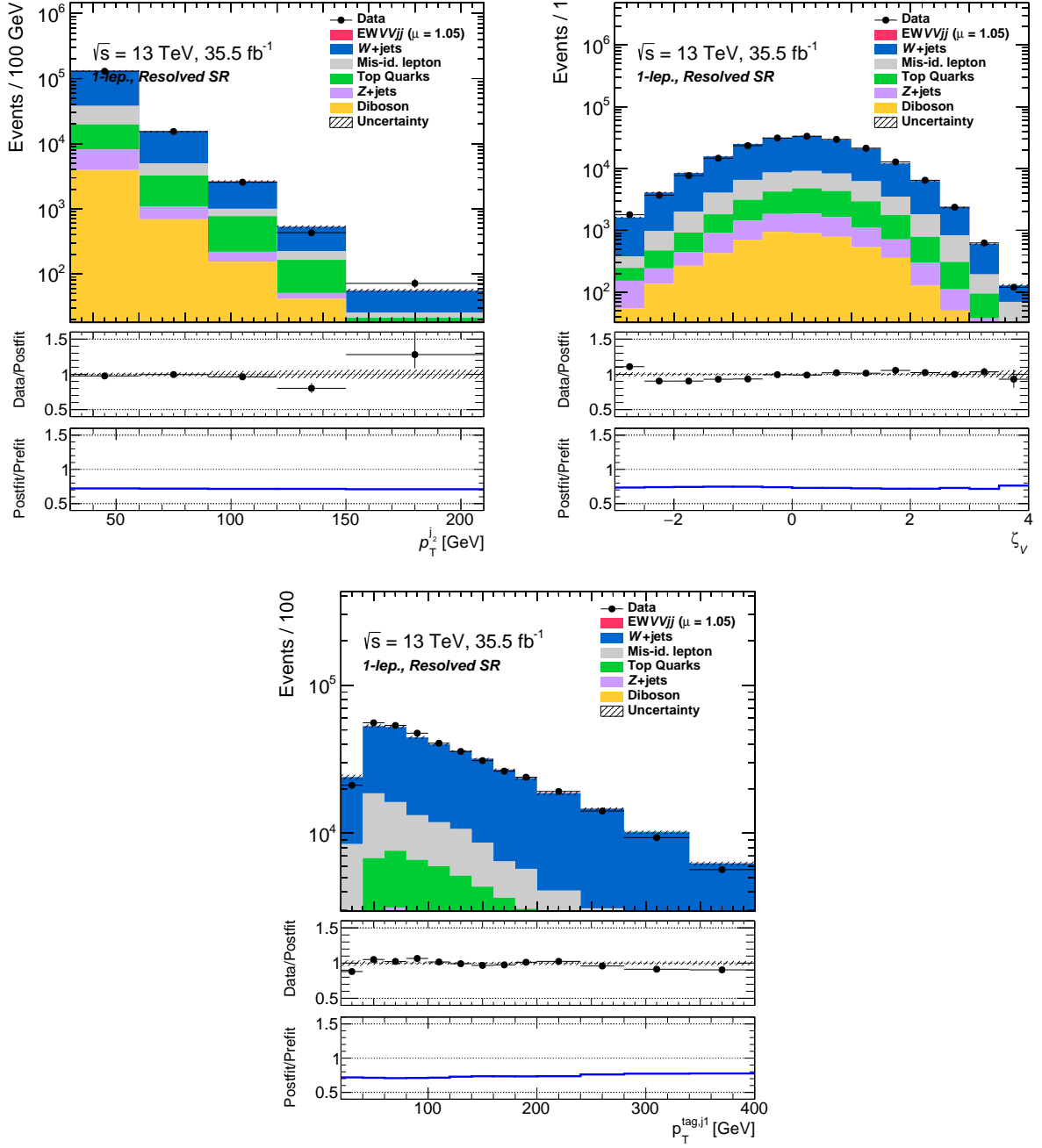


Fig. B.14: Distributions of variables used in the BDT training in the resolved region for the 1-lepton channel applying post-fit uncertainties are shown.

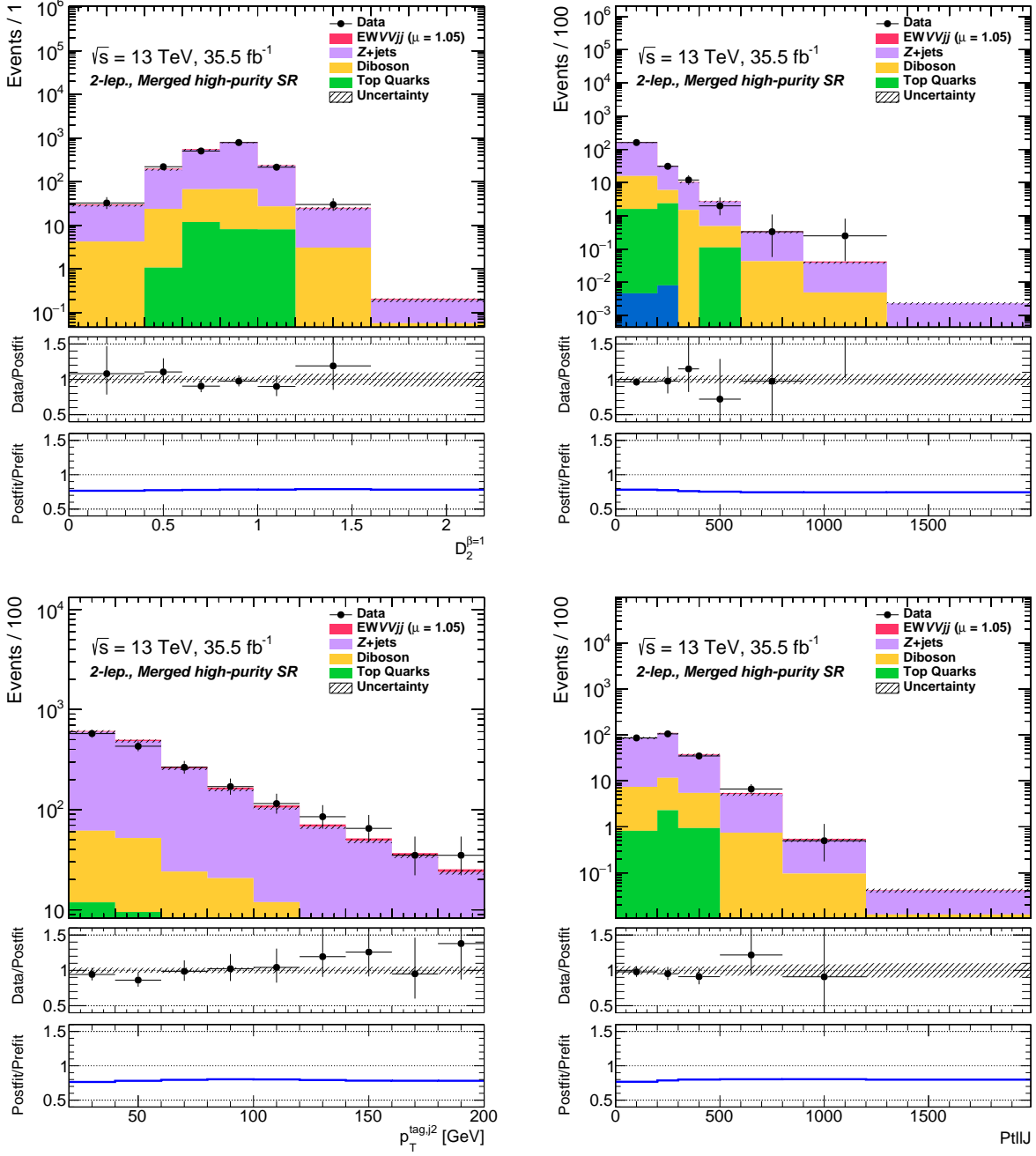


Fig. B.15: Distributions of variables used in the BDT training in the merged high-purity region for the 2-lepton channel applying post-fit uncertainties are shown.

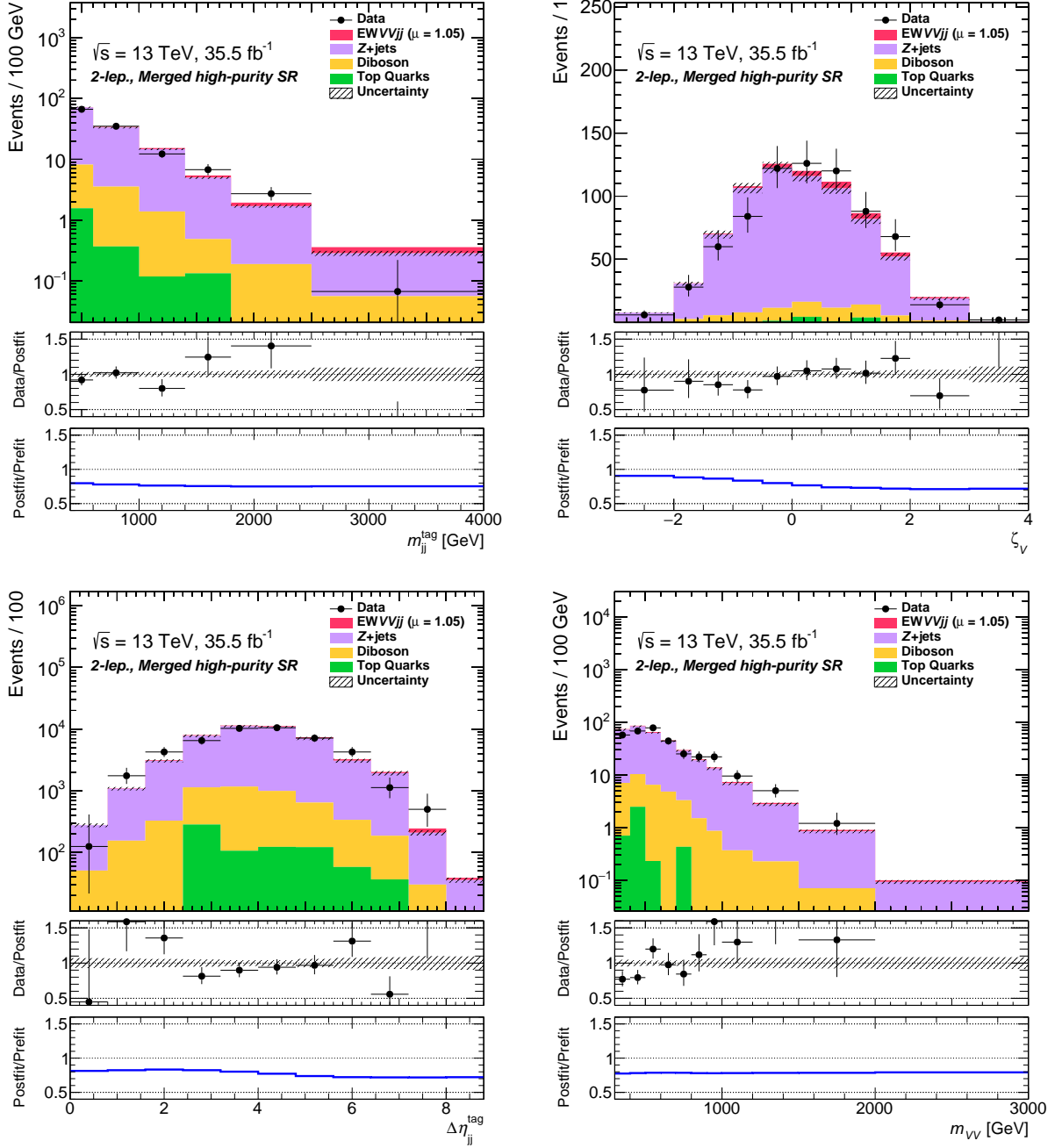


Fig. B.16: Distributions of variables used in the BDT training in the merged high-purity region for the 2-lepton channel applying post-fit uncertainties are shown.

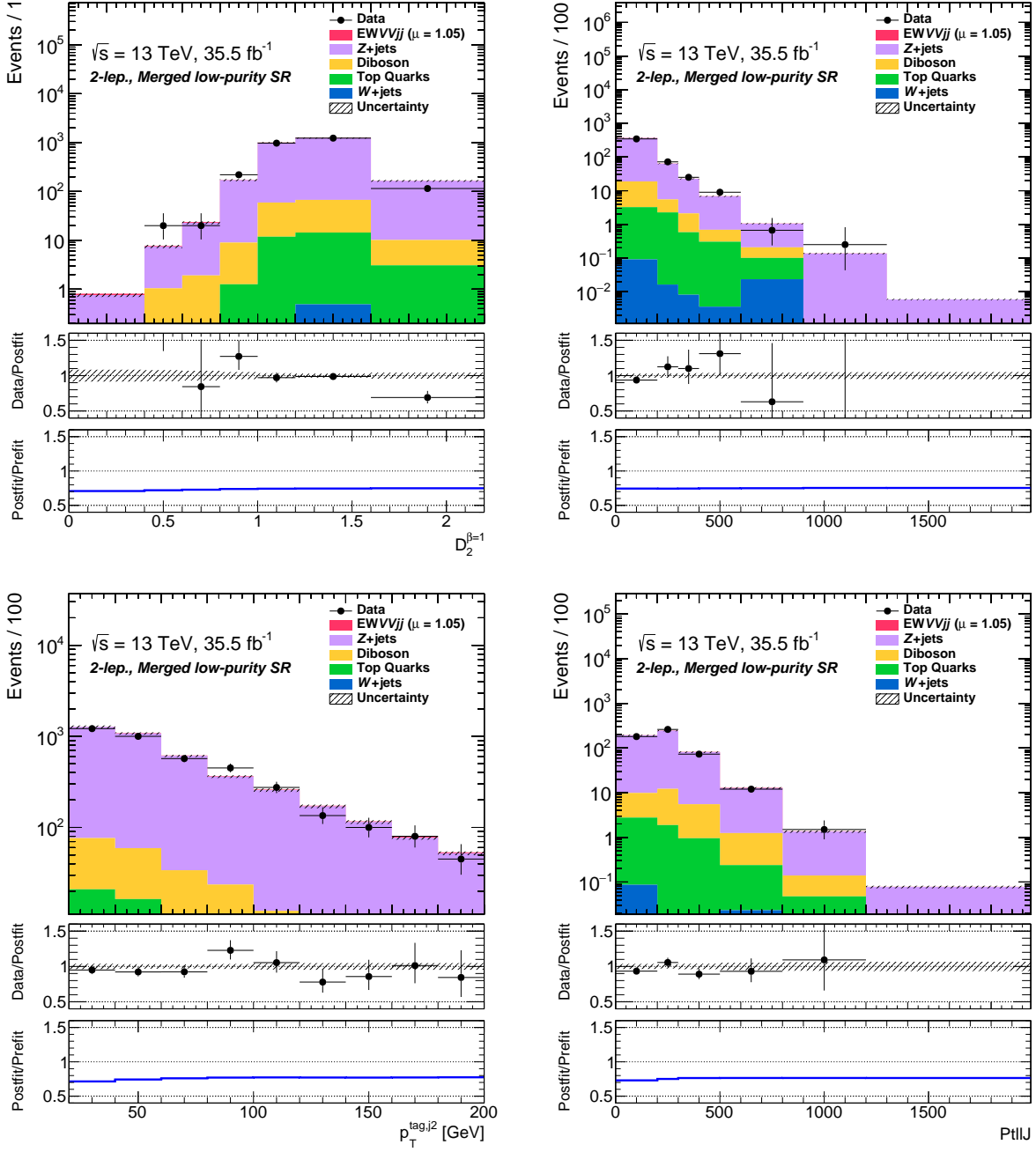


Fig. B.17: Distributions of variables used in the BDT training in the merged low-purity region for the 2-lepton channel applying post-fit uncertainties are shown.

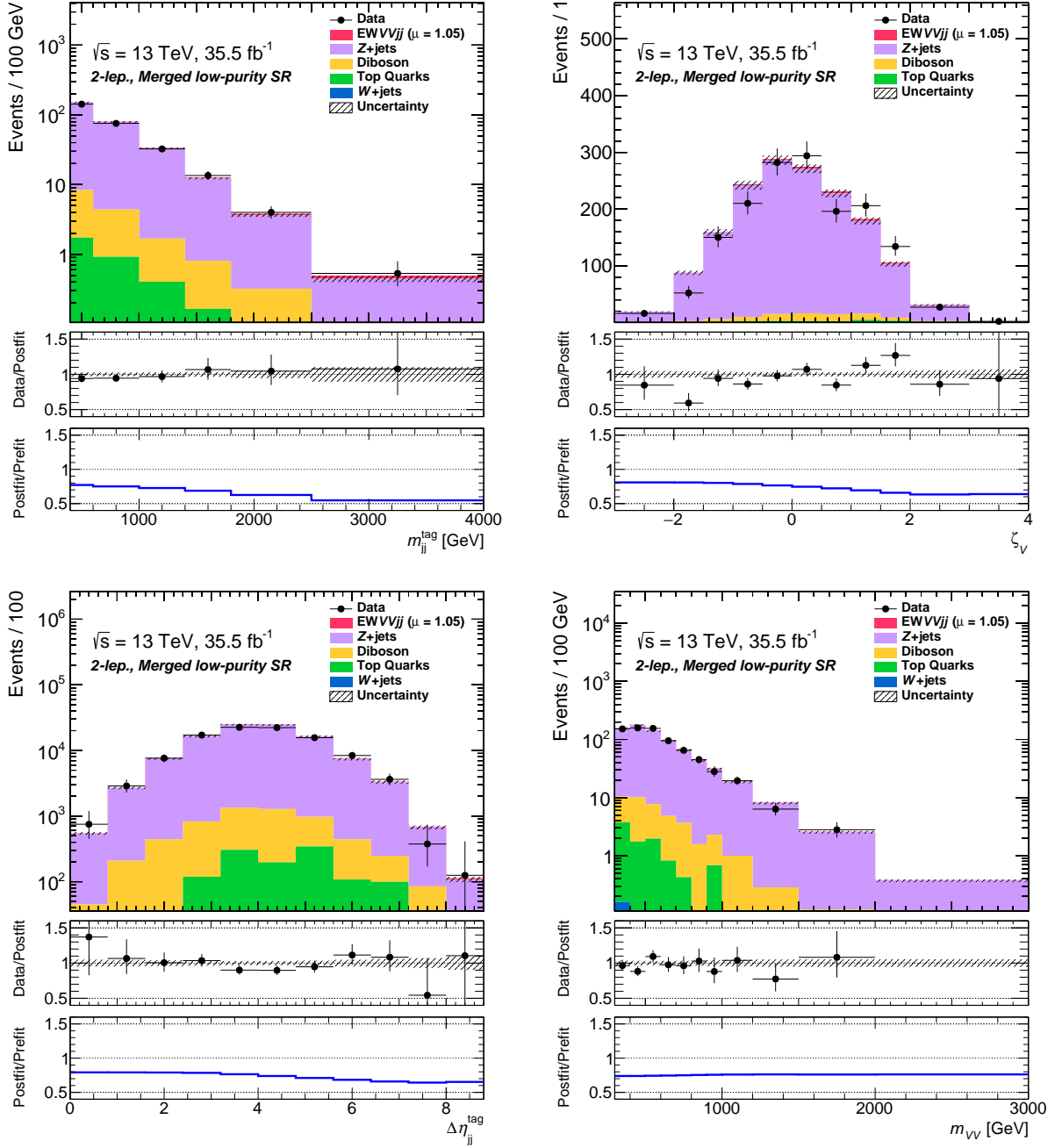


Fig. B.18: Distributions of variables used in the BDT training in the merged low-purity region for the 2-lepton channel applying post-fit uncertainties are shown.

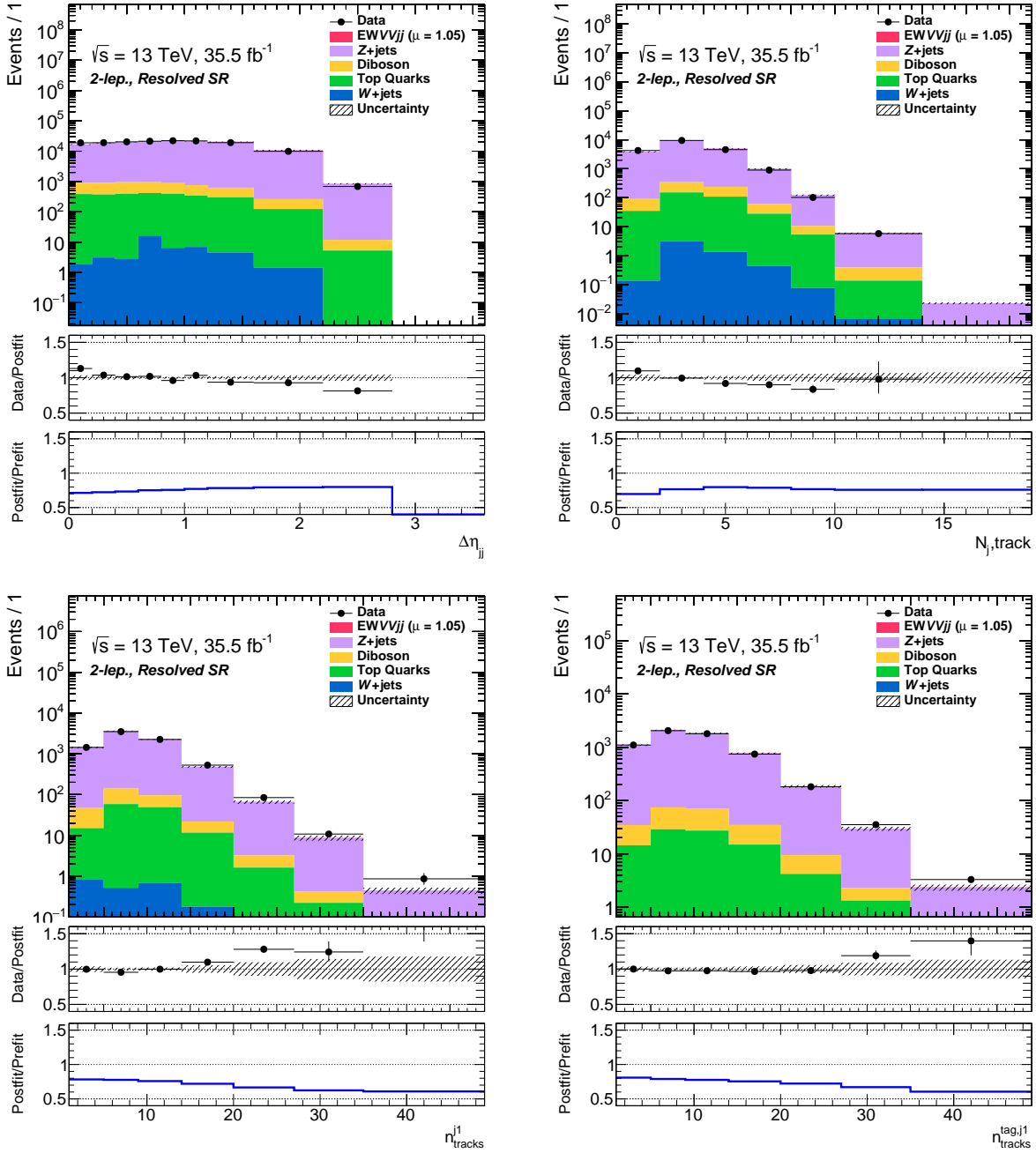


Fig. B.19: Distributions of variables used in the BDT training in the resolved region for the 2-lepton channel applying post-fit uncertainties are shown.

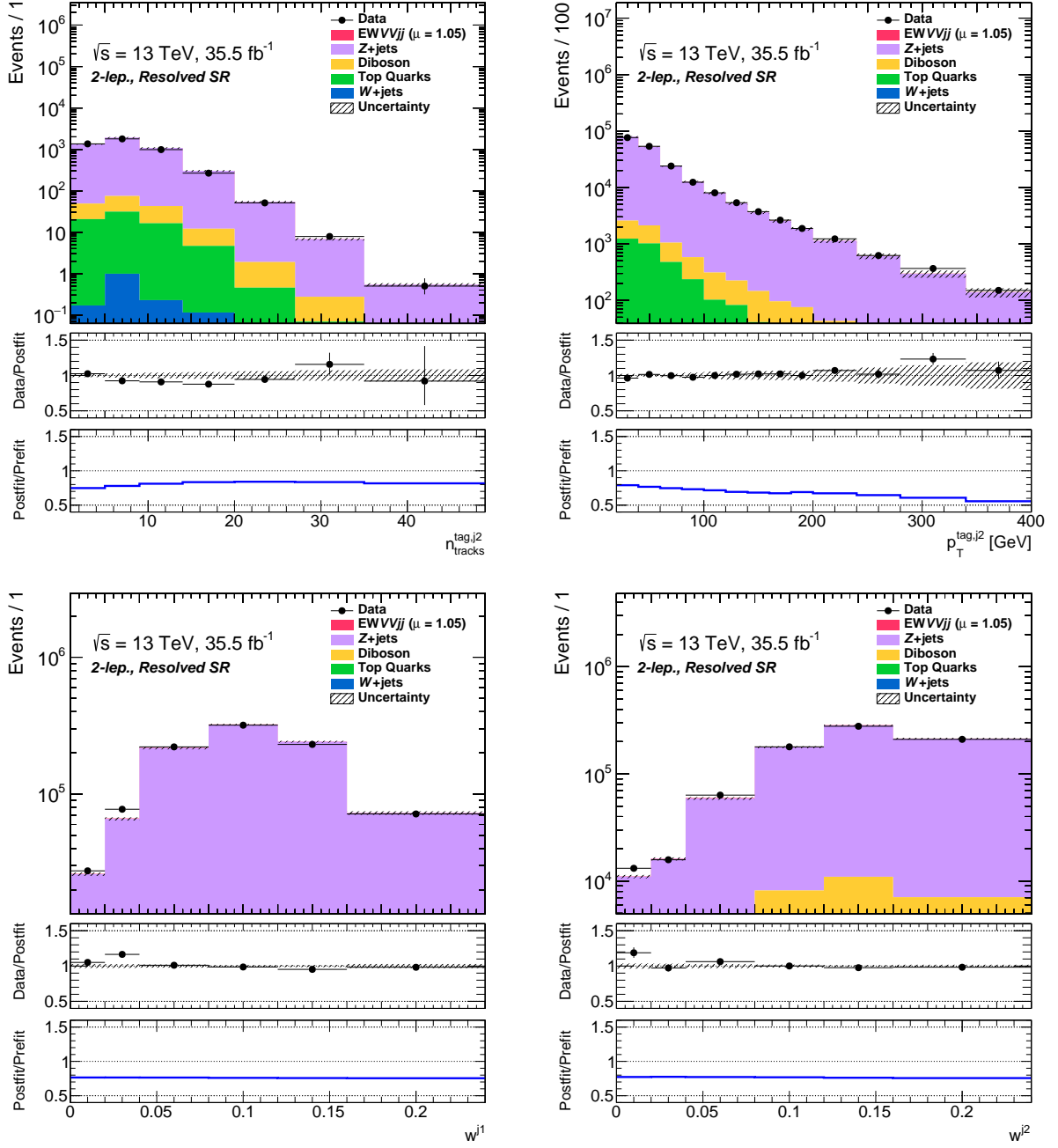


Fig. B.20: Distributions of variables used in the BDT training in the resolved region for the 2-lepton channel applying post-fit uncertainties are shown.

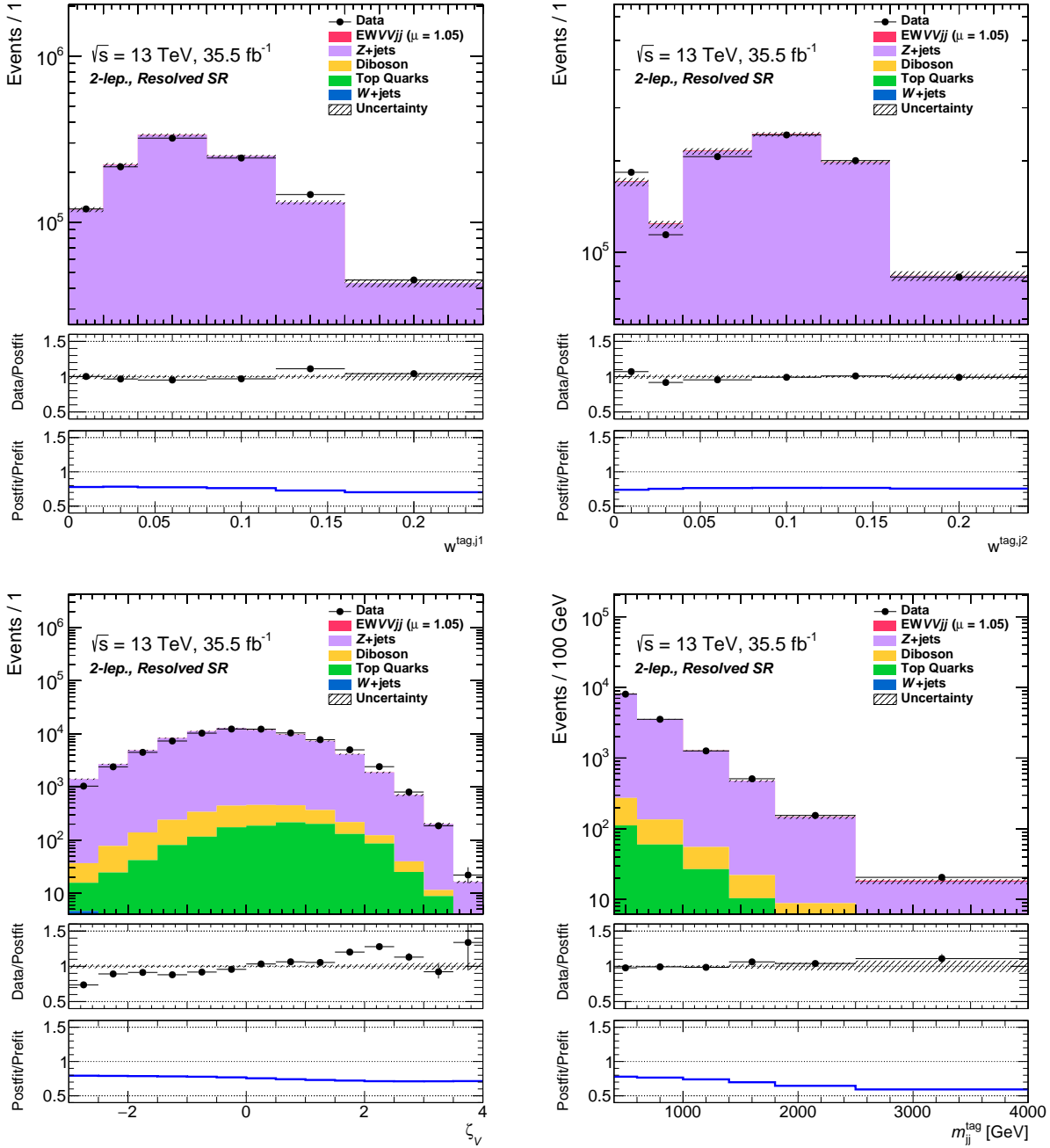


Fig. B.21: Distributions of variables used in the BDT training in the resolved region for the 2-lepton channel applying post-fit uncertainties are shown.

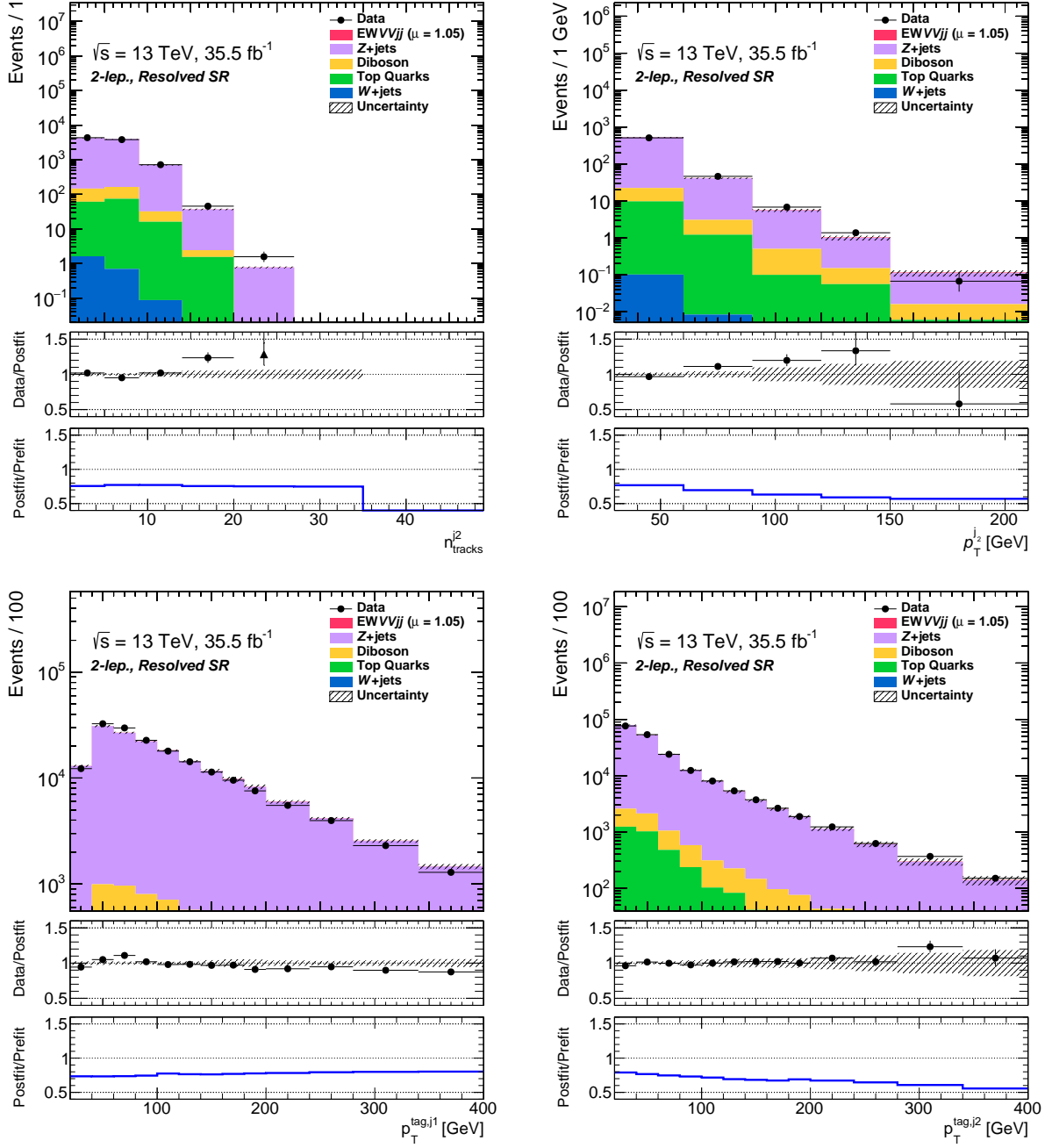


Fig. B.22: Distributions of variables used in the BDT training in the resolved region for the 2-lepton channel applying post-fit uncertainties are shown.

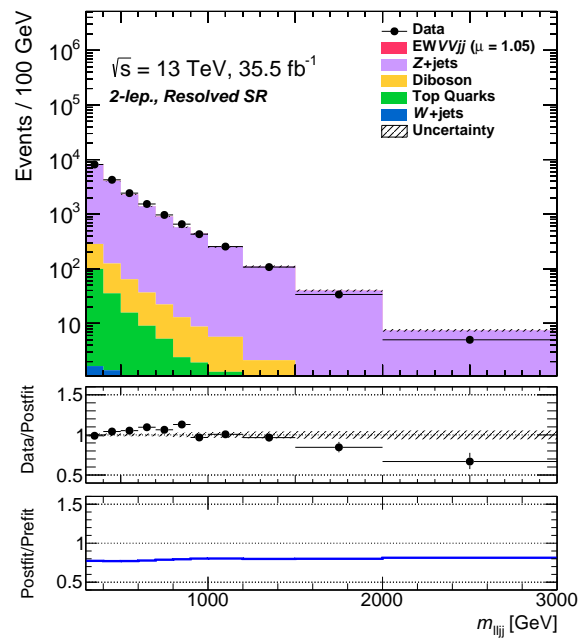


Fig. B.23: A distribution of variable used in the BDT training in the resolved region for the 2-lepton channel applying post-fit uncertainties are shown.

APPENDIX C

Understanding of BDT Input Correlation for Semileptonic VBS Analysis

The correlations between BDT inputs are particularly important because the advantage of BDT against cut-based analysis comes from exploiting the correlation between inputs. The linear correlation coefficients between input variables are shown in Figure C.1 and C.2, Figure C.3 and C.4, and Figure C.5 and C.6, respectively. Most of the pairs of variables are weakly correlated. Significant correlations emerge among p_T^{j1} , p_T^{j2} , and $\Delta\eta_{jj}$, which come from a simple correlation between p_T and η . Also there are correlations among $p_T^{\text{tag},j1}$, $p_T^{\text{tag},j2}$, and jet width variables, which is because of a higher p_T jet narrower than that of lower p_T jet.

Modeling of correlations are checked by comparing the observed data and MC predictions for the 0, 1, and 2-lepton channels as shown in Figure C.8 and C.7, Figure C.10 and C.9, and Figure C.12 and C.11, respectively. Most of the correlations for the observed data are fairly compatible with MC simulations.

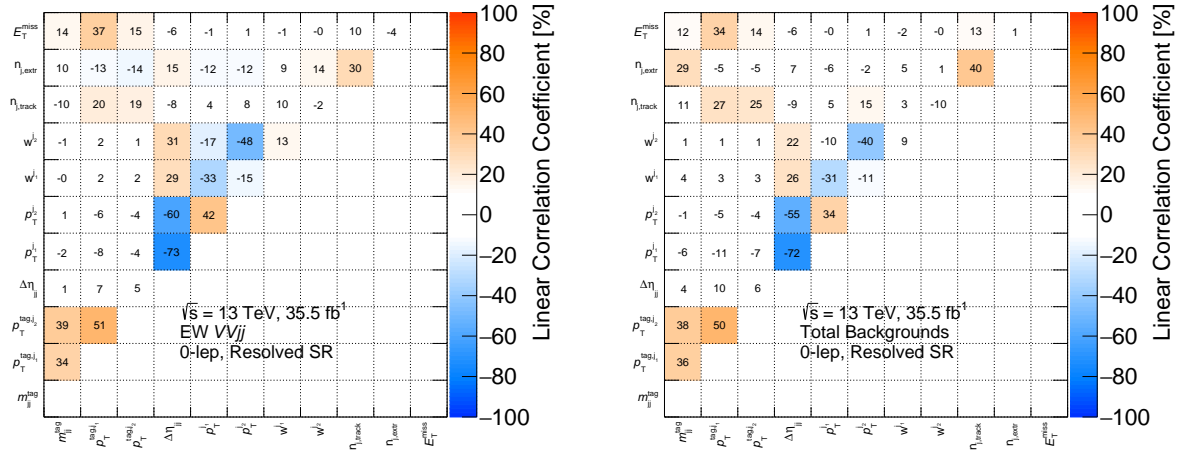


Fig. C.1: Linear correlation coefficients between input variables for signal EWVWjj events (left) and sum of background events (right) at the 0-lepton resolved SR. 100% (-100%) means completely correlated (anti-correlated).

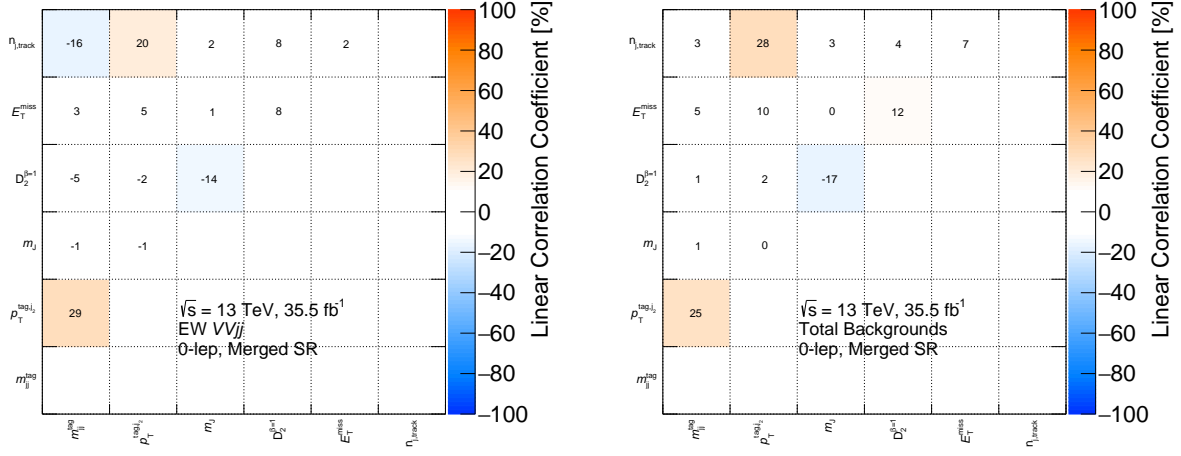


Fig. C.2: Linear correlation coefficients between input variables for signal EWWjj events (left) and sum of background events (right) at the 0-lepton resolved SR. 100% (-100%) means completely correlated (anti-correlated).

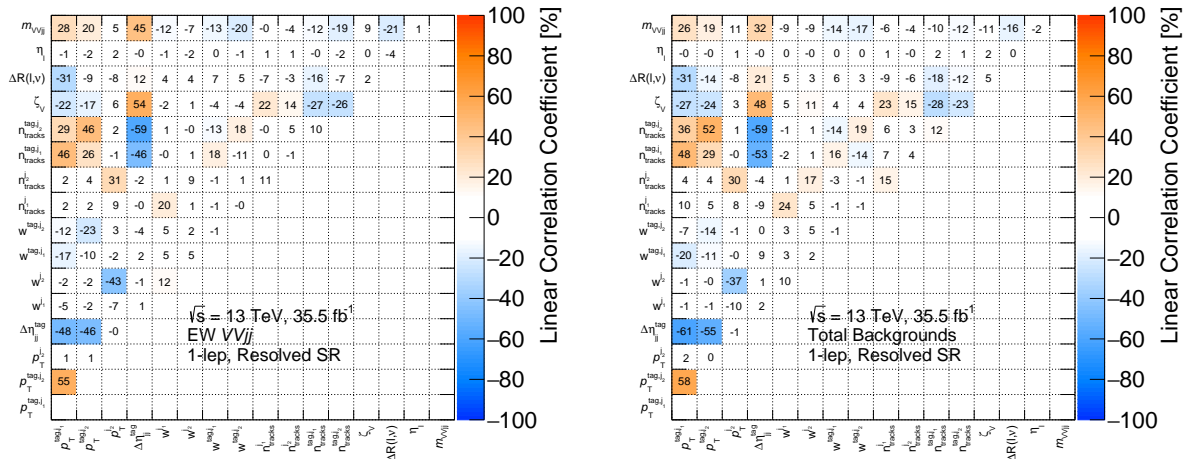


Fig. C.3: Linear correlation coefficients between input variables for signal EWWjj events (left) and sum of background events (right) at the 1-lepton resolved SR. 100% (-100%) means completely correlated (anti-correlated).

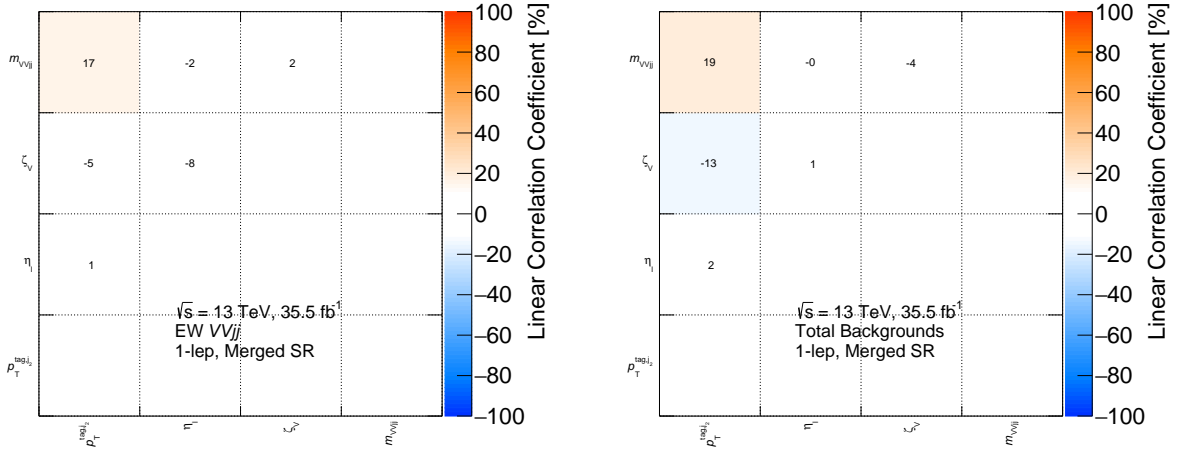


Fig. C.4: Linear correlation coefficients between input variables for signal EWVj events (left) and sum of background events (right) at the 1-lepton resolved SR. 100% (-100%) means completely correlated (anti-correlated).

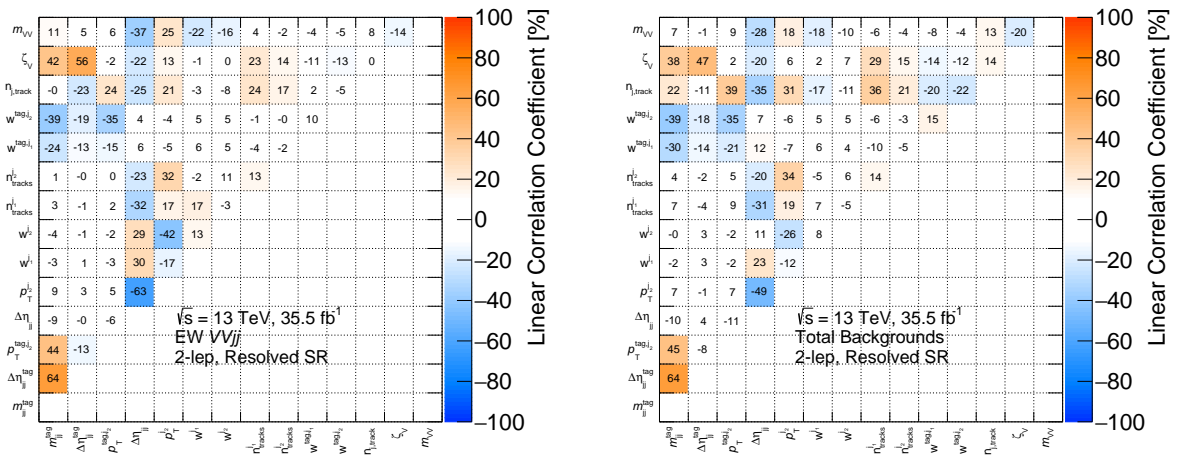


Fig. C.5: Linear correlation coefficients between input variables for signal EWVj events (left) and sum of background events (right) at the 2-lepton resolved SR. 100% (-100%) means completely correlated (anti-correlated).

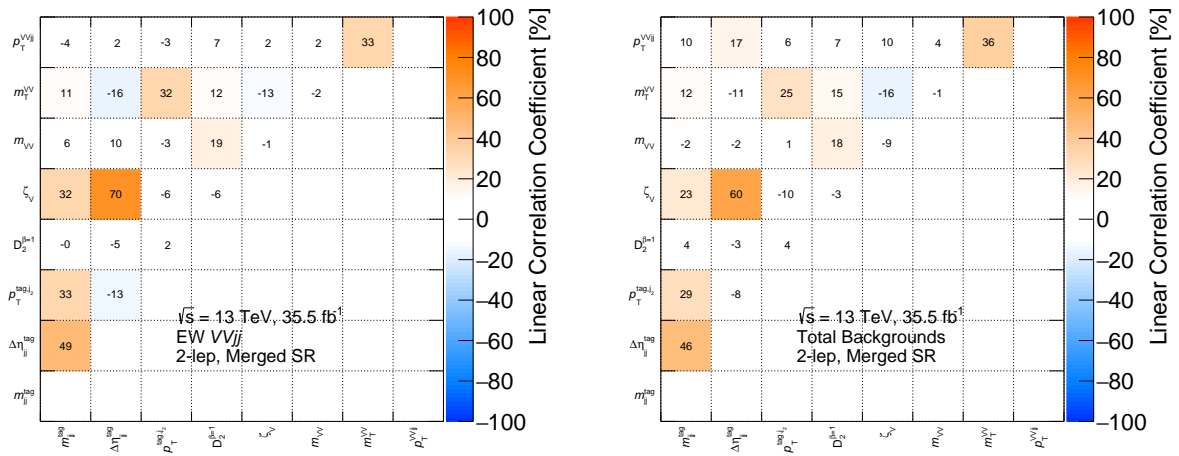


Fig. C.6: Linear correlation coefficients between input variables for signal EW VVjj events (left) and sum of background events (right) at the 2-lepton resolved SR. 100% (-100%) means completely correlated (anti-correlated).

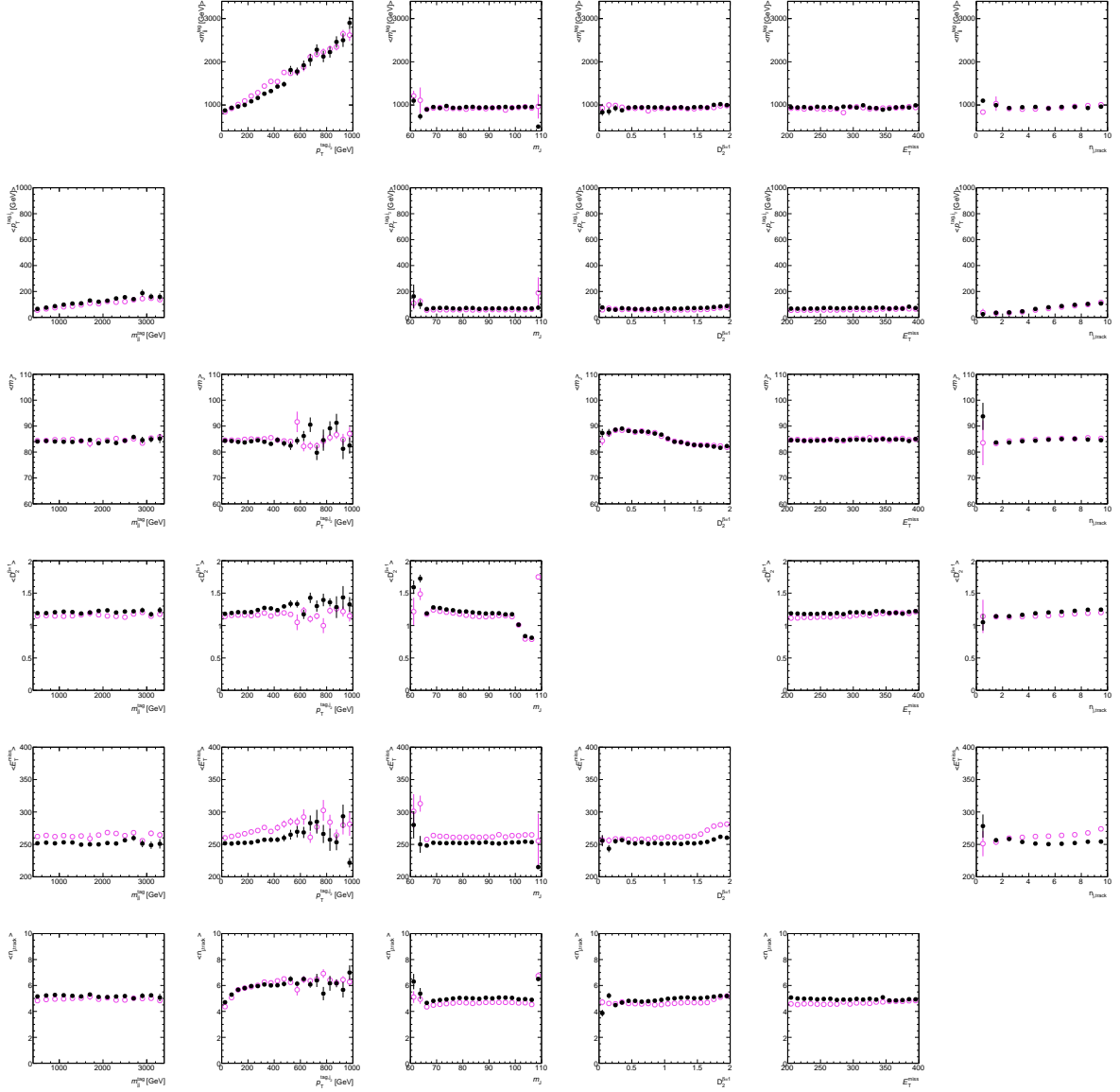


Fig. C.7: The correlations between BDT input variables for the 0-lepton merged signal region are shown. The magenta and black marker represent the MC prediction and observed data. The $\langle X \rangle$ represents mean of the variable X distribution. Only statistical uncertainty in the mean is shown.

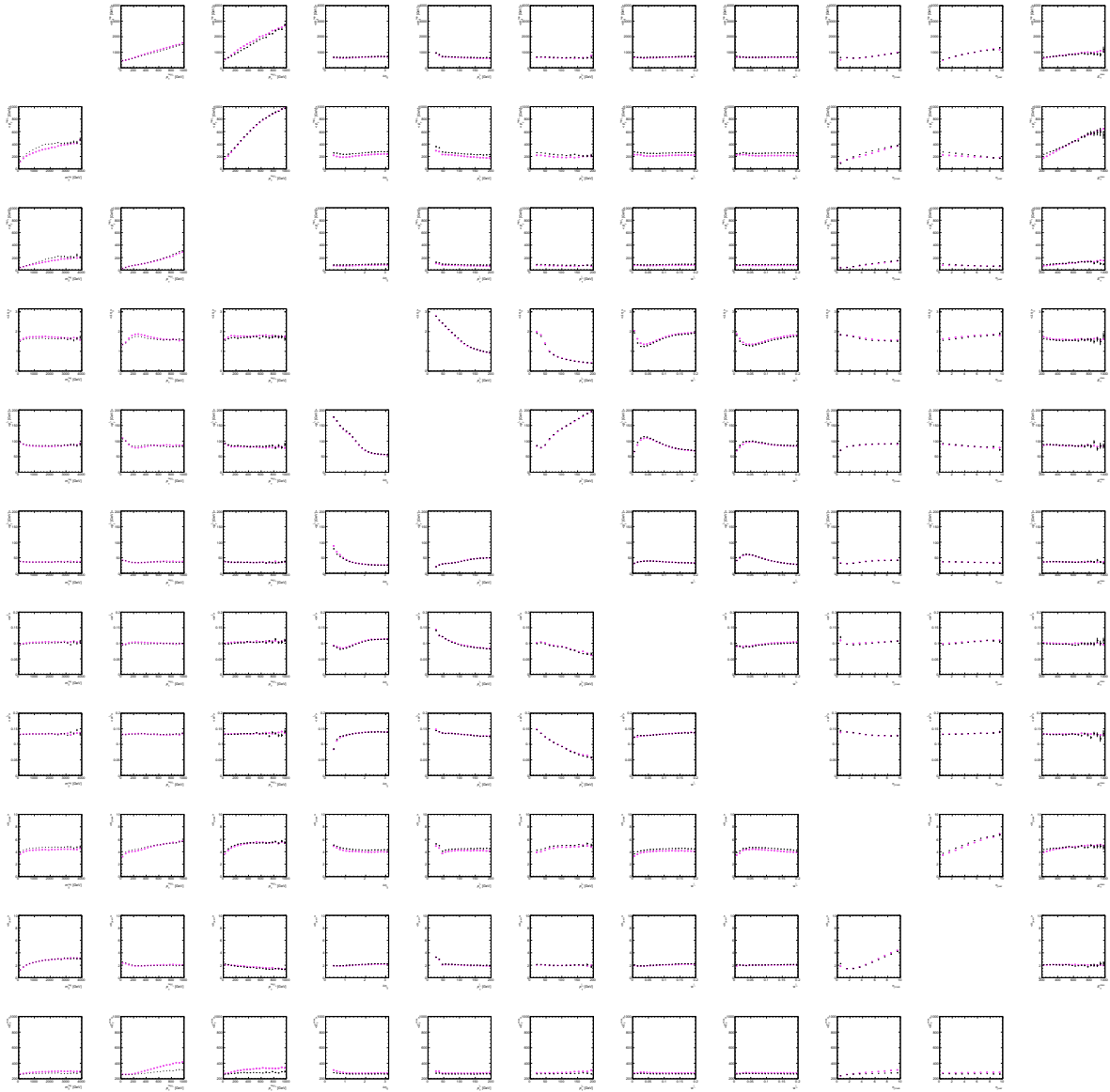


Fig. C.8: The correlations between BDT input variables for the 0-lepton resolved signal region are shown. The magenta and black marker represent the MC prediction and observed data. The $\langle X \rangle$ represents mean of the variable X distribution. Only statistical uncertainty in the mean is shown.

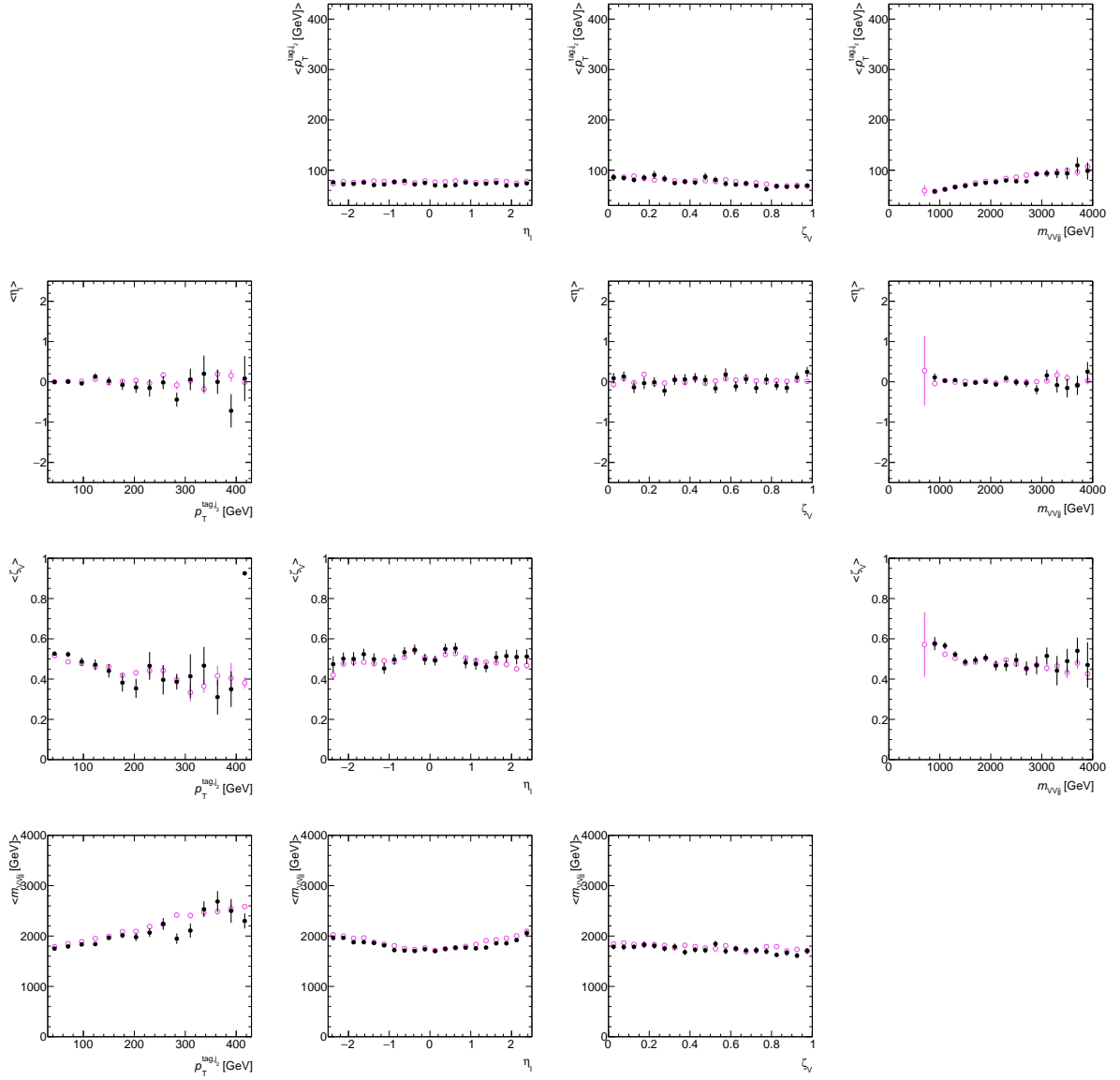


Fig. C.9: The correlations between BDT input variables for the 1-lepton merged signal region are shown. The magenta and black marker represent the MC prediction and observed data. The $\langle X \rangle$ represents mean of the variable X distribution. Only statistical uncertainty in the mean is shown.

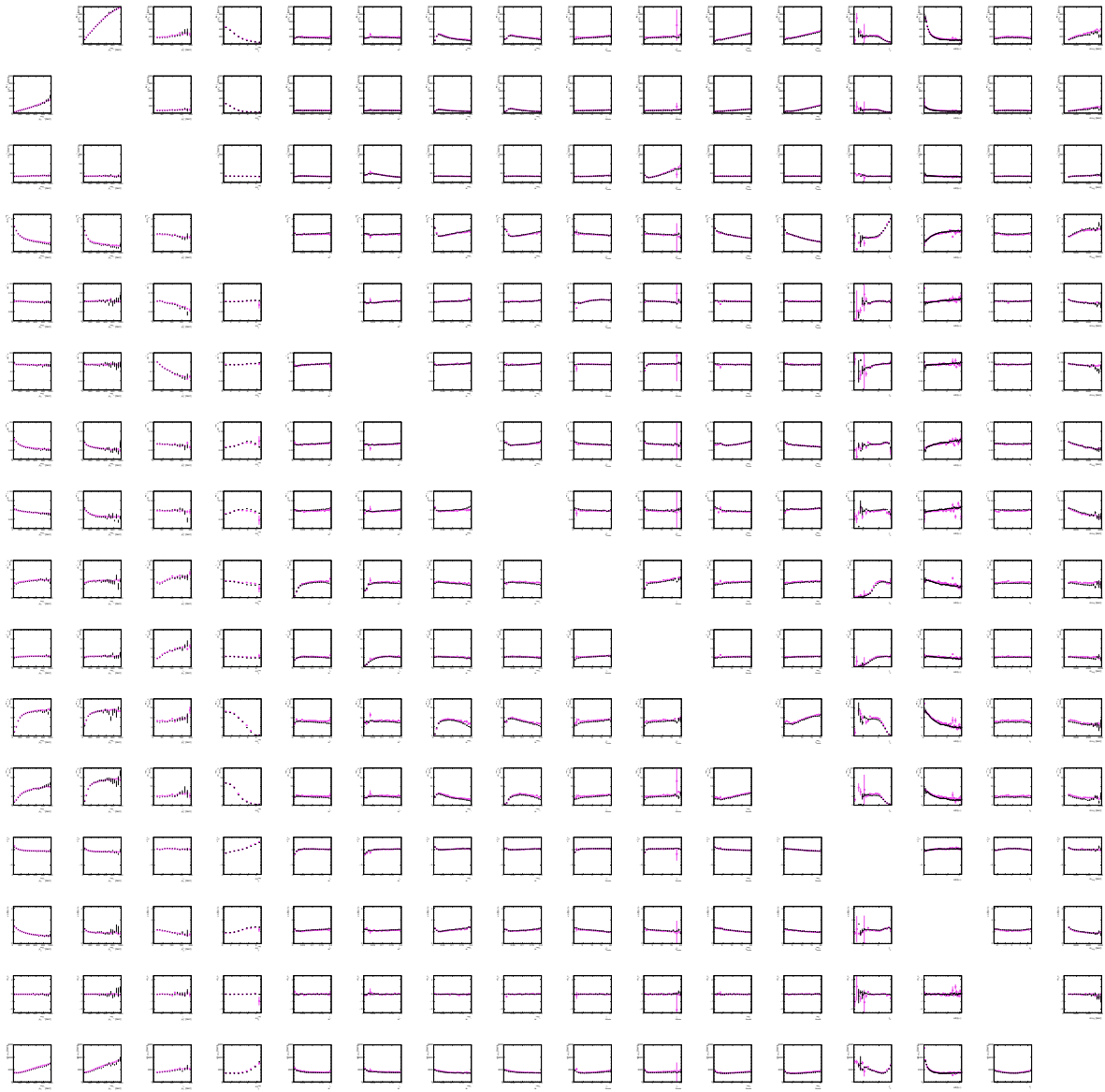


Fig. C.10: The correlations between BDT input variables for the 1-lepton resolved signal region are shown. The magenta and black marker represent the MC prediction and observed data. The $\langle X \rangle$ represents mean of the variable X distribution. Only statistical uncertainty in the mean is shown.

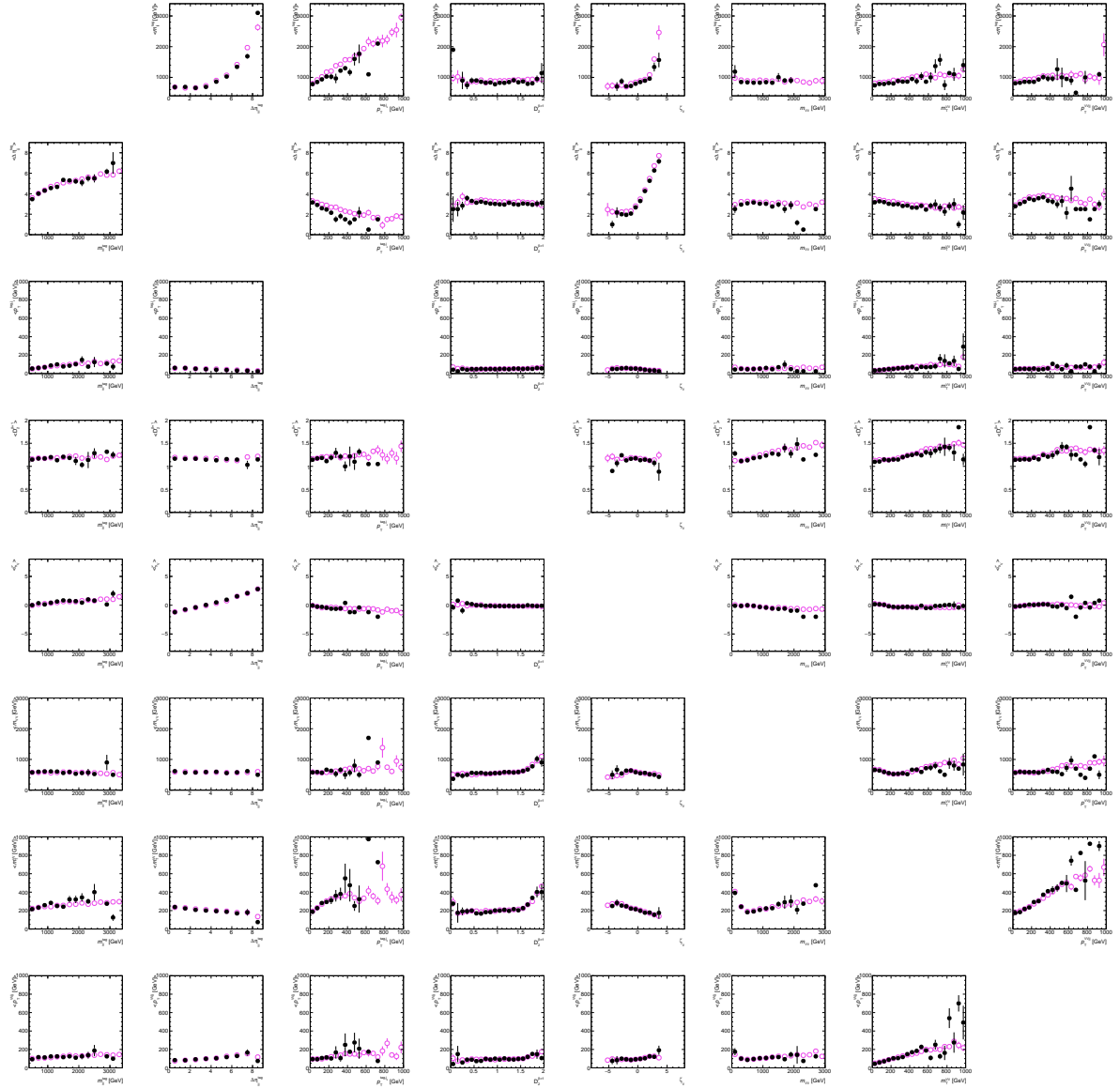


Fig. C.11: The correlations between BDT input variables for the 2-lepton merged signal region are shown. The magenta and black marker represent the MC prediction and observed data. The $\langle X \rangle$ represents mean of the variable X distribution. Only statistical uncertainty in the mean is shown.

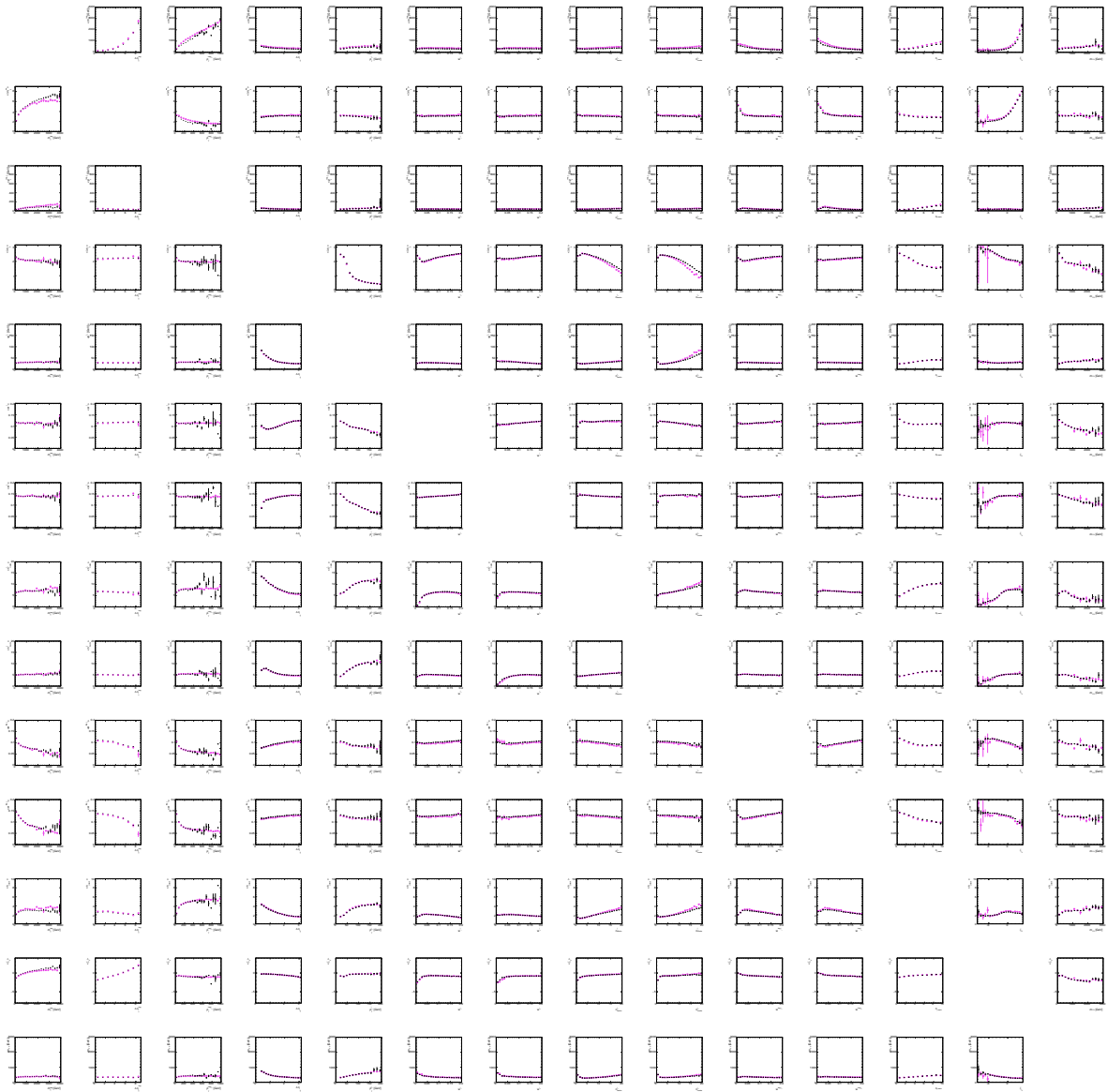


Fig. C.12: The correlations between BDT input variables for the 2-lepton resolved signal region are shown. The magenta and black marker represent the MC prediction and observed data. The $\langle X \rangle$ represents mean of the variable X distribution. Only statistical uncertainty in the mean is shown.

APPENDIX D

Summary of Nuisance Parameters for Semileptonic VBS Analysis

This appendix summarizes the nuisance parameters used in fitting for the semileptonic VBS analysis as described in Section 6.8. Lists of normalization factors, shape systematic uncertainties are shown in Table D.1, D.2, and D.3, respectively.

Table D.1: A summary of normalization factors is shown. Float in the Value column implies that the normalization factor moves freely.

Nuisance Parameter	Sample	Category	Value
norm.WLepMerged	W+ jets	merged	Float
norm.WLepResolved	W+ jets	resolved	Float
norm.ZLepMerged	Z+ jets	merged	Float
norm.ZLepResolved	Z+ jets	resolved	Float
norm.ttbarLepMerged	$t\bar{t}$	merged	Float
norm.ttbarLepResolved	$t\bar{t}$	resolved	Float
SysVNorm	diboson	common in all regions	30%
SysStopNorm	single top	common in all regions	20%
SysWjetsNorm0LepResolved	W+ jets	0lep,resolved	14%
SysWjetsNorm0LepMerged	W+ jets	0lep,merged	8%
SysZjetsNorm0LepResolved	Z+ jets	0lep,resolved	22%
SysZjetsNorm0LepMerged	Z+ jets	0lep,merged	42%

Table D.2: A summary of shape modeling systematics is shown.

Nuisance Parameter	Sample	Category	Description
SysMODEL_Wjets_MadGraph	W+ jets	VCR,SR	SHERPA v.s. MADGRAPH5_aMC@NLO
SysMODEL_Zjets_MadGraph	Z+ jets	VCR,SR	SHERPA v.s. MADGRAPH5_aMC@NLO
SysMODEL_VV_PwPy	Diboson	SR	SHERPA v.s. POWHEG+PYTHIA8
SysMODEL_ttbar_rad	$t\bar{t}$	SR	QCD-scale
SysMODEL_ttbar_Herwig	$t\bar{t}$	SR	POWHEG+PYTHIA8 v.s. POWHEG+HERWIG
SysMODEL_ttbar_aMcAtNlo	$t\bar{t}$	SR	POWHEG v.s. MADGRAPH5_aMC@NLO
SysINTERFERENCE_VBSvsQCDVV	signal	SR	Interference: $\text{Re}(M_{EW} \cdot M_{QCD}^*)$
SysMJ_El_EWK	multijet	1-lepton	Twice of EWK scale factor
SysMJ_Mu_EWK	multijet	1-lepton	Difference of electron id in MET reconstruction
SysMJ_Mu_METstr	multijet	1-lepton	Difference of muon isolation in MET reconstruction

Table D.3: A qualitative summary of the systematic uncertainties included in this analysis is shown.

Source	Description	Nuisance Parameter
Electrons	Trigger	EL.EFF_Trigger_TOTAL_1NPCOR_PLUS_UNCOR
	Energy scale	EG.SCALE_ALL
	Energy resolution	EG.RESOLUTION_ALL
	ID efficiency SF	EL.EFF_ID_TOTAL_1NPCOR_PLUS_UNCOR
	Isolation efficiency SF	EL.EFF_Iso_TOTAL_1NPCOR_PLUS_UNCOR
	Reconstruction efficiency SF	EL.EFF_Reco_TOTAL_1NPCOR_PLUS_UNCOR
Muons	p_T scale	MUONS_SCALE
	p_T scale (charge dependent)	MUON_SAGITTA_RHO
	p_T scale (charge dependent)	MUON_SAGITTA_RESBIAS
	p_T resolution MS	MUONS_MS
	p_T resolution ID	MUONS_ID
	Isolation efficiency SF	MUON_ISO_SYS
	Isolation efficiency SF	MUON_ISO_STAT
	Muon reco & ID efficiency SF	MUONS_EFF_STAT
	Muon reco & ID efficiency SF	MUONS_EFF_STAT_LOWPT
	Muon reco & ID efficiency SF	MUONS_EFF_SYST
	Muon reco & ID efficiency SF	MUONS_EFF_SYST_LOWPT
	Track-to-vertex association efficiency SF	MUON_TTVA_SYS
Track-to-vertex association efficiency SF	MUON_TTVA_STAT	
E_T^{miss}	Trigger scale factor	METTrigStat
	Trigger scale factor	METTrigTop
	Soft term	MET_SoftTrk_ResoPerp
	Soft term	MET_SoftTrk_ResoPara
	Soft term	MET_SoftTrk_Scale
	Trigger SF	METTrigStat
	Trigger SF	METTrigTop
Small-R jets	JES globally reduced	JET_BJES_Response
	JES globally reduced	JET_EffectiveNP_1
	JES globally reduced	JET_EffectiveNP_2
	JES globally reduced	JET_EffectiveNP_3
	JES globally reduced	JET_EffectiveNP_4
	JES globally reduced	JET_EffectiveNP_5
	JES globally reduced	JET_EffectiveNP_6
	JES globally reduced	JET_EffectiveNP_7
	JES globally reduced	JET_EffectiveNP_8restTerm
	JES globally reduced	JET_EtaIntercalibration_Modelling
	JES globally reduced	JET_EtaIntercalibration_NonClosure
	JES globally reduced	JET_EtaIntercalibration_TotalStat
	JES globally reduced	JET_Flavor_Composition
	JES globally reduced	JET_Flavor_Responce
	JES globally reduced	JET_Pileup_OffsetMu
	JES globally reduced	JET_Pileup_OffsetNPV
	JES globally reduced	JET_Pileup_PtTerm
	JES globally reduced	JET_Pileup_RhoTopology
	JES globally reduced	JET_PunchThrough_MC15
	JES globally reduced	JET_SingleParticle_HighPt
Energy resolution	JET_JER_SINGLE_NP	

Table D.4: A qualitative summary of the systematic uncertainties included in this analysis is shown.

Large-R jets	p_T scale and mass scale	Jet_Comb_Modeling_Kin
	p_T scale and mass scale	Jet_Comb_Tracking_Kin
	p_T scale and mass scale	Jet_Comb_Baselining_Kin
	p_T scale and mass scale	Jet_Comb_TotalStat_Kin
	$D_2^{(\beta=1)}$ scale	Jet_Rtrk_Modeling_D2
	$D_2^{(\beta=1)}$ scale	Jet_Rtrk_Tracking_D2
	$D_2^{(\beta=1)}$ scale	Jet_Rtrk_Baselining_D2
	$D_2^{(\beta=1)}$ scale	Jet_Rtrk_TotalStat_D2
	p_T resolution	FATJET_JER
	$D_2^{(\beta=1)}$ resolution	FATJET_D2R
	Mass resolution	FATJET_JMR
b-tagging	Flavor tagging scale factors	FT_EFF_Eigen_Light0
	Flavor tagging scale factors	FT_EFF_Eigen_Light1
	Flavor tagging scale factors	FT_EFF_Eigen_Light2
	Flavor tagging scale factors	FT_EFF_Eigen_Light3
	Flavor tagging scale factors	FT_EFF_Eigen_Light4
	Flavor tagging scale factors	FT_EFF_Eigen_B0
	Flavor tagging scale factors	FT_EFF_Eigen_B1
	Flavor tagging scale factors	FT_EFF_Eigen_B2
	Flavor tagging scale factors	FT_EFF_Eigen_C0
	Flavor tagging scale factors	FT_EFF_Eigen_C1
	Flavor tagging scale factors	FT_EFF_Eigen_C2
	Flavor tagging scale factors	FT_EFF_Eigen_C3
	Flavor tagging scale factors	FT_EFF_Eigen_extrapolation
	Flavor tagging scale factors	FT_EFF_Eigen_extrapolation_from_charm
	Pileup reweighting	PRW_DATASF
	Luminosity	LumiNP
Theory	Signal	Signal_PDF
	Signal	Signal_ISR_FSR

Bibliography

- [1] F. Zwicky. “Die Rotverschiebung von extragalaktischen Nebeln”. In: *Helvetica Physica Acta* 6 (1933), pp. 110–127.
- [2] N. Aghanim et al. *Planck 2018 results. VI. Cosmological parameters*. 2018. arXiv: 1807.06209 [astro-ph.CO].
- [3] Edwin Hubble. “A relation between distance and radial velocity among extra-galactic nebulae”. In: *Proceedings of the National Academy of Sciences* 15.3 (1929), pp. 168–173. ISSN: 0027-8424. DOI: 10.1073/pnas.15.3.168. eprint: <https://www.pnas.org/content/15/3/168.full.pdf>. URL: <https://www.pnas.org/content/15/3/168>.
- [4] J. Zuntz et al. “Dark Energy Survey Year 1 Results: Weak Lensing Shape Catalogues”. In: *Mon. Not. Roy. Astron. Soc.* 481.1 (2018), pp. 1149–1182. DOI: 10.1093/mnras/sty2219. arXiv: 1708.01533 [astro-ph.CO].
- [5] M. Aaboud et al. “Measurement of the Higgs boson mass in the $H \rightarrow ZZ^* \rightarrow 4l$ and $H \rightarrow \gamma\gamma$ channels with $\sqrt{s} = 13$ TeV pp collisions using the ATLAS detector”. In: *Physics Letters B* 784 (2018), pp. 345–366. ISSN: 0370-2693. DOI: <https://doi.org/10.1016/j.physletb.2018.07.050>. URL: <http://www.sciencedirect.com/science/article/pii/S0370269318305884>.
- [6] The CMS collaboration. “Measurements of properties of the Higgs boson decaying into the four-lepton final state in pp collisions at $\sqrt{s} = 13$ TeV”. In: *Journal of High Energy Physics* 2017.11 (Nov. 2017), p. 47. ISSN: 1029-8479. DOI: 10.1007/JHEP11(2017)047. URL: [https://doi.org/10.1007/JHEP11\(2017\)047](https://doi.org/10.1007/JHEP11(2017)047).
- [7] R. D. Peccei and Helen R. Quinn. “CP Conservation in the Presence of Pseudoparticles”. In: *Phys. Rev. Lett.* 38 (25 June 1977), pp. 1440–1443. DOI: 10.1103/PhysRevLett.38.1440. URL: <https://link.aps.org/doi/10.1103/PhysRevLett.38.1440>.
- [8] Steven Weinberg. “A New Light Boson?” In: *Phys. Rev. Lett.* 40 (4 Jan. 1978), pp. 223–226. DOI: 10.1103/PhysRevLett.40.223. URL: <https://link.aps.org/doi/10.1103/PhysRevLett.40.223>.
- [9] F. Wilczek. “Problem of Strong P and T Invariance in the Presence of Instantons”. In: *Phys. Rev. Lett.* 40 (5 Jan. 1978), pp. 279–282. DOI: 10.1103/PhysRevLett.40.279. URL: <https://link.aps.org/doi/10.1103/PhysRevLett.40.279>.
- [10] Lyndon Evans and Philip Bryant. “LHC Machine”. In: *JINST* 3 (2008), S08001. DOI: 10.1088/1748-0221/3/08/S08001.
- [11] ATLAS Collaboration. “The ATLAS Experiment at the CERN Large Hadron Collider”. In: *JINST* 3 (2008), S08003. DOI: 10.1088/1748-0221/3/08/S08003.

- [12] CMS Collaboration. “The CMS experiment at the CERN LHC”. In: *JINST* 3 (2008), S08004. DOI: 10.1088/1748-0221/3/08/S08004.
- [13] The ATLAS Collaboration. “Observation of a new particle in the search for the Standard Model Higgs boson with the ATLAS detector at the LHC”. In: *Physics Letters B* 716.1 (2012), pp. 1–29. ISSN: 0370-2693. DOI: <https://doi.org/10.1016/j.physletb.2012.08.020>. URL: <http://www.sciencedirect.com/science/article/pii/S037026931200857X>.
- [14] The CMS Collaboration. “Observation of a new boson at a mass of 125 GeV with the CMS experiment at the LHC”. In: *Physics Letters B* 716.1 (2012), pp. 30–61. ISSN: 0370-2693. DOI: <https://doi.org/10.1016/j.physletb.2012.08.021>. URL: <http://www.sciencedirect.com/science/article/pii/S0370269312008581>.
- [15] Sheldon L. Glashow. “Partial-symmetries of weak interactions”. In: *Nuclear Physics* 22.4 (1961), pp. 579–588. ISSN: 0029-5582. DOI: [https://doi.org/10.1016/0029-5582\(61\)90469-2](https://doi.org/10.1016/0029-5582(61)90469-2). URL: <http://www.sciencedirect.com/science/article/pii/0029558261904692>.
- [16] Steven Weinberg. “A Model of Leptons”. In: *Phys. Rev. Lett.* 19 (21 Nov. 1967), pp. 1264–1266. DOI: 10.1103/PhysRevLett.19.1264. URL: <https://link.aps.org/doi/10.1103/PhysRevLett.19.1264>.
- [17] Abdus Salam. “Weak and Electromagnetic Interactions”. In: *Conf. Proc.* C680519 (1968), pp. 367–377.
- [18] Kaustubh Agashe and Roberto Contino. “The minimal composite Higgs model and electroweak precision tests”. In: *Nuclear Physics B* 742 (May 2006), pp. 59–85. DOI: 10.1016/j.nuclphysb.2006.02.011.
- [19] Ryuichiro Kitano and Masafumi Kurachi. “Electroweak-Skyrmion as topological dark matter”. In: *Journal of High Energy Physics* 2016.7 (July 2016), p. 37. ISSN: 1029-8479. DOI: 10.1007/JHEP07(2016)037. URL: [https://doi.org/10.1007/JHEP07\(2016\)037](https://doi.org/10.1007/JHEP07(2016)037).
- [20] ATLAS Collaboration. *Observation of electroweak production of a same-sign W boson pair in association with two jets in pp collisions at $\sqrt{s} = 13$ TeV with the ATLAS detector*. ATLAS-CONF-2018-030. 2018. URL: <https://cds.cern.ch/record/2629411>.
- [21] CMS Collaboration. “Observation of Electroweak Production of Same-Sign W Boson Pairs in the Two Jet and Two Same-Sign Lepton Final State in Proton–Proton Collisions at 13 TeV”. In: *Phys. Rev. Lett.* 120 (2018), p. 081801. DOI: 10.1103/PhysRevLett.120.081801. arXiv: 1709.05822 [hep-ex].
- [22] ATLAS Collaboration. “Observation of electroweak $W^{\pm}Z$ boson pair production in association with two jets in pp collisions at $\sqrt{s} = 13$ TeV with the ATLAS detector”. In: *Phys. Lett.* (2018). arXiv: 1812.09740 [hep-ex].
- [23] *Observation of electroweak production of two jets in association with a Z-boson pair in pp collisions at $\sqrt{s} = 13$ TeV with the ATLAS detector*. Geneva, July 2019. URL: <https://cds.cern.ch/record/2682845>.

- [24] CMS Collaboration. *Measurement of electroweak production of $Z\gamma$ in association with two jets in proton-proton collisions at $\sqrt{s} = 13$ TeV*. URL: <https://cds.cern.ch/record/2682214/files/SMP-18-007-pas.pdf>.
- [25] CMS Collaboration. “Measurement of electroweak WZ boson production and search for new physics in WZ + two jets events in pp collisions at $\sqrt{s} = 13$ TeV”. In: (2019). arXiv: 1901.04060 [hep-ex].
- [26] ATLAS Collaboration. “Measurements of $W^\pm Z$ production cross sections in pp collisions at $\sqrt{s} = 8$ TeV with the ATLAS detector and limits on anomalous gauge boson self-couplings”. In: *Phys. Rev. D* 93 (2016), p. 092004. DOI: 10.1103/PhysRevD.93.092004. arXiv: 1603.02151 [hep-ex].
- [27] ATLAS Collaboration. “Studies of $Z\gamma$ production in association with a high-mass dijet system in pp collisions at $\sqrt{s} = 8$ TeV with the ATLAS detector”. In: *JHEP* 07 (2017), p. 107. DOI: 10.1007/JHEP07(2017)107. arXiv: 1705.01966 [hep-ex].
- [28] CMS Collaboration. “Measurement of electroweak-induced production of $W\gamma$ with two jets in pp collisions at $\sqrt{s} = 8$ TeV and constraints on anomalous quartic gauge couplings”. In: *JHEP* 06 (2017), p. 106. DOI: 10.1007/JHEP06(2017)106. arXiv: 1612.09256 [hep-ex].
- [29] CMS Collaboration. “Study of Vector Boson Scattering and Search for New Physics in Events with Two Same-Sign Leptons and Two Jets”. In: *Phys. Rev. Lett.* 114 (2015), p. 051801. DOI: 10.1103/PhysRevLett.114.051801. arXiv: 1410.6315 [hep-ex].
- [30] ATLAS Collaboration. “Measurements of electroweak Wjj production and constraints on anomalous gauge couplings with the ATLAS detector”. In: *Eur. Phys. J. C* 77 (2017), p. 474. DOI: 10.1140/epjc/s10052-017-5007-2. arXiv: 1703.04362 [hep-ex].
- [31] CMS Collaboration. “Evidence for exclusive $\gamma\gamma \rightarrow W^+W^-$ production and constraints on anomalous quartic gauge couplings in pp collisions at $\sqrt{s} = 7$ and 8 TeV”. In: *JHEP* 08 (2016), p. 119. DOI: 10.1007/JHEP08(2016)119. arXiv: 1604.04464 [hep-ex].
- [32] ATLAS Collaboration. “Search for anomalous electroweak production of WW/WZ in association with a high-mass dijet system in pp collisions at $\sqrt{s} = 8$ TeV with the ATLAS detector”. In: *Phys. Rev. D* 95 (2017), p. 032001. DOI: 10.1103/PhysRevD.95.032001. arXiv: 1609.05122 [hep-ex].
- [33] CMS Collaboration. “Measurement of the cross section for electroweak production of $Z\gamma$ in association with two jets and constraints on anomalous quartic gauge couplings in proton-proton collisions at $\sqrt{s} = 8$ TeV”. In: *Phys. Lett. B* 770 (2017), p. 380. DOI: 10.1016/j.physletb.2017.04.071. arXiv: 1702.03025 [hep-ex].
- [34] CMS Collaboration. “Search for anomalous electroweak production of $WW/WZ/ZZ$ boson pairs in association with two jets in proton-proton collisions at 13 TeV”. In: (2019). arXiv: 1905.07445 [hep-ex].

- [35] Hideki Yukawa. “On the Interaction of Elementary Particles. I”. In: *Progress of Theoretical Physics Supplement* 1 (Jan. 1955), pp. 1–10. ISSN: 0375-9687. DOI: 10.1143/PTPS.1.1. eprint: <http://oup.prod.sis.lan/ptps/article-pdf/doi/10.1143/PTPS.1.1/5310694/1-1.pdf>. URL: <https://doi.org/10.1143/PTPS.1.1>.
- [36] M. Tanabashi et al. “Review of Particle Physics”. In: *Phys. Rev. D* 98 (3 Aug. 2018), p. 030001. DOI: 10.1103/PhysRevD.98.030001. URL: <https://link.aps.org/doi/10.1103/PhysRevD.98.030001>.
- [37] A. Denner and T. Hahn. “Radiative corrections to $W^+W^- \rightarrow W^+W^-$ in the electroweak standard model”. In: *Nuclear Physics B* 525.1 (1998), pp. 27–50. ISSN: 0550-3213. DOI: [https://doi.org/10.1016/S0550-3213\(98\)00287-9](https://doi.org/10.1016/S0550-3213(98)00287-9). URL: <http://www.sciencedirect.com/science/article/pii/S0550321398002879>.
- [38] J. Alwall et al. “The automated computation of tree-level and next-to-leading order differential cross sections, and their matching to parton shower simulations”. In: *JHEP* 07 (2014), p. 079. DOI: 10.1007/JHEP07(2014)079. arXiv: 1405.0301 [hep-ph].
- [39] Steven Weinberg. “Implications of dynamical symmetry breaking”. In: *Phys. Rev. D* 13 (4 Feb. 1976), pp. 974–996. DOI: 10.1103/PhysRevD.13.974. URL: <https://link.aps.org/doi/10.1103/PhysRevD.13.974>.
- [40] Tommi Alanne, Stefano Di Chiara, and Kimmo Tuominen. “LHC data and aspects of new physics”. In: *Journal of High Energy Physics* 2014.1 (Jan. 2014), p. 41. ISSN: 1029-8479. DOI: 10.1007/JHEP01(2014)041. URL: [https://doi.org/10.1007/JHEP01\(2014\)041](https://doi.org/10.1007/JHEP01(2014)041).
- [41] Marcela Carena, Leandro Da Rold, and Eduardo Pontón. “Minimal composite Higgs models at the LHC”. In: *Journal of High Energy Physics* 2014.6 (June 2014), p. 159. ISSN: 1029-8479. DOI: 10.1007/JHEP06(2014)159. URL: [https://doi.org/10.1007/JHEP06\(2014\)159](https://doi.org/10.1007/JHEP06(2014)159).
- [42] Ryuichiro Kitano and Masafumi Kurachi. “More on Electroweak-Skyrmion”. In: *JHEP* 04 (2017), p. 150. DOI: 10.1007/JHEP04(2017)150. arXiv: 1703.06397 [hep-ph].
- [43] T.H.R. Skyrme. “A unified field theory of mesons and baryons”. In: *Nuclear Physics* 31 (1962), pp. 556–569. ISSN: 0029-5582. DOI: [https://doi.org/10.1016/0029-5582\(62\)90775-7](https://doi.org/10.1016/0029-5582(62)90775-7). URL: <http://www.sciencedirect.com/science/article/pii/0029558262907757>.
- [44] Najimuddin Khan et al. *Exploring the extended scalar sector with resonances in vector boson scattering*. Aug. 2016. eprint: <https://arxiv.org/pdf/1608.05673.pdf>.
- [45] John F. Gunion et al. “The Higgs Hunter’s Guide”. In: *Front. Phys.* 80 (2000), pp. 1–404.
- [46] H. Georgi. “Effective field theory”. In: *Ann. Rev. Nucl. Part. Sci.* 43 (1993), pp. 209–252. DOI: 10.1146/annurev.ns.43.120193.001233.
- [47] CMS Collaboration. *Search for anomalous couplings in semileptonic WW and WZ decays at $\sqrt{s} = 13$ TeV*. 2019.

- [48] Morad Aaboud et al. *Measurement of ZZ production in the $\ell\ell\nu\nu$ final state with the ATLAS detector in pp collisions at $\sqrt{s} = 13$ TeV*. 2019. arXiv: 1905.07163 [hep-ex].
- [49] O J. P. Eboli and M C. Gonzalez-Garcia. *Mapping the genuine bosonic quartic couplings*. Apr. 2016.
- [50] Vardan Khachatryan et al. “Evidence for exclusive $\gamma\gamma \rightarrow W^+W^-$ production and constraints on anomalous quartic gauge couplings in pp collisions at $\sqrt{s} = 7$ and 8 TeV”. In: *JHEP* 08 (2016), p. 119. DOI: 10.1007/JHEP08(2016)119. arXiv: 1604.04464 [hep-ex].
- [51] CMS Collaboration. “Measurement of vector boson scattering and constraints on anomalous quartic couplings from events with four leptons and two jets in proton–proton collisions at $\sqrt{s} = 13$ TeV”. In: *Phys. Lett. B* 774 (2017), p. 682. DOI: 10.1016/j.physletb.2017.10.020. arXiv: 1708.02812 [hep-ex].
- [52] David J. Gross and Frank Wilczek. “Ultraviolet Behavior of Non-Abelian Gauge Theories”. In: *Phys. Rev. Lett.* 30 (26 June 1973), pp. 1343–1346. DOI: 10.1103/PhysRevLett.30.1343. URL: <https://link.aps.org/doi/10.1103/PhysRevLett.30.1343>.
- [53] Richard D. Ball et al. “Parton distributions with LHC data”. In: *Nucl. Phys. B* 867 (2013), pp. 244–289. DOI: 10.1016/j.nuclphysb.2012.10.003. arXiv: 1207.1303 [hep-ph].
- [54] J. Pumplin et al. “New generation of parton distributions with uncertainties from global QCD analysis”. In: *JHEP* 07 (2002), p. 012. DOI: 10.1088/1126-6708/2002/07/012. arXiv: hep-ph/0201195.
- [55] Torbjorn Sjöstrand, Stephen Mrenna, and Peter Z. Skands. “A brief introduction to PYTHIA 8.1”. In: *Comput. Phys. Commun.* 178 (2008), pp. 852–867. DOI: 10.1016/j.cpc.2008.01.036. arXiv: 0710.3820 [hep-ph].
- [56] Stefan Gieseke, Christian Rohr, and Andrzej Siodmok. “Colour reconnections in Herwig++”. In: *Eur. Phys. J. C* 72 (2012), p. 2225. DOI: 10.1140/epjc/s10052-012-2225-5. arXiv: 1206.0041 [hep-ph].
- [57] T. Sjöstrand and P. Skands. “Transverse-Momentum-Ordered Showers and Interleaved Multiple Interactions”. In: *The European Physical Journal C* 39 (Aug. 2004). DOI: 10.1140/epjc/s2004-02084-y.
- [58] Michael Dinsdale, Marko Ternick, and Stefan Weinzierl. “Parton showers from the dipole formalism”. In: *Phys. Rev. D* 76 (2007), p. 094003. DOI: 10.1103/PhysRevD.76.094003. arXiv: 0709.1026 [hep-ph].
- [59] Bryan R. Webber. *Fragmentation and Hadronization*. eprint: <https://www.slac.stanford.edu/econf/C990809/docs/webber.pdf>.
- [60] Bo Andersson et al. “Parton Fragmentation and String Dynamics”. In: *Phys. Rept.* 97 (1983), pp. 31–145. DOI: 10.1016/0370-1573(83)90080-7.
- [61] G. Marchesini and B. R. Webber. “Simulation of QCD Jets Including Soft Gluon Interference”. In: *Nucl. Phys. B* 238 (1984), pp. 1–29. DOI: 10.1016/0550-3213(84)90463-2.

- [62] Ian James Mould. *Effective Field Theories for the LHC*. 2016. eprint: <https://arxiv.org/pdf/1605.00573.pdf>.
- [63] *The CERN accelerator complex*. URL: <https://cds.cern.ch/record/1260465>.
- [64] Oliver Sim Bruning et al. *LHC Design Report*. CERN Yellow Reports: Monographs. Geneva: CERN, 2004. DOI: 10.5170/CERN-2004-003-V-1. URL: <http://cds.cern.ch/record/782076>.
- [65] José Jimenez et al. “Observations, Analysis and Mitigation of Recurrent LHC Beam Dumps Caused by Fast Losses in Arc Half-Cell 16L2”. In: *Proceedings, 9th International Particle Accelerator Conference (IPAC 2018): Vancouver, BC Canada, April 29-May 4, 2018*. 2018, MOPMF053. DOI: 10.18429/JACoW-IPAC2018-MOPMF053.
- [66] ATLAS Collaboration. *Luminosity determination in pp collisions at $\sqrt{s} = 13$ TeV using the ATLAS detector at the LHC*. ATLAS-CONF-2019-021. 2019. URL: <https://cds.cern.ch/record/2677054>.
- [67] ATLAS Collaboration. *ATLAS Insertable B-Layer Technical Design Report*. ATLAS-TDR-19. 2010. URL: <https://cds.cern.ch/record/1291633>. Addendum: ATLAS-TDR-19-ADD-1. 2012. URL: <https://cds.cern.ch/record/1451888>.
- [68] “Performance of the electronic readout of the ATLAS liquid argon calorimeters”. In: *Journal of Instrumentation* 5.09 (2010), P09003. DOI: 10.1088/1748-0221/5/09/p09003.
- [69] *Overview of TDAQ system*. URL: <https://twiki.cern.ch/twiki/pub/AtlasPublic/ApprovedPlotsDAQ/tdaqFullNew2017.pdf>.
- [70] M. zur Nedden. “The LHC Run 2 ATLAS trigger system: design, performance and plans”. In: *JINST* 12.03 (2017), p. C03024. DOI: 10.1088/1748-0221/12/03/C03024.
- [71] Azriel Rosenfeld and John L. Pfaltz. “Sequential Operations in Digital Picture Processing”. In: *J. ACM* 13.4 (Oct. 1966), pp. 471–494. ISSN: 0004-5411. DOI: 10.1145/321356.321357. URL: <http://doi.acm.org/10.1145/321356.321357>.
- [72] ATLAS Collaboration. “A neural network clustering algorithm for the ATLAS silicon pixel detector”. In: *JINST* 9 (2014), P09009. DOI: 10.1088/1748-0221/9/09/P09009. arXiv: 1406.7690 [hep-ex].
- [73] Tony Lacey. *Tutorial: The Kalman Filter*. URL: <http://web.mit.edu/kirtley/kirtley/binlustuff/literature/control/Kalman%5C%20filter.pdf>.
- [74] ATLAS Collaboration. *The Optimization of ATLAS Track Reconstruction in Dense Environments*. ATL-PHYS-PUB-2015-006. 2015. URL: <https://cds.cern.ch/record/2002609>.
- [75] *Performance of the ATLAS Inner Detector Track and Vertex Reconstruction in the High Pile-Up LHC Environment*. 2012.
- [76] Wolfgang Waltenberger, Rudolf Frühwirth, and Pascal Vanlaer. “Adaptive vertex fitting”. In: *Journal of Physics G: Nuclear and Particle Physics* 34.12 (Nov. 2007), N343–N356. DOI: 10.1088/0954-3899/34/12/n01. URL: <https://doi.org/10.1088/0954-3899/34/12/n01>.

- [77] ATLAS Collaboration. “Electron reconstruction and identification in the ATLAS experiment using the 2015 and 2016 LHC proton–proton collision data at $\sqrt{s} = 13$ TeV”. In: (2019). arXiv: 1902.04655 [hep-ex].
- [78] Andreas Hoecker et al. *TMVA: Toolkit for Multivariate Data Analysis*. 2007. arXiv: physics/0703039 [physics.data-an].
- [79] ATLAS Collaboration. “Electron and photon energy calibration with the ATLAS detector using 2015–2016 LHC proton–proton collision data”. In: *JINST* 14 (2019), P03017. DOI: 10.1088/1748-0221/14/03/P03017. arXiv: 1812.03848 [hep-ex].
- [80] ATLAS Collaboration. *Improved electron reconstruction in ATLAS using the Gaussian Sum Filter-based model for bremsstrahlung*. ATLAS-CONF-2012-047. 2012. URL: <https://cds.cern.ch/record/1449796>.
- [81] The ATLAS Collaboration. “Readiness of the ATLAS liquid argon calorimeter for LHC collisions”. In: *The European Physical Journal C* 70.3 (Dec. 2010), pp. 723–753. ISSN: 1434-6052. DOI: 10.1140/epjc/s10052-010-1354-y. URL: <https://doi.org/10.1140/epjc/s10052-010-1354-y>.
- [82] ATLAS Collaboration. *Trigger Menu in 2016*. ATL-DAQ-PUB-2017-001. 2017. URL: <https://cds.cern.ch/record/2242069>.
- [83] “Electron and photon energy calibration with the ATLAS detector using 2015 2016 LHC proton–proton collision data”. In: *Journal of Instrumentation* 14.03 (Mar. 2019), P03017–P03017. DOI: 10.1088/1748-0221/14/03/p03017.
- [84] *Muon trigger performances in 2016*. URL: https://twiki.cern.ch/twiki/bin/view/AtlasPublic/MuonTriggerPublicResults#Plots_for_2016_data_13_TeV.
- [85] J. Illingworth and J. Kittler. “A survey of the hough transform”. In: *Computer Vision, Graphics, and Image Processing* 44.1 (1988), pp. 87–116. ISSN: 0734-189X. DOI: [https://doi.org/10.1016/S0734-189X\(88\)80033-1](https://doi.org/10.1016/S0734-189X(88)80033-1). URL: <http://www.sciencedirect.com/science/article/pii/S0734189X88800331>.
- [86] ATLAS Collaboration. “Muon reconstruction performance of the ATLAS detector in proton–proton collision data at $\sqrt{s} = 13$ TeV”. In: *Eur. Phys. J. C* 76 (2016), p. 292. DOI: 10.1140/epjc/s10052-016-4120-y. arXiv: 1603.05598 [hep-ex].
- [87] Matteo Cacciari, Gavin P. Salam, and Gregory Soyez. “The anti- k_t jet clustering algorithm”. In: *JHEP* 04 (2008), p. 063. DOI: 10.1088/1126-6708/2008/04/063. arXiv: 0802.1189 [hep-ph].
- [88] Matteo Cacciari, Gavin P. Salam, and Gregory Soyez. “FastJet user manual”. In: *Eur. Phys. J. C* 72 (2012), p. 1896. DOI: 10.1140/epjc/s10052-012-1896-2. arXiv: 1111.6097 [hep-ph].
- [89] Matteo Cacciari and Gavin P. Salam. “Pileup subtraction using jet areas”. In: *Phys. Lett. B* 659 (2008), pp. 119–126. DOI: 10.1016/j.physletb.2007.09.077. arXiv: 0707.1378 [hep-ph].

- [90] ATLAS Collaboration. “Jet energy scale measurements and their systematic uncertainties in proton–proton collisions at $\sqrt{s} = 13$ TeV with the ATLAS detector”. In: *Phys. Rev. D* 96 (2017), p. 072002. DOI: 10.1103/PhysRevD.96.072002. arXiv: 1703.09665 [hep-ex].
- [91] *Jet energy scale and uncertainties in 2015-2017 data and simulation*. URL: <https://atlas.web.cern.ch/Atlas/GROUPS/PHYSICS/PLOTS/JETM-2018-006/>.
- [92] ATLAS Collaboration. “Performance of pile-up mitigation techniques for jets in pp collisions at $\sqrt{s} = 8$ TeV using the ATLAS detector”. In: *Eur. Phys. J. C* 76 (2016), p. 581. DOI: 10.1140/epjc/s10052-016-4395-z. arXiv: 1510.03823 [hep-ex].
- [93] ATLAS Collaboration. “Performance of b-jet identification in the ATLAS experiment”. In: *JINST* 11 (2016), P04008. DOI: 10.1088/1748-0221/11/04/P04008. arXiv: 1512.01094 [hep-ex].
- [94] ATLAS Collaboration. *Optimisation and performance studies of the ATLAS b-tagging algorithms for the 2017-18 LHC run*. ATL-PHYS-PUB-2017-013. 2017. URL: <https://cds.cern.ch/record/2273281>.
- [95] ATLAS Collaboration. *Secondary vertex finding for jet flavour identification with the ATLAS detector*. ATL-PHYS-PUB-2017-011. 2017. URL: <https://cds.cern.ch/record/2270366>.
- [96] R. Frühwirth. “Application of Kalman filtering to track and vertex fitting”. In: *Nuclear Instruments and Methods in Physics Research Section A: Accelerators, Spectrometers, Detectors and Associated Equipment* 262.2 (1987), pp. 444–450. ISSN: 0168-9002. DOI: [https://doi.org/10.1016/0168-9002\(87\)90887-4](https://doi.org/10.1016/0168-9002(87)90887-4). URL: <http://www.sciencedirect.com/science/article/pii/0168900287908874>.
- [97] Georges Aad et al. “ATLAS b-jet identification performance and efficiency measurement with $t\bar{t}$ events in pp collisions at $\sqrt{s} = 13$ TeV”. In: *Eur. Phys. J. C* 79.11 (2019), p. 970. DOI: 10.1140/epjc/s10052-019-7450-8. arXiv: 1907.05120 [hep-ex].
- [98] ATLAS Collaboration. “Performance of missing transverse momentum reconstruction with the ATLAS detector using proton–proton collisions at $\sqrt{s} = 13$ TeV”. In: *Eur. Phys. J. C* 78 (2018), p. 903. DOI: 10.1140/epjc/s10052-018-6288-9. arXiv: 1802.08168 [hep-ex].
- [99] ATLAS Collaboration. E_T^{miss} performance in the ATLAS detector using 2015–2016 LHC pp collisions. ATLAS-CONF-2018-023. 2018. URL: <https://cds.cern.ch/record/2625233>.
- [100] *MET trigger performances in 2016*. URL: https://twiki.cern.ch/twiki/bin/view/AtlasPublic/MissingEtTriggerPublicResults#May_2016.
- [101] Jonathan M. et.al. *Jet substructure as a new Higgs search channel at the LHC*. arXiv: 0802.2470 [hep-ph].
- [102] Stephen D. Ellis et.al. *Recombination Algorithms and Jet Substructure: Pruning as a Tool for Heavy Particle Searches*. arXiv: 0912.0033 [hep-ph].

- [103] David Krohn, Jesse Thaler, and Lian-Tao Wang. “Jet trimming”. In: *JHEP* 02 (2010), p. 084. DOI: 10.1007/JHEP02(2010)084. arXiv: 0912.1342 [hep-ph].
- [104] ATLAS Collaboration. *Performance of Boosted W Boson Identification with the ATLAS Detector*. ATL-PHYS-PUB-2014-004. 2014. URL: <https://cds.cern.ch/record/1690048>.
- [105] ATLAS Collaboration. *ATLAS Pythia 8 tunes to 7 TeV data*. ATL-PHYS-PUB-2014-021. 2014. URL: <https://cds.cern.ch/record/1966419>.
- [106] ATLAS Collaboration. “In situ calibration of large-radius jet energy and mass in 13 TeV proton–proton collisions with the ATLAS detector”. In: *Eur. Phys. J. C* 79 (2019), p. 135. DOI: 10.1140/epjc/s10052-019-6632-8. arXiv: 1807.09477 [hep-ex].
- [107] ATLAS Collaboration. “Performance of top-quark and W-boson tagging with ATLAS in Run 2 of the LHC”. In: *Eur. Phys. J. C* 79.5 (2019), p. 375. DOI: 10.1140/epjc/s10052-019-6847-8. arXiv: 1808.07858 [hep-ex].
- [108] ATLAS Collaboration. “Jet energy measurement with the ATLAS detector in proton–proton collisions at $\sqrt{s} = 7$ TeV”. In: *Eur. Phys. J. C* 73 (2013), p. 2304. DOI: 10.1140/epjc/s10052-013-2304-2. arXiv: 1112.6426 [hep-ex].
- [109] ATLAS Collaboration. *Track Reconstruction Performance of the ATLAS Inner Detector at $\sqrt{s} = 13$ TeV*. ATL-PHYS-PUB-2015-018. 2015. URL: <https://cds.cern.ch/record/2037683>.
- [110] ATLAS Collaboration. “Performance of the ATLAS track reconstruction algorithms in dense environments in LHC Run 2”. In: *Eur. Phys. J. C* 77 (2017), p. 673. DOI: 10.1140/epjc/s10052-017-5225-7. arXiv: 1704.07983 [hep-ex].
- [111] ATLAS Collaboration. *Studies of radial distortions of the ATLAS Inner Detector*. ATL-PHYS-PUB-2018-003. 2018. URL: <https://cds.cern.ch/record/2309785>.
- [112] ATLAS Collaboration. *Public plots of in-situ large-R jet reconstruction performance*. 2016. URL: <https://atlas.web.cern.ch/Atlas/GROUPS/PHYSICS/PLOTS/JETM-2016-007/>.
- [113] Guido Altarelli, B. Mele, and M. Ruiz-Altaba. “Searching for New Heavy Vector Bosons in $p\bar{p}$ Colliders”. In: *Z. Phys.* C45 (1989). [Erratum: *Z. Phys.*C47,676(1990)], p. 109. DOI: 10.1007/BF01552335, 10.1007/BF01556677.
- [114] Andrew J. Larkoski, Duff Neill, and Jesse Thaler. “Jet Shapes with the Broadening Axis”. In: *JHEP* 04 (2014), p. 017. DOI: 10.1007/JHEP04(2014)017. arXiv: 1401.2158 [hep-ph].
- [115] ATLAS Collaboration. *Jet mass reconstruction with the ATLAS Detector in early Run 2 data*. ATLAS-CONF-2016-035. 2016. URL: <https://cds.cern.ch/record/2200211>.
- [116] Andrew J. Larkoski, Gavin P. Salam, and Jesse Thaler. “Energy Correlation Functions for Jet Substructure”. In: *JHEP* 06 (2013), p. 108. DOI: 10.1007/JHEP06(2013)108. arXiv: 1305.0007 [hep-ph].

- [117] Andrew J. Larkoski, Ian Moutl, and Duff Neill. “Power counting to better jet observables”. In: *JHEP* 12 (2014), p. 009. DOI: 10 . 1007 / JHEP12 (2014) 009. arXiv: 1409 . 6298 [hep-ph].
- [118] Jesse Thaler and Ken Van Tilburg. “Identifying Boosted Objects with N-subjettiness”. In: *JHEP* 03 (2011), p. 015. DOI: 10 . 1007 / JHEP03 (2011) 015. arXiv: 1011 . 2268 [hep-ph].
- [119] Jesse Thaler and Ken Van Tilburg. “Maximizing Boosted Top Identification by Minimizing N-subjettiness”. In: *JHEP* 02 (2012), p. 093. DOI: 10 . 1007 / JHEP02 (2012) 093. arXiv: 1108 . 2701 [hep-ph].
- [120] Geoffrey C. Fox and Stephen Wolfram. “Observables for the Analysis of Event Shapes in e+ e- Annihilation and Other Processes”. In: *Phys. Rev. Lett.* 41 (1978), p. 1581. DOI: 10 . 1103 / PhysRevLett . 41 . 1581.
- [121] Jesse Thaler and Lian-Tao Wang. “Strategies to Identify Boosted Tops”. In: *JHEP* 07 (2008), p. 092. DOI: 10 . 1088 / 1126 - 6708 / 2008 / 07 / 092. arXiv: 0806 . 0023 [hep-ph].
- [122] ATLAS Collaboration. “Measurement of k_T splitting scales in $W \rightarrow \ell\nu$ events at $\sqrt{s} = 7\text{TeV}$ with the ATLAS detector”. In: *Eur. Phys. J. C* 73 (2013), p. 2432. DOI: 10 . 1140 / epjc / s10052 - 013 - 2432 - 8. arXiv: 1302 . 1415 [hep-ex].
- [123] Leandro G. Almeida et al. “Top Jets at the LHC”. In: *Phys. Rev.* D79 (2009), p. 074012. DOI: 10 . 1103 / PhysRevD . 79 . 074012. arXiv: 0810 . 0934 [hep-ph].
- [124] ATLAS Collaboration. “ATLAS measurements of the properties of jets for boosted particle searches”. In: *Phys. Rev. D* 86 (2012), p. 072006. DOI: 10 . 1103 / PhysRevD . 86 . 072006. arXiv: 1206 . 5369 [hep-ex].
- [125] Chunhui Chen. “New approach to identifying boosted hadronically-decaying particle using jet substructure in its center-of-mass frame”. In: *Phys. Rev.* D85 (2012), p. 034007. DOI: 10 . 1103 / PhysRevD . 85 . 034007. arXiv: 1112 . 2567 [hep-ph].
- [126] S. Catani et al. “Longitudinally invariant K_t clustering algorithms for hadron hadron collisions”. In: *Nucl. Phys.* B406 (1993), pp. 187–224. DOI: 10 . 1016 / 0550 - 3213 (93) 90166 - M.
- [127] ATLAS Collaboration. *Identification of Hadronically-Decaying W Bosons and Top Quarks Using High-Level Features as Input to Boosted Decision Trees and Deep Neural Networks in ATLAS at $\sqrt{s} = 13\text{TeV}$* . ATL-PHYS-PUB-2017-004. 2017. URL: <https://cds.cern.ch/record/2259646>.
- [128] François Chollet. *Keras*. <https://github.com/fchollet/keras>. 2015.
- [129] Ian Goodfellow, Yoshua Bengio, and Aaron Courville. *Deep Learning*. <http://www.deeplearningbook.org>. MIT Press, 2016.
- [130] Diederik P. Kingma and Jimmy Ba. “Adam: A Method for Stochastic Optimization”. In: *CoRR* abs/1412.6980 (2014). arXiv: 1412 . 6980.

- [131] Xavier Glorot and Yoshua Bengio. “Understanding the difficulty of training deep feedforward neural networks”. In: *Proceedings of the Thirteenth International Conference on Artificial Intelligence and Statistics, AISTATS 2010, Chia Laguna Resort, Sardinia, Italy, May 13-15, 2010*, pp. 249–256. URL: <http://www.jmlr.org/proceedings/papers/v9/glorot10a.html>.
- [132] Sergey Ioffe and Christian Szegedy. “Batch Normalization: Accelerating Deep Network Training by Reducing Internal Covariate Shift”. In: *CoRR* abs/1502.03167 (2015). arXiv: 1502.03167.
- [133] ATLAS Collaboration. *Performance of mass-decorrelated jet substructure observables for hadronic two-body decay tagging in ATLAS*. ATL-PHYS-PUB-2018-014. 2018. URL: <https://cds.cern.ch/record/2630973>.
- [134] Vernon D. Barger et al. “Strong W^+W^+ scattering signals at pp supercolliders”. In: *Phys. Rev. D* 42 (1990), pp. 3052–3077. DOI: 10.1103/PhysRevD.42.3052.
- [135] *Data Quality Information for Data*. URL: <https://twiki.cern.ch/twiki/bin/view/AtlasPublic/RunStatsPublicResults2010>.
- [136] “COMA Period Documentation”. In: (). URL: https://atlas-tagservices.cern.ch/tagservices/RunBrowser/runBrowserReport/rBR_Period_Report.php.
- [137] ATLAS Collaboration. “Performance of the ATLAS trigger system in 2015”. In: *Eur. Phys. J. C* 77 (2017), p. 317. DOI: 10.1140/epjc/s10052-017-4852-3. arXiv: 1611.09661 [hep-ex].
- [138] T. Gleisberg et al. “Event generation with SHERPA 1.1”. In: *JHEP* 02 (2009), p. 007. DOI: 10.1088/1126-6708/2009/02/007. arXiv: 0811.4622 [hep-ph].
- [139] Tanju Gleisberg and Stefan Höche. “Comix, a new matrix element generator”. In: *JHEP* 12 (2008), p. 039. DOI: 10.1088/1126-6708/2008/12/039. arXiv: 0808.3674 [hep-ph].
- [140] Fabio Cascioli, Philipp Maierhofer, and Stefano Pozzorini. “Scattering Amplitudes with Open Loops”. In: *Phys. Rev. Lett.* 108 (2012), p. 111601. DOI: 10.1103/PhysRevLett.108.111601. arXiv: 1111.5206 [hep-ph].
- [141] Stefano Frixione, Paolo Nason, and Giovanni Ridolfi. “A Positive-weight next-to-leading-order Monte Carlo for heavy flavour hadroproduction”. In: *JHEP* 09 (2007), p. 126. DOI: 10.1088/1126-6708/2007/09/126. arXiv: 0707.3088 [hep-ph].
- [142] Simone Alioli et al. “NLO single-top production matched with shower in POWHEG: s- and t-channel contributions”. In: *JHEP* 09 (2009). [Erratum: *JHEP* 02 (2010) 011], p. 111. DOI: 10.1007/JHEP02(2010)011, 10.1088/1126-6708/2009/09/111. arXiv: 0907.4076 [hep-ph].
- [143] Rikkert Frederix, Emanuele Re, and Paolo Torrielli. “Single-top t-channel hadroproduction in the four-flavour scheme with POWHEG and aMC@NLO”. In: *JHEP* 09 (2012), p. 130. DOI: 10.1007/JHEP09(2012)130. arXiv: 1207.5391 [hep-ph].

- [144] Emanuele Re. “Single-top Wt-channel production matched with parton showers using the POWHEG method”. In: *Eur. Phys. J. C* 71 (2011), p. 1547. DOI: 10.1140/epjc/s10052-011-1547-z. arXiv: 1009.2450 [hep-ph].
- [145] D. J. Lange. “The EvtGen particle decay simulation package”. In: *Nucl. Instrum. Meth. A* 462 (2001), p. 152. DOI: 10.1016/S0168-9002(01)00089-4.
- [146] Torbjorn Sjöstrand, Stephen Mrenna, and Peter Z. Skands. “PYTHIA 6.4 physics and manual”. In: *JHEP* 05 (2006), p. 026. DOI: 10.1088/1126-6708/2006/05/026. arXiv: hep-ph/0603175.
- [147] Stefan Höche et al. “NLO matrix elements and truncated showers”. In: *JHEP* 08 (2011), p. 123. DOI: 10.1007/JHEP08(2011)123. arXiv: 1009.1127 [hep-ph].
- [148] M. Czakon, P. Fiedler, and A. Mitov. “Total Top-Quark Pair-Production Cross Section at Hadron Colliders Through $O(\alpha_s^4)$ ”. In: *Phys. Rev. Lett.* 110 (2013), p. 252004. DOI: 10.1103/PhysRevLett.110.252004. arXiv: 1303.6254 [hep-ph].
- [149] Michal Czakon and Alexander Mitov. “Top++: A program for the calculation of the top-pair cross-section at hadron colliders”. In: *Comp. Phys. Comm.* 185 (2014), p. 2930. DOI: 10.1016/j.cpc.2014.06.021. arXiv: 1112.5675 [hep-ph].
- [150] N. Kidonakis. “NNLL resummation for s-channel single top quark production”. In: *Phys. Rev. D* 81 (2010), p. 054028. DOI: 10.1103/PhysRevD.81.054028. arXiv: 1001.5034 [hep-ph].
- [151] N. Kidonakis. “Two-loop soft anomalous dimensions for single top quark associated production with a W^- or H^- ”. In: *Phys. Rev. D* 82 (2010), p. 054018. DOI: 10.1103/PhysRevD.82.054018. arXiv: 1005.4451 [hep-ph].
- [152] ATLAS Collaboration. “The ATLAS Simulation Infrastructure”. In: *Eur. Phys. J. C* 70 (2010), p. 823. DOI: 10.1140/epjc/s10052-010-1429-9. arXiv: 1005.4568 [physics.ins-det].
- [153] S. Agostinelli et al. “GEANT4: A simulation toolkit”. In: *Nucl. Instrum. Meth. A* 506 (2003), pp. 250–303. DOI: 10.1016/S0168-9002(03)01368-8.
- [154] ATLAS Collaboration. “Searches for heavy ZZ and ZW resonances in the $\ell\ell q\bar{q}$ and $\nu\nu q\bar{q}$ final states in pp collisions at $\sqrt{s} = 13$ TeV with the ATLAS detector”. In: *JHEP* 03 (2018), p. 009. DOI: 10.1007/JHEP03(2018)009. arXiv: 1708.09638 [hep-ex].
- [155] “ROOT - An Object Oriented Data Analysis Framework”. In: *Proceedings AIHENP’96 Workshop, Lausanne, Sep. 1996*. Vol. 389. 1997, pp. 81–86. URL: <http://root.cern.ch/>.
- [156] ATLAS Collaboration. *Discrimination between Light Quark and Gluon Jets in pp collisions at $\sqrt{s} = 8$ TeV with the ATLAS Detector*. ATLAS-CONF-2016-034. 2016. URL: <https://cds.cern.ch/record/2200202>.
- [157] ATLAS Collaboration. *Proposal for particle-level object and observable definitions for use in physics measurements at the LHC*. ATL-PHYS-PUB-2015-013. 2015. URL: <https://cds.cern.ch/record/2022743>.

- [158] Jun Gao et al. “CT10 next-to-next-to-leading order global analysis of QCD”. In: *Phys. Rev. D* 89.3 (2014), p. 033009. DOI: 10.1103/PhysRevD.89.033009. arXiv: 1302.6246 [hep-ph].
- [159] L. A. Harland-Lang et al. “Parton distributions in the LHC era: MMHT 2014 PDFs”. In: *Eur. Phys. J. C* 75.5 (2015), p. 204. DOI: 10.1140/epjc/s10052-015-3397-6. arXiv: 1412.3989 [hep-ph].
- [160] ATLAS Collaboration. “Measurement of the cross-section for producing a W boson in association with a single top quark in pp collisions at $\sqrt{s} = 13$ TeV with ATLAS”. In: *JHEP* 01 (2018), p. 063. DOI: 10.1007/JHEP01(2018)063. arXiv: 1612.07231 [hep-ex].
- [161] Ayana Arce and Christoph Anders. *Jet Substructure Status 09/02/2015*. URL: https://indico.cern.ch/event/441619/contributions/1099656/attachments/1148550/1647846/Jet_Substructure_Status_09_02_2015-Updated.pdf.
- [162] ATLAS Collaboration. “Combined search for the Standard Model Higgs boson in pp collisions at $\sqrt{s} = 7$ TeV with the ATLAS detector”. In: *Phys. Rev. D* 86 (2012), p. 032003. DOI: 10.1103/PhysRevD.86.032003. arXiv: 1207.0319 [hep-ex].
- [163] Wouter Verkerke and David P. Kirkby. “The RooFit toolkit for data modeling”. In: (2003). arXiv: physics/0306116 [physics.data-an].
- [164] Lorenzo Moneta et al. “The RooStats Project”. In: (2010). arXiv: 1009.1003 [physics.data-an].
- [165] T. Junk. “Confidence level computation for combining searches with small statistics”. In: *Nucl. Instrum. Meth. A* 434 (1999), pp. 435–443. arXiv: 9902006.
- [166] G. Cowan et. al. “Asymptotic formulae for likelihood-based tests of new physics”. In: *Eur. Phys. J. C* 75 (2011), p. 153. arXiv: 1007.1727 [hep-ex].
- [167] A. Wald. “Tests of statistical hypotheses concerning several parameters when the number of observations is large”. In: *Transactions of the American Mathematical Society* 54 (1943), pp. 426–482.
- [168] ATLAS Collaboration. “Search for WW/WZ resonance production in $\ell\nu qq$ final states in pp collisions at $\sqrt{s} = 13$ TeV with the ATLAS detector”. In: *JHEP* 03 (2018), p. 042. DOI: 10.1007/JHEP03(2018)042. arXiv: 1710.07235 [hep-ex].
- [169] ATLAS Collaboration. “Evidence for Electroweak Production of $W^\pm W^\pm jj$ in pp Collisions at $\sqrt{s} = 8$ TeV with the ATLAS Detector”. In: *Phys. Rev. Lett.* 113 (2014), p. 141803. DOI: 10.1103/PhysRevLett.113.141803. arXiv: 1405.6241 [hep-ex].
- [170] CMS Collaboration. “Search for W boson decays to three charged pions”. In: *Phys. Rev. Lett.* (2019). arXiv: 1901.11201 [hep-ex].
- [171] Kumar Rao et. al. *W boson polarization as a measure of gauge-Higgs anomalous couplings at the LHC*. 2018. eprint: <https://arxiv.org/pdf/1805.06602.pdf>.
- [172] ATLAS Collaboration. “Search for diboson resonances with boson-tagged jets in pp collisions at $\sqrt{s} = 13$ TeV with the ATLAS detector”. In: *Phys. Lett. B* 777 (2018), p. 91. DOI: 10.1016/j.physletb.2017.12.011. arXiv: 1708.04445 [hep-ex].

- [173] ATLAS Collaboration. “Measurement of the W boson polarisation in $t\bar{t}$ events from pp collisions at $\sqrt{s} = 8$ TeV in the lepton+jets channel with ATLAS”. In: *Eur. Phys. J. C* 77 (2017), p. 264. DOI: 10.1140/epjc/s10052-017-4819-4. arXiv: 1612.02577 [hep-ex].
- [174] ATLAS Collaboration. *Performance and Calibration of the JetFitterCharm Algorithm for c-Jet Identification*. ATL-PHYS-PUB-2015-001. 2015. URL: <https://cds.cern.ch/record/1980463>.
- [175] Andrzej Czarnecki et.al. *Helicity fractions of W bosons from top quark decays at NNLO in QCD*. May 2010. eprint: <https://arxiv.org/pdf/1005.2625.pdf>.

Publication List

Selected Publications

1. T. Nitta et. al., ATLAS Collaboration, “Search for the electroweak diboson production in association with a high-mass dijet system in semileptonic final states in pp collisions at $\sqrt{s} = 13$ TeV with the ATLAS detector”, *Phys. Rev. D*, 100, 032007, 2019
2. T. Nitta et. al., ATLAS Collaboration, “In situ calibration of large-R jet energy and mass in 13 TeV proton-proton collisions with the ATLAS detector”, *The European Physical Journal C*, 79, 135, 2019
3. T. Nitta et. al., ATLAS Collaboration, “Performance of top-quark and W-boson tagging with ATLAS in Run 2 of the LHC”, *The European Physical Journal C*, 79, 375, 2019

Selected Public Analysis Note

1. T. Nitta et. al., ATLAS Collaboration, Identification of Hadronically-Decaying W Bosons and Top Quarks Using High-Level Features as Input to Boosted Decision Trees and Deep Neural Networks in ATLAS at $\sqrt{s} = 13$ TeV, ATL-PHYS-PUB-2017-004

Conference Proceedings

1. Tatsumi Nitta for the ATLAS Collaboration, “Identification of hadronically decaying W bosons and top quarks using multivariate techniques at ATLAS”, ACAT2017, *Journal of Physics: Conference Series*, 1085, 042012, 2017
2. Tatsumi Nitta for the ATLAS Collaboration, “Vector boson scattering, triple gauge-boson final states and limits on anomalous quartic gauge couplings with the ATLAS detector”, *Proceedings of Science, PoS(DIS2018)*, 101, 2018

Conference Talks

1. Tatsumi Nitta for the ATLAS Collaboration, “Identification of hadronically decaying W bosons and top quarks using multivariate techniques at ATLAS”, ACAT2017, Seattle, United States, August 2017
2. Tatsumi Nitta for the ATLAS Collaboration, “Vector boson scattering, triple gauge-boson final states and limits on anomalous quartic gauge couplings with the ATLAS detector”, DIS2018, Kobe, Japan, April 2018

Conference Poster

1. Tatsumi Nitta for the ATLAS Collaboration, “Identification of Hadronically-Decaying W Boson Top Quarks Using High-Level Features as Input to Boosted Decision Trees and Deep Neural Networks in ATLAS at \sqrt{s} 13 Te”, BOOST2017, Buffalo, United States, July, 2017

Invited Seminar

1. Tatsumi Nitta, “Search for Vector Boson Scattering with W/Z boson jet at ATLAS”, CEMPA Seminar, University of Washington, February, 2019